Publishing House ASV

begell house, inc. publishers

Scientific coordination is carried out by the Russian Academy of Architecture and Construction Sciences (RAACS)

Volume 22 • Issue 2 • 2026

ISSN 2588-0195 (Online)
ISSN 2587-9618 (Print) Continues ISSN 1524-5845

International Journal for

Computational Civil and Structural Engineering

Международный журнал по расчету гражданских и строительных конструкций

https://ijccse.iasv.ru/

DOI: 10.22337/2587-9618
GICID: 71.0000.1500.2830

PUBLISHER

ASV Publishing House
(ООО «Издательство АСВ»)
19/1,12, Yaroslavskoe Shosse, 120338, Moscow, Russia
Tel. +7(925)084-74-24; E-mail: iasv@iasv.ru; Интернет-сайт: http://iasv.ru/

ADVISORY EDITORIAL BOARD

TECHNICAL EDITOR

EDITORIAL TEAM

INVITED REVIEWERS

AIMS AND SCOPE

The aim of the Journal is to advance the research and practice in structural engineering through the application of computational methods. The Journal will publish original papers and educational articles of general value to the field that will bridge the gap between high-performance construction materials, large-scale engineering systems and advanced methods of analysis.

The scope of the Journal includes papers on computer methods in the areas of structural engineering, civil engineering materials and problems concerned with multiple physical processes interacting at multiple spatial and temporal scales. The Journal is intended to be of interest and use to researches and practitioners in academic, governmental and industrial communities.

ОБЩАЯ ИНФОРМАЦИЯ О ЖУРНАЛЕ

International Journal for Computational Civil and Structural Engineering

(Международный журнал по расчету гражданских и строительных конструкций)

Международный научный журнал "International Journal for Computational Civil and Structural Engineering (Международный журнал по расчету гражданских и строительных конструкций)" (IJCCSE) является ведущим научным периодическим изданием по направлению «Инженерные и технические науки», издаваемым, начиная с 1999 года (ISSN 2588-0195 (Online); ISSN 2587-9618 (Print) Continues ISSN 1524-5845). В журнале на высоком научно-техническом уровне рассматриваются проблемы численного и компьютерного моделирования в строительстве, актуальные вопросы разработки, исследования, развития, верификации, апробации и приложений численных, численно-аналитических методов, программно-алгоритмического обеспечения и выполнения автоматизированного проектирования, мониторинга и комплексного наукоемкого расчетно-теоретического и экспериментального обоснования напряженно-деформированного (и иного) состояния, прочности, устойчивости, надежности и безопасности ответственных объектов гражданского и промышленного строительства, энергетики, машиностроения, транспорта, биотехнологий и других высокотехнологичных отраслей.

В редакционный совет журнала входят известные российские и зарубежные деятели науки и техники (в том числе академики, члены-корреспонденты, иностранные члены, почетные члены и советники Российской академии архитектуры и строительных наук). Основной критерий отбора статей для публикации в журнале − их высокий научный уровень, соответствие которому определяется в ходе высококвалифицированного рецензирования и объективной экспертизы, поступающих в редакцию материалов.

Журнал входит в Перечень ВАК РФ ведущих рецензируемых научных изданий, в которых должны быть опубликованы основные научные результаты диссертаций на соискание ученой степени кандидата наук, на соискание ученой степени доктора наук по научным специальностям и соответствующим им отраслям науки:

- 1.1.8 – Механика деформируемого твердого тела (технические науки),
- 1.2.2 – Математическое моделирование численные методы и комплексы программ (технические науки),
- 2.1.1 – Строительные конструкции, здания и сооружения (технические науки),
- 2.1.2 – Основания и фундаменты, подземные сооружения (технические науки),
- 2.1.5 – Строительные материалы и изделия (технические науки),
- 05.23.07 – Гидротехническое строительство (технические науки),
- 2.1.9 – Строительная механика (технические науки)

В Российской Федерации журнал индексируется Российским индексом научного цитирования (РИНЦ).

Журнал входит в базу данных Russian Science Citation Index (RSCI), полностью интегрированную с платформой Web of Science. Журнал имеет международный статус и высылается в ведущие библиотеки и научные организации мира.

Издатели журнала – *Издательство Ассоциации строительных высших учебных заведений /АСВ/* (Россия, г. Москва) и до 2017 года *Издательский дом Begell House Inc*. (США, г. Нью-Йорк). Официальными партнерами издания является *Российская академия архитектуры и строительных наук* (РААСН), осуществляющая научное курирование издания, и *Научно-исследовательский центр СтаДиО* (ЗАО НИЦ СтаДиО).

Цели журнала – демонстрировать в публикациях российскому и международному профессиональному сообществу новейшие достижения науки в области вычислительных методов решения фундаментальных и прикладных технических задач, прежде всего в области строительства.

Задачи журнала:

• предоставление российским и зарубежным ученым и специалистам возможности публиковать результаты своих исследований;

• привлечение внимания к наиболее актуальным, перспективным, прорывным и интересным направлениям развития и приложений численных и численно-аналитических методов решения фундаментальных и прикладных технических задач, совершенствования технологий математического, компьютерного моделирования, разработки и верификации реализующего программно-алгоритмического обеспечения;

• обеспечение обмена мнениями между исследователями из разных регионов и государств.

Тематика журнала. К рассмотрению и публикации в журнале принимаются аналитические материалы, научные статьи, обзоры, рецензии и отзывы на научные публикации по фундаментальным и прикладным вопросам технических наук, прежде всего в области строительства. В журнале также публикуются информационные материалы, освещающие научные мероприятия и передовые достижения Российской академии архитектуры и строительных наук, научно-образовательных и проектно-конструкторских организаций.

Тематика статей, принимаемых к публикации в журнале, соответствует его названию и охватывает направления научных исследований в области разработки, исследования и приложений численных и численно-аналитических методов, программного обеспечения, технологий компьютерного моделирования в решении прикладных задач в области строительства, а также соответствующие профильные специальности, представленные в диссертационных советах профильных образовательных организациях высшего образования.

Редакционная политика. Политика редакционной коллегии журнала базируется на современных юридических требованиях в отношении авторского права, законности, плагиата и клеветы, изложенных в законодательстве Российской Федерации, и этических принципах, поддерживаемых сообществом ведущих издателей научной периодики.

За публикацию статей плата с авторов не взымается. Публикация статей в журнале бесплатная. На платной основе в журнале могут быть опубликованы материалы рекламного характера, имеющие прямое отношение к тематике журнала.

Журнал предоставляет непосредственный открытый доступ к своему контенту, исходя из следующего принципа: свободный открытый доступ к результатам исследований способствует увеличению глобального обмена знаниями.

Индексирование. Публикации в журнале входят в системы расчетов индексов цитирования авторов и журналов. «Индекс цитирования» – числовой показатель, характеризующий значимость данной статьи и вычисляющийся на основе последующих публикаций, ссылающихся на данную работу.

Авторам. Прежде чем направить статью в редакцию журнала, авторам следует ознакомиться со всеми материалами, размещенными в разделах сайта журнала (интернет-сайт Российской академии архитектуры и строительных наук (http://raasn.ru); подраздел «Издания РААСН» или интернет-сайт Издательства АСВ (http://iasv.ru); подраздел «Журнал IJCCSE»): с основной информацией о журнале, его целями и задачами, составом редакционной коллегии и редакционного совета, редакционной политикой, порядком рецензирования направляемых в журнал статей, сведениями о соблюдении редакционной этики, о политике авторского права и лицензирования, о представлении журнала в информационных системах (индексировании), информацией о подписке на журнал, контактными данными и пр. Журнал работает по лицензии Creative Commons типа cc by-nc-sa (Attribution Non-Commercial Share Alike) – Лицензия «С указанием авторства – Некоммерческая – Копилефт».

Рецензирование. Все научные статьи, поступившие в редакцию журнала, проходят обязательное двойное слепое рецензирование (рецензент не знает авторов рукописи, авторы рукописи не знают рецензентов).

Заимствования и плагиат. Редакционная коллегия журнала при рассмотрении статьи проводит проверку материала с помощью системы «Антиплагиат». В случае обнаружения многочисленных заимствований редакция действует в соответствии с правилами COPE.

Подписка. Журнал зарегистрирован в Федеральном агентстве по средствам массовой информации и охраны культурного наследия Российской Федерации. Индекс в общероссийском каталоге РОСПЕЧАТЬ − 18076.

По вопросам подписки на международный научный журнал “International Journal for Computational Civil and Structural Engineering (Международный журнал по расчету гражданских и строительных конструкций)” обращайтесь в Агентство «Роспечать» (Официальный сайт в сети Интернет: http://www.rosp.ru/) или в издательство Ассоциации строительных вузов (АСВ) в соответствии со следующими контактными данными:

ООО «Издательство АСВ»

Юридический адрес: 129337, Россия, г. Москва, Ярославское ш., д. 26, офис 705;

Фактический адрес: 129337, Россия, г. Москва, Ярославское ш., д. 19, корп. 1, 5 этаж, офис 12 (ТЦ Соле Молл);

Телефоны: +7 (925) 084-74-24;

Интернет-сайт: www.iasv.ru. Адрес электронной почты: iasv@iasv.ru.

Контактная информация. По всем вопросам работы редакции, рецензирования, согласования правки текстов и публикации статей следует обращаться к главному редактору журнала академику РААСН *Сидорову Владимиру Николаевичу* (адреса электронной почты: sidorov.vladimir@gmail.com, sidorov@iasv.ru, iasv@iasv.ru, sidorov@raasn.ru) или к техническому редактору журнала советнику РААСН *Кайтукову Таймуразу Батразовичу* (адреса электронной почты: tkaytukov@gmail.com; kaytukov@raasn.ru). Кроме того, по указанным вопросам, а также по вопросам размещения в журнале рекламных материалов можно обращаться к генеральному директору ООО «Издательство АСВ» *Никитиной Надежде Сергеевне* (адреса электронной почты: iasv@iasv.ru, nsnikitina@mail.ru, ijccse@iasv.ru).

Журнал становится технологичнее. Издательство АСВ с сентября 2016 года является членом Международной ассоциации издателей научной литературы (Publishers International Linking Association (PILA)), осуществляющей свою деятельность на платформе CrossRef. Оригинальным статьям, публикуемым в журнале, будут присваиваться уникальные номера (индексы DOI – Digital Object Identifier), что значительно облегчит поиск метаданных и местонахождение полнотекстового произведения. DOI – это система определения научного контента в сети Интернет.

С октября 2016 года стал возможен прием статей на рассмотрение и рецензирование через онлайн систему приема статей Open Journal Systems на сайте журнала (электронная редакция): https://ijccse.iasv.ru.

Автор имеет возможность следить за продвижением статьи в редакции журнала в личном кабинете Open Journal Systems и получать соответствующие уведомления по электронной почте.

В феврале 2018 года журнал был зарегистрирован в Directory of open access journals (DOAJ) (это один из самых известных поисковых сервисов в мире, который предоставляет открытый доступ к материалам и индексирует не только заголовки журналов, но и научные статьи), в сентябре 2018 года включен в продукты EBSCO Publishing.

В ноябре 2020 года журнал начал индексироваться в международной базе Scopus.

Журнал International Journal for Computational Civil and Structural Engineering входит в первый уровень Единого государственного перечня научных изданий – «Белого списка» – Министерства Науки и высшего образования Российской Федерации (ЕГПНИ)

International Journal for
Computational Civil and Structural Engineering
(Международный журнал по расчету гражданских и строительных конструкций)
Volume 22, Issue 2 ***2026***

Scientific coordination is carried out by the Russian Academy of Architecture and Construction Sciences (RAACS)

CONTENTS

International Journal for
Computational Civil and Structural Engineering
(Международный журнал по расчету гражданских и строительных конструкций)
Volume 22, Issue 2 ***2026***

Scientific coordination is carried out by the Russian Academy of Architecture and Construction Sciences (RAACS)

СОДЕРЖАНИЕ

DOI:10.22337/2587-9618-2026-22-2-14-31

STUDY OF THE DEFORMATION CHARACTERISTICS AND CREEP COEFFICIENT OF HIGH-STRENGTH SELF-COMPACTING HEAVY-WEIGHT AND LIGHT-WEIGHT CONCRETES AT VARIOUS RELATIVE HUMIDITY OF THE ENVIRONMENT

Semyon S. Kaprielov [1,2], Pyotr D. Arleninov [1,2], Andrey V. Sheinfeld [1,2], Polina S. Kalmakova [1,2], Nikita M. Selyutin[1,3]

[1] A.A. Gvozdev Research, Design, and Technological Institute of Concrete and Reinforced Concrete, JSC Research Center Construction, Moscow, RUSSIA
[2] National Research Moscow State University of Civil Engineering, Moscow, RUSSIA
[3] Master Beton Enterprise LLC, Moscow, RUSSIA

Abstract: The paper presents the results of an experimental study of the characteristics of high-strength self-compacting heavyweight and lightweight concretes of strength classes B60–B100 at different ambient relative humidity levels. The aim of the study was to evaluate the effect of environmental humidity on strength, elastic modulus, shrinkage and creep strains, creep compliance, and creep coefficient of high-strength self-compacting modified concretes. The tests were carried out in accordance with GOST 24452 and GOST 24544 in climatic chambers at relative air humidity levels of 20, 60, and 90% for 240 days. A formula for the numerical determination of the creep coefficient is proposed and recommended for inclusion in GOST 24544. It was found that a decrease in ambient relative humidity may lead to an increase in creep strains by more than 1.7 times. It is shown that the calculation procedure specified in GOST 24544 may, in some cases, overestimate ultimate creep strains, with the overestimation becoming more pronounced as the concrete strength class increases and the ambient humidity decreases. The creep coefficient values of high-strength heavyweight and lightweight concretes do not exceed 1 and are more than two times lower than the standard values specified in SP 63.13330.2018 and EN 12390. The obtained results demonstrate that experimental determination of creep coefficients can significantly improve the efficiency of using modern modified concretes in the construction of unique buildings and structures.

Keywords: high-strength concrete; self-compacting concrete; lightweight concrete; heavyweight concrete relative humidity; shrinkage; creep; creep coefficient; elastic modulus; long-term deformations

ИССЛЕДОВАНИЕ ДЕФОРМАЦИОННЫХ ХАРАКТЕРИСТИК И КОЭФФИЦИЕНТА ПОЛЗУЧЕСТИ ВЫСОКОПРОЧНЫХ САМОУПЛОТНЯЮЩИХСЯ ТЯЖЕЛЫХ И ЛЕГКИХ БЕТОНОВ ПРИ РАЗНОЙ ОТНОСИТЕЛЬНОЙ ВЛАЖНОСТИ ОКРУЖАЮЩЕЙ СРЕДЫ

С.С. Каприелов [1,2], П.Д. Арленинов [1,2], А.В. Шейнфельд [1,2], П.С. Калмакова [1,2], Н.М. Селютин [1,3]

[1] Научно-исследовательский, проектно-конструкторский и технологический институт бетона и железобетона им А.А. Гвоздева АО «НИЦ «Строительство», г. Москва, РОССИЯ
[2] Национально-исследовательский Московский Государственный Строительный Университет, г. Москва, РОССИЯ
[3] ООО «Предприятие Мастер Бетон», г. Москва, РОССИЯ

Аннотация: В статье представлены результаты экспериментального исследования характеристик высокопрочных самоуплотняющихся тяжелых и легких бетонов классов B60–B100 при различной относительной влажности окружающей среды. Цель работы заключалась в оценке влияния влажности среды на прочность,

модуль упругости, деформации усадки и ползучести, меру ползучести и коэффициент ползучести высокопрочных самоуплотняющихся модифицированных бетонов. Испытания выполнялись по ГОСТ 24452 и ГОСТ 24544 в климатических камерах при относительной влажности воздуха 20, 60 и 90 % в течение 240 суток. Предложена формула для численного определения коэффициента ползучести, которую рекомендуется внести в ГОСТ 24544. Установлено, что снижение относительной влажности среды может приводить к увеличению деформаций ползучести более чем в 1,7 раза. Показано, что расчетная методика ГОСТ 24544 в ряде случаев завышает предельные деформации ползучести, причем в большей степени при повышении класса бетона и снижении влажности среды. Значения коэффициентов ползучести высокопрочных тяжелых и легких бетонов не превышают 1 и более чем в 2 раза ниже нормативных значений по СП 63.13330.2018 и EN 12390. Полученные результаты показали, что экспериментальное определение коэффициентов ползучести, позволит значительно повысить эффективность использования современных модифицированных бетонов при строительстве уникальных зданий и сооружений.

Ключевые слова: высокопрочный бетон; самоуплотняющийся бетон; легкий бетон; тяжелый бетон; относительная влажность; усадка; ползучесть; коэффициент ползучести; модуль упругости; длительные деформации

INTRODUCTION

High-strength concretes based on highly fluid and self-compacting concrete mixes are currently widely used in civil, industrial, and transportation construction, both in reinforced concrete and steel-reinforced concrete structures [1–3]. However, while the influence of various technological factors on the structure, strength, and corrosion characteristics of these concretes has been sufficiently studied [4–7], the influence of service conditions—primarily relative humidity—on long-term deformation characteristics still requires further investigation [8–10].

The consideration of the long-term deformation characteristics of concrete in the design of reinforced concrete structures according to SP 63. 13330.2018 is achieved by reducing the initial modulus of elasticity of concrete according to Equation (1) using a creep coefficient that depends on the concrete's compressive strength class and the relative humidity of the ambient air.

$$E_{b,\tau}=\frac{E_b}{1+\varphi_{b,cr}} \quad (1)$$

where:

E_b is the modulus of elasticity of concrete, MPa

$E_{b,\tau}$ is the effective deformation modulus of concrete under long-term loading, MPa;

$\varphi_{b,cr}$ is the creep coefficient

The creep coefficient $\varphi_{b,cr}$ is a parameter that reflects the ratio of ultimate plastic strains to elastic strains. It should be noted that no regulatory document in the Russian Federation contains a formula that expresses the physical meaning of the creep coefficient ($\varphi_{b,cr}$). However, in [11], it is derived by substituting the ratios of stresses to strains (2) for the initial modulus of elasticity and the modulus of deformation under sustained loading, provided that the concrete specimens are subjected to the same loading level during testing in accordance with GOST 24452 and GOST 24544.

$$E_b=\frac{\sigma}{\varepsilon_{el}}, \quad E_{b,\tau}=\frac{\sigma}{\varepsilon_{cr}+\varepsilon_{el}}, \quad (2)$$

where:

σ is the stress in a concrete specimen during short-term tests for elastic modulus and long-term tests for concrete creep, MPa;

ε_{el} is the elastic component of strains when loading a concrete specimen to a constant stress σ in accordance with GOST 24452, when setting it up for long-term tests to determine concrete creep;

ε_{cr} - ultimate creep strains of concrete obtained under long-term stresses σ in the specimen according to GOST 24544.

Then, the formula for determining the creep coefficient is expressed as in (3), confirming its physical meaning, which lies in the ratio of the ultimate creep strains to the elastic strains of the concrete.

$$\varphi_{b,cr}=\frac{\varepsilon_{cr}}{\varepsilon_{el}}, \quad (3)$$

The method for determining the ultimate creep strains of concrete is specified in GOST 24544 and is based on probabilistic prediction of the behavior of the decay curve of creep obtained from tests lasting 180 days, assuming an infinitely long time. For this purpose, this function is linearized from the ε–t coordinates to the t/ε–t coordinates. After constructing a regression line in these coordinates, the ultimate value of the creep strains is determined as the cotangent of the angle of inclination of this line to the x-axis (t). This method of extrapolating deformation curves over time is not new. It was actively used by O. Ya. Berg [8] in the 1970s, but was first proposed as early as the 1950s [12]. This approach first appeared in GOST 24544 in 1981, as at that time it yielded satisfactory results that, on the whole, did not contradict physical concepts regarding the nature of concrete creep. It has remained unchanged since then. However, the values of the ultimate creep strains of modified high-strength concretes obtained using this approach do not always correspond to experimental data for longer test durations, as will be shown below.

Consider the evolution of the creep coefficient values for concrete, including high-strength concrete, in the regulatory documents of the USSR and Russia.

In 2002–2003, at the A.A. Gvozdev Research Institute of Civil Engineering Structures, A.S. Zalesov, V.A. Klevtsov, and V.V. Shugaev conducted a review of foreign literature, based on which the creep coefficient $\varphi_{b,cr}$ for high-strength concrete of class B60 was adopted at the following relative humidity levels: over 75%—1.0, at 40–75% – 1.4, and at less than 40% – 2.0. These values were included in the subsequently published SP 52-01-2003 for B60-class concrete. As a precaution, the authors recommended extending these values to higher concrete classes up to B100 [13].

As the Russian construction industry was already producing high-strength concretes of classes B60–B100 in the early 2000s, and these were in demand for the construction of reinforced concrete structures for unique buildings, and there were no large-scale experimental studies of the long-term deformation characteristics of such concretes, based on the above review, the creep coefficient values for B60 concrete were extended in SP 63.13330.2012 to high-strength concretes of classes B70–B100. Since then, the creep coefficients φ_{bcr} for high-strength concretes of classes B60 to B100, as specified in the currently valid standard SP 63.13330.2018, have remained unchanged.

Over the past 20 years, Russian researchers have published data on the long-term deformation characteristics of high-strength heavy concretes of classes up to B80 [9, 10, 13], which are not fully reflected in regulatory documents. However, that the standards of the European Committee on Concrete, as well as the regulatory documents of Norway, Finland, the Netherlands, and Sweden already contained extensive information on heavy-duty concrete of classes B90–B100; German standards already included information on concrete up to class B115; and the Model Code 2010 already included characteristics for concrete up to class B120.

The importance of differentiating the creep coefficient has already been noted by many experts [14, 15], since the constant values of creep coefficients adopted in current codes which are overestimated for classes B70–B100 on the one hand, assume an insufficiently justified increased deformability of building frame elements. To compensate for this, an increase in the cross-sections of the elements is required. On the other hand, the actual redistribution of forces changes in rigid joints, which will already lead to a distortion of the calculation results relative to the actual stress-strain state (SSS) of the building.

As high-strength, self-compacting lightweight structural concretes of classes B60–B70 with an average density grade of D1800–D2000 were developed in Russia in 2023 [4, 16, 17, 18], evaluating the deformation characteristics of such concretes in comparison with those of heavy concretes will provide a more complete view of the behavior of high-strength modified concretes under long-term loading.

This is relevant because, as noted in publications [18–21], concretes of equal strength may differ significantly in their deformation characteristics (modulus of elasticity, ultimate strains, shrinkage and creep strains, etc.) depending on technological factors. At the same time, it should be admitted that publications containing data on the influence of ambient relative

humidity on the long-term characteristics of high-strength concretes are few in number [22].

Therefore, the objective of this study was to conduct comparative long-term tests in accordance with GOST 24452 and GOST 24544 on high-strength, self-compacting modified heavy and lightweight concretes of classes B60–B100, determining their strength, initial modulus of elasticity, shrinkage and creep deformations, as well as the creep coefficient, using various methods for calculating ultimate creep deformations at different relative ambient humidity levels (20, 60, and 90% in accordance with the classification in SP 63.13330.2018).

2. MATERIALS AND TEST METHODS

To produce high-strength self-compacting concrete, materials (Portland cement, organomineral modifier, microfiller, aggregates) were used that are mass-produced in the Russian Federation and are employed in the production of concrete mixes for various construction projects, including:

- Portland cement CEM I 42.5 ZHI, compliant with the requirements of GOST R 55224;
- MB10-50S A-II-2 organomineral concrete modifier, comprising microsilica (45%), fly ash (45%), and superplasticizer (10%), complying with the requirements of GOST R 56178;
- Microfiller – non-activated mineral powder (ground limestone) grade MP-1, 0–1.25 mm fraction, complying with the requirements of GOST R 52129 and GOST R 56592;
- Class I quartz sand with a particle size modulus of M_{kr} = 2.42, meeting the requirements of GOST 8736;
- Granite crushed stone, 5–10 mm fraction, meeting the requirements of GOST 8267;
- expanded clay gravel, 5–10 mm fraction, bulk density grade M500, strength grade P125, average density 910 kg/m³, complying with the requirements of GOST 32496;
- water, complying with the requirements of GOST 23732.

Under laboratory conditions, self-compacting concrete mixtures were prepared from the above materials, including three heavy concrete mixes of classes B70, B80, and B100, and one lightweight concrete mix of class B60, with a cement content of 349 –495 kg/m³, with the addition of the organomineral modifier MB10-50S in an amount ranging from 14 to 26% of the cement mass and a water-to-cement ratio (W/(C+MB)) ranging from 0.23 to 0.39.

It is worth noting that B60 lightweight concrete has approximately the same composition and volume of cement paste as B100 heavy concrete, and the reduction in average density is achieved by replacing 0.254 m³ of heavy granite crushed stone with a density of 2,700 kg/m³ with lightweight expanded clay gravel with an average density of 910 kg/m³ [23]. At the same time, the true water-cement ratio will also be approximately the same, due to the higher water demand of porous expanded clay gravel, whose water absorption is 14.5% by mass.

The compositions and properties of self-compacting concrete mixtures are presented in Table 1.

Table 1. Compositions and Properties of Self-Compacting Concrete Mixes

Composition No.	Compositions and Properties of Self-Compacting Concrete Mixes, kg/m³							Properties of Self-Compacting Concrete Mixes			
	C	MB	MP	S	CS	GEC	W	SF, cm	ρ, kg/m³	V_{cs}, m³/m³	W/(C+MB)
1	349	50	150	818	868	-	155	63	2390	0.351	0.39
2	444	99	0	809	808	-	146	60	2405	0.334	0.27
3	497	129	0	745	914	-	144	62	2430	0.363	0.23
4	495	105	0	743	229	218	160	57	1950	0.355	0.27

Notes: C – Portland cement; MB – organo-mineral modifier; MP – microfiller; S – sand; CS – granite crushed stone; GEC – expanded clay gravel; W – water; SF – standard cone slump; ρ – average density of the concrete mix; Vcs – volume of cement paste; W/(C+MB) – water-cement ratio.

The mixtures were prepared in a 0.050 m³ forced-action mixer and mixed for 5 minutes.

The test results for the mixtures showed (Table 1) that the average density of the heavy concrete mixtures falls within a narrow range of 2390–2430 kg/m³ and meets the requirements of GOST 26633 (2000–2600 kg/m³), while the average density of the lightweight concrete mixture is 1950 kg/m³ and meets the requirements of GOST 25820 (no more than 2000 kg/m³).

The slump of all mixtures, determined by the spread of a standard cone according to GOST R 59715, ranges from 57 to 63 cm. This allows them to be classified as self-compacting, taking into account the absence of signs of bleeding and segregation of the mixtures, in accordance with GOST R 59714.

Specimens were cast from the prepared concrete mixtures and stored under standard conditions (at a temperature of 20±2 °C and relative humidity of 95±5%):

- 12 cubes measuring 100×100×100 mm for determining average density and cube compressive strength in accordance with GOST 27005, GOST 10180, and GOST 31914;
- 21 prisms measuring 100×100×400 mm for determining prismatic compressive strength and modulus of elasticity in accordance with GOST 24452, as well as shrinkage and creep deformations in accordance with GOST 24544.

To better align the results of long-term tests with the actual performance of structures using various concrete classes and the design age typically specified for them in the working documentation, the specimens were tested at ages ranging from 28 to 90 days.

The modulus of elasticity was determined at a load level of 30% of the prismatic strength (R_b). The prisms were loaded in increments of $0.1R_b$, with a 5-minute dwell time at each increment.

Tests of the specimens for shrinkage and creep were conducted in standard spring-loaded test rigs for one and two specimens in automated climatic chambers at a constant temperature of 20±2 °C, but with different relative humidity levels of 20, 60, and 90% (±5%) over a period of 240 days [11]. During long-term testing, the deformation readings of the samples were determined using a portable deformometer, the operating principle of which is described in [25].

Moisture loss in concrete was determined by the difference in the average density of the same cubic specimens after curing under normal conditions and after additional curing for 240 days at various relative humidity levels [11].

The residual water content of high-strength concretes was determined by drying the cube specimens to a constant mass at a temperature of +105 °C after they had been cured at various relative humidity levels for 240 days [11].

The water absorption of high-strength concretes was determined in accordance with GOST 12730.3 on cube specimens after they had been cured at various relative humidity levels for 240 days [11].

The ultimate creep strains of high-strength concretes, required for calculating the creep coefficient, were determined using two methods for comparison:

- using the calculation method specified in GOST 24544, with a regression line;
- based on experimental data obtained when the creep strains reached a plateau.

The duration of exposing the samples to load during the experimental determination of the ultimate creep strains of concrete was carried out until their attenuation—for 240 days, which exceeds the duration of tests according to GOST 24544 (180 days) by 33%. It was assumed that the data from the experimental studies are the most reliable results, since the use of a computational method for prediction can lead to significant errors in the estimation of ultimate creep strain values.

3. RESULTS AND DISCUSSION

Test results for heavy and lightweight modified high-strength self-compacting concretes in terms of: cube strength (R) and actual compressive strength class (B_f), prism strength (R_b) and mod-

ulus of elasticity (E_b), moisture loss (Δ_{ml}), residual moisture content (Δ_{rwc}), and water absorption (Δ_{wa}) of the concretes before and after testing at different ambient relative humidity levels (W) are presented in Tables 2 and 3.

Table 2. Strength and deformation characteristics of high-strength concretes under short-term loading and at various relative humidity levels

Composition No	W, %	Properties of high-strength concrete before and after 240 days of testing, MPa							
		R		B_f		R_b		$E_b \cdot 10^{-3}$	
		prior to testing	after 240 days	prior to testing	after 240 days	prior to testing	after 240 days	prior to testing	after 240 days
1	20	-	-	-	-	-	74,4	-	41,3
	60	-	-	-	-	-	76,7	-	41,7
	90	81,2	88,4	71	77	76,8	82,0	40,5	42,8
2	20	-	-	-	-	-	85,7	-	42,8
	60	-	-	-	-	-	88,3	-	44,2
	90	92,3	104,2	81	91	88,7	99,2	42,4	45,0
3	20	-	-	-	-	-	107,1	-	44,9
	60	-	-	-	-	-	110,0	-	46,4
	90	114,3	116,8	100	100	104,6	112,2	44,6	47,2
4	20	-	-	-	-	-	66,4	-	35,0
	60	-	-	-	-	-	65,3	-	34,6
	90	69,5	70,2	61	61	64,5	64,6	33,3	34,5

Notes: W – relative humidity; R – cube compressive strength; Bf – actual compressive strength class; Rb – prism compressive strength; Eb – initial modulus of elasticity; "-" – value not determined.

Table 3. Moisture characteristics of high-strength concrete after curing for 240 days under varying relative humidity conditions

Composition No.	W, %	Properties of high-strength concrete after 240 days of testing			
		B_f	Δ_{ml}, mass.%	Δ_{rwc}, mass.%	Δ_{wa}, mass.%
1	20	-	0,67	2,99	0,85
	60	-	0,47	3,24	0,50
	90	77	0,18	3,98	0,25
2	20	-	0,46	2,38	0,46
	60	-	0,33	2,72	0,28
	90	91	0,15	3,10	0,12
3	20	-	0,33	2,04	0,33
	60	-	0,25	2,24	0,16
	90	100	0,01	2,80	0,08
4	20	-	1,00	4,91	1,21
	60	-	0,62	5,32	1,05
	90	61	0,00	5,98	0,97

Notes: W – relative humidity; B_f – actual compressive strength class; Δ_{ml} – moisture loss; Δ_{rwc} – residual moisture; Δ_{wa} – water absorption.

As shown in Tables 2 and 3, the curing of heavyweight concrete at the same temperature but under different relative humidity conditions over a 240-day period results in a significant increase in the concrete's strength and initial modulus of elasticity. As the concrete class and relative humidity increase, moisture loss and water absorption decrease, while the residual moisture content, compressive strength, and initial modulus of elasticity of the concrete increase. Thus, at an

ambient relative humidity of 90%, the increase in prism strength of heavy-duty concrete ranges from 7% to 12%, and the initial modulus of elasticity increases by 6%. When the ambient relative humidity decreases from 60% to 20%, the increase decreases and amounts to no more than 5% for prismatic strength and no more than 4% for the modulus of elasticity.

The curing of lightweight concrete at a constant temperature but under varying relative humidity conditions over a period of 240 days results in a slight increase in strength of up to 3% and in the initial modulus of elasticity of up to 5% as shown in Table 3. As relative humidity increases, moisture loss and water absorption in lightweight concrete decrease, while residual water content increases as shown in Table 4. At the same time, unlike heavy concrete, when relative humidity decreases from 90% to 20%, the prismatic strength and initial modulus of elasticity of lightweight concrete increase by 2–3%.

These results can be explained by the structural characteristics of the cement paste in high-strength modified concretes. Previous studies of the structure of high-strength cement paste [5, 9, 25] have shown that it is characterized by a 30–50% increase in the volume of gel pores at the supramolecular level of dispersion with diameters of $1 \cdot 10^{-3}$… 5×10^{-3} μm, which are insensitive to changes in the relative humidity of the environment. The formation of such pores is associated with a 1.5–2.5-fold increase in the content of highly dispersed CSH(I)-type calcium hydrosilicates, which constitute an ultradisperse solid structure of a lamellar ("scaly") form with a size, in one direction, of no more than 2.5×10^{-3} μm (2.5 nm), with the interlayer space filled with water as shown in Figure 1.

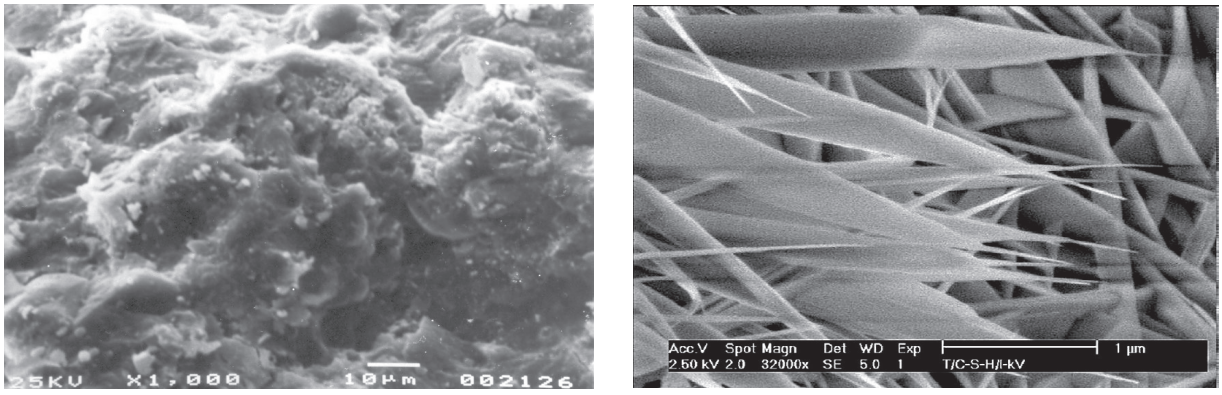

a) b)

Figure 1. Structure of high-strength cement stone (a) and low-alkali calcium silicate hydrates[1] of the CSH(I) type (b)

[1] The photograph of low-base calcium hydrosilicates was taken by B. Möser at the Finger Institute for Building Materials

The interlayer water, or hydration shell, has a density of 1200–1350 kg/m³, which contributes to the system's stiffness and increases its modulus of elasticity [26–29]. Taken together, this forms a high-density, strong, and rigid gel-like tobermorite mass. The structural feature described above determines the ultra-low water absorption and permeability to water and gases of modified cement stone and concretes, as noted by N.K. Rosental et al. [6–7].

The minimal (3–5%) increase in the compressive strength and initial modulus of elasticity of lightweight concrete over time can be explained by the fact that a significant volume of lightweight, porous expanded clay gravel (0.240 m³/m³), which has low strength and deformation characteristics, reduces their increase due to the compaction of the cement paste.

The summary results of relative shrinkage and creep deformations, as well as the creep modulus and coefficient, obtained during long-term tests of high-strength self-compacting heavy and lightweight concretes at different relative air humidity levels are presented in Table 4.

Based on the results of long-term tests of heavy and lightweight high-strength concretes, kinetics curves were plotted showing the increase in their relative shrinkage and creep deformations at various relative air humidity levels.

Table 4. Deformation characteristics of high-strength concrete under a load applied for 240 days at different relative humidity levels

Composition No.	W, %	$\varepsilon_{sh} \cdot 10^5$	Stress and creep strains						Creep coefficient, $\varphi^1_{b,cr}$ / $\varphi^2_{b,cr}$
			σ, MPa	$\varepsilon_{el} \cdot 10^5$	$\varepsilon^1_{cr} \cdot 10^5$	$\varepsilon^2_{cr} \cdot 10^5$	$\varepsilon^1_{cr} / \varepsilon^2_{cr}$	C·10^5, MPa^{-1}	
1	20	**38.0**	24.5	**57.0**	50.6	**40.5**	1.25	1.65	0.89 / **0.71**
	60	**28.5**	24.5	**55.0**	28.6	**27.5**	1.04	1.12	0.52 / **0.50**
	90	**4.5**	24.5	**54.0**	18.1	**17.3**	1.05	0.71	0.33 / **0.32**
2	20	**36.1**	28.0	**62.0**	55.6	**39.7**	1.40	1.42	0.89 / **0.64**
	60	**25.2**	28.0	**61.0**	35.4	**27.5**	1.29	0.98	0.58 / **0.45**
	90	**2.2**	28.0	**63.0**	29.0	**23.9**	1.21	0.85	0.46 / **0.38**
3	20	**33.3**	32.0	**63.8**	63.2	**39.2**	1.61	1.23	0.99 / **0.61**
	60	**22.5**	32.0	**62.1**	37.0	**25.5**	1.41	0.80	0.59 / **0.41**
	90	**2.0**	32.0	**62.1**	26.6	**20.5**	1.30	0.64	0.43 / **0.33**
4	20	**27.5**	19.4	**59.3**	28.2	**25.8**	1.09	1.33	0.48 / **0.44**
	60	**21.1**	19.4	**60.2**	24.4	**19.0**	1.28	0.98	0.41 / **0.32**
	90	**5.5**	19.4	**62.7**	13.3	**10.1**	1.32	0.52	0.21 / **0.16**

Notes: W is the relative humidity; σ is the stress in concrete specimens under long-term loading; εsh is the shrinkage strains; εel is the elastic component of relative strains when loading a concrete specimen to a constant stress σ; ε^1_{cr} is the ultimate relative creep strains calculated according to GOST 24544; ε^2_{cr} is the ultimate relative creep strains obtained experimentally after 240 days of testing; $\varphi^1_{b,cr}$ and $\varphi^2_{b,cr}$ are the creep coefficients obtained using formula (1) at different ultimate relative creep strains, calculated according to GOST 24544 and obtained experimentally; C is a measure of creep, determined by the formula C=ε^2_{cr}/ σ.

Figures 2 and 3 show approximate graphs of the relative shrinkage and creep deformations of high-strength self-compacting heavy concrete of class B100 and lightweight concrete of class B60 under long-term loading at various relative air humidity levels. The kinetics of shrinkage and creep in heavy concrete of classes B70 and B80 do not differ qualitatively from those of heavy concrete of class B100.

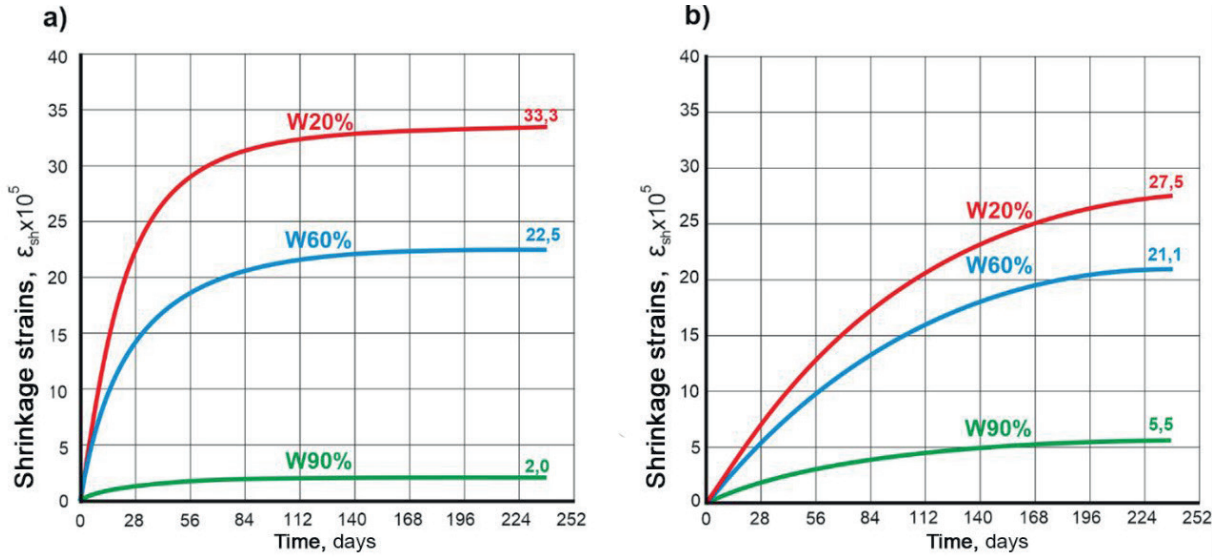

Figure 2. Shrinkage strains of high-strength self-compacting heavy concrete of class B100 (a) and lightweight concrete of class B60 (b) over time at different relative air humidity levels

As shown in Table 5, relative humidity has a significant effect on the shrinkage strains ε_{sh} of both heavy and lightweight concretes, which is consistent with the results of determining the moisture characteristics of high-strength concretes after curing for 240 days under various relative humidity conditions as can be seen from Table 4.

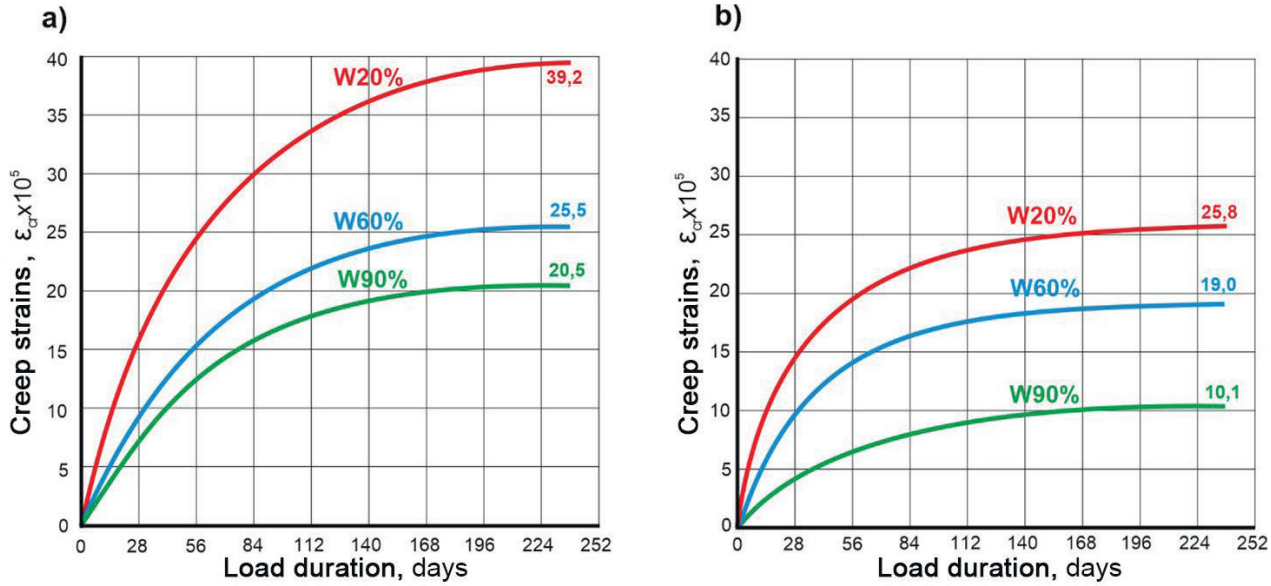

Figure 3. Creep strains of high-strength self-compacting heavy concrete of class B100 (a) and lightweight concrete of class B60 (b) under long-term loading at different relative air humidity levels

s relative humidity decreases, the shrinkage deformation of high-strength concrete increases significantly, ranging from 2.0–5.5 × 10^{-5} at 90% humidity, 21.1–28.5 × 10^{-5} at 60% humidity, and 27.5–38.0 × 10^{-5} at 20% humidity, but do not exceed the value of 43.0 × 10^{-5} recommended in [30] for B60-grade concrete. At the same time, the strength and type of concrete have a significantly smaller effect on the shrinkage deformations of concrete as can be seen from Table 5 and Figure 3. However, while the shrinkage strains of heavy concretes of classes B70–B100 decay rapidly and stabilize at 120–140 days, lightweight concrete of class B60 is characterized by relatively linear shrinkage deformation curves up to 150–170 days of observation. This is likely due to the fact that, in the presence of porous aggregate in the composition of lightweight concrete, in a partially water-saturated state, two mass-moisture transfer processes overlap. On the one hand, there is moisture loss from the cement paste due to evaporation at low relative air humidity. On the other hand, there is moisture influx into the cement paste from the porous aggregate, which acts as a reserve water volume uniformly distributed throughout the volume of the lightweight concrete.

An analysis of the results of determining the creep strains of high-strength self-compacting heavy and lightweight concretes under long-term loading (over a period of 240 days) revealed the following patterns:

- the time-dependent growth of creep strains follows a decaying exponential function, which for high-strength self-compacting heavy and lightweight concretes stabilizes at 180–200 days, depends on relative air humidity and does not contradict known physical laws (see Figure 3);
- The values of elastic strain ε_{el} for all four concrete mixtures fall within a fairly narrow range of 54.0–63.8 × 10^{-5}. Despite a significant difference in prismatic strength from 64.6 to 112.2 MPa and elastic modulus from 34.5 to 47.2 GPa, they differ by no more than 18%. This circumstance is a consequence of the wide range of specimen loading levels, from 19.4 to 32.0 MPa, regulated by GOST 24452 and GOST 24544 at 0.3 times the prismatic strength as can be seen from Table 5;

- As relative humidity decreases, the ultimate creep strains ε_{cr}^2 of high-strength heavy and lightweight concretes, obtained experimentally at 240 days of age, increase and range from 10.1–23.9 × 10^{-5} at 90% humidity, 19.0–27.5 × 10^{-5} at 60% humidity, and 25.8–40.5 × 10^{-5} at 20% humidity. At the same time, the strength of heavy concrete has virtually no effect on the ultimate relative creep strains, which for concrete grades B70–B100 fall within a narrow range: at 90% humidity—39.2–40.5 × 10^{-5}, at 60% humidity—25.5–27.5 × 10^{-5}, and at 20% humidity—17.3–23.9 × 10^{-5} as shown in Table 5;
- The ultimate creep strains ε_{cr}^1 of high-strength heavy and lightweight concretes, determined using the method specified in GOST 24544 with a regression line, exceed the experimental values by 4–9% to 21–61% as shown in Table 5. Considering that the duration of the long-term load was 240 days and exceeded the 180-day duration specified in GOST 24544 by 33%, as well as the stabilization of creep strains after 180–200 days of testing, it can be concluded that the values of ultimate creep strains calculated according to GOST 24544 are, in some cases, overestimated. At the same time, the accuracy of the standard method for calculating ultimate creep strains decreases with an increase in concrete class and a decrease in relative air humidity. This is clearly evident in a comparison of the values of ultimate creep strains in Table 5 and Figure 3a. Accordingly, the creep coefficients calculated using Equation (3) will also be overestimated;
- The creep strains of lightweight high-strength concrete of class B60 are lower than those of heavy concrete of classes B70–B100 (see Figure 3 and Table 5). This result can be explained by the fact that the composition and volume of the cement paste, which characterizes creep strains under long-term loading, were practically identical for heavy concrete of class B100 and lightweight concrete of class B60, while the loading levels applied to the specimens, taken as 0.3 times the prismatic strength of the concrete, differed by 65% and ranged from 32.0 to 19.4 MPa. This is confirmed by the results of determining the creep modulus of high-strength concretes, which are practically identical for heavy concrete of class B100 and lightweight concrete of class B60 as shown in Table 5 and Figure 4;
- the creep modulus of high-strength self-compacting heavy and lightweight concretes of classes B60–B100 ranges from 0.52 to 1.65 × 10^{-5} MPa^{-1} and does not exceed the value of 3.9 × 10^{-5} MPa^{-1} recommended in [30] for B60 concrete in the absence of data on the characteristics of the concrete mix composition. As relative air humidity decreases, the creep modulus of high-strength concretes increases and amounts to: 0.52–0.85 × 10^{-5} MPa^{-1} at 90% humidity, 0.80–1.12 × 10^{-5} MPa^{-1} at 60% humidity, and 1.23–1.65 × 10^{-5} MPa^{-1} at 20% humidity as can be seen from Figure 4.

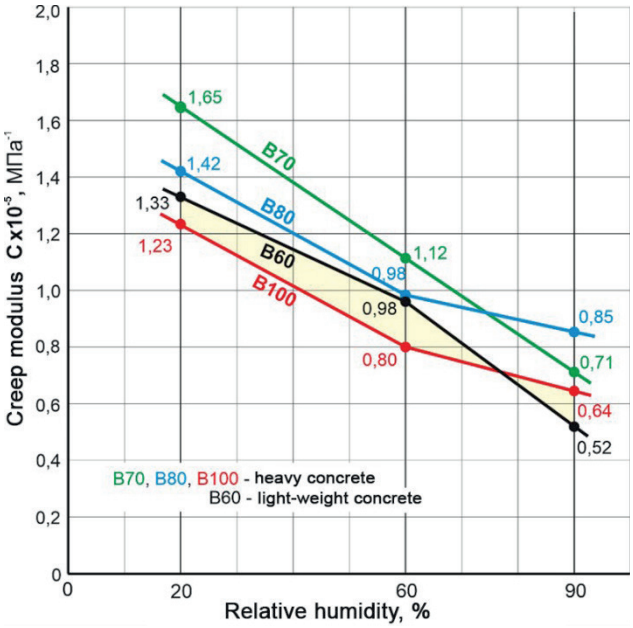

Figure 4. Creep modulus of high-strength self-compacting heavy and lightweight concretes under prolonged (240-day) loading at various relative air humidity

Based on the obtained results for elastic and ultimate relative creep strains, the creep coefficients for high-strength self-compacting heavy and lightweight concretes of classes B60–B100 were determined using Equation (3), used for the design of reinforced concrete structures under long-term loading, and a comparison was made with the values given in SP 63.13330.2018 and EN

12390. In this case, the values of the creep coefficients were determined taking into account the ultimate relative creep strains calculated according to the GOST 24544 method (ε_{cr}^{1}) and obtained from experimental data (ε_{cr}^{2}) as shown in Table 5.

Analysis of the results of determining the creep coefficients of high-strength self-compacting heavy and lightweight concretes under long-term loading revealed the following patterns:

- As relative humidity decreases, the creep coefficients ($\varphi_{b,cr}^{1}$ and $\varphi_{b,cr}^{2}$) of high-strength heavy and lightweight concretes of classes B60–B100, obtained by calculation and experiment, increase and range from 0.16 to 0.46 at 90% humidity, 0.32–0.59 at 60% humidity, and 0.44–0.99 at 20% humidity as can be seen from Table 5;
- The creep coefficients of high-strength heavy concretes of classes B70–B100 depend to a lesser extent on the compressive strength grade than on the relative humidity of the air, which can be explained by the similar quality of the cement paste, determined by the use of the organomineral modifier MB10 -50S in an amount of 14–24% of the cement mass, and the identical volume of cement paste (334–363 m³/m³) in the composition of self-compacting concretes;
- The creep coefficients of lightweight concrete are 30–100% lower than those of heavy concrete, which is clearly due to the lower loading on lightweight concrete specimens during long-term tests, while the quality, and the amount of cement paste (MB10-50S dosage of 21% of cement mass and true cement paste volume of 355 m³/m³);
- The creep coefficients determined by calculation exceed the experimentally obtained values by 4 to 62%. At the same time, the differences in creep coefficient values for heavy concrete increase with a decrease in relative air humidity and an increase in strength, while for lightweight concrete, they decrease with an increase in relative air humidity. These results show that the determination of ultimate relative strains at low relative air humidity values using the calculation method specified in GOST 24544 requires adjustment.

Table 5 and Figure 5 present a comparison of experimentally determined creep coefficients for high-strength self-compacting heavy and lightweight concretes at various air humidity levels (20, 60, and 90%) and their standard values, referenced to the classification adopted in the code of rules SP 63.13330.2018 and Eurocode EN 12390.

Table 5. Experimental and standard values of the creep coefficients for high-strength concrete at different relative air humidity levels

W, %	Creep coefficient $\varphi_{b,cr}$ for high-strength concrete of B60-B100 grades							
	experimental data				According to СП 63.13330.2018		According to EN 12390	
	B60[1)]	B70[2)]	B80[2)]	B100[2)]	B60-100	Δ, %	C60-C100	Δ, %
> 75	0.16	0.32	0.38	0.33	1.0	-(62…84)	0.97-0.71	-(54…83)
40-75	0.32	0.50	0.45	0.41	1.4	-(64…77)	1.41-0.98	-(58…77)
< 40	0.44	0.71	0.64	0.61	2.0	-(65…78)	-	-

Notes: W – relative humidity; 1) – lightweight concrete; 2) – heavyweight concrete; Δ – difference between experimental data and standard values.

A comparison of the creep coefficients of high-strength self-compacting heavy and lightweight concretes of classes B60–B100, obtained experimentally, with their standard values according to SP 63.13330.2018 and EN 12390 showed that:

- The standard values of creep coefficients for concrete classes B60–B70 according to SP 63.13330.2018 generally correspond to the values in EN 12390. However, for higher-grade concretes (B80–B100), the standard values in EN 12390 are 30% lower than those in SP 63.13330.2018 (see Table 5);
- values of the creep coefficients ($\varphi_{b,cr}^{1}$ and $\varphi_{b,cr}^{2}$) for high-strength heavy concretes of classes

B70–B100, obtained by calculation and experiment at various relative air humidity levels (from 20% to 90%), do not exceed 1.0 and are more than two times lower than the standard values specified in SP 63. 13330.2018 and EN 12390 (see Figure 5);
- the insignificant difference in creep coefficients for heavy concretes of different classes B70, B80, and B100 indicates that a single value can be used for them at the same relative air humidity;
- The values of the creep coefficients ($\varphi_{b,cr}^{1}$ and $\varphi_{b,cr}^{2}$) for high-strength lightweight concrete of class B60, obtained through calculation and experimentation at various relative air humidity (from 20% to 90%), do not exceed 0.5 and are four times lower than the standard values specified in SP 63.13330.2018 and EN 12390 (see Figure 5).

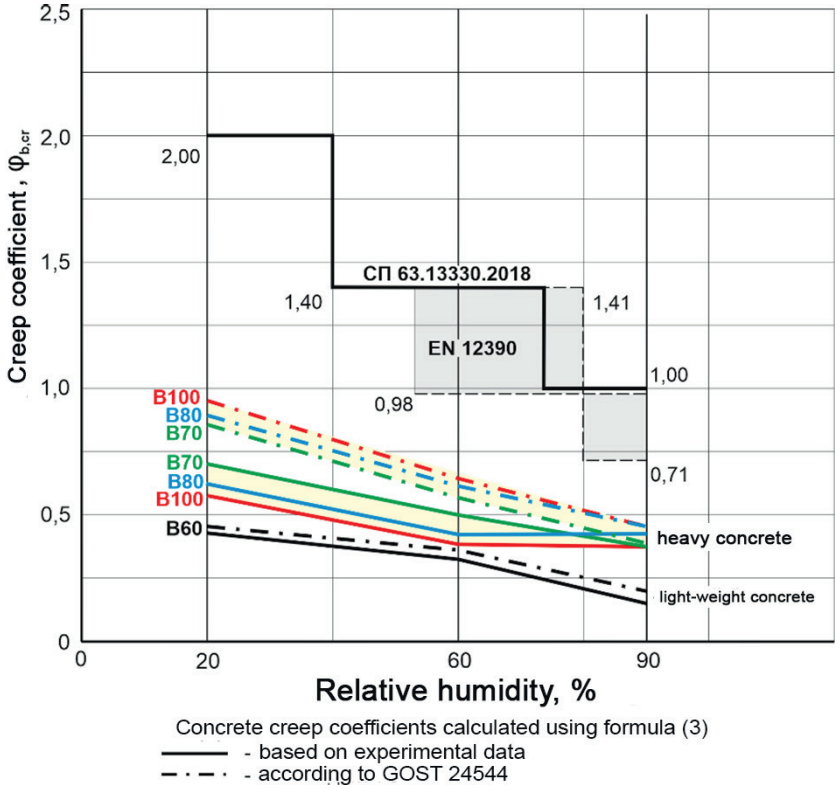

Figure 5. Comparison of experimental creep coefficients for high-strength heavy and lightweight concretes of classes B60–B100 at different relative air humidity levels with their standard values according to SP 63.13330.2018 and Eurocode EN 12390

The results obtained are determined both by the structural characteristics of the modified cement paste and by its content in the concrete mixture, which determines the concrete's strength and deformation properties. It can be assumed that in low-cement concretes of classes below B60, prepared using organomineral modifiers of the MB type or individual components included in its composition (microsilica and fly ash), the values of the creep coefficients ($\varphi_{b,cr}$) at various relative air humidity levels will be lower than those specified in the SP 63.13330.2018 code.

4. CONCLUSIONS

1. Comparative tests have been carried out on high-strength self-compacting heavy and lightweight concretes of classes B60–B100 with a Portland cement content of 350–500 kg/m³ and an organo-mineral modifier MB10-50S added at

a rate of 14–26% of the cement mass. The strength (cubic and prismatic compressive strength) and deformation (initial modulus of elasticity, shrinkage and creep strains, measure and coefficient of creep) characteristics of the concretes during their curing before and after prolonged (240 days) loading at various relative ambient humidity levels of 20, 60, and 90% in accordance with GOST 10180, GOST 31914, GOST 24452, and GOST 24544.

2. A decrease in ambient relative humidity from 90% to 20% slows down, but does not halt, the hardening processes of high-strength heavy and lightweight concretes over a period of 240 days. The increase in compressive strength and modulus of elasticity of heavy concretes at minimum humidity decreases from 7–12% to 4–5%, while for lightweight concrete, it even increases slightly by 1–3%, which is consistent with previous studies of the structure of high-strength cement stone with organo-mineral modifiers of the MB type.

One of the main features of the pore structure of modified cement stone is a shift in the balance between the volumes of capillary pores at the macro-level of dispersion, responsible for the migration (mass transfer) of moisture, and the so-called gel pores at the supramolecular level of dispersion with a diameter of 1–5 nm—toward the latter. Thus, the 30–50% increase in the volume of more dispersed and less permeable to water and gases gel pores in the cement stone structure makes high-strength concretes less sensitive to changes in the relative humidity of the environment.

3. The shrinkage strains of high-strength self-compacting heavy and lightweight concretes of classes B60–B100 increase significantly by a factor of 7–13 as the relative humidity of the air decreases from 90% to 20%, ranging from 2.0–5.5 × 10^{-5} to 27.5–38.0 × 10^{-5}. At the same time, the strength and type of concrete have a significantly smaller effect on the shrinkage strains of concrete. The shrinkage strains of heavy concretes of classes B70–B100 decay rapidly and stabilize at 120–140 days. For lightweight concrete of class B60, the shrinkage deformation curves exhibit relative linearity up to 150–170 days of observation. This is likely due to the superposition of two moisture-mass transfer processes: moisture loss by the cement pastes due to evaporation at low relative air humidity, and moisture influx into the cement paste from the porous aggregate, which acts as a reserve of water uniformly distributed throughout the volume of lightweight concrete.

4. The elastic strains of high-strength self-compacting heavy and lightweight concretes fall within a narrow range of 54.0–63.8 × 10^{-5}, and despite a significant difference in prismatic strength (from 64.6 to 112.2 MPa) and modulus of elasticity (from 34. 5 to 47.2 GPa), they differ by no more than 18%, which is a consequence of the wide range of specimen loading levels (from 19.4 to 32.0 MPa), regulated by GOST 24452 and GOST 24544 at a uniform value of 0.3 times the prismatic strength.

5. The ultimate creep strains of high-strength heavy and lightweight concretes, obtained experimentally at 240 days of age, increase with decreasing relative air humidity and range from 10.1–23.9 × 10^{-5} at 90% humidity, 19.0–27.5 × 10^{-5} at 60% humidity, and 25.8–40.5 × 10^{-5} at 20% humidity.

The ultimate creep strains, determined using the method specified in GOST 24544, exceed the experimental values by 4 to 61 percent. At the same time, the accuracy of the standard calculation method decreases as the concrete class increases and relative air humidity decreases, which necessitates revisions to the method.

6. The creep modulus of high-strength self-compacting heavy and lightweight concretes of classes B60–B100 increases as relative air humidity decreases and is as follows: 0.52–0.85 × 10^{-5} MPa^{-1} at 90% humidity, 0.80–1.12 × 10^{-5} MPa^{-1} at 60% humidity, and 1.23–1.65 × 10^{-5} MPa^{-1} at 20% humidity.

7. The creep coefficients of high-strength self-compacting heavy concretes of classes B70–B100, obtained by calculation and experiment, increase with decreasing relative air humidity and amount to 0.32–0.46 at 90% humidity, 0.41–

0.59 at 60% humidity, and 0.61–0.99 at 20% humidity, which is two times or more lower than the standard values specified in Eurocode EN 12390 and the code of rules SP 63.13330.2018.

The creep coefficients of high-strength, self-compacting lightweight concrete of class B60, obtained through calculation and experimentation, increase as relative air humidity decreases, ranging from 0.16 to 0.21 at 90% humidity, 0.32–0.41 at 60% humidity, and 0.44–0.48 at 20% humidity, which is four times lower than the standard values specified in Eurocode EN 12390 and the design code SP 63.13330.2018.

8. Based on the results obtained, it is recommended that GOST 24544 include a direct formula for determining the creep coefficient of concrete, extend the duration of long-term tests on high-strength concretes to 270 days, and amend the procedure for determining the ultimate creep strains of concrete in Appendix G, and to include in SP 63.13330.2018 a provision regarding the possibility of experimentally determining the concrete creep coefficient, which will significantly improve the efficiency of using modern modified concretes in the construction of unique buildings and structures.

REFERENTS

1. **S.S. Kaprielov, V.I. Travush, N.I. Karpenko, A.V. Sheinfeld, G.S. Kardumyan, Yu.A. Kiseleva, and O.V. Prigozhenko.** Modified High-Strength Concretes of Classes B80 and B90 in Monolithic Structures. Construction Materials, No. 3, 2008, pp. 9-13.
2. **Kaprielov S.S., Sheinfeld A.V., Chilin I.A., Dondukov V.G., and Selyutin N.M**. Modified Concretes: Reality and Prospects. Vestnik NITs Stroitelstvo. 2024;40(1):92-104. https://doi.org/10.37538/2224-9494-2024-1(40)-92-104.
3. **Kaprielov S.S., Sheinfeld A.V., Jalal A., Zaitsev A.S., and Amirov R.A.** Technology for the Construction of High-Rise Building Frames from High-Strength Concretes of Classes B60-B100. Vestnik NITs Stroitelstvo. 2022;33(2):106-121. https://doi.org/10.37538/2224-9494.
4. **S.S. Kaprielov, A.V. Sheinfeld, G.S. Kardumyan.** New Modified Concretes. Moscow, Paradiz Printing House LLC, 2010, p. 258.
5. **Sheinfeld A.V.** Features of the Formation of a Hierarchical Micro- and Nano-Structure of Cement Systems with Complex Organomineral Modifiers. Concrete and Reinforced Concrete, No. 2, 2016, pp. 16-21.
6. **Rozental, N.K.** Corrosion Resistance of Low- and Very-Low-Permeability Cement Concretes. – Moscow: FSUE TsPP, 2006 – 520p.
7. **Sheinfeld, A.V.** Organomineral modifiers as a factor increasing the durability of reinforced concrete structures / Concrete and reinforced concrete. - No. 3. – 2014. - P.16-21.
8. **Berg O.Ya., Shcherbakov E.N., Pisanko G.N.** High-strength concrete. M.: Publishing house of construction literature, 1971. 208 p.
9. **S.S. Kaprielov, A.V. Sheinfeld, N.I. Karpenko, E.N.** Kuznetsov On the regulation of the modulus of elasticity and creep of high-strength concretes with the modifier MB-50S. // Concrete and reinforced concrete, No. 6, 2003, p.8-12.
10. **S.S. Kaprielov, A.V. Sheinfeld, N.I. Karpenko, E.N. Kuznetsov** Influence of the organomineral modifier MB-50S on the structure and deformability of cement stone and high-strength concrete. // Concrete and reinforced concrete, No. 3, 2003, p.2-7.
11. **S.S. Kaprielov, P. D. Arleninov, A. V. Sheinfeld, P. S. Kalmakova** Influence of the relative humidity of the air on the creep coefficient of high-strength self-compacting concretes / Construction materials. – 2025. – No. 10. – P. 25-35. – DOI 10.31659/0585-430X-202.
12. **Wagner O.** Das Kriechen unbewehrten Betons. Deutscher Ausschuss für Stahlbeton. Verlag Ernst und Sohh, Berlin, H. 131. 1958..

13. **Залесов А.С., Клевцов В.А., Шугаев В.В.** Научно технический отчет по теме «Анализ состояния использования в строительстве высокопрочных бетонов, имеющихся данных по проектированию, области рационального применения особо высокопрочных бетонов и составление рабочей программы исследований». НИИЖБ –Москва: 2001-2002. – 80 с.
14. **Bezgodov I.M., Kapustin D.E., Efishov L.I.** (2024) Physical-mechanical and rheologi-cal characteris-tics of high-strength concrete and granite. Industrial and Civil Construction, no. 8, pp. 48–56. DOI: 10.33622/0869-7019.2024.08.48-56.
15. **Domarova E.V.** (2022) Influence of creep on the stress-strain state of reinforced concrete multi-story buildings. Construction and Reconstruction, №9.
16. **Kaprielov S.S., Sheinfeld A.V., Selyutin N.M.** Self-compacting high-strength expanded clay concrete of classes B50–B65 – a new generation of lightweight concretes for high-rise buildings. Stroitelnye materialy. 2023. No. 4. Pp. 42–50. DOI: https://doi.org/10.31659/05.
17. **Kaprielov S.S., Sheynfeld A.V., Karpenko N.I., Selyutin N.M., Moiseenko G.A., Bezgodov I.M.** Influence of the type of aggregate on the physical and technical characteristics of high-strength self-compacting cement systems // Concrete and reinforced concrete. 2025. No. 2 (627). Pp. 27-42. D.
18. **Kaprielov S.S., Sheynfeld A.V., Karpenko N.I., Selyutin N.M., Moiseenko G.A., Bezgodov I.M.** Strength and deformation characteristics of high-strength self-compacting lightweight concretes with artificial and natural porous aggregates // Concrete and reinforced concrete.
19. **Kaprielov S., Sheynfeld A. & Selyutin N.** (2022). Control of heavy concrete characteristics affecting structural stiffness / International Journal for Computational Civil and Structural Engineering, 18(1), 24–39. https://doi.org/10.22337/2587-9618-2022-18-.
20. **Bezgodov I., Kaprielov S. & Sheynfeld A.** (2022). Relationship between strength and deformation characteristics of high-strength self-comacting concrete / International Journal for Computational Civil and Structural Engi-neering, 18(2), 175–183. https://doi.
21. **Kaprielov S.S., Sheynfeld A.V., Travush V.I., Karpenko N.I., Krylov S.B.** Assessment of the strength and deformation characteristics of high-strength concretes in structures and the dynamics of their change // Construction Materials. 2023. No. 11. Pp. 28-38. DOI: https://doi.org/1.
22. **Nastic M.** et al. Shrinkage and creep strains of concrete exposed to low relative hu-midity and high temperature environments / Nuclear Engineering and Design. 2019. Vol. 352. P. 110154.
23. **Kaprielov S.S., Sheinfeld A.V., Selyutin N.M., Chilin I.A., Arzumanov I.A., Dondukov V.G.** Concrete mix for structural lightweight concrete. Patent RF No. 2835462 dated 25.02.2025.
24. **Travush V.I., Arleninov P.D., Desyatkin M.A., Ivashchenko A.N., Kalmakova P.S., Kaprielov S.S., Konin D.V., Krylov A.S., Krylov S.B., Chilin I.A., Sheinfeld A.V.** Study of the creep of steel-concrete samples. Construction and Reconstruction. 2024 ;(1):49-63.
25. **Shurbert-Hetzel C., Daneshvar D., Robisson A., Shafei B.** Data-enabled compar-ison of six prediction models for concrete shrinkage and creep. Case Studies in Construc-tion Materials. 2023. Vol. 19. e02406. EDN: OVNDON.
https://doi.org/10.1016/j.cscm.2023.e02.
26. **Akhverdov I.N.** Fundamentals of Concrete Physics / I.N. Akhverdov. – Moscow: Stroyizdat, 1981. – 464 p.
27. **Ramachandran V.S.** Science of Concrete / V.S. Ramachandran, R.F. Feldman, J. Boduen. – Moscow: Stroyizdat, 1986. – 280 p.
28. **Taylor, H.F.W.** Chemistry of Cements / H.F.W. Taylor. – Moscow: Publishing House of Construction Literature, 1969. – 501 p.

29. **Sheikin, A.E.** Structure and Properties of Cement Concrete / A.E. Sheikin, Yu.V. Chekhovsky, and M.I. Bruser. – Moscow: Stroyizdat, 1979. – 344 p.
30. Recommendations for Accounting for Concrete Creep and Settlement in the Calculation of Concrete and Reinforced Concrete Structures: NIIZhB – Moscow: Stroyizdat, 1988. – 121 p.

СПИСОК ЛИТЕРАТУРЫ

1. **С.С. Каприелов, В.И. Травуш, Н.И. Карпенко, А.В. Шейнфельд, Г.С. Кардумян, Ю.А. Киселева, О.В. Пригоженко** Модифицированные высокопрочные бетоны классов В80 и В90 в монолитных конструкциях // Строительные материалы, №3, 2008, с. 9-13.
2. **Каприелов С.С., Шейнфельд А.В., Чилин И.А., Дондуков В.Г., Селютин Н.М.** Модифицированные бетоны: реальность и перспективы. Вестник НИЦ «Строительство». 2024;40(1):92-104. https://doi.org/10.37538/2224-9494-2024-1(40)-92-104.
3. **Каприелов С.С., Шейнфельд А.В., Джалаль А., Зайцев А.С., Амиров Р.А.** Технология возве-дения конструкций каркасов высотных зданий из высокопрочных бетонов классов В60–В100. Вестник НИЦ «Строительство». 2022;33(2):106-121. https://doi.org/10.37538/2224-9494.
4. **С.С.Каприелов, А.В.Шейнфельд, Г.С.Кардумян** Новые модифицированные бетоны // Москва, ООО «Типография «Парадиз», 2010 г., с.258.
5. **Шейнфельд А.В.** Особенности формирования иерархической микро- и наноструктуры цементных систем с комплексными органоминеральными модификаторами. // Бетон и железобетон, № 2, 2016, стр.16-21.
6. **Розенталь, Н.К.** Коррозионная стойкость цементных бетонов низкой и особо низкой проницаемости / Н.К. Розенталь. – Москва: ФГУП ЦПП, 2006 – 520с.
7. **Шейнфельд, А.В.** Органоминеральные модификаторы как фактор, повышающий долговеч-ность железобетонных конструкций / Бетон и железобетон. - № 3. – 2014. - С.16-21.
8. **Берг О.Я., Щербаков Е.Н., Писанко Г.Н.** Высокопрочный бетон. М.: Издательство литерату-ры по строительству, 1971. 208 с.
9. **С.С. Каприелов, А.В. Шейнфельд, Н.И. Карпенко, Е.Н. Кузнецов** О регулировании модуля упругости и ползучести высокопрочных бетонов с модификатором МБ-50С. // Бетон и железобетон, № 6, 2003, с.8-12.
10. **С.С.Каприелов, А.В.Шейнфельд, Н.И.Карпенко, Е.Н.Кузнецов** Влияние органоминерального модификатора МБ-50С на структуру и деформативность цементного камня и высокопрочного бетона. // Бетон и железобетон, № 3, 2003, с.2-7.
11. **С.С. Каприелов, П. Д. Арленинов, А. В. Шейнфельд, П. С. Калмакова** Влияние относительной влажности воздуха на коэффициент ползучести высокопрочных самоуплотняющихся бетонов / Строительные материалы. – 2025. – № 10. – С. 25-35. – DOI 10.31659/0585-430X-202.
12. **Wagner O.** Das Kriechen unbewehrten Betons. Deutscher Ausschuss für Stahlbeton. Verlag Ernst und Sohh, Berlin, H. 131. 1958..
13. **Zalesov A.S., Klevtsov V.A., Shugaev V.V.** Scientific and technical report on the topic “Analysis of the state of use of high-strength concretes in construction, available design data, areas of rational application of ultra-high-strength concretes, and preparation of a research work program.” NIIZhB, Moscow, 2001–2002, 80 p.
14. **Bezgodov I.M., Kapustin D.E., Efishov L.I.** (2024) Physical-mechanical and rheological characteris-tics of high-strength concrete and granite. Industrial and Civil Construction, no. 8, pp. 48–56. DOI: 10.33622/0869-7019.2024.08.48-56.

15. **Domarova E.V.** (2022) Vliyanie polzuchesti na napryazhenno-deformirovannoe sostoyanie zhelezo-betonnykh mnogoetazhnykh zdanii [Influence of creep on the stress-strain state of reinforced concrete multi-story buildings]. Construction and Reconstruction, №9.
16. **Каприелов С.С., Шейнфельд А.В., Селютин Н.М.** Самоуплотняющийся высокопрочный ке-рамзитобетон классов В50–В65 – новое поколение легких бетонов для конструкций высотных зданий // Строительные материалы. 2023. № 4. С. 42–50. DOI: https://doi.org/10.31659/05.
17. **Каприелов С.С., Шейнфельд А.В., Карпенко Н.И., Селютин Н.М., Моисеенко Г.А., Безгодов И.М.** Влияние вида заполнителя на физико-технические характеристики высокопрочных са-моуплотняющихся цементных систем // Бетон и железобетон. 2025. № 2 (627). С. 27-42. D.
18. **Каприелов С.С., Шейнфельд А.В., Карпенко Н.И., Селютин Н.М., Моисеенко Г.А., Безгодов И.М.** Прочностные и деформационные характеристики высокопрочных самоуплотняющихся легких бетонов на искусственных и природных пористых заполнителях // Бетон и железобетон.
19. **Kaprielov S., Sheynfeld A. & Selyutin N.** (2022). Control of heavy concrete characteristics affecting structural stiffness / International Journal for Computational Civil and Structural Engineering, 18(1), 24–39. https://doi.org/10.22337/2587-9618-2022-18-.
20. **Bezgodov I., Kaprielov S. & Sheynfeld A**. (2022). Relationship between strength and deformation characteristics of high-strength self-comacting concrete / International Journal for Computational Civil and Structural Engineering, 18(2), 175–183. https://doi.
21. **Каприелов С.С., Шейнфельд А.В., Травуш В.И., Карпенко Н.И., Крылов С.Б.** Оценка прочностных и деформационных характеристик высокопрочных бетонов в конструкциях и динамика их изменения // Строительные материалы. 2023. № 11. С.28-38. DOI: https://doi.org/1.
22. **Nastic M**. et al. Shrinkage and creep strains of concrete exposed to low relative humidity and high temperature environments / Nuclear Engineering and Design. 2019. Vol. 352. P. 110154.
23. **Каприелов С.С., Шейнфельд А.В., Селютин Н.М., Чилин И.А., Арзуманов И.А., Дондуков В.Г.** Бетонная смесь для конструкционного легкого бетона. Патент РФ № 2835462 от 25.02.2025 г.
24. **Травуш В.И., Арленинов П.Д., Десяткин М.А., Иващенко А.Н., Калмакова П.С., Каприелов С.С., Конин Д.В., Крылов А.С., Крылов С.Б., Чилин И.А., Шейнфельд А.В**. Исследование ползучести сталежелезобетонных образцов. Строительство и реконструкция. 2024 ;(1):49-63.
25. **Shurbert-Hetzel C., Daneshvar D., Robisson A., Shafei B.** Data-enabled comparison of six prediction models for concrete shrinkage and creep. Case Studies in Construction Materials. 2023. Vol. 19. e02406. EDN: OVNDON.
https://doi.org/10.1016/j.cscm.2023.e02.
26. **Ахвердов И.Н.** Основы физики бетона /И.Н. Ахвердов. – Москва: Стройиздат, 1981. - 464 с.
27. **Рамачандран В.С.** Наука о бетоне / В.С. Рамачандран, Р.Ф. Фельдман, Дж. Бодуэн. – Москва: Стройиздат, 1986. - 280 с.
28. **Тейлор, Х.Ф.У.** Химия цементов / Ч.Ф.У. Тейлор. – Москва: Издательство литературы по строительству, 1969. - 501с.
29. **Шейкин, А.Е.** Структура и свойства цементных бетонов / А.Е. Шейкин, Ю.В. Чеховский, М.И. Бруссер. – Москва: Стройиздат, 1979. - 344с.
30. Рекомендации по учету ползучести и усадки бетона при расчете бетонных и железобетонных конструкций: НИИЖБ – Москва: Стройиздат, 1988. – 121 с.

Semyon Surenovich Kaprielov - Ph.D. in Technical Sciences, Head of Laboratory No. 16 "Chemical Additives and Modified Concretes", Joint Stock Company "Research Center "Construction" (JSC "Research Center "Construction"), 6, 2-ya Institutskaya St., Moscow, 109428, Professor of the Department of Construction Materials Science at the National Re-search Moscow State University of Civil Engineering, 26, Yaroslavskoye Shosse, Moscow, Russia, 129337 sska-pri@gmail.com

Petr Dmitrievich Arleninov – Ph.D. in Technical Sciences, Deputy Head of Laboratory No. 8 "Reinforced Concrete Me-chanics", Joint Stock Company "Research Center "Construction" (JSC "Research Center "Construction"), 6, 2-ya Institutskaya St., Moscow, 109428, Russia, docent Department of Reinforced Concrete and Masonry Structures of the National Research Moscow State University of Civil Engineering, 26, Yaroslavskoye Shosse, Moscow, Russia, 129337, ar-leninoff@gmail.com

Andrey Vladimirovich Sheinfeld - Ph.D. in Technical Sciences, Deputy Head of Laboratory No. 16 "Chemical Additives and Modified Concretes", Joint Stock Company "Research Center "Construction" (JSC "Research Center "Construction"), 6, 2-ya Institutskaya St., Moscow, 109428, Professor of the Department of Construction Materials Science at the National Research Moscow State University of Civil Engineering, 26, Yaroslavskoye Shosse, Moscow, Russia, 129337, sheyn-feld@masterbeton-mb.ru

Polina Sergeevna Kalmakova - researcher at Laboratory No. 8 «Mechanics of Reinforced Concrete», Joint Stock Company "Research Center "Construction" (JSC "Research Center "Construction"), 6, 2-ya Institutskaya St., Moscow, 109428, Russia, postgraduate student of the Department «Construction Materials Science» at the National Research Moscow State University of Civil Engineering, 26, Yaroslavskoye Shosse, Moscow, Russia, 129337 polina15kalmakowa@gmail.com

Nikita Mikhailovich Selyutin - engineer at Laboratory No. 16 «Chemical Additives and Modified Concretes», Joint Stock Company "Research Center "Construction" (JSC "Research Center "Construction"), 6, 2-ya Institutskaya St., Moscow, 109428, Head of the Laboratory at Master Beton Enterprise LLC, Moscow, Russia 89165046672@mail.ru

Семен Суренович Каприелов – д.т.н., зав. лаборатории №16 «Химических добавок и модифицированных бетонов», Акционерное Общество «Научно-исследовательский центр «Строительство» (АО «НИЦ «Строительство»), 6, 2-я Институтская, Москва, 109428, профессор кафедры «Строительного материаловедения» Национально-исследовательского Московского Государственного Строительного Университета, sskapri@gmail.com

Петр Дмитриевич Арленинов – к.т.н., зам. зав. лаборатории №8 «Механики железобетона», Акционерное Общество «Научно-исследовательский центр «Строительство» (АО «НИЦ «Строительство»), 6, 2-я Институтская, Москва, 109428, Доцент кафедры «Железобетонных и каменных конструкций» Национально-исследовательского Московского Государственного Строительного Университета, arleninoff@gmail.com

Андрей Владимирович Шейнфельд – д.т.н., зам. зав. лаборатории №16 «Химических добавок и модифицированных бетонов», Акционерное Общество «Научно-исследовательский центр «Строительство» (АО «НИЦ «Строительство»), 6, 2-я Институтская, Москва, 109428, профессор кафедры «Строительного материаловедения» Национально-исследовательского Московского Государственного Строительного Университета,, sheynfeld@masterbeton-mb.ru

Полина Сергеевна Калмакова – научный сотрудник лаборатории №8 «Механики железобетона», Акционерное Общество «Научно-исследовательский центр «Строительство» (АО «НИЦ «Строительство»), 6, 2-я Институтская, Москва, 109428, аспирант кафедры «Строительного материаловедения» Национально-исследовательского Московского Государственного Строительного Университета, polina15kalmakowa@gmail.com

Никита Михайлович Селютин – инженер лаборатории №16 «Химических добавок и модифицированных бетонов», Акционерное Общество «Научно-исследовательский центр «Строительство» (АО «НИЦ «Строительство»), 6, 2-я Институтская, Москва, 109428, начальник лаборатории ООО «Предприятие Мастер Бетон», Москва, Россия, 89165046672@mail.ru

DOI:10.22337/2587-9618-2026-22-2-32-39

IMPROVING THE PROPERTIES OF CEMENT COMPOSITES BY CURING THEM USING AGGRESSIVE INFLUENCES

Anatoly P. Fedortsov [1], Vladimir T. Erofeev [2]

[1] Research Institute of Building Physics of the Russian Academy of Architecture and Construction Sciences, Moscow, RUSSIA
[2] National Research Moscow State University of Civil Engineering, Moscow, RUSSIA

Abstract: It is noted that the curing of cement composites is impossible without effects and is a reaction to them. In this case, the forces of the resulting resistance, according to the laws of thermodynamics, are aimed at weakening the impact. Experimental prerequisites and arguments are given that by choosing the time, intensity and duration of aggressive action on cement composites during their curing, it is possible to obtain more impact-resistant or ordered and durable structures of the material. The creation of conditions for the hardening of cement composites using liquid aggressive media leads to the formation of a dense inert layer on their surface, more adapted to the effects of this type. Using temperature and humidity influences, freezing and thawing, and loads, more durable composites were obtained. Thus, the curing of cement composites using time- and intensity-determined harsh temperature and humidity conditions, freezing and thawing, aggressive liquids, and loads makes it possible to obtain more durable or resistant structures of the material to specific destructive factors.

Keywords: cement composites, curing, aggressive effects, strength, loads, freezing and thawing, structure, material

УЛУЧШЕНИЕ СВОЙСТВ ЦЕМЕНТНЫХ КОМПОЗИТОВ ПУТЕМ ИХ ОТВЕРЖДЕНИЯ С ПРИМЕНЕНИЕМ АГРЕССИВНЫХ ВОЗДЕЙСТВИЙ

А.П. Федорцов [1], В.Т. Ерофеев [2]

[1] Научно-исследовательский институт строительной физики РААСН, г. Москва, РОССИЯ
[2] Национальный исследовательский Московский государственный строительный университет, г. Москва, РОССИЯ

Аннотация: Отмечается, что отверждение цементных композитов невозможно без воздействий и является реакцией на них. При этом силы возникающего сопротивления, согласно законам термодинамики, направлены на ослабление воздействия. Приводятся экспериментальные предпосылки и доводы, что подбирая время, интенсивность и длительность агрессивного воздействия на цементные композиты в период их отвердевания можно получать более приспособленные к воздействиям или упорядоченные и прочные структуры материала. Создание условий отвердевания цементных композитов с применением жидких агрессивных сред приводит к формированию на их поверхности плотного инертного слоя, более приспособленного к воздействиям такого вида. С применением температурно-влажностных воздействий, замораживания и оттаивания, нагрузок были получены более прочные композиты. Таким образом, отверждение цементных композитов с применением, установленных по времени и интенсивности, жестких температурно-влажностных воздействий, замораживания и оттаивания, агрессивных жидкостей, нагрузок позволяет получать более прочные или стойкие к конкретным разрушающим факторам структуры материала.

Ключевые слова: цементные композиты, отверждение, агрессивные воздействия, прочность, нагрузки, замораживание и оттаивание, структура, материал

INTRODUCTION

In the 1970s, Professor V.I. Solomatov proposed the idea that the interaction of liquid aggressive media with concrete components can lead not only to deterioration but also contribute to compaction, structural strengthening, etc., i.e., improve their properties. We have termed

processes of this kind "positive corrosion of concrete" [1], and its consequences such as compaction and strengthening are the "positive effect of corrosion" [2].

These experimentally confirmed propositions were further developed in the study [3] . This was based on the fact that if liquid aggressive media can cause effects such as compaction, hardening, and increased physicochemical resistance, then under the action of other destructive environmental factors (loads, freezing and thawing, etc.), corresponding positive changes are also feasible.

The scientific literature contains some instances where the action of an aggres-sive factor was thought to have improved or contributed to the improvement of a material's properties. For example, according to L. A. Malinina [4], reducing the relative humidity of the environment during the initial hardening period can regulate the evaporation of moisture from concrete and result in a finer-pored structure. According to our research [5], there is always such an initial curing time for cement concrete in air (t = 20 ± 2°C, W = 65–75%), at which its compressive strength during subsequent hardening in water is greater than that of a material that initially hardened for 24 hours under normal conditions.

Concrete curing also occurs through loading [6, 7, 8], freezing [9, 10, 11], and exposure to aggressive liquids [12]. According to research by A. V. Satalkin [6], concrete at an early age under compressive stresses up to no more than 0.6 Rpr experiences an increase in its compressive strength. It is evident that in this case, the material is strengthened due to resistance forces that contributed to the formation of a structure better adapted to this particular load.

Investigations by I. A. Kireenko, S. A. Mironova, and I. N. Akhverdov show that freezing cement concrete at specific stages of its hardening can improve its structure and, consequently, increase its strength [9]. However, this should not occur before the induction period has completed. According to the data in [13], cement concrete subjected to a single freeze-thaw cycle after two weeks of storage in water increased its strength by 17%. Studies by A. G. Olginsky and V.L. Chernyavsky [14, 15] indicate that cement composites can adapt to the effects of a low-intensity aggressive environment even in their mature state. There are cases where loading concrete, both in the early and mature stages, with compressive or tensile forces led to a corresponding increase in strength of up to 20% [16].

Based on the above studies, the issue of applying aggressive treatments to ce-ment composites to improve their properties has not been fully investigated. It is necessary to determine the optimal age at which cement concrete should be subjected to such treatments. Furthermore, what is needed is not merely data, but specific methodologies (protocols) for applying aggressive treatments to composites to improve their properties. In this regard, the proposed study is relevant, as it aims to address these objectives.

METHODOLOGY

This study presents the results of investigations conducted to demonstrate that a cement composite can more effectively resist a specific destructive factor if, during a certain stage of its evolution (hardening), it is exposed to that same factor at a predetermined intensity and for a predetermined duration. Thus, the following objectives were stated:

- theoretical justification of the possibility of improving the properties of cement composites by applying aggressive environmental factors during the hardening process;
- experimental studies to determine the effect on cement composites of an initial "harsher" air curing environment, as well as the effects of freezing and thawing and exposure to aggressive liquid media during a specified period of hardening;
- analysis of the correlation between experimental data and theoretical justification.

Portland cement M500 D0 from the Alekseevsky Cement Plant in Mordovia was used to produce cement stone and fine-grained concrete. The compressive strength of the cement stone was determined by testing specimens of 20 × 20 × 20 mm, while that of the fine-grained concrete was determined by testing halves of specimens measuring 40 × 40 × 160 mm in accordance with GOST 310.4-81.

The composition ratios of the cement stone and fine-grained concrete are presented throughout the paper. The following curing conditions were adopted, including exposure to aggressive environments:

Cement stone with W/C = 0.33

- Curing under normal conditions (t = 20 ± 2°C, W = 95–100%);
- 1 day under normal conditions, then 27 days in water (t = 20 ± 2°C);
- 1 day under normal conditions, then 13 days in 0.5% H_2SO_4, then 14 days in water;
- 1 day under normal conditions, then 27 days in 2% $(NH_4)_2SO_4$ solution;
- 1 day under normal conditions, then 27 days in 2% $Al_2(SO_4)_3$ solution.

Fine-grained concrete with mix proportion 1:3 and W/C = 0.45

- 1 day under normal conditions, then 27 days in water (t = 20 ± 2°C);
- 1 day under normal conditions, then 27 days in 0.5% H_2SO_4;
- 1 day under normal conditions, then 1 day in water, then 26 days in 0.5% H_2SO_4;
- 1 day under normal conditions, then 3 days in water, then 24 days in 0.5% H_2SO_4.

Other exposure conditions: The duration and parameters of exposure to a "harsh" air environment, as well as the number of freeze-thaw cycles, are shown in the figures of the text. Frost resistance was determined according to GOST 10060-2012 (Method 1).

RESULTS AND DISCUSSION

A hardening cementitious composite is a dynamic system which, according to [17], contains more microstates than it would if it were in a mature state. This means there are more competing structures, from which the ones best adapted to the external environment can be "strictly" selected.

Consider the possibilities of open systems from the perspective of thermodynamics. The tendency of physicochemical systems toward irreversible motion toward equilibrium is expressed by entropy (S). It is also a measure of the system's degree of order, i.e., a measure of structure formation. The rate of change of entropy for open systems can be determined by the expression [18]:

$$\frac{dS}{dt}=\frac{d_eS}{dt}+\frac{d_iS}{dt} \quad (1)$$

where $\frac{d_eS}{dt}$ is the rate of change in entropy due to external influences, $\frac{d_iS}{dt}$ is the same due to internal processes.

For isolated systems

$$\frac{d_eS}{dt}=0 \quad (2)$$

Then

$$\frac{dS}{dt}=\frac{d_iS}{dt} \quad (3)$$

The second law of thermodynamics states that entropy is always produced by internal processes, i.e.

$$\frac{d_iS}{dt}\geq 0 \quad (4)$$

As a result, for an isolated system, we have

$$\frac{dS}{dt}\geq 0 \quad (5)$$

This means that the entropy of an isolated system increases if the processes within it are out of equilibrium. The disorder of the system (material) increases, with the resulting negative consequences. While the value $\frac{d_iS}{dt}$ is never negative, $\frac{d_eS}{dt}$ has no definite sign. This allows us

to view evolution as a process in which the system can reach a state of lower entropy through the exchange of matter and energy with the external environment. It is evident that by adjusting mass and heat fluxes, one can influence the entropy increase, i.e., achieve the creation of an ordered or more adapted material structure, which is then fixed as a result of curing.

Thus, there are arguments that suggest that the application of aggressive influences to improve the properties of cement composites is most effective during the hardening phase. Furthermore, it is recommended that the material be adapted to aggressive environmental factors—not only liquid ones—in advance, during the hardening stages, to avoid disrupting the equilibrium of its structure during service [5].

Based on the above, it is possible to determine the timing, intensity, and duration of exposure to a high-temperature air environment during the curing of composites, when structural formation processes will prevail over degradation, and to consolidate the formed structures through curing. Thus, by pre-curing the molded fine-grained concrete with an open surface at a temperature of 40 ± 3°C and a humidity of 70–80%, followed by curing for up to 28 days in water, an increase in compressive strength in water of more than 20% was achieved (Fig. 1).

For comparison, a material was used that initially cured for 24 hours under normal conditions and then for up to 28 days in water. In Fig. 1, the strength value of such concrete was taken as the initial reference point.

Figure 2 shows the results of studies in which fine-grained cement concrete, af-ter two weeks of storage in water, was subjected to three cycles of alternating freez-ing and thawing, followed by a 28-day immersion in water, and gained approximately 18% in strength. The increase in material strength is attributed to more complete cement hydration resulting from increased water penetration into the concrete structure due to the rise in water pressure during freezing and its activity during thawing.

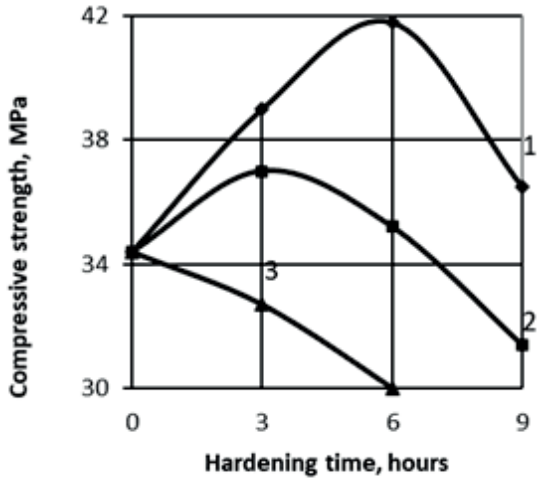

Figure 1. The relationship between the strength of concrete with a 1:3 mix ratio (W/C = 0.45) and the duration of initial air-setting at elevated temperatures and relative humidity (RH) of 70–80%: 1 – hardening at 40 ± 3°C; 2 – same at 50 ± 3°C; 3 – same at 60 ± 3°C

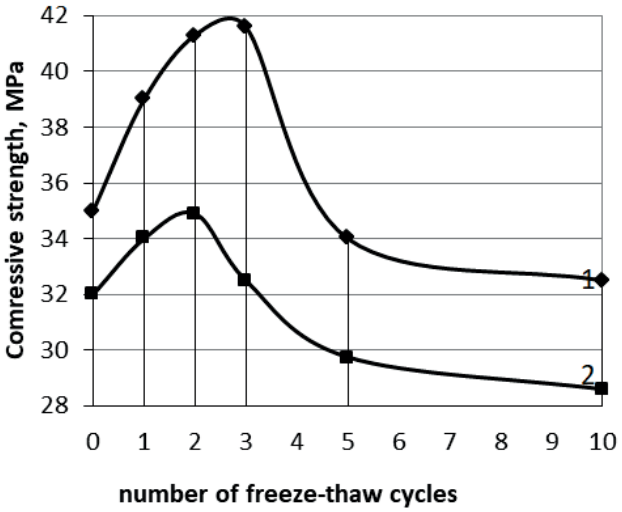

Figure 2. The effect of alternate freezing and thawing of fine-grained concrete during its hardening in water (after 14 days) on compressive strength: 1 – composition 1:3 with W/C = 0.45; 2 – the same with W/C = 0.5

According to [9], this is a result of the increased density of the crystalline hy-drate structure and the reduced porosity of the cement paste. It is evident that freezing leads to the emergence of structural features in concrete that, according to established theory, contribute to increased

resistance to this same type of stress. And the curing of cement paste (W/C = 0.33) using a 0.5% sulfuric acid solution led to an increase in its resistance in a 2% solution of the same acid (Fig. 3).

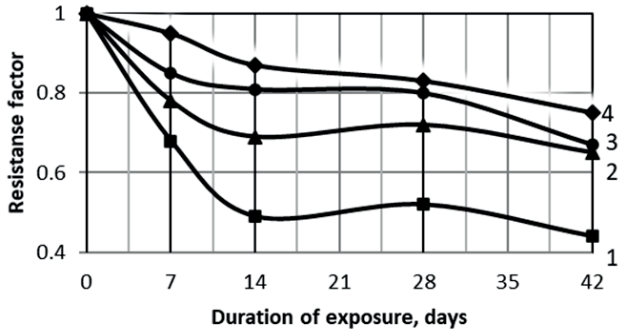

Figure 3. Effect of curing conditions on the stone's resistance in a 2% H_2SO_4 solution: 1 – cured for 1 day under standard conditions, 27 days in water;2 – 1 day under standard conditions, 13 days in a 0.5% H_2SO_4 solution, 14 days in water; 3 – 1 day under normal conditions, 27 days in a 2% solution of $(NH_4)_2SO_4$;4 – 1 day under normal conditions, 27 days in a 2% solution of $Al_2(SO_4)_3$

The physical and chemical resistance of concrete also increases when the com-ponents of the curing medium are merely individual constituents of that medium. Thus, the curing of cement paste (W/C = 0.33) using 2% acidic salts—ammonium sulfate and aluminum sulfate—contributed to a significant increase in its resistance to a 2% H_2SO_4 solution. It should be noted, however, that the use of curing media containing aggressive components in all cases led to a partial loss of initial strength. The initial strength values, according to Fig. 1, were: 1 – 68 MPa, 2 – 56 MPa, 3 – 54 MPa, 4 – 47 MPa. At the same time, cement stone cured under such conditions always exhibited higher strength (by 18–22%) after aging in an aggressive environment than that aged in water.

The table presents the results of a test on the resistance of fine-grained concrete with a 1:3 mix ratio and a water-cement ratio (W/C) of 0.45 to a 1% H_2SO_4 solution; which, during the hardening period, was exposed at specified intervals to the same medium but at a lower concentration (0.5%) and under different conditions than those applied to the cement paste.

Table 1. The Effect of the Curing Environment on the Resistance of Fine-Grained Concrete to 1% H_2SO_4

Curing Environment	σ_0, MPa	Duration of exposure, days	σ_τ, MPa	$K_{ст}$
1 days under standard conditions, 27 days in water	21.9	20	13.1	0.6
1 days under standard conditions, 1 days in water, 26 days under 0.5% solution of H_2SO_4	21.7	20	16.9	0.78
1 days under standard conditions, 3 days in water, 24 days under 0.5% solution of H_2SO_4	19.8	20	16.6	0.84

The table shows that concrete specimens exposed to an aggressive agent of a specified intensity and duration during the hardening period are more resistant, once matured, to the same type of environment but at a higher concentration. Their compressive strength after exposure to the environment is 27% and 29% higher than that of concrete that hardened in water.

Cement paste and fine-grained concrete, which were partially adapted to a weak sulfuric acid solution, had a dense protective layer on their surface, the main components of which were: silicic acid gel, sulfates, and cement paste minerals modified by them.

The condition for the formation of a composite more resistant to a specific aggressive influence during its hardening with the formation of adapted bonds can be expressed as follows:

$$V_{\text{o}}(t) \geq V_{\text{п}}(t), \quad (6)$$

where $V_{\text{o}}(t)$ is the rate at which defects are eliminated and adapted bonds are formed as a result of positive interactions over a period of time Δt, $V_{\text{п}}(t)$ is the the rate of decay of initial bonds over a time interval Δt.

Previous studies [5] also confirm the positive effect of early loading on the performance properties of concrete. At the same time, the application of a bending load to the concrete during the curing period—amounting to approximately 5% of the ultimate load at the moments of its application, which is significantly less than in known studies—did not lead to an increase in the average flexural strength but contributed to a 5.2-fold reduction in the coefficient of variation of the flexural test results. At the same time, the flexural strength guaranteed with 95% confidence increased by 13%, while deflections and their deviations from the mean value decreased by more than 12% and 30%, respectively.

Studies have also shown that the duration of load application during the concrete hardening period depends on the magnitude of the load. The failure factor should not lead to material failure.

CONCLUSION

1. The hardening of cementitious composites through the application of temperature and humidity stresses, freezing and thawing cycles, and aggressive liquids—with precisely controlled duration and intensity—enables the creation of material structures that are stronger or more resistant to specific destructive factors.

2. To produce a composite that would more effectively resist a specific destruc-tive factor, it is necessary for the composite to be exposed to that same factor during a specific period of its development, but at a predetermined intensity and duration. In this case, the aggressive factor must not lead to the destruction of the composite.

3. Since exposure to liquid corrosive media of a certain intensity and duration during the specified curing periods of cement composites can lead to their partial or complete adaptation to the exposure, it can be concluded that during the adaptation of the composite (system), a selection of processes occurs that contribute to increasing its resistance to a specific impact.

FUNDING

The research was funded by the National Research Moscow State University of Civil Engineering.

REFERENCES

1. **Solomatov V.I., Fedortsov A.P. Positive Corrosion of Concretes / V.I. Solomatov, A.P. Fedortsov** // Performance of Composite Building Materials under Various Operational Factors. – Kazan : Publishing House of KCTI named after S. M. Kirov, 1982. – P. 10 – 13.
2. **Solomatov V.I., Fedortsov A.P.** Positive Effect of Corrosion of Polymer Concretes / V. I. Solomatov, A. P. Fedortsov // Concrete and Reinforced Concrete. – 1981. - No. 2. – P. 20 – 21.
3. **Fedortsov A.P.** Positive Corrosion of Concretes as a Prerequisite for Improving Their Properties by Aggressive Influences / A. P. Fedortsov // Bull. of Mordov. Univ. – 2002. - No. 1 – 2. – P. 152 – 156.
4. **Malinina L.A.** Heat and Moisture Treatment of Heavy Concrete / L. A. Malinina. – M. : Stroyizdat, 1977. – 159 p.
5. **Fedortsov A.P.** Physicochemical Resistance of Building Composites and Ways to Increase It : monograph / A.P. Fedortsov. – Saransk : Publishing House of Mordov. Univ., 2015. – 464 p.
6. **Satalkin A.V., Senchenko B.A.** Early Loading of Concrete and Reinforced Concrete in Bridge Construction / A.V.

Satalkin, B.A. Senchenko. – M. : Avtotransizdat, 1956. – 214 p.
7. **Baiburin A.Kh.** Investigation of Strength and Deformability of Heavy Concrete under Early Loading / A.Kh. Baiburin // Engineering Bulletin of the Don. – 2022. - No. 6.URL: ivdon.ru/ru/magazine/archive/n6y2022/7603
8. **Obayes O., Gad E., Pokharel T., Lee J. et al.** Evaluation of Concrete Material Properties at Early Age // Civil Engineering. – 2020 – Vol. 1 – Pp. 326 – 350.
9. **Akhverdov I.N.** Fundamentals of Concrete Physics / I. N. Akhverdov. – M. : Stroyizdat, 1981. – 464 p.
10. **Trinker A.B.** Winter Concreting and Work in Permafrost Conditions / A. B. Trinker // Concrete Technologies. – 2013 .– No. 2 .– P. 42 – 44.
11. **Batyanovsky E.I., Gurienko N.S., Korsun A.M.** Increasing the Frost Resistance of Cement Concrete / E. I. Batyanovsky, N. S. Gurienko, A. M. Korsun // Mechanics and Technology Scientific Journal. – 2022. - No. 2(7). – P. 148 – 159.
12. **Fedortsov A.P., Erofeev V.T.** Increasing the Physicochemical Resistance of Cement Composites by Using Aggressive Media during Their Curing / A. P. Fedortsov, V. T. Erofeev // Bull. of the Volga Region Branch of the RAASN [N. Novgorod]. – 2002. – Iss. 5. – P. 98 – 101.
13. **Fedortsov A.P.** Improving the Properties of Concretes by Aggressive Influences / A. P. Fedortsov // Bull. of Mordov. Univ. – 2003. - No. 1 – 2. – P. 135 – 138.
14. **Olginsky A.G., Chernyavsky V.L.** Influence of the Environment on the Adaptation of the Aggregate-Cement Stone Contact Zone in Concrete / A.G. Olginsky, V.L. Chernyavsky // Concrete and Reinforced Concrete. – 2000. - No. 4. – P. 5 – 8.
15. **Chernyavsky V.L.** The Role of Adaptation in the Formation of Concrete Corrosion Resistance / V.L. Chernyavsky // Proceedings of Universities. Construction Series [Novosibirsk]. – 1995. - No. 4. – P. 34 – 39.
16. **Makarenko L.P.** Change in Physicomechanical Properties of Concretes under Compression and Tension under Repeated Loading / L. P. Makarenko // Concrete and Reinforced Concrete. – 1989. - No. 2. – P. 38 – 40.
17. **Haken H.** Synergetics : trans. from English / H. Haken. – M. : Mir, 1980. – 404 p.
18. **Nicolis G., Prigogine I.** Self-Organization in Nonequilibrium Systems : trans. from English / G. Nicolis, I. Prigogine. – M. : Mir, 1979. – 512 p.

СПИСОК ЛИТЕРАТУРЫ

1. **Соломатов В.И., Федорцов А.П.** Положительная коррозия бетонов / В.И. Соломатов, А.П. Федорцов // Эксплуатационные характеристики композитных строительных материалов при различных эксплуатационных факторах. – Казань: Издательство КЦТИ им. С. М. Кирова, 1982. – С. 10–13.
2. **Соломатов В.И., Федорцов А.П.** Положительное влияние коррозии полимерных бетонов / В. И. Соломатов, А. П. Федорцов // Бетон и железобетон. – 1981. – № 2. – С. 20–21.
3. **Федорцов А.П.** Положительная коррозия бетонов как предпосылка для улучшения их свойств агрессивными воздействиями / А. П. Федорцов // Вестник Мордовского университета. – 2002. – № 1 – 2. – С. 152 – 156.
4. **Малинина Л.А.** Тепловая и влагозащитная обработка тяжелого бетона / Л. А. Малинина. – М.: Стройиздат, 1977. – 159 с.
5. **Федорцов А.П.** Физико-химическая стойкость строительных композитов и способы ее повышения: монография / А. П. Федорцов. – Саранск: Издательство Мордовского университета, 2015. – 464 с.

6. **Саталкин А.В., Сенченко Б.А.** Ранняя нагрузка бетона и железобетона при строительстве мостов / А. В. Саталкин, Б. А. Сенченко. – М.: Автотрансиздат, 1956. – 214 с.
7. **Байбурин А.Х.** Исследование прочности и деформируемости тяжелого бетона при ранней нагрузке / А.Х. Байбурин // Инженерный вестник Дона. – 2022. – № 6. URL: ivdon.ru/ru/magazine/archive/n6y2022/7603.
8. **Обайес О., Гад Е., Покхарел Т., Ли Дж. и др.** Оценка свойств бетонных материалов в раннем возрасте // Гражданское строительство. – 2020 – Т. 1 – С. 326 – 350.
9. **Ахвердов И.Н.** Основы физики бетона / И. Н. Ахвердов. – М.: Стройиздат, 1981. – 464 с.
10. **Тринкер А.Б.** Зимнее бетонирование и работы в условиях вечной мерзлоты / А. Б. Тринкер // Технологии бетона. – 2013. – № 2. – С. 42–44.
11. **Батяновский Е.И., Гуриенко Н.С., Корсун А.М.** Повышение морозостойкости цементного бетона / Е.И. Батяновский, Н.С. Гуриенко, А.М. Корсун // Научно-технический журнал «Механика и техника». – 2022. – № 2(7). – С. 148–159.
12. **Федорцов А.П., Ерофеев В.Т.** Повышение физико-химической стойкости цементных композитов с использованием агрессивных сред в процессе их твердения / А. П. Федорцов, В. Т. Ерофеев // Вестник Поволжского отделения РААКС [Н. Новгород]. – 2002. – Вып. 5. – С. 98 – 101.
13. **Федорцов А.П.** Улучшение свойств бетона агрессивными воздействиями / А. П. Федорцов // Вестник Мордовского университета – 2003. – № 1 – 2. – С. 135 – 138.
14. **Ольгинский А.Г., Чернявский В.Л.** Влияние окружающей среды на адаптацию зоны контакта заполнителя и цементного камня в бетоне / А. Г. Ольгинский, В. Л. Чернявский // Бетон и железобетон. – 2000. – № 4. – С. 5 – 8.
15. **Чернявский В.Л.** Роль адаптации в формировании коррозионной стойкости бетона / В. Л. Чернявский // Труды университетов. Строительная серия [Новосибирск]. – 1995. – № 4. – С. 34–39.
16. **Макаренко Л.П.** Изменение физико-механических свойств бетона при сжатии и растяжении при многократной нагрузке / Л.П. Макаренко // Бетон и железобетон. – 1989. – № 2. – С. 38–40.
17. **Хакен Г.** Синергетика: перевод с английского / Г. Хакен. – М.: Мир, 1980. – 404 с.
18. **Николис Г., Пригожин И.** Самоорганизация в неравновесных системах: перевод с английского / Г. Николис, И. Пригожин. – М.: Мир, 1979. – 512 с.

Anatoly Petrovich Fedortsov, PhD, Docent, Research Institute of Building Physics of the Russian Academy of Architecture and Construction Sciences (NIISF RAASN), 127238, Russia, Moscow, Lokomotivny proezd, 21b3. e-mail: antoliy.fedortsov@mail.ru

Vladimir Trofimovich Erofeev, Dr. Sc., Professor, Academician of the Russian Academy of Architecture and Construction Sciences (RAASN), Professor of the Department of Construction Materials of the National Research Moscow State University of Civil Engineering (NRU MGSU), 129337, Russia, Moscow, Yaroslavskoe Shosse, 26, e-mail: ErofeevaIV@gic.mgsu.ru

Анатолий Петрович Федорцов, кандидат технических наук, доцент, главный научный сотрудник Научного-исследовательского института строительной физики (НИИСФ РААСН), 127238 г. Москва, Локомотивный проезд, 21с3. e-mail: antoliy.fedortsov@mail.ru

Владимир Трофимович Ерофеев, доктор технических наук, профессор, академик РААСН, профессор кафедры «Строительных материалов» Национального исследовательского Московского государственного строительного университета (НИУ МГСУ) 129337, г. Москва, Ярославское шоссе, д. 26. e-mail: erofeevvt@bk.ru

DOI:10.22337/2587-9618-2026-22-2-40-50

EFFECT OF THE WAVE PROCESSES CAUSED BY EXTERNAL INFLUENCE ON THE FILTERING OF AQUEOUS SOLUTIONS IN THE EXPANDED LOADING LAYER

Yuri A. Chirkunov [1], Yuri L. Skolubovich [1], Vladimir N. Sidorov [2], Evgeniy V. Alekseev [2]

[1] Novosibirsk State University of Architecture and Civil Engineering (Sibstrin), Novosibirsk, RUSSIA
[2] National Research Moscow State University of Civil Engineering, Moscow, RUSSIA

Abstract: In this paper, the influence of traveling waves arising from external action on the filtering process of aqueous solutions in the expanded loading layer is investigated. A three-dimensional dynamic generalized model of fluid motion in a porous medium under a nonlinear external influence is used as the primary mathematical model. A model describing traveling waves is obtained. Nine particular cases of this model with three types of nonlinearity process of filtering are examined: power, exponential, and logarithmic. The external influence is also selected power, exponential, and logarithmic. The particular models describe both expansion and contraction of the loading layer on the type of filtration nonlinearity, the type of external influence, and the traveling wave parameters. For filtering with the expanding loading layer we found the time at which maximum it's expansion is achieved. When the loading layer contaminates we found the time at which it will be destroyed.

Keywords: filtering of aqueous solutions, expanded loading layer, traveling wave, nonlinear external influence, porous medium

ВЛИЯНИЕ ВОЛНОВЫХ ПРОЦЕССОВ, ВЫЗВАННЫХ ВНЕШНИМ ВОЗДЕЙСТВИЕМ, НА ФИЛЬТРОВАНИЕ ВОДНЫХ РАСТВОРОВ В РАСШИРЕННОМ СЛОЕ ЗАГРУЗКИ

Ю.А. Чиркунов [1], Ю.Л. Сколубович [1], В.Н. Сидоров [2], Е.В. Алексеев [2]

[1] Новосибирский государственный архитектурно-строительный университет (Сибстрин), Новосибирск, РОССИЯ
[2] Национальный исследовательский Московский государственный строительный университет, МОСКВА, РОССИЯ

Аннотация: В настоящей работе исследуется влияние возникающих при внешнем воздействии бегущей волн на процесс фильтрования водных растворов в расширенном слое загрузки. В качестве основной математической модели используется трехмерная динамическая обобщенная модель движения жидкости в пористой среде при наличии нелинейного внешнего воздействия. Получена модель, описывающая бегущие волны. Исследовано 9 частных случаев этой модели с тремя видами нелинейности процесса фильтрования: степенной, экспоненциальной и логарифмической. Внешнее воздействие при этом также выбрано степенным, экспоненциальным и логарифмическим. Эти частные модели описывают как расширение, так и загрязнение слоя загрузки в зависимости от вида нелинейности процесса фильтрования, вида внешнего воздействия и параметров бегущей волны. Для фильтрования с расширяющимся слоем загрузки мы нашли время, при котором достигается максимальное его расширение. При загрязнении слоя загрузки мы нашли время, за которое он разрушится.

Ключевые слова: фильтрование водных растворов, расширенный слой загрузки, бегущая волна, нелинейное внешнее воздействие, пористая среда

INTRODUCTION

The science of the movement of fluids, gases, and their mixtures in porous media iscalledsubsurface hydromechanics. The object of study in subsurface hydromechanics is filtration flow - the flow of a fluid (gas, gas- fluid mixture) in a porous medium. Subsurface hydromechanics has

extensive applications in other sciences, including hydrogeology, engineering geology, soil studies during the initial stages of building and structure construction, hydraulic engineering, and others. The first experiments to study water filtration in saturated soils were conducted by the French scientist A. Darcy, who in 1856 formulated an experimental law expressing the dependence of filtration rate on pressure gradient. During this same period, another French scientist, J. Dupuis, published a monograph outlining the theory of groundwater filtration, deriving formulas for well flow rates, and solving other filtration problems. American scientists C. Slichter and M. Musket made significant contributions to the development of subsurface hydromechanics. The founders of the Russian school of filtration theory were N.E. Zhukovsky and N.N. Pavlovsky. Underground hydromechanics is one of the constituent theories of oil and gas field development and oil and gas production technology. The founder of Russian oil and gas underground hydromechanics is L.S. Leibenzon. He became the founder of underground hydraulics, which played a major role in creating the scientific foundations for oil field development. Scientists S.A. Khristianovich, B.B. Lapuk, I.A. Charny, V.N. Shchelkachev and others, made outstanding contributions to the development of the theory of fluid and gas filtration in oil-gas-water-bearing formations. All these studies arebased on the classical mathematical model of a porous medium. The classical model of a porous medium and some of its simple generalizations have been studied in many works [1–7]. In these studies, boundary value problems related to the motion of fluids and gases in porous media were investigated using analytical and numerical methods.

Studying the motion of fluids or gases in porous media using classical models does not always adequately describe real processes. This is due to the fact that these models do not take into account the presence of an external influence. For more adequately describe real processes, it is necessary to develop and study new, more complex models with an external influence. The study of a general three-dimensional nonlinear dynamic model of fluid or gas motion in a porous medium with a non-stationary source was initiated in the works of the authors [8–11].

In our study, we investigate the influence of a traveling wave on the filtering of aqueous solutions in an expanded loading layer. As a model for describing this influence, we used a general three-dimensional nonlinear dynamic model of fluid motion in a porous medium with a nonlinear an external influence. This model is defined by the following equation

$$p_t = \Delta\Phi\left(p\right) - f\left(p\right), \qquad (1)$$

where $p = p\left(t,\boldsymbol{x}\right)$ is a pressure in the loading layer, $\boldsymbol{x} = \left(x,y,z\right) \in R^3$, $\Delta = \partial_x^2 + \partial_y^2 + \partial_z^2$, t is a time, $\Phi\left(p\right)$ and $f\left(p\right)$ are any functions, which are determined empirically. $\Phi\left(p\right) > 0$ defines a nonlinearity of the process, $f\left(p\right)$ defines nonlinear nature of the influence of a traveling wave on the filtering of aqueous solutions in an expanded loading layer. A case $f\left(p\right) < 0$ corresponds, for example, to the presence of a source. A case $f\left(p\right) > 0$ corresponds, for example, to the presence of an absorption. The functions $\Phi\left(p\right)$ and $f\left(p\right)$ satisfy to the condition

$$\Phi''\left(p\right) f'\left(p\right) \neq 0.$$

This condition means that the process is nonlinear and the influence is not a constant value.

METHODS

The primary research method in our work is the modeling of physically significant problems using group analysis of differential equations,

which is one of the most effective methods for obtaining maximum information about solutions to differential equations.

The concepts and algorithms of modern group analysis of differential equations can be found, for example, in [12–16] and the references cited therein.

In the specific examples considered, for each obtained nonlinear model, the equation defining this model is reduced to an equivalent system of first-order differential equations. The resulting Cauchy problem for each such system is solved numerically using the Runge-Kutta-Felberg method, the concepts and algorithms of which can be found, for example, in [17] and the references cited therein.

RESULTS AND DISCUSSION

The study conducted in this paper is new and has not been previously reported in the literature.

A general traveling wave for a porous medium has the form

$$p = \phi(\xi), \quad \xi = t + \alpha x + \beta y + \gamma z, \tag{2}$$

Where α, β, γ are arbitrary real numbers, satisfying the condition $\alpha^2 + \beta^2 + \gamma^2 \neq 0$.

Substituting (2) into (1) yields the following differential equation

$$\left(\alpha^2 + \beta^2 + \gamma^2\right)\left(\frac{d}{d\xi}\left(\frac{d\Phi(\phi)}{d\phi}\frac{d\phi(\xi)}{d\xi}\right)\right) - \frac{d\phi(\xi)}{d\xi} + f(\phi) = 0. \tag{3}$$

The functions $\Phi(\phi)$, $f(\phi)$ and constants α, β, γ specifies each particular model of a traveling wave.

We will be study at some particular models and indicate what influence in these models have on the filtering in the expanded loading layer.

1. First particular models

At $\Phi(\phi) = \mu\phi^{\lambda}$ where λ, μ are arbitrary real numbers, satisfying the condition $\lambda\mu \neq 0$, equation (3) takes a form

$$\lambda\mu\left(\alpha^2 + \beta^2 + \gamma^2\right)\phi^{\lambda-2}\left(\phi\frac{d^2\phi}{d\xi^2} + (\lambda-1)\left(\frac{d\phi}{d\xi}\right)^2\right) - \frac{d\phi}{d\xi} + f(\phi) = 0. \tag{4}$$

This equation defined model depending on α, β, γ, λ, μ and $f(\phi)$.

Equation (4) is equivalent to the following system

$$\frac{d\phi}{d\xi} = \phi^{1-\lambda}\psi, \quad \frac{d\psi}{d\xi} = \frac{\phi^{1-\lambda}\psi - f(\phi)}{\lambda\mu\left(\alpha^2 + \beta^2 + \gamma^2\right)}, \tag{5}$$

where $\psi = \psi(\xi)$ is new unknown function.

Let at initial time $t = t_0 \geq 0$ at a fixed point $\boldsymbol{x}_0 = \left(x_0,\ y_0,\ z_0\right)$ the pressure and the rate of its change are given

$$p\left(t_0,\ \boldsymbol{x}_0\right) = p_0 > 0, \quad \frac{\partial p}{\partial t}\left(t_0,\ \boldsymbol{x}_0\right) = p_1. \tag{6}$$

We will find a function $\phi(\xi)$ satisfying system (5) to solve this problem.

The initial data for system (5) has a form

$$\phi(\xi_0) = p_0, \ \psi(\xi_0) = \left(p_0\right)^{\lambda-1} p_1, \ \xi_0 = t_0 + \alpha x_0 + \beta y_0 + \gamma z_0. \tag{7}$$

Due to the smoothness of the right-hand sides of system (5), the solution of the Cauchy problem (5), (7) exists and is unique in the neighborhood of the point ξ_0.

1.1. In the first example, we obtain this solution at $f(\phi)=a\phi^b$ (a, b are arbitrary real numbers). At $\alpha=1$, $\beta=1$, $\gamma=1$, $\lambda=2$, $\mu=1$, $t_0=1$, $x_0=1$, $y_0=1$, $z_0=1$, $p_0=1$, $p_1=-5$, $a=1$, $b=1$ we solved numerically the Cauchy problem (5), (7) by the Runge-Kutta-Fehlberg method [17] (with order of accuracy 4). The graph of the function $\phi=\phi(\xi)$ is shown in the Fig. 1.

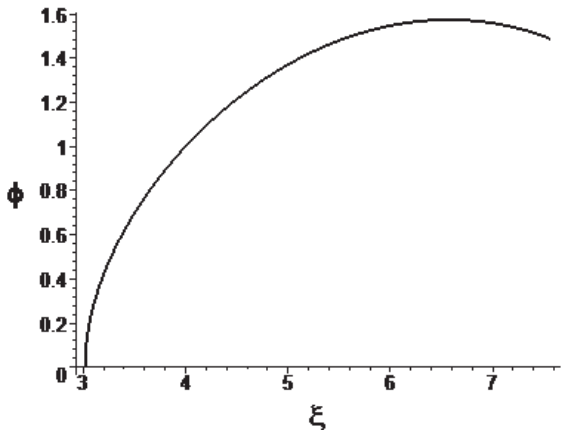

Figure 1. Pressure distributions for the model 1.1

This graph shows that the pressure in the loading layer L increases at $\xi\in[3;\ 6{,}6]$. This means that the loading layer gets clogged. At $\xi=6{,}6$ the pressure reaches its maximum value and begins to decrease at $\xi>6{,}6$. This means that at $\xi=6{,}6$, filtering ceases and the loading layer is destroyed. The onset of destruction time is:

$$t=\sup_{\boldsymbol{x}\in L}\left(6{,}6-x-y-z\right).$$

1.2. In the second example, we obtain this solution at $f(\phi)=a\exp(b\phi)$ (a, b are arbitrary real numbers). At $\alpha=1$, $\beta=1$, $\gamma=1$, $\lambda=5$, $\mu=1$, $t_0=1$, $x_0=1$, $y_0=1$, $z_0=1$, $p_0=1$, $p_1=-5{,}5$, $a=1$, $b=0{,}5$ we solved numerically the Cauchy problem (5), (7) by the Runge-Kutta-Fehlberg method [17] (with order of accuracy 4). The graph of the function $\phi=\phi(\xi)$ is shown in the Fig. 2.

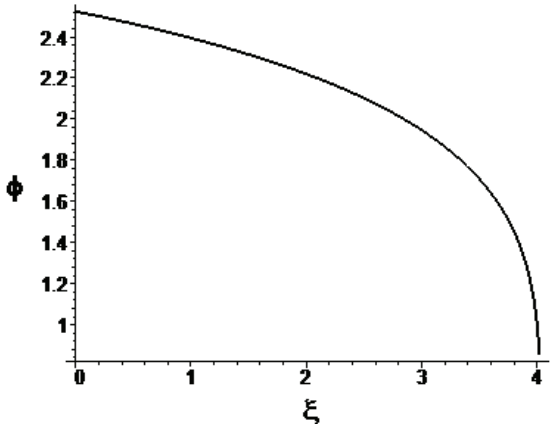

Figure 2. Pressure distributions for the model 1.2

This graph shows that the pressure in the loading layer decreases. This means that the loading layer expands. Let p_* is the pressure at which the maximum expansion of the loading layer L is achieved. And this pressure is reached at the point $\boldsymbol{x}=(x,y,z)$ in the loading layer at $\xi=\xi_*$ $\left(0<\xi_*<4\right)$. This solution has a physical meaning at $\xi\in(0;\ \xi_*]$. The time to reach maximum expansion of the loading layer is determined by the formula

$$t_*=\sup_{\boldsymbol{x}\in L}\left(\xi_*-x-y-z\right).$$

1.3. In the second example, we obtain this solution at $f(\phi)=a\ln\phi$ (a is arbitrary real number). At $\alpha=1$, $\beta=1$, $\gamma=1$, $\lambda=1{,}5$, $\mu=1$, $t_0=1$, $x_0=1$, $y_0=1$, $z_0=1$, $p_0=1$, $p_1=-0{,}05$, $a=1$, $b=1$ we solved numerically the Cauchy problem (5), (7) by the Runge-Kutta-Fehlberg method [17] (with order of accuracy 4). The graph of the function $\phi=\phi(\xi)$ is shown in the Fig.3.

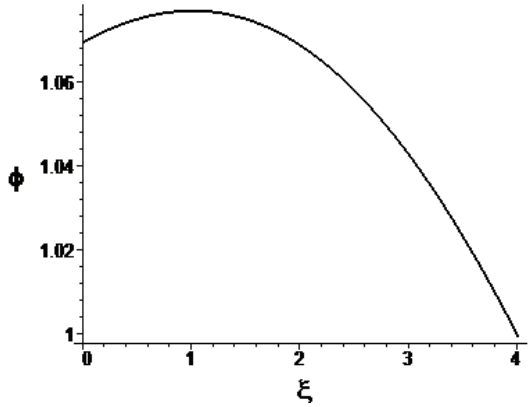

Figure 3. Pressure distributions for the model 1.2.

From this graph, it follows that the pressure increases briefly at $\xi \in (0;\ 1,2]$ and reaches its maximum value at $\xi = 1,2$, then the pressure at $\xi > 1,2$ decreases. This means that the loading layer L is heavily contaminated and is rapidly beginning to deteriorate. The onset of destruction time is:

$$t = \sup_{\boldsymbol{x} \in L} \left(1,2 - x - y - z\right).$$

2. Second particular models

At $\Phi(\phi) = \mu \exp(\lambda\phi)$ where $\lambda,\ \mu$ are arbitrary real numbers, satisfying the condition $\lambda\mu \neq 0$, equation (3) takes a form

$$\lambda\mu\left(\alpha^2 + \beta^2 + \gamma^2\right)\exp(\lambda\phi)\left(\frac{d^2\phi}{d\xi^2} + \right.$$
$$\left. + \left(\lambda\frac{d\phi}{d\xi}\right)^2\right) - \frac{d\phi}{d\xi} + f(\phi) = 0. \qquad (8)$$

This equation defined model depending on $\alpha,\ \beta,\ \gamma,\ \lambda,\ \mu$ and $f(\phi)$.

Equation (8) is equivalent to the following system

$$\frac{d\phi}{d\xi} = \exp(-\lambda\phi)\psi,$$
$$\frac{d\psi}{d\xi} = \frac{\exp(-\lambda\phi)\psi - f(\iota)}{\lambda\mu\left(\alpha^2 + \beta^2 + \gamma^2\right)}, \qquad (9)$$

where $\psi = \psi(\xi)$ is new unknown function.

We use the function $\phi(\xi)$ satisfying this system and conditions (6).

The initial data for system (5) has a form

$$\phi(\xi_0) = p_0,\ \psi(\xi_0) = p_1 \exp(\lambda p_0),$$
$$\xi_0 = t_0 + \alpha x_0 + \beta y_0 + \gamma z_0. \qquad (10)$$

Due to the smoothness of the right-hand sides of system (9), the solution of the Cauchy problem (9), (10) exists and is unique in the neighborhood of the point ξ_0.

2.1. In the first example, we obtain this solution at $f(\phi) = a\phi^b$ ($a,\ b$ are arbitrary real numbers At $\alpha = 1,\ \beta = 1,\ \gamma = 1,\ \lambda = 5,\ \mu = 1,\ t_0 = 1,$ $x_0 = 1,\ y_0 = 1,\ z_0 = 1,\ p_0 = 1,\ p_1 = -1,\ a = 1,$ $b = 2$ we solved numerically the Cauchy problem (9), (10) by the Runge-Kutta-Fehlberg method [17] (with order of accuracy 4). The graph of the function $\phi = \phi(\xi)$ is shown in the Fig. 4.

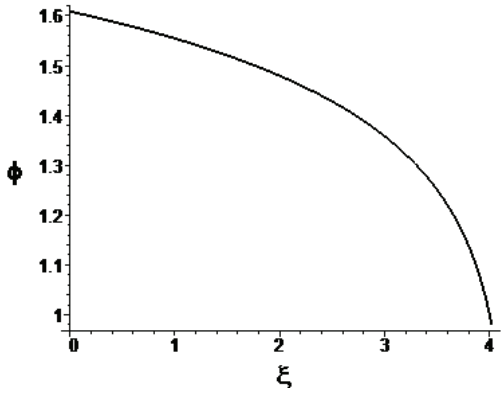

Figure 4. Pressure distributions for the model 2.1.

From this graph, it follows that the pressure in the loading layer decreases. This means that the loading layer expands. Let p_* is the pressure at which the maximum expansion of the loading layer L is achieved. And this pressure is reached at the point $\boldsymbol{x} = (x,y,z)$ in the loading layer at $\xi = \xi_*$ $(0 < \xi_* < 4)$. This solution

has a physical meaning at $\xi \in \left(0;\ \xi_*\right]$. The time to reach maximum expansion of the loading layer is determined by the formula

$$t_* = \sup_{\boldsymbol{x}\in L}\left(\xi_* - x - y - z\right).$$

2.2. In the second example, we obtain this solution at $f(\phi) = a\exp(b\phi)$ (a, b are arbitrary real numbers) At $\alpha = 1,\ \beta = 1,\ \gamma = 1,\ \lambda = 2,\ \mu = 1,\ t_0 = 1,\ x_0 = 1,\ y_0 = 1,\ z_0 = 1,\ p_0 = 1,\ p_1 = -0,01,\ a = 1,\ b = -1$ we solved numerically the Cauchy problem (9), (10) by the Runge-Kutta-Fehlberg method [17] (with order of accuracy 4). The graph of the function $\phi = \phi(\xi)$ is shown in the Fig. 5.

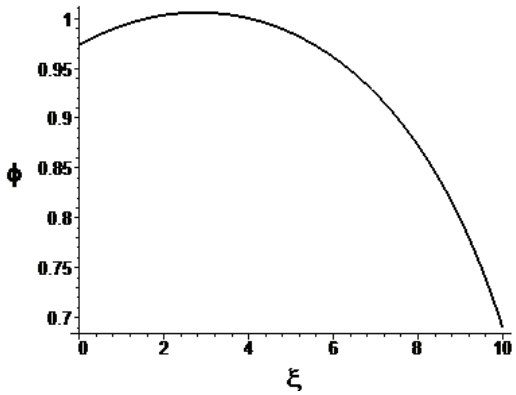

Figure 5. Pressure distributions for the model 2.2.

From this graph, it follows that the pressure increases briefly at $\xi \in \left(0;\ 3\right]$ and reaches its maximum value at $\xi = 3$, then the pressure at $\xi > 3$ decreases. This means that the loading layer L is heavily contaminated and is rapidly beginning to deteriorate. The onset of destruction time is:

$$t = \sup_{\boldsymbol{x}\in L}\left(3 - x - y - z\right).$$

2.3. In the second example, we obtain this solution at $f(\phi) = a\ln\phi$ (a is arbitrary real number). At $\alpha = 1,\ \beta = 1,\ \gamma = 1,\ \lambda = 2,$ $t_0 = 1,\ x_0 = 1,\ y_0 = 1,\ z_0 = 1,\ p_0 = 1,\ p_1 = 0,$ $a = 1,\ b = 1$ we solved numerically the Cauchy problem (9), (10) by the Runge-Kutta-Fehlberg method [17] (with order of accuracy 4). The graph of the function $\phi = \phi(\xi)$ is shown in the Fig.6.

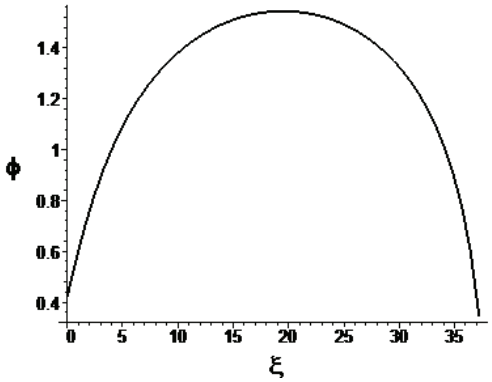

Figure 6. Pressure distributions for the model 2.2.

From this graph, it follows that the pressure increases at $\xi \in \left(0;\ 29\right]$ and reaches its maximum value at $\xi = 29$, then the pressure at $\xi > 29$ decreases. This means that the loading layer L is heavily contaminated and is rapidly beginning to deteriorate. The onset of destruction time is:

$$t = \sup_{\boldsymbol{x}\in L}\left(29 - x - y - z\right).$$

3. Third particular models

At $\Phi(\phi) = \lambda\ln\phi$ where λ is arbitrary real nonzero number, , equation (3) takes a form

$$\frac{\lambda}{\phi^2}\left(\alpha^2+\beta^2+\gamma^2\right)\left(\phi\frac{d^2\phi}{d\xi^2} - \left(\frac{d\phi}{d\xi}\right)^2\right) - \frac{d\phi}{d\xi} + f(\phi) = 0. \tag{11}$$

This equation defined model depending on α, β, γ, λ and $f(\phi)$.

Equation (11) is equivalent to the following system

$$\frac{d\phi}{d\xi} = \phi\psi,$$
$$\frac{d\psi}{d\xi} = \frac{\phi\psi - f(\phi)}{\lambda\left(\alpha^2+\beta^2+\gamma^2\right)}, \qquad (12)$$

where $\psi = \psi(\xi)$ is new unknown function.

We use the function $\phi(\xi)$ satisfying this system and conditions (6).

The initial data for system (12) has a form

$$\phi(\xi_0) = p_0,\ \psi(\xi_0) = \frac{p_1}{p_0},\ . \qquad (13)$$
$$\xi_0 = t_0 + \alpha x_0 + \beta y_0 + \gamma z_0.$$

Due to the smoothness of the right-hand sides of system (12), the solution of the Cauchy problem (12), (13) exists and is unique in the .neighborhood of the point ξ_0.

3.1. In the first example, we obtain this solution at $f(\phi) = a\phi^b$ (a, b are arbitrary real numbers). At $\alpha = 1,\ \beta = 1,\ \gamma = 1,\ \lambda = 5,\ \mu = 1,\ t_0 = 1,\ x_0 = 1,\ y_0 = 1,\ z_0 = 1,\ p_0 = 1,\ p_1 = -1,\ a = 1,\ b = -1$ we solved numerically the Cauchy problem (12), (13) by the Runge-Kutta-Fehlberg method [17] (with order of accuracy 4). The graph of the function $\phi = \phi(\xi)$ is shown in the Fig. 7.

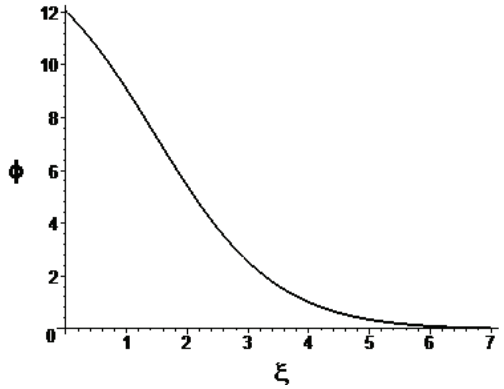

Figure 7. Pressure distributions for the model 3.1.

From this graph, it follows that the pressure corresponding to maximum expansion of the loading layer L is reached at $\xi = \xi_*\ \left(0 < \xi_* < 6\right)$. This solution has a physical meaning at $\xi \in \left(0;\ \xi_*\right]$. The time to reach maximum expansion of the loading layer is determined by the formula

$$t_* = \sup_{\boldsymbol{x}\in L}\left(\xi_* - x - y - z\right).$$

3.2. In the second example, we obtain this solution at $f(\phi) = a\exp(b\phi)$ (a, b are arbitrary real numbers). At $\alpha = 1,\ \beta = 1,\ \gamma = 1,\ \lambda = 5,\ \mu = 1,\ t_0 = 1,\ x_0 = 1,\ y_0 = 1,\ z_0 = 1,\ p_0 = 1,\ p_1 = 0.1,\ a = 1,\ b = -1$ we solved numerically the Cauchy problem (12), (13) by the Runge-Kutta-Fehlberg method [17] (with order of accuracy 4). The graph of the function $\phi = \phi(\xi)$ is shown in the Fig.8.

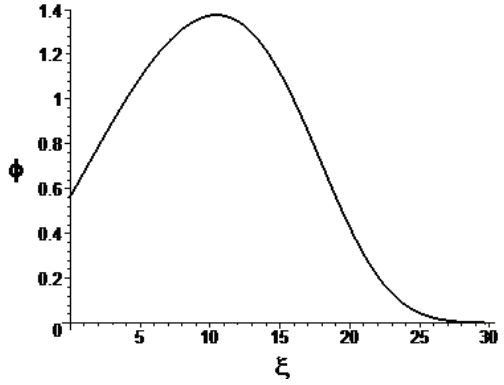

Figure 8. Pressure distributions for the model 3.2.

From this graph, it follows that the pressure increases at $\xi \in \left(0;\ 11\right]$ and reaches its maximum value at $\xi = 11$, then the pressure at $\xi > 11$ decreases. This means that the loading layer L is heavily contaminated and is rapidly beginning to deteriorate. The onset of destruction time is:

$$t = \sup_{\boldsymbol{x}\in L}\left(29 - x - y - z\right).$$

3.3. In the second example, we obtain this solution at $f(\phi)=a\ln\phi$ (a is arbitrary real number). At $\alpha=1,\ \beta=1,\ \gamma=1,\ \lambda=6,\ \mu=1,\ t_0=1,\ x_0=1,\ y_0=1,\ z_0=1,\ p_0=1,\ p_1=-0{,}1,\ a=1,\ b=-1$ we solved numerically the Cauchy problem (12), (13) by the Runge-Kutta-Fehlberg method [17] (with order of accuracy 4). The graph of the function $\phi=\phi(\xi)$ is shown in the Fig. 9.

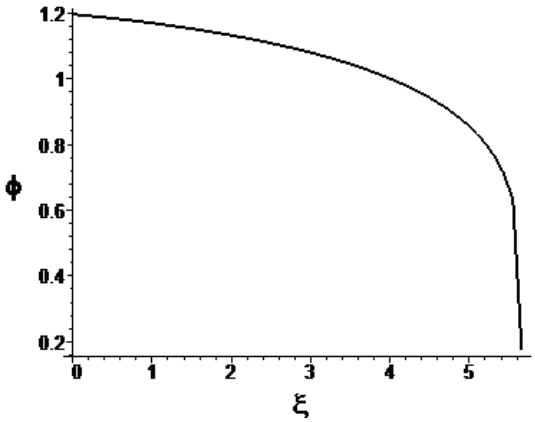

Figure 9. Pressure distributions for the model 2.2.

From this graph, it follows that From this graph, it follows that the pressure corresponding to experimentally determined maximum expansion of the loading layer L is reached at $\xi=\xi_*\ \left(0<\xi_*<5{,}5\right)$. This solution has a physical meaning at $\xi\in\left(0;\ \xi_*\right]$. The time to reach maximum expansion of the loading layer is determined by the formula

$$t_*=\sup_{\boldsymbol{x}\in L}\left(\xi_*-x-y-z\right).$$

ACKNOWLEDGEMENTS

The research was carried out with the financial support of the Industry Consortium "Construction and Architecture".

CONCLUSION

In this paper, we investigate the influence of externally applied traveling waves on the filtering of aqueous solutions in an expanded loading layer. To describe this process, we used a three-dimensional nonlinear dynamic generalized mathematical model of fluid motion in a porous medium with a nonlinear external influence. A general model describing traveling waves, defined by equation (3), was obtained.

Specific cases of this model with three types of filtering process nonlinearity werestudied: power, exponential, and logarithmic. These nonlinear models are defined by equations (4), (8), and (11), respectively. For each of these models, three special cases were examined, for which the external influence was chosen as power, exponential, and logarithmic. The resulting nine models depend on seven arbitrary constants, which are determined empirically depending on the filtering process.

For each of these nine models, we investigated the problem of determining the pressure of an aqueous solution in a loading layer assuming that the pressure and its rate of change at a fixed point in the bed are known at the initial time. For specific values of the constants on which these models depend, this problem was solved numerically. The results are shown in Figures 1, 2, 3, 4, 5, 6, 7, 8, and 9. These solutions describe both the expansion and fouling of the bed, depending on the type of nonlinearity in the filtering process, the type of external influence, and the parameters of the traveling wave. For filtering with an expanding loading layer, we found the time at which maximum expansion is achieved. For fouled loading layers, we found the time it takes for the loading layer to collapse.

The presence of seven arbitrary constants on which the nine models studied depend allows these models to beused to solve other physically significant problems.

REFERENCES

1. **L.S. Leibenzon.** Collection of works: V. 2. Underground Hydro and Gas Dynamics. Moscow: Publishing house of the Academy of Sciences of the USSR. (1953). (in Russian).
2. **L.S. Leibenzon.** Collection of works: V. 3. Oil field mechanics. Moscow: Publishing house of the Academy of Sciences of the USSR. (1955). (in Russian).
3. **G.I. Barenblatt.** On some unsteady motions of a liquid or a gas in a porous medium. Prikl. Mat. Mekh. 16 (1). (1952), 67–78. (In Russian).
4. **Otto F.** "The geometry of dissipative evolution equations: The porous medium equation," Commun. Partial Differ. Equations. 26 (1-2). (2001). 101–174.
5. **J.L. Vrazquez.** The Porous Medium Equation. Mathematical Theory, vol. Oxford Mathematical Monographs. Oxford University Press. Oxford. (2007).
6. **C. Kienzler, H. Koch, and J.L. Vrazquez.** Flatness implies smoothness for solutions of the porous medium equation. preprint arXiv:1609.09048.vl
7. **P.S. Casas and R. Quintanilla.** Exponential decay in one-dimensional porous-thermo-elasticity," Mech. Res. Commun. 32. (2005). 652–658.
8. **Yu.A. Chirkunov, Yu.L. Skolubovich.** Nonlinear three-dimensional diffusion models of porous medium in the presence of non-stationary source or absorption and some exact solutions. Int. J. Non-Linear Mech. 106. (2018). 29–37.
9. **Yu.A. Chirkunov.** Self-similar waves in a three-dimensional porous medium in the presence of non-stationary singular source or absorption. Int. J. Non-Linear Mech. 117. (2019). 103205.
10. **Yu.A. Chirkunov, M.Yu. Chirkunov.** Submodels of 2-d model of the motion of fluid or gas in a porous medium with an external non-stationary source or absorption. Int. J. Non-Linear Mech. V. 163 (2024). 104759.
11. **Yuri A. Chirkunov, Yuri L. Skolubovich, Mihail Yu. Chirkunov, Sergey V. Fedosov, Vladimir N. Sidorov, Evgeniy V. Alekseev.** Axisymmetric fluid motion in a porous medium in the presence of a non-stationary external source or absorption. Int. J. for Comp. Civil Struct. Eng.). 21(3) (2025). 148–157.
12. **L.V. Ovsyannikov.** Group Analysis of Differential Equations. New York: Academic Press). (1982).
13. **P.J. Olver.** Application of Lie groups to differential equations. Springer-Verlag. New York. (1986).
14. **Yu.A. Chirkunov.** Group analysis of linear and quasilinear differential equations. Novosibirsk: NSUEM. (2007). (in Russian).
15. **Yu.A. Chirkunov, S.V. Khabirov.** The Elements of Symmetry Analysis of Differential Equations of Continuous Mechanics. Novosibirsk. NSTU. (2012). (in Russian).
16. **Yu.A. Chirkunov.** Generalized Equivalence Transformations and group classification of systems of differential equations. J. Appl. Mech. Techn. Phys. 53 (2). (2012). 147–155.
17. **Butcher John C.** Numerical Methods for Ordinary Differential Equations. 3rd Edition. John Wiley & Sons. New York.

СПИСОК ЛИТЕРАТУРЫ

1. **L.S. Leibenzon.** Collection of works: V. 2. Underground Hydro and Gas Dynamics. Moscow: Publishing house of the Academy of Sciences of the USSR. (1953). (in Russian).
2. **L.S. Leibenzon.** Collection of works: V. 3. Oil field mechanics. Moscow: Publishing house of the Academy of Sciences of the USSR. (1955). (in Russian).
3. **G.I. Barenblatt.** On some unsteady motions of a liquid or a gas in a porous medium. Prikl. Mat. Mekh. 16 (1). (1952), 67–78. (In Russian).
4. **Otto F.** "The geometry of dissipative evolution equations: The porous medium

equation," Commun. Partial Differ. Equations. 26 (1-2). (2001). 101–174.
5. **J.L. Vrazquez.** The Porous Medium Equation. Mathematical Theory, vol. Oxford Mathematical Monographs. Oxford University Press. Oxford. (2007).
6. **C. Kienzler, H. Koch, and J.L. Vrazquez.** Flatness implies smoothness for solutions of the porous medium equation. preprint arXiv:1609.09048.vl
7. **P.S. Casas and R. Quintanilla.** Exponential decay in one-dimensional porous-thermo-elasticity," Mech. Res. Commun. 32. (2005). 652–658.
8. **Yu.A. Chirkunov, Yu.L. Skolubovich.** Nonlinear three-dimensional diffusion models of porous medium in the presence of non-stationary source or absorption and some exact solutions. Int. J. Non-Linear Mech. 106. (2018). 29–37.
9. **Yu.A. Chirkunov.** Self-similar waves in a three-dimensional porous medium in the presence of non-stationary singular source or absorption. Int. J. Non-Linear Mech. 117. (2019). 103205.
10. **Yu.A. Chirkunov, M.Yu. Chirkunov.** Submodels of 2-d model of the motion of fluid or gas in a porous medium with an external non-stationary source or absorption. Int. J. Non-Linear Mech. V. 163 (2024). 104759.
11. **Yuri A. Chirkunov, Yuri L. Skolubovich, Mihail Yu. Chirkunov, Sergey V. Fedosov, Vladimir N. Sidorov, Evgeniy V. Alekseev.** Axisymmetric fluid motion in a porous medium in the presence of a non-stationary external source or absorption. Int. J. for Comp. Civil Struct. Eng.). 21(3) (2025). 148–157.
12. **L.V. Ovsyannikov.** Group Analysis of Differential Equations. New York: Academic Press). (1982).
13. **P.J. Olver.** Application of Lie groups to differential equations. Springer-Verlag. New York. (1986).
14. **Yu.A. Chirkunov.** Group analysis of linear and quasilinear differential equations. Novosibirsk: NSUEM. (2007). (in Russian).
15. **Yu.A. Chirkunov, S.V. Khabirov.** The Elements of Symmetry Analysis of Differential Equations of Continuous Mechanics. Novosibirsk. NSTU. (2012). (in Russian).
16. **Yu.A. Chirkunov.** Generalized Equivalence Transformations and group classification of systems of differential equations. J. Appl. Mech. Techn. Phys. 53 (2). (2012). 147–155.
17. **Butcher John C.** Numerical Methods for Ordinary Differential Equations. 3rd Edition. John Wiley & Sons. New York.

Chirkunov Yuri Aleksandrovich – Doctor of Physical and Mathematical Sciences, Associate Professor, Head of the Department of Higher Mathematics of the Federal State Budgetary Educational Institution of Higher Education " Novosibirsk State University of Architecture and Civil Engineering (Sibstrin)" (FGBOU "NGASU (Sibstrin)", office 305, building 113, Leningradskaya Street, Novosibirsk, 630008, Russia; e-mail: chr101@mail.ru

Чиркунов Юрий Александрович – доктор физико-математических наук, доцент, заведующий кафедрой высшей математики Федерального государственного бюджетного образовательного учреждения высшего образования «Новосибирский государственный архитектурно-строительный университет (Сибстрин)» (ФГБОУ «НГАСУ (Сибстрин)», офис 305, дом 113, улица Ленинградская, город Новосибирск, 630008, Россия; e-mail: chr101@mail.ru

Skolubovich Yuri Leonidovich – Doctor of Technical Sciences, Professor, Corresponding Member of the Russian Academy of Architecture and Civil Engineering, Rector of the Federal State Budgetary Educational Institution of Higher Education "Novosibirsk State University of Architecture and Civil Engineering (Sibstrin)" (FGBOU "NGASU (Sibstrin)", office 239, building 113, Leningradskaya Street, Novosibirsk, 630008, Russia; e-mail: rector@sibstrin.ru

Сколубович Юрий Леонидович – доктор технических наук, профессор, член-корреспондент РААСН, ректор Федерального государственного бюджетного образовательного учреждения высшего образования «Новосибирский государственный архитектурно-строительный университет (Сибстрин)» (ФГБОУ «НГАСУ (Сибстрин)», офис 239, дом 113, улица Ленинградская, город Новосибирск, 630008, Россия; e-mail: rector@sibstrin.ru

Sidorov Vladimir Nikolaevich - Doctor of Technical Sciences, Professor, Academician of the Russian Academy of Architecture and Construction Sciences, Head of the Department of Informatics and Applied Mathematics of the Federal State Budgetary Educational Institution of Higher Education "National Research Moscow State University of Civil Engineering" (NRU MGSU), office 414 kmk, building 26, Yaroslavskoe shosse, Moscow, 129337, Russia; e-mail: SidorovVN@mgsu.ru

Evgeny Valerievich Alekseev - Doctor of Technical Sciences, Professor, Professor of the Department of Water Supply and Sanitation of the Federal State Budgetary Educational Institution of Higher Education "National Research Moscow State University of Civil Engineering" (NRU MGSU), office 314, building 26, Yaroslavskoe shosse, Moscow, 129337, Russia; e-mail: AlekseevE@mgsu.ru

Сидоров Владимир Николаевич - доктор технических наук, профессор, академик РААСН, заведующий кафедрой информатики и прикладной математики Федерального государственного бюджетного образовательного учреждения высшего образования «Национальный исследовательский Московский государственный строительный университет» (НИУ МГСУ), Москва, 129337, Россия; офис 414 кмк, дом 26, Ярославское шоссе, город e-mail: SidorovVN@mgsu.ru

Алексеев Евгений Валерьевич - доктор технических наук, профессор, профессор кафедры водоснабжения и водоотведения Федерального государственного бюджетного образовательного учреждения высшего образования «Национальный исследовательский Московский государственный строительный университет» (НИУ МГСУ), офис 314, дом 26, Ярославское шоссе, город Москва, 129337, Россия; e-mail: AlekseevE@mgsu.ru

DOI:10.22337/2587-9618-2026-22-2-51-72

LES SENSITIVITY TO DOMAIN SIZE AND GRID RESOLUTION IN IDEALIZED URBAN STREET CANYON

Norharyati Saleh [1], Mohd Hisbany Mohd Hashim [1], Mohd Faizal Mohamad [2], Roslin Ramli [3], Herlien D. Setio [4]

[1] Faculty of Civil Engineering, Universiti Teknologi MARA Shah Alam, MALAYSIA
[2] Faculty of Mechanical Engineering, Universiti Teknologi MARA Shah Alam, MALAYSIA
[3] Maritime Engineering Technology, Malaysian Institute of Marine Engineering Technology, Universiti Kuala Lumpur, Lumut, Perak, MALAYSIA
[4] Falcuty of Civil and Environmental Engineering, Institut Teknologi Bandung, Bandung, Jawa Barat, INDONESIA

Abstract: A series of large-eddy simulations (LES) was performed to investigate the effects of computational domain size and grid resolution on flow prediction within an idealized urban street canyon. Three streamwise domain lengths were examined in combination with coarse, medium, and fine grid resolutions. The building height, H, was kept constant, and the canyon aspect ratio (street width to building height) was set to unity. Flow statistics were evaluated at the central canyon of each configuration and compared with available wind-tunnel data.The LES results indicate that the simulated mean velocity profiles agree well with experimental measurements for all cases. Both domain size and grid resolution exhibited minimal influence on the mean velocity components, suggesting that mean flow within a street canyon can be reliably predicted using a relatively small computational domain when combined with medium or fine grid resolutions. This offers a computationally efficient option for mean flow analysis. In contrast, turbulence statistics were found to be more sensitive to grid resolution than to domain size. Fine grid resolution significantly improved the prediction of velocity fluctuations and momentum transport, whereas smaller domains tended to produce less consistent turbulence results. Consequently, while small or medium domains may be suitable for mean flow assessment, they are not recommended for detailed turbulence analysis.Overall, this study highlights the importance of balancing domain size and grid resolution to obtain reliable LES results while minimizing computational cost, providing practical guidance for CFD–LES studies of urban street canyon flows.

Keywords: Computational Fluid Dynamic (CFD), Street Canyon, Turbulence flow, Large-eddy simulation (LES), Wind-tunnel, Computational parameters

ЧУВСТВИТЕЛЬНОСТЬ МЕТОДА КРУПНЫХ ВИХРЕЙ К РАЗМЕРУ РАСЧЁТНОЙ ОБЛАСТИ И РАЗРЕШЕНИЮ СЕТКИ В ИДЕАЛИЗИРОВАННОМ ГОРОДСКОМ УЛИЧНОМ КАНЬОНЕ

Норхьяти Салех [1], Мохд Хисбани Мохд Хашим [1], Мохд Файзал Мохамад [2], Рослин Рамли [3], Херлиен Д. Сетио [4]

[1] Факультет гражданского строительства, Технологический университет МАРА, г. Шах-Алам, МАЛАЙЗИЯ
[2] Факультет механической инженерии, Технологический университет МАРА, г. Шах-Алам, МАЛАЙЗИЯ
[3] Малазийский институт морских инженерных технологий, Университет Куала-Лумпур, г. Лумут, Перак, МАЛАЙЗИЯ
[4] Факультет гражданского и экологического строительства, Технологический институт Бандунга, г. Бандунг, Западная Ява, ИНДОНЕЗИЯ

Аннотация: Была выполнена серия расчетов с использованием метода моделирования крупных вихрей (LES) для исследования влияния размера расчетной области и разрешения сетки на прогнозирование течения в идеализированном городском уличном каньоне. Были рассмотрены три продольных размера области в сочетании с грубым, средним и мелким размером сетки. Высота зданий H сохранялась

постоянной, а коэффициент формы каньона (отношение ширины улицы к высоте зданий) был принят равным единице. Статистические характеристики потока оценивались в центральном каньоне каждой конфигурации и сравнивались с доступными данными продувки в аэродинамической трубе. Результаты моделирования с помощью LES показывают, что рассчитанные профили средней скорости хорошо согласуются с экспериментальными измерениями для всех случаев. Как размер области, так и разрешение сетки оказали минимальное влияние на компоненты средней скорости, что позволяет предположить, что среднее течение внутри уличного каньона может быть надежно предсказано с использованием относительно небольшой расчетной области в сочетании со средним или мелким разрешением сетки. Это дает вычислительно эффективный вариант для анализа среднего течения. С другой стороны, было обнаружено, что турбулентные характеристики более чувствительны к разрешению сетки, чем к размеру области. Мелкое разрешение сетки значительно улучшает прогнозирование пульсаций скорости и переноса импульса, тогда как меньшие области, как правило, дают менее согласованные результаты по турбулентности. Следовательно, хотя малые или средние области могут быть пригодны для оценки среднего течения, они не рекомендуются для детального анализа турбулентности. В целом, данное исследование подчеркивает важность балансировки размера области и разрешения сетки для получения надежных результатов при использовании LES с учетом минимизации вычислительных затрат, предоставляя практические рекомендации для исследований CFD-LES течений в городских уличных каньонах.

Ключевые слова: вычислительная гидродинамика (CFD), уличный каньон, турбулентное течение, моделирование крупных вихрей (LES), аэродинамическая труба, расчетные параметры

INTRODUCTION

Urban areas are major contributors to air pollution due to dense human activities [1]. At the same time, the urban mobility landscape is undergoing rapid transformation as cities confront increasingly complex challenges related to transportation, sustainability, and urban development [2]. A substantial portion of this pollution originates from vehicular emissions trapped within street canyons, one of the most characteristic micro-environments of contemporary cities [3]. A street canyon is formed by rows of adjacent buildings flanking both sides of a roadway, creating a confined geometric unit within the urban canopy layer [4]. The airflow within these canyons is strongly influenced by wind-driven circulation patterns, which are governed by microscale meteorological processes. Understanding these flow behaviours is essential, as they directly affect pollutant dispersion, thermal comfort, and overall urban environmental quality as well as better energy-efficient construction implementation. [5-7].

The poor understanding of the unsteady and intermittent wind field inside the canyon has been considered as one of the major obstacles that cause the build engineer not sufficiently able to minimize and avoid the creation of an inhospitable environment within the urban area. Thus, the extensive investigation and particular guideline for the analysis of atmospheric processes in the street canyons should be continued as an active and growth research within this century [8].

The majority of the previous studies focus on a street with perpendicular background wind conditions, as this is the worst case situation for ventilation and pollutant removal [9-13]. On regards to street canyon geometries, Oke [9] reported the occurrence of three distinct flow regimes inside a street canyon at various aspect ratio threshold, namely isolated roughness flow, wake interference flow and skimming flow. The skimming flow was shown to be the most adverse effect for the ventilation and pollution removal while comparing with the three flow regimes profile. The normal velocity in the street canyon is often a significant degree lower than the free-stream velocity in the atmosphere in this flow regime. Thus, a wind vortex forms inside a street canyon when the mean wind direction is perpendicular to the street [10].

Furthermore, the pollutant concentrations are higher on the leeward side rather than the windward side due to flushes effect by the vortex flow pattern. Meanwhile, according to Meroney et al., [11], a constant rotating vortex has been generated within the urban canyon under perpendicular wind direction, limiting the ventilation process and trapping pollution inside the canyon. Vardoulakis et al. [12] further claimed that when the wind speed is greater than 1.5 to 2 m/s and the flow is perpendicular to the canyon, the free-stream velocity over the canyon in typical canyons results in the skimming flow, which is identifiable by the formation of a single vortex within the canyon. According to research conducted by Li et al. [13], the perpendicular inflow wind direction to the street had the worst effects on pollution transport in street canyons due to the formation of a recirculating vortex within an even street canyon and a significant shear layer at the roof level.

The fluid stream pattern inside the street canyons has govern the mechanism of passive and inert pollutant. Previous literature have looked on the characteristics of stream flow and mechanism pollutant dispersion in urban street canyons using field measurements, laboratory experiments, and CFD [13-18]. On-site measurement is a useful research method for demonstrating the real-world microclimate of a street canyon, such as the reduced wind speed and enhanced pollution levels. However, a number of factors influence this approach, including the continuously changing meteorological conditions [15]. Wind tunnels, on the other hand, have been widely employed in both industry and research for many years. Wind tunnels have been used to verify aerodynamic theories and facilitate the design of aircraft, as well as to build new aircraft, wind turbines, and other designs that included dynamic interaction with an airflow [16].

The field measurement and wind tunnel measurement have a distinct drawback since most of the data sampled only a one-point measurement [17]. In addition, due to the time and cost issues associated with in-field measurement and wind tunnel testing, CFD has become the primary tool used to explore and predict flow fields. CFD can provide a comprehensive data of the flow structure and pollutant distributions in temporal and spatial scale, whereas other methods are still lack of this criteria [18-19]. The three type of CFD methods that have been adopted and successfully used in urban street canyon environment are include Direct Numerical Model (DNS), Large Eddy Simulation (LES), and Reynolds-Averaged Navier-Stokes (NS) equations (RANS) modelling.

By resolving the full field of spatial and temporal scales of turbulence, the DNS technique directly simulates, computes, and solves the Navier-Stokes equation. This signifies that no turbulence model was used. As a result, DNS providing a high-fidelity resolution for fluid flow simulation and has frequently regarded as a numerical experiment. However, in term of computing resources, the DNS method acquires highly cost as compare to RANS and LES and thus not really used for industrial flow computations [20]. As a consequence, the most comprehensive applications of CFD is seen to be the RANS equations and the LES.

The RANS method, in general, is based on mean flow properties where the time-averaging of the Navier-Stokes equations has been applied. Due to its minimal computational resource requirements and reasonably computed accurate flow field, this method has been widely employed in engineering flow computations throughout the previous few decades [21]. Several previous studies used RANS for various flow conditions in street canyon have been reported; Mishra et al. [22] looked on the influence of street canyon configurations on the pollutant dispersion and ventilation performance with various aspect ratios and different street length. Lien [23] has been studied of the disrupted flow for buildings immersed in a neutrally stratified deep rough walled turbulent boundary-layer flow, Cheng et al. [24] focused

on how street canyon geometry could affect the ventilation and pollutant removal process, Ai et al. [25] investigates the buildings located in long street canyon under a wind-caused single-sided natural ventilation and Cui et al. [26] looked on the impact of three type of envelope features on wind flow and pollution exposure to occupants within street canyon. However, the conventional *k*-model has an obvious flaw in terms of model correctness, despite the fact that most RANS models serve the most economical cost in terms of computational resources. One of the significant flaws in the model assessments is the concept of a steady-state solution that could be the major source of the inconsistencies.

Meanwhile, LES used the separated filtered in the transport equations where it permitted only bigger eddies to be resolved, in the meantime the smallest eddies are being modelled. [27]. The use of LES to accommodate the inadequacies of RANS has recently gained popularity. Due to its consistency and precision, the LES approach has been more superior than the RANS method [28].

A list of LES-based studies on flow structures and pollution related issues in street canyons that has been published; Alwi et al. [29] conducted the LES model to investigated the effect of various eave design on the modification of flow structure and turbulent characteristic for 2D semi-open street canyons. Meanwhile, Liu et al. [30] used model of street canyon for various aspect ratio to simulate the performance of air and pollutant exchange rate, Li et al. [31] further explored the pollutant dispersion process for deep canyons geometries, Mohamad et al. [32] looked on the mechanism of average and fluctuation for air flow for building with overhang and Munixta et al. [33] performed the evaluation of mean and turbulence structure flow under building geometry effect such as roof and façade aspect.

Base on literatures, it is noticed that CFD is one of the most widely used tools for studying such flow problems in an urban environment due to its ability to provides detailed information on the relevant flow variables under controlled conditions [34]. However, the accuracy and reliability of the data have found to have some skepticism issue involve while applying numerical modelling to problems associated with wind engineering [35-37]. Due of their limitations and errors, CFD models still require further improvement [37].

The fundamental objection to this issue, according to Franke et al. [38], is the approach's availability of various physical and numerical factors that can be freely chosen by the user. The physical modelling based on models of turbulence used and the type of boundary conditions are considering as one of sources of error in CFD results accuracy. Meanwhile, the second contribution is made by numerical simulation factors such as size of computational domain, design for grid resolution, and numerical iteration method. While CFD models have been widely used to examine atmospheric processes in street canyons, the need for adequate computational parameters is one of the most essential elements to determine predictive accuracy. The computational dimensions, as well as the grid design and quality, are some of the computational parameters that have a considerable impact on the predictability and accuracy of the flow field.

Liu and Barth [39] used an LES model to explore the flow and turbulence scalar transfer mechanism in a 3D-idealized street canyon. Before validating the results, a grid dependence analysis was performed to ensure grid solution accuracy. Cui et al. [40] investigated a turbulent structure flow within a three-dimensionally modelled street canyon. The comparison of grid resolution (fine and coarse only) and initial wind profile, as well as the variation of Smagorinsky constant for the LES model, was carried out for the purpose of accuracy and validation.

Cheng and Liu [41], on the other hand, used a two-dimensional idealized street canyon to evaluate the flow field and pollutant dispersion case using the LES model simulation. The study is motivated by the concept of the influence of computational domain size, which suggested

that increasing the domain size would result in higher resolution data. Meanwhile, Michioka et al. [42] investigated the impact of the computational domain size on the flow field within the street canyon. The LES simulation analysis was used to predict the effects of the coherent structure on pollutant removal in general. Meanwhile, Dai et al. [43] show application of LES to realistic building problems and discuss setup/validation best practices that translate to street-canyon studies.

The accuracy performance of the CFD models was found to be affected by parameter characteristics such as computational domain and grid resolution in previous research. However, to the author's knowledge, no specific and rigorous examination of the effect and correlation for both parameters on the accuracy of flow statistics has been done. By knowing the proper approach for the selection of those computational setting is certainly useful to optimize the time and cost consumption for CFD simulation particularly for the LES model for instance [44].

Therefore, the motivation for the overall current study is to use the LES model as a tool to validate and statistically analyses in detail the correlation of the two computational parameters; computational domain and grid resolution towards the accuracy of the flow field within the idealized urban street canyon environment.

The LES method was chosen primarily because of its capacity to provide deeper insights into the mean flow and statistics of the resolved fluctuation, which were obviously appropriate for the study's goals. Finding should be expected to enrich the fundamental understanding and also increase the confidence in the used of CFD simulations.

METHODS

2.1 Governing Equations

By applying a filter operation, the flow equations that consists of the continuity (1), momentum and mass conservation equations (2) as follow is assumed to be isothermal and incompressible,

$$\frac{\partial \bar{u}_i}{\partial x_i}=0 \tag{1}$$

$$\frac{\partial \bar{u}_i}{\partial_t}+\frac{\partial \bar{u}_j\bar{u}_i}{\partial x_j}=-\frac{\partial \bar{P}}{\partial \bar{x}_i}+\frac{\partial}{\partial x_j}\left(\mu\frac{\partial \bar{u}_i}{\partial x_j}\right)-\frac{\partial \tau_{ij}}{\partial_j} \tag{2}$$

where the filtered value is indicated by the overbar, u is the velocity vector and P is the pressure and υ is the fluid kinematic viscosity. For this study, the sub-grid scale (SGS) stress was modelled by the standard Smagorinsky model with Smagorinsky's constant Cs of 0.12 to reproduce the turbulent nature due to elements of roughness. The Reynolds number is defined as Re = uH/ν for this study (H= square block height) and all the terms are calculated and analyze by using an open-source software of OpenFOAM v2.3.1.

2.2 Simulation Domain

Three different computational domains are adopted in this study as shown in Fig. 1 (a and b). Each domain is characterised by the length in each direction in term of streamwise (*Lx*), spanwise (*Ly*) and vertical (*Lz*) directions. Case1 is defined as *2H x H x 6H* (one canyon: small), *6H x H x 6H* for Case2 (three canyons: medium) and *10H x H x 6H* for Case3 (five canyons: large) (see Table 1). Case1 with a grid size of *H/16* is used for validation with the wind tunnel experiment by Michioka [42] and Brown [45] as depicted in Fig. 1a.

To investigate the correlation of the domain size and grid resolution size, three runs are implemented (see Fig. 2, 3 and 4) for coarse (*H/8*), medium (*H/16*) and fine (*H/32*) resolution run where define as G8C, G16C and G32C, respectively. A uniform height (*H=0.12 m*) of square arrays are arranged at the bottom surface corresponds with the domain size. As the aspect ratio of all simulations is unity, the height of the domain was set to *6H* as proposed

by Franke [46] and the spanwise domain length was kept at *H,* since the effects of the spanwise direction was not concerned in this study, which adopted the two-dimensional analysis.

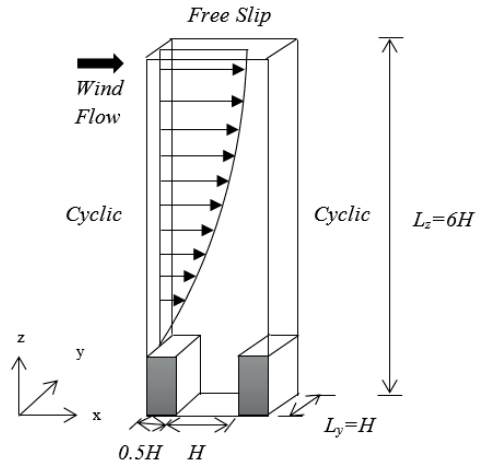

(a)

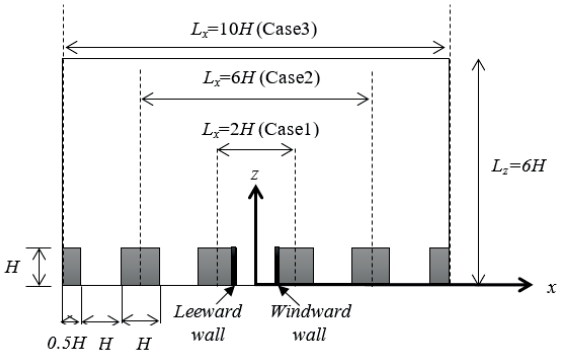

(b)

Figure 1. Schematic of the computational domain adopted in this study (a) Case 1 for validation purpose (b) Configurations of simulated urban street canyon for Case 1, Case 2 and Case 3

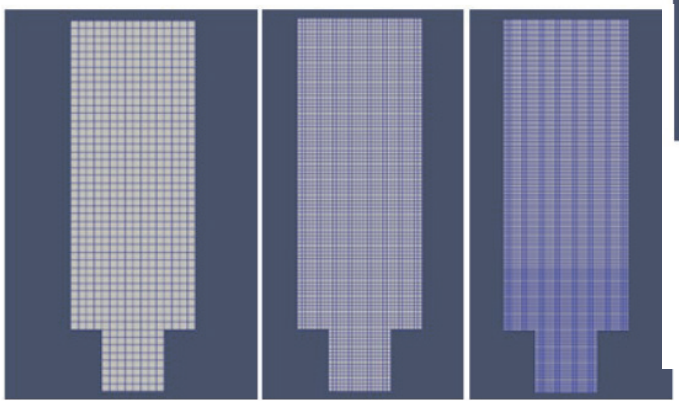

Figure 2. Diagrams of the Run Case 1 for Grid Size Resolution of H/8, H/16 and H/32

Table 1. Computational Domains and Total Grids

G8	Case 1	Case 2	Case 3
L_x/H	2	6	10
L_y/H	1	1	1
L_z/H	6	6	6
N_x	16	48	80
N_y	8	8	8
N_z	48	48	48
Number of cells	5632	45056	229376
G16			
L_x/H	2	6	10
L_y/H	1	1	1
L_z/H	6	6	6
N_x	32	96	160
N_y	16	16	16
N_z	96	96	96
Number of cells	16896	135168	688128
G32			
L_x/H	2	6	10
L_y/H	1	1	1
L_z/H	6	6	6
N_x	64	192	320
N_y	32	32	32
N_z	192	192	192
Number of cells	28160	225280	1146880

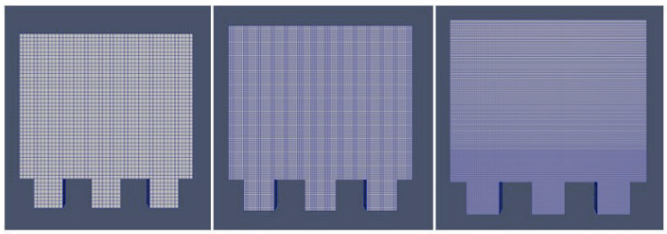

Figure 3. Diagrams of the Run Case 2 for Grid Size Resolution of H/8, H/16 and H/32

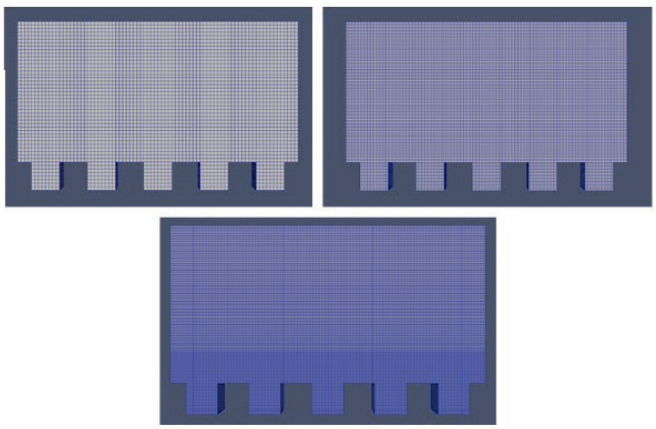

Figure 4. Diagrams of the Run Case 3 for Grid Size Resolution of H/8, H/16 and H/32

To simulate infinitely repeated street canyons cyclic boundary conditions are applied for both directions of streamwise and spanwise. The bottom surface and building surfaces are subjected to no-slip boundary conditions, while the velocity components at the top boundary are subjected to free-slip boundary conditions. This conditions allowed for the velocity normal to the boundary and the velocity gradient along the wall to be zero. The summary inflow boundary condition for the LES model is shown in Table 2.

Table 2.

LES Boundary Conditions

Boundary condition	Velocity (u)
Inlet	Cyclic
Outlet	Cyclic
Top	Slip
Bottom	Non-slip
Side Wall	Cyclic
Block	Non-slip

To keep the mean velocity over a cross-section at 2 m/s, an additional source term in the Navier-Stokes (NS) equations is used to drive the flow. The time step is set to 1.0×10^{-4} to ensure the mean Courant number is less than one. The sampling frequency of the data is 500Hz. For all cases of simulations for this study, the Reynolds number was in the range of 10000-12000, indicating that a fully developed turbulence flow was produced by using current LES model.

RESULTS AND DISCUSSION

3.1 Model Validation

As is well known, the validation process is required to determine the accuracy and dependability of the CFD simulation results. The degree to which a model accurately represents the real world from the perspective of the intended model uses can be defined through validation. One of the most effective approaches to get perfect practice with a CFD is to compare it to published or experimental data Oberkampf [47].

For this study, the dimensions of the building model and computational domain were chosen to compare the obtained results of this study with the experimental study results of Michioka [42] and Brown [45]. Michioka [42] performed the research in the Central Research Institute of Electric Power Industry's wind tunnel facility (CRIEPI) for two-dimensional street canyon model. The wind tunnel was built in a bigger test section (17.0 m x 3.0 m x 1.7 m) and consisted of a series of 25 evenly spaced bars. Meanwhile, Brown [45] carried out the experiment in the US Environmental Protection Agency's meteorological wind tunnel. An idealised street canyon with unity aspect ratio are made up of six identical canyons formed from seven identical square cross-section building components (0.15 m x 3.8 m x 0.15 m). The turbulent flow sample was taken at the sixth street canyon, which features fully developed wind profiles.

Fig.5 shows a vertical profile of the streamwise mean velocities of current LES at three vertical plane positions within a target street canyon together with the wind tunnel experiments. As mentioned before, the validation has been performed by using Case 1 (one street canyon). The current LES results agree well with the previous wind tunnel by Brown [45] and Michioka [42] particularly inside the canyon. At ($z/H<1$), the reversed flow is successfully reproduced at all measured positions. However, approximately at ($z/H>1$), the profile of mean vertical velocity for current LES is quite steep compared to the profile of wind-tunnel experiment by Michioka [42] and more obvious in Brown [45]. The difference may have resulted from the coarse roof-level mesh resolution near the roof level where strong wind shear is present as well as due to limited domain size as suggested by Cui [40] The current LES does not have a refined mesh structure near the building level and thus attribute to the insufficient numbers of small eddies within the LES system.

On the other hand, the current LES adopts a limited domain size that allows only those eddies

whose sizes are smaller than half the canyon width (e.g. 0.12 m) to be developed where this is not the case in the wind tunnel experiments. The larger eddies whose sizes are larger than canyon width can be properly produced by the roughness elements and instability of flow in upstream locations resulted from the fact that those maximum eddies are confined by the dimension of the cross-section of the tunnel itself.

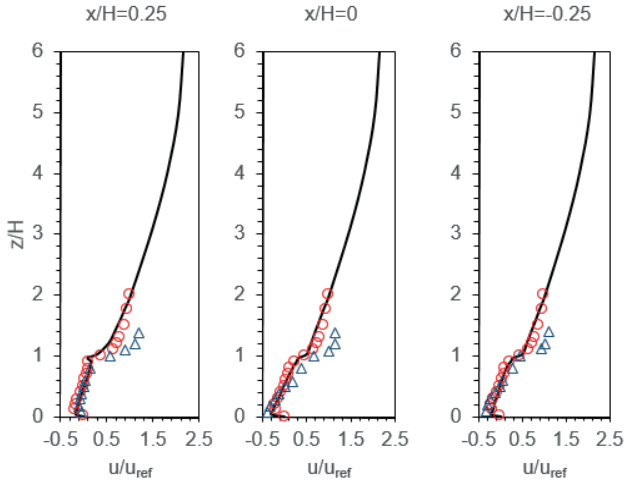

Figure 5. Vertical profiles of streamwise mean velocity at x/H=0.25, x/H=0 and x/H=-0.25 respectively. Current LES: solid line, Michioka et al., [42]: empty circle and Brown et al., [45]: empty triangular

Therefore, with the availability of these extra eddies, more intensive momentum transfer from the mean wind to inside the canyon could happen and thus developed a stronger primary vortex. Apart from the differences, considering the profiles of current LES become smoother across the building height as predicted in the wind-tunnel experiment, it is acceptable that the current LES reproduces the mean flow field inside and over the street canyon and the fully developed wind profiles have been sampled. It should be noted that the limited domain size has been selected for this study for economic reasons as well as due to limitations of computer resources.

3.2 Flow and Turbulent Statistic

This section analyzes the influence of two key computational parameters; domain size and grid resolution on the turbulent flow structure within the idealized street canyon. The subsequent discussion also examines the corresponding effects on momentum transport statistics. The LES results were obtained by decomposing instantaneous flow variables into mean and fluctuating components, as the mean values provide a more reliable representation of overall flow characteristics. Due to computational constraints, the analysis was conducted along the central plane of the domain, excluding variations in the spanwise (y) direction. Comparisons among cases were performed along five vertical lines within the canyon to assess velocity and turbulence distributions as shown in Fig. 6. To characterize the overall flow behavior, spatial and temporal averages of the flow field were evaluated in the x–z plane at the centerline ($y/H = 0$). Results are presented in statistical profiles for each grid resolution (C1G, C2G, C3G) and domain size (G8C, G16C, G32C).

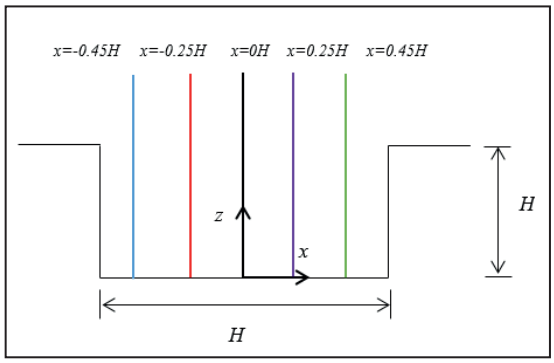

Figure 6. The Positions for Data Comparison where the Blue Line is x/H = −0.45, Red Line is x/H = -0.25, Black Line is x/H= 0, Purple Line is x/H = 0.25 and Green Line is x/H = 0.45

3.2.1 Mean Velocities Components

Fig. 8 and Fig. 9 presents the vertical distribution of the normalized streamwise velocity (u) and vertical velocity (w) at five positions within the target street canyon of unity aspect ratio. The first measurement point (x/H = –0.45) corresponds to the upstream wall on the leeward side, while the subsequent positions at x/H = –0.25, 0, 0.25, and 0.45 represent the

leeward quarter line, canyon centerline, windward quarter line, and windward wall, respectively. The vertical coordinate (z) was normalized by the building height (H), and the velocity statistics were normalized by the reference velocity ($u_{(}$ref$_{)}$) measured at z = 2H, where the flow field was relatively uniform and the wind speed remained nearly constant. The comparison includes all three computational domains—Case 1, Case 2, and Case 3—each simulated with coarse (G8C), medium (G16C), and fine (G32C) grid resolutions.

As shown in Fig. 8, all cases produced similar streamwise velocity (u) profiles. LES effectively captured the reversed flow region (z/H < 1.0), indicating the primary vortex, and the shear layer formation near the building height due to flow separation similar to previous studies by Cui et. al. [40], Michioka et. al. [42] and Liu & Wong [48]. Above the rooftop, the velocity gradients became smoother across all cases, reflecting frictional damping. Variations above the canyon (z/H > 2.5) were more pronounced for coarse grids, where the streamwise velocity gradient was noticeably steeper. At z/H = 5, the mean velocity differences between coarse and fine grids ranged from 8.5–10.3% (C1G), 2.9–11.2% (C2G), and 1.9–7.4% (C3G), confirming improved consistency with grid refinement.

Fig. 9 shows the vertical velocity (w) distribution, where all cases exhibited comparable trends within the canyon (z/H < 1.0). The upward flow transported aged air outward, while the downward motion recirculated cleaner air toward the canyon core. However, coarse-resolution runs slightly underestimated w values, reflecting limited resolution accuracy. At z/H = 0.5, variations between coarse and fine grids ranged from 50.7–60.1% (C1G), 65.5–70.3% (C2G), and 31.7–46.8% (C3G). Overall, finer and medium grids produced smoother and more stable profiles compared with the coarse grid.

These findings highlight that LES performance strongly depends on grid resolution. The coarse grid failed to resolve the full range of large eddies responsible for momentum and scalar transport, leading to deviations in the velocity fields. Since LES resolves large, energy-containing structures while modeling smaller eddies via subgrid-scale closure, adequate grid density is essential. Hence, finer meshes (H/16 and H/32) yielded better prediction accuracy and more realistic flow representation within the street canyon [49].

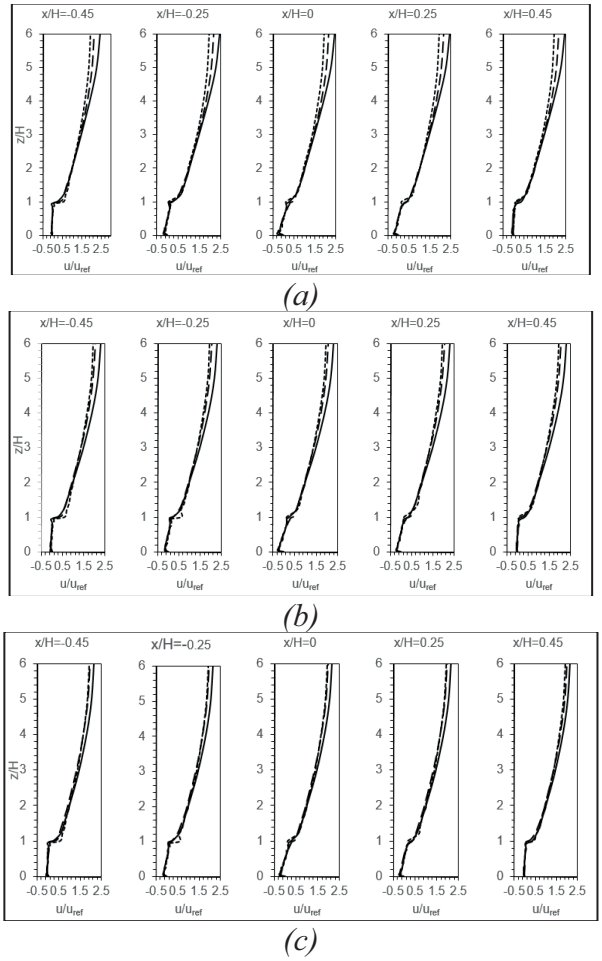

Figure 8. Vertical Profiles of the Mean Streamwise Velocity for All Cases of Domain Sizes; (a) Case1 (b) Case2 and (c) Case3 with Different Grid Resolution at x/H=-0.45, -0.25, 0, 0.25 and 0.45. The Square Dot Lines Refer to the: Grid 8 (Coarse), Dash Line: Grid 16 (Medium) and Solid Line: Grid 32 (Fine)

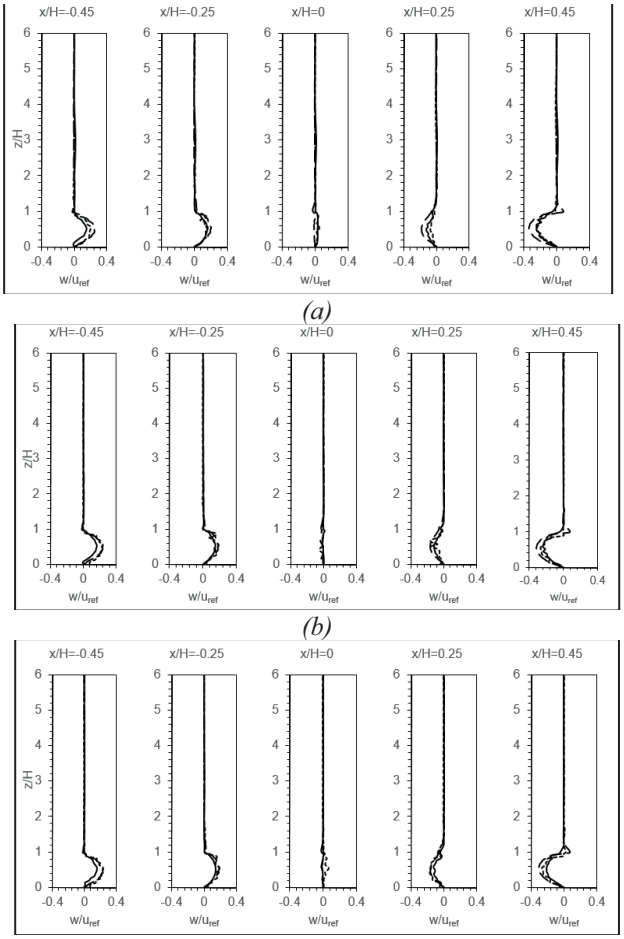

Figure 9. Vertical Profiles of the Mean Vertical Velocity for All Cases of Domain Sizes; (a) Case1 (b) Case2 and (c) Case3 with Different Grid Resolution at x/H=-0.45, -0.25, 0, 0.25 and 0.45. The Square Dot Lines Refer to the: Grid 8 (Coarse), Dash Line: Grid 16 (Medium) and Solid Line: Grid 32 (Fine)

3.2.2 Standard Deviation Components

Fig. 10 and Fig. 11 show the vertical distributions of the standard deviations of streamwise and vertical velocities ($\sigma_{(u)}$ and $\sigma_{(w)}$), highlighting the effect of grid resolution on LES performance within the 2D street canyon with various size domains. Within the canyon ($z/H \leq 1.0$), all runs produced comparable results, except for the coarse grid, which exhibited noticeable deviations in $\sigma_{(u)}$ (Fig. 10). The maximum $\sigma_{(u)}$ and $\sigma_{(w)}$ occurred near the rooftop, representing strong shear-induced turbulence, and were well captured in the medium and fine grid cases but underpredicted by the coarse grid.

Both $\sigma_{(u)}$ and $\sigma_{(w)}$ decreased toward the canyon floor due to the no-slip boundary condition, where viscous effects dampened velocity fluctuations and suppressed turbulence generation. Above the canyon ($z/H \geq 1.0$), stronger variability in $\sigma_{(u)}$ appeared, particularly in the small domain (C1G). At $z/H = 5$, $\sigma_{(u)}$ for the coarse grid (G8) was about 20% lower than for the medium (G16) and fine (G32) grids, while percentage differences for C2G and C3G ranged from 3.2–11.4% and 2.4–28%, respectively. A steeper $\sigma_{(u)}$ gradient was also observed for the fine grid in the large domain (C3G) above $z/H > 4$, indicating improved resolution of shear structures.

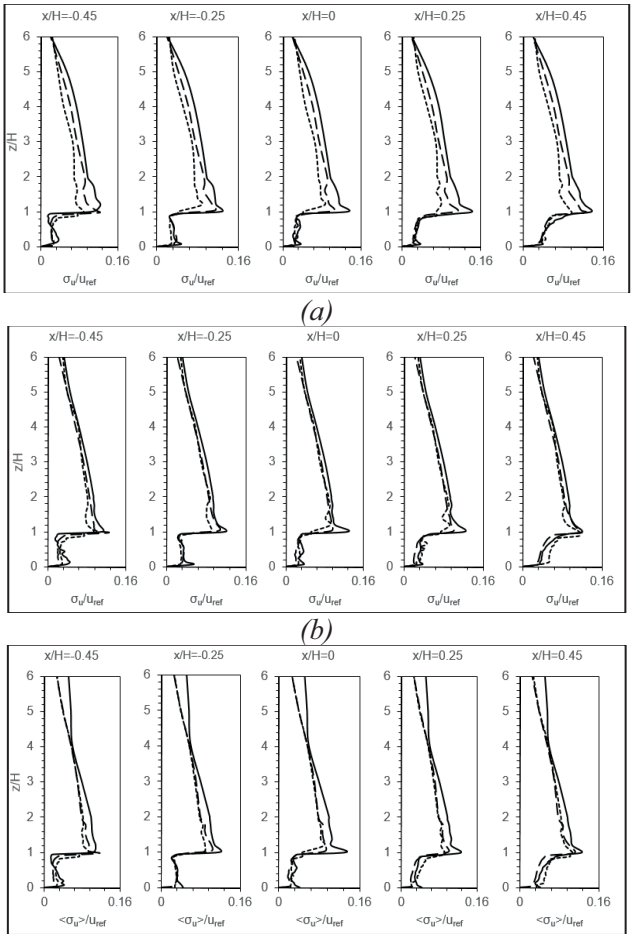

Figure 10. Vertical Profiles of the Streamwise Standard Deviation for All Cases of Domain Sizes; (a) Case1 (b) Case2 and (c) Case3 with Different Grid Resolution at x/H=-0.45, -0.25, 0, 0.25 and 0.45. The Square Dot Lines Refer to the: Grid 8 (Coarse), Dash Line: Grid 16 (Medium) and Solid Line: Grid 32 (Fine)

As shown in Fig. 11, $\sigma_{(w)}$ exhibited similar behavior with greater variation above the canyon. At z/H = 5, differences among grid resolutions were 20.5–42.8% for C1G, 14.2–25.5% for C2G, and 3.7–16.7% for C3G. Both $\sigma_{(u)}$ and $\sigma_{(w)}$ magnitudes increased from leeward to windward, reflecting intensified shear and recirculation near the windward wall. Overall, coarse grids dissipated small-scale turbulence and underestimated velocity fluctuations, whereas finer grids more accurately resolved the energy-containing eddies and provided higher fidelity in representing the canyon flow dynamics.

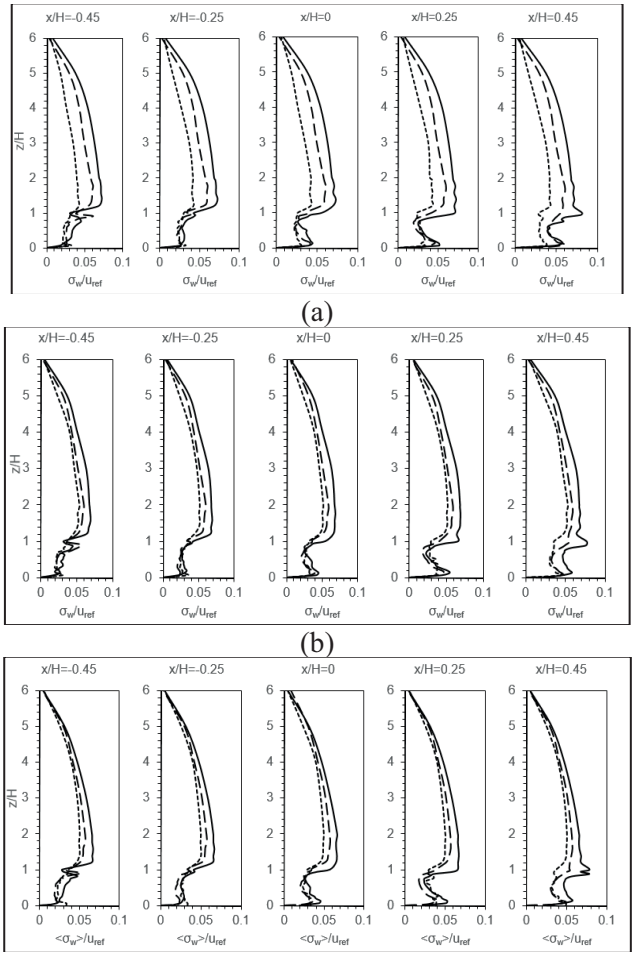

Figure 11. Vertical Profiles of the Vertical Standard Deviation for All Cases of Domain Sizes; (a) Case1 (b) Case2 and (c) Case3 with Different Grid Resolution at x/H=-0.45, -0.25, 0, 0.25 and 0.45. The Square Dot Lines Refer to the: Grid 8 (Coarse), Dash Line: Grid 16 (Medium) and Solid Line: Grid 32 (Fine)

3.2.3 Turbulence Kinetic Energy (TKE)

Similar to the mean velocity components, the turbulence kinetic energy (TKE) was normalized using the reference velocity ($u_{(ref)}$) measured at z = 2H, as shown in Fig. 12. The decomposition of instantaneous flow into mean and fluctuating components produced variance terms, whose square roots represent the velocity fluctuations. Half the sum of these variances corresponds to the mean kinetic energy per unit mass contained in the turbulent motions. TKE is a key parameter for evaluating LES performance, as it reflects the ability of the model to capture energy-containing eddies. To examine the effects of grid and domain size, TKE values were extracted at z/H = 1.0 (roof level) and z/H = 5.0 (above the canyon) for all simulation cases.

Fig.12 shows the vertical profiles of TKE inside and above the street canyon. A distinct TKE peak appeared near the rooftop (z/H = 1.0) for all simulations except the coarse-resolution case (G8), where only a mild peak was observed. Large discrepancies were evident among the coarse-grid runs (C1G, C2G, and C3G), confirming the resolution sensitivity of LES results. In general, TKE values above the canyon were substantially higher than those within the canyon, as the shear layer generated strong turbulence over the roof, while the weaker recirculating flow below produced relatively uniform and low TKE distribution [48].

To quantify the grid resolution effect, the TKE variation ratio between coarse and fine grids was computed. At z/H = 1.0, variations of 27–55.6%, 23.2–30.2%, and 25.5–32.0% were recorded for runs C1G, C2G, and C3G, respectively. Above the canyon, the coarse-grid profile exhibited a steeper gradient than the finer-resolution cases, indicating less stable turbulence representation. Despite general agreement below roof level, the differences near z/H = 1.0 highlight the critical influence of grid size on LES performance in urban canyon flows.

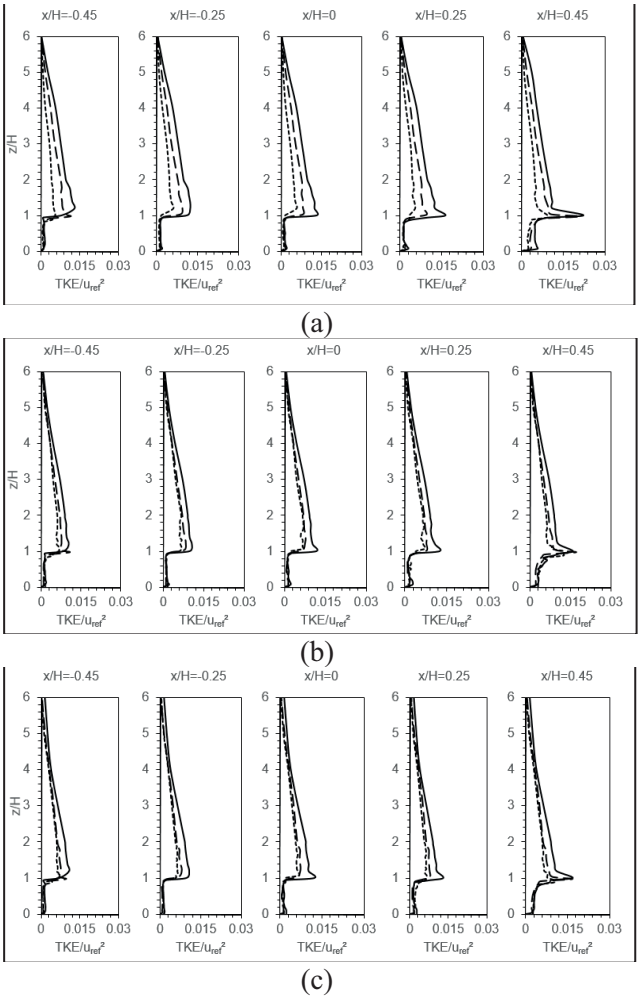

Figure 12. Vertical Profiles of TKE for All Cases of Domain Sizes; (a) Case 1 (b) Case 2 and (c) Case 3 with Different Grid Resolution at x/H=-0.45, -0.25, 0, 0.25 and 0.45. The Square Dot Lines Refer to the: Grid 8 (Coarse), Dash Line: Grid 16 (Medium) and Solid Line: Grid 32 (Fine)

The TKE peak near the windward wall corresponded to the shear layer formed by flow separation at the leeward building edge—recognized as the primary source of turbulence in isothermal canyon flows. High TKE values at the roof corners confirm this mechanically driven turbulence production. Conversely, smaller and more uniform TKE distributions near the leeward wall indicated low local velocity gradients. Among the simulations, C3G (fine resolution, large domain) produced the most consistent and realistic TKE distribution, while coarse-grid runs systematically underestimated TKE magnitudes. These discrepancies align with the observed underprediction of velocity (Fig. 8-9) and standard deviation components (Fig. 10–11), suggesting that coarse grids failed to fully capture the energy exchange between the high-momentum flow above the canyon and the low-momentum recirculating air below, as similarly reported by Cui et al. [40].

3.2.4 Reynold Shear Stress

Fig. 13 presents the Reynolds shear stress profiles obtained from the LES simulations for different grid resolutions (C1G, C2G, and C3G) at five locations within the target street canyon. An increase in Reynolds shear stress magnitude was observed above the canyon for all cases as grid resolution improved from coarse to fine. The coarse and medium grid runs generally underestimated the Reynolds shear stress and failed to capture a distinct peak near the building height. In contrast, the fine grid simulations produced well-defined profiles, showing clear maxima at the windward roof edge, consistent with the expected location of strong shear-layer formation.

The most pronounced increase in Reynolds shear stress with grid refinement occurred in the small-domain case (C1G), as shown in Fig. 13 (a). At z/H = 1.0, the coarse grid predicted values approximately 32.4–59.9% lower than the medium and fine resolutions. For C2G and C3G, the variation was less significant, with percentage differences of 25.4–36.8% and 27.3–32.6%, respectively. At higher elevations ($z/H \geq 4$), the shear stress profiles tended to converge across all cases, indicating improved agreement above the canyon except for the coarse grid in the small domain. Within the canyon, all simulations showed relatively small shear stress values compared to those above the rooftop, consistent with weaker turbulence intensity below the shear layer.

The discrepancies observed for coarse and medium grids were consistent with the low TKE values reported in Fig. 12. This correlation

suggests that reduced TKE production is associated with lower Reynolds shear stress, highlighting the coupling between turbulent kinetic energy and momentum transport in the flow field. The insufficient grid resolution limits the ability of LES to resolve small-scale eddies, resulting in underpredicted shear stress magnitudes.

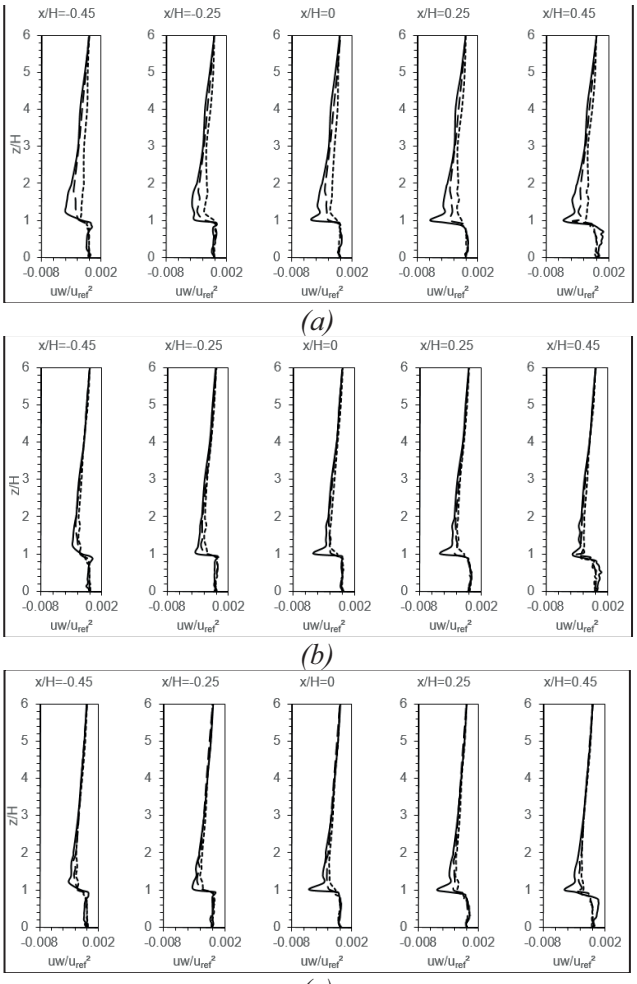

Figure 13. Vertical Profiles of Reynold Shear Stress for All Cases of Domain Sizes; (a) Case 1 (b) Case 2 and (c) Case 3 with Different Grid Resolution at x/H=-0.45, -0.25, 0, 0.25 and 0.45. The Square Dot Lines Refer to the: Grid 8 (Coarse), Dash Line: Grid 16 (Medium) and Solid Line: Grid 32 (Fine)

Overall, the fine grid resolution (G32) yielded the most accurate and consistent representation of Reynolds shear stress, effectively capturing the momentum exchange between the velocity fluctuations within and above the canyon. Furthermore, regardless of the domain size (Case 1, Case 2, or Case 3), the Reynolds shear stress profiles were in good agreement when simulated with fine grid resolution, confirming that grid refinement has a more dominant influence on LES performance than the computational domain size.

3.3 Data Comparison: Computational Domain and Grid Resolution

The streamwise mean velocity and velocity fluctuation of standard deviation as well as the Reynold shear stress components were used to represent the performance of the LES data. The percentage variation of ratio value for each component cases are presented in graph to determine the contribution of both parameters that could influence the accuracy of LES simulation inside and above the street canyon. Secondly, comparison was then conducted on those three components using the results from the wind tunnel data by Michioka et. al., [42].

3.3.1 Mean Velocity

Fig. 14 compares the streamwise mean velocity profiles from the LES simulations with the wind tunnel measurements of Michioka et al. [42] at x/H = 0. All simulation cases showed good agreement with the experimental data, particularly within the canyon and near the rooftop level. Noticeable variations among cases appeared only at higher elevations, especially for the grid resolution runs (Figures 14 a–c).

Overall, the current LES successfully reproduced the mean velocity distribution and yielded comparable results regardless of the computational domain size. In contrast, variations in grid resolution had a minor but consistent effect, where refinement from coarse to fine grids slightly increased the mean velocity magnitude without significantly altering the overall statistical profile. This suggests that the mean velocity field is relatively insensitive to both domain size and grid resolution, a trend

consistent with the findings of Cui et al. [40] and Cheng and Liu [41]. Considering computational efficiency, the use of a smaller domain with medium or fine grid resolution is deemed sufficient and reliable for predicting mean flow characteristics in a two-dimensional urban street canyon.

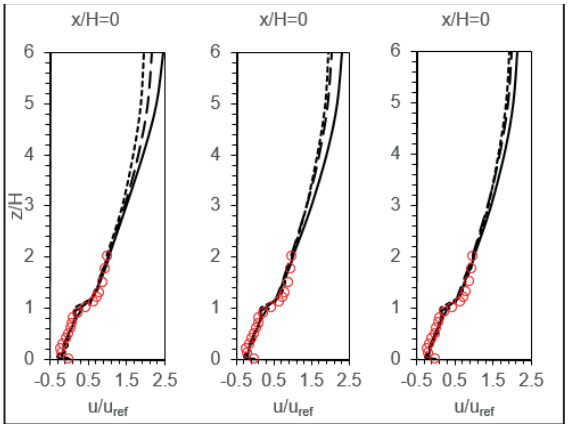

(a) (b) (c)

Figure 14. Comparison of Vertical Profile Streamwise Mean Velocity by Domain Run and Grid Resolution Run; (a)(b) and (c) with Wind Tunnel Experiment by Michioka et al., (2011) [6]. Symbol Refer as Previous

3.3.2 Standard Deviation

Fig. 15 compare the streamwise velocity fluctuation components (standard deviation) for different computational domains and grid resolutions. Larger variations were observed in the coarse-resolution (G8C) and small-domain (C1G) simulations compared to other cases, indicating stronger grid dependence under limited domain conditions.

When compared with the wind tunnel experiment by Michioka et al. [42], the LES-predicted standard deviations were generally lower, as shown in Fig. 15. This discrepancy can be attributed to the restricted computational domain and the absence of a refined mesh near the roof level, where strong wind shear and turbulent mixing occured. The smaller domain may have constrained the shear layer development above the buildings, resulting in weaker resolved velocity fluctuations [50]. Additionally, the exchange of high-momentum air above the canyon and low-momentum air within the canyon was less active in the coarse-grid simulations compared with the fine-resolution cases [40], further reducing turbulence intensity.

Despite these limitations, the overall profile patterns indicated that fine-grid LES runs successfully captured the dominant turbulent velocity fluctuations inside the canyon, largely independent of domain size (Fig. 15 (a)–(c)). This finding suggests that a medium computational domain combined with a fine grid resolution offers a practical balance between computational efficiency and simulation accuracy. Such a configuration was able to reproduce the essential turbulent characteristics within the street canyon while minimizing computational cost without significant loss of fidelity.

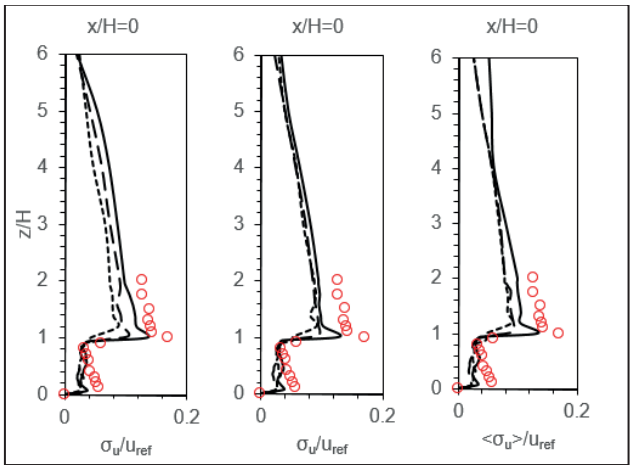

(a) (b) (c)

Figure 15. Comparison of Vertical Profile Streamwise Standard Deviation by Domain Run and Grid Resolution Run; (a)(b) and c with Wind Tunnel Experiment by Michioka et al., (2011) [6]. Symbol Refer as Previous

3.3.3 Reynold Shear Stress

Fig. 16 presents the comparison of Reynolds shear stress for the different computational domains and grid resolution cases. As observed in Fig. 16 (a), the trend closely mirrors that of the velocity fluctuation results discussed in Section 3.3.2, where larger variations occurred

in the coarse-resolution (G8C) and small-domain (C1G) simulations compared with other cases. The Reynolds shear stress within the street canyon showed minimal sensitivity to domain length, indicating that extending the computational domain did not substantially enhance turbulence representation. However, grid resolution had a more pronounced effect on the momentum transport characteristics within the urban boundary layer. The fine-grid simulations (G32) provided better-resolved and more comparable results, effectively capturing the shear-layer dynamics and momentum exchange processes above the canyon.

These results also aligned well with the wind tunnel data, although the LES slightly underpredicted the Reynolds shear stress magnitude. This difference is likely due to the limitations in grid resolution and subgrid-scale modeling, which may dampen small-scale turbulence production.

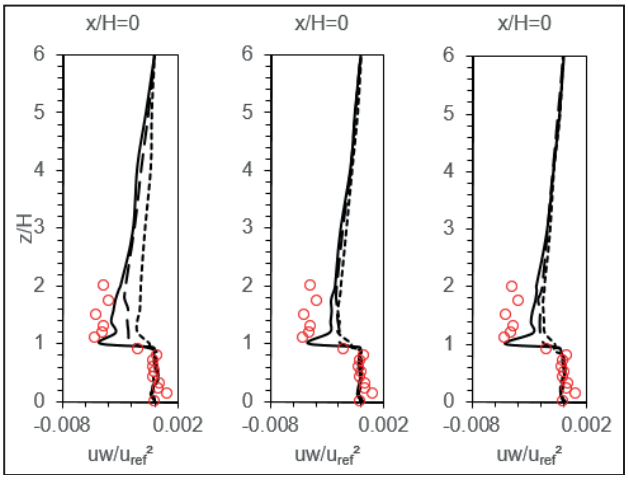

Figure 16. Comparison of Vertical Profile Reynold Shear Stress by Domain Run and Grid Resolution Run; (a)(b) and (c) with Wind Tunnel Experiment by Michioka et al., (2011) [6]. Symbol Refer as Previous

Overall, grid resolution was found to have a greater influence on LES performance than domain size. While the small-domain simulation adequately reproduced the general fluctuation trends, it exhibited less smoothness compared with the medium and large domains. Hence, the present study suggests that a medium computational domain, coupled with a fine grid resolution, offers an optimal balance between computational efficiency and accuracy for momentum transport analysis in urban street canyons.

CONCLUSION

This study evaluated how grid resolution and computational domain size influence LES predictions of turbulent flow within an idealized street canyon. The results show that mean velocity profiles were only marginally affected by grid refinement and were largely independent of domain size, with all simulations agreeing well with available wind-tunnel data. Mean flow characteristics could therefore be captured reliably even with a small domain when medium or fine grid resolutions were used.

In contrast, turbulence quantities such as velocity fluctuations, Reynolds shear stress, and momentum transport, were strongly dependent on grid resolution. Domain size had a weaker influence, and LES systematically underpredicted these turbulence statistics compared with wind-tunnel measurements. This discrepancy was attributed to limited domain extent and insufficient mesh refinement near the roof level, which restricted the formation of large eddies and reduced momentum transfer.

Overall, grid resolution played a more critical role than domain size in reproducing the turbulent structure of canyon flow. For accurate turbulence analysis, a fine grid combined with a sufficiently large domain is recommended. However, a medium domain with fine resolution may offer an acceptable balance between computational cost and accuracy, particularly when mesh refinement is applied in key regions. These findings provide practical guidance for optimizing numerical resources in LES studies of urban street canyons without compromising predictive reliability.

ACKNOWLEDGEMENTS

The authors thank the Wind Engineering & Building Physics Center (WEBPC), Faculty of Mechanical Engineering, Universiti Teknologi MARA (UiTM) for providing access to software needed to complete this work.

REFERENCES

1. **C.H. Liu, C.C.C. Wong.** On the Pollutant Removal, Dispersion, and Entrainment over Two-dimensional Idealized Street Canyons. Atmospheric Research, 135-136, 128-142, 2014.
2. **Ali N, Alias A., Hamzah H., Muhammad I., Othman K.N.** Transformative Urban Mobility: Comparative Analysis of Global Transit-Oriented Development Strategies. Journal of Sustainable Civil Engineering and Technology. e-ISSN: 2948-4294, Volume 4 Issue 1 (March 2025), 37-50.
3. **Zhang X., Wen., Weerasuriya A.U., Ye X., and Zhang B**. Investigating Vehicle Effects on Wind and Pollutant Fields in Street Canyon using the Dynamic Mesh and Source Term Methods. Sustainable Cities and Society 130 (2025) 106620.
4. **Qin P., Ricci A., and Blocken B.** CFD Simulation of Pollutant Dispersion in a Street Canyon with Realistic Car Sources: The Potential of Green Infrastructure Configurations. Urban Climate 62 (2025) 102544.
5. **Bakhary N.A.** Green Building Material and Technologies: Assessing Their Potential in Sustainable Construction. Journal of Sustainable Civil Engineering and Technology. e-ISSN: 2948-4294, Volume 4 Issue 1 (March 2025), 7-18.
6. **Mustaffa, N.K., Abdul Kudus, S., Abdul Aziz, M.F.H., & Anak Joseph, V.R.** Strategies and way forward of low carbon construction in Malaysia. Building Research & Information. (2022). 50(6), 628–645.
7. **W.M.Y. Afiq, C.S.N. Azwadi, K.M. Saqr.** Effects of Buildings Aspect Ratio, Wind speed and Wind direction on Flow Structure and Pollutant Dispersion in Symmetric Street Canyons: A Review, International Journal of Mechanical and Materials Engineering (IJMME), Vol. 7, No. 2, 158-165, 2012.
8. **Qin P., Ricci A., and Blocken B.** Modeling Traffic Pollutants in a Street Canyon by CFD: Idealized Line Sources Versus Multiple Realistic Car Sources. Science of The Total Environment 955 (2024) 177099.
9. **T.R. Oke.** Street Design and Urban Canopy Layer Climate, Energy and Buildings, Vol. 11 :103- 113, 1998.
10. **Maison A., Flageul C., Carissimo B., Wang Y., Tuzet A., and Sartelet K.** Parameterizing the Aerodynamic Effect of Trees in Street Canyons for a Street Network Model MUNICH using the CFD Model Code_Saturne. Atmos. Chem. Phys., 22, 9369-9388 (2022).
11. **R.N. Meroney, M. Pavageau, S. Rafailidis & M. Schatzmann.** Study of line source characteristics for 2-D physical modelling of pollutant dispersion in street canyons. Journal of Wind Engineering and Industrial Aerodynamics, 62(1), 37–56, 1996.
12. **S. Vardoulakis, B.E.A. Fisher, K. Pericleous and N.G. Flesca.** Modelling Air Quality in Street Canyons: A Review, Atmospheric environment, Vol. 37 (2), 155-182, 2003.
13. **W. Li, Y. He, Y. Zhang, Q. Shui, X. Wu, C. Wah., Yu and Z. Gu.** Numerical Study of the Composite Effects of Uneven Street Canyons and Time-varying Inflows on the Air Flows and Pollutant Dispersion, Aerosol and Air Quality Research, Vol. 20, 1440–1453, 2020.
14. **X.X. Li, C H. Liu, D.Y.C. Leung**. Large-Eddy Simulation of Flow and Pollutant Dispersion in High-Aspect-Ratio Urban Street Canyons with Wall Model,

Boundary-Layer Meteorol, 129:249–268, 2008.

15. **J. Zhong, X.M. Cai and W.J. Bloss**. Modelling the dispersion and transport of reactive pollutants in a deep urban street canyon: Using large-eddy simulation, Environmental Pollution, Vol. 200, 42-52, 2015.
16. **Z.T. Ai and C.M. Mak**, CFD simulation of flow in a long street canyon under a perpendicular wind direction: Evaluation of three computational settings, Building and Environment, 114, 293–306, 2017.
17. **B. Blocken.** Computational Wind Engineering: Theory and Applications, Environmental Wind Engineering and Design of Wind Energy Structures, CISM Courses and Lectures, Vol 531, 2011.
18. **Qin P., Ricci A., and Blocken B.** On the Accuracy of Idealized Sources in CFD Simulations of Pollutant Dispersion in an Urban Street Canyon. Building and Environment 265 (2024) 111950.
19. **Ahmad F., Majumder D., Ranjit R., Gupta A., and Manhart M.** Preliminary Study on the Spread of Air-bone Pollutant in Urban Environment: a CFD Simulation Approach. Scientific Reports (2025) 15:18836.
20. **F. Roelofs, A. Shams**. CFD-Introduction Nuclear Research & Consultancy Group (NRG), Petten, The Netherlands, 2019.
21. **H.K. Versteeg, W. Malalasekera,** An Introduction to Computational Fluid Dynamics," Second edition, 2007.
22. **Mishra N., Patra A. K., Penchala A., and Santra S.** Numerical Investigation of the Influence of Street Length and Building Configurations on Ventilation and Pollutant Dispersion in Idealized Street Canyons. Journal of Wind Engineering & Industrial Aerodynamics 257 (2025) 106016.
23. **F.S. Lien, E. Yee, Y. Cheng.** Simulation of Mean Flow and Turbulence Over A 2D Building Array Using High-Resolution CFD and A Distributed Drag Force Approach, Journal of Wind Engineering and Industrial Aerodynamics, Vol. 92, 117–158, 2004.
24. **W.C. Cheng, C.H. Liu, D.Y.C. Leung.** Computational Formulation for The Evaluation of Street Canyon Ventilation and Pollutant Removal Performance, Atmospheric Environment 42, 9041–9051, 2008.
25. **Z.T. Ai, C.M. Mak,** Wind-Induced Single-Sided Natural Ventilation in Buildings Near a Long Street Canyon: CFD Evaluation of Street Configuration and Envelope Design, Journal of Wind Engineering & Industrial Aerodynamics 172, 96–106, 2018.
26. **D. Cui, X. Li, Y. Du, C.M. Mak, K. Kwok**, Effects of Envelope Features On Wind Flow and Pollutant Exposure in Street Canyons, Building and Environment 176, 106862, 2020.
27. **S.M. Salim, K. C. Ong.** Performance of RANS, URANS and LES in the Prediction of Airflow and Pollutant Dispersion, IAENG Transactions on Engineering Technologies. Lecture Notes in Electrical Engineering, 263-274, Vol. 170, 2013.
28. **P. Gousseaua, B. Blocken, T. Stathopoulos, G.J.F.V. Heijst.** Near-Field Pollutant Dispersion in an Actual Urban Area: Analysis of The Mass Transport Mechanism by High Resolution Large Eddy Simulations, Computers & Fluids, 2015.
29. **Alwi A., Mohamad M.F., Ikegaya N., and Razak A.A.** Effect of Protuding Eave on the Turbulence Structures over Two-dimensional Semi-open Street Canyon Building and Environment 228 (2023) 109921
30. **C.H. Liu, D.Y.C. Leung, M.C. Barth**. On The Prediction of Air and Pollutant Exchange Rates in Street Canyons of Different Aspect Ratios Using Large-Eddy Simulation, Atmospheric Environment, Vol. 39, 1567–1574, 2005.
31. **X.X. Li, C.H. Liu, D.Y.C. Leung**. Numerical Investigation of Pollutant Transport Characteristics Inside Deep

Urban Street Canyons, Atmospheric Environment, Vol.43, 2410–2418, 2009.

32. **M.F. Mohamad, A. Hagishima, N. Ikegaya, J. Tanimoto, A.R. Omar**. Aerodynamic Effect of Overhang on a Turbulent Flow Field within a Two-dimensional Street Canyon, Engineering Sciences Reports, Kyushu University, Vol. 37, No. 1,1-7, 2015.
33. **M.L. Munitxaa, E.B. Zeida, M. Hultmark,** The Influence of Building Geometry On Street Canyon Air Flow: Validation of Large Eddy Simulations Against Wind Tunnel Experiments, Journal of Wind Engineering & Industrial Aerodynamics vol.165, 115–130, 2017.
34. **Lauriks T., Longo R., Baetens D., Derudi M., Parente A., Bellemans A., Beeck V. J., and Denys S.** Application on Improves CDF Modeling for Prediction and Mitigation of Traffic-related Air Pollution Hotspot in a Realistic Urban Street.Atmospheric Environment 246 (2021) 118127
35. **N. Saleh, M.H.M. Hashim, M.F. Mohamad**. Large-eddy Simulation of Turbulent Flow in an Idealized Street Canyon, CFD Letters 11, Issue 11, 48-57, 2019.
36. **N. Saleh, M.H.M. Hashim, M.F. Mohamad.** The Influence of Computational Parameterization on Mean Flow and Turbulence Statistic in 2D Idealized Street Canyon: Computational Domain, CFD Letters 12, Issue 7, 37-47, 2020.
37. **Y. Sanjaya, D. Priambodo, P.W. Sarli, H.D. Setio.** The Effect of Street Canyon Width Towards Wind Flow in Between High-Rise Buildings, IOP Conf. Series: Materials Science and Engineering, 930, 012044, 2020.
38. **J. Franke, C. Hirsch, G. Jensen, H.W. Krüs, S.D. Miles, M. Schatzmann, P.S. Westbury, J.A. Wisse and N. Wright**. Recommendations On the Use of CFD in Wind Engineering, Proceedings of the International Conference on Urban Wind Engineering and Building Aerodynamics, 2004.
39. **C.H. Liu and M.C. Barth**. Large-Eddy Simulation of Flow and Scalar Transport in a Modeled Street Canyon, Journal of Applied Meteorology, Vol. 41, 2001.
40. **Z. Cui, X. Cai, C.J. Baker**. Large-eddy simulation of turbulent flow in a street canyon, Q.J.R. Meteorol. Soc., Vol. 130,1373–1394, 2004.
41. **W.C. Cheng, C.H. Liu.** Large-Eddy Simulation of Flow and Pollutant Transports in and Above Two-Dimensional Idealized Street Canyons, Boundary-Layer Meteorol, Vol. 139,411–437, 2011.
42. **T. Michioka, A. Sato, H. Takimoto, M. Kanda.** Large-Eddy Simulation for the Mechanism of Pollutant Removal from a Two-Dimensional Street Canyon, Boundary-Layer Meteorol 138, 195–213, 2011.
43. **Dai S.F., Liu H.J., Lam H.F. and Peng H.Y.** Interference effect of photovoltaic solar arrays on wind load of building roof by large eddy simulations. Engineering Structures 336 (2025) 120453
44. **Ciarlatani M.F. and Gorlé C.** A neural network-based multi-fidelity modeling approach for large-eddy simulations with application to wind loading predictions. Engineering Structures 343 (2025) 120780.
45. **M.J. Brown, R.E. Lawson, D.S. Decroix, R.L. Lee.** Mean Flow and Turbulence Measurement Around a 2-D Array of Buildings in a Wind Tunnel, 11th Joint AMS/AWMA Conference on the Applications of Air Pollution Meteorology Long Beach, 2000.
46. **J. Franke, A. Hellsten, H. Schlünzen, B. Carissimo.** Best Practice Guideline for The CFD Simulation of Flows in The Urban Environment, Cost Action 732, Quality Assurance and Improvement of Microscale Meteorological Models, 2007.
47. **W.L. Oberkampf, T.G. Trucano.** Verification and Validation in

Computational Fluid Dynamics, Progress in Aerospace Sciences 38, 209–272, 2002.
48. **C.H. Liu and C.C.C. Wong.** On the Pollutant Removal, Dispersion, and Entrainment over Two-dimensional Idealized Street Canyons. Atmospheric Research, 135-136, 128-142, 2014.M.
49. **S. Mohamed.** Computational Study of Wind Flow and Pollutant Dispersion Near Tree Canopies, PhD thesis, University of Nottingham, 2011.
50. **Kanda, R. Moriwaki and F. Kasamatsu**. Large-Eddy Simulation of Turbulent Organized Structures Within and Above Explicitly Resolved Cube Arrays. Boundary-Layer Meteorol*,* Vol. 112, 343–368, 2004.

СПИСОК ЛИТЕРАТУРЫ

1. **C.H. Liu, C.C.C. Wong.** On the Pollutant Removal, Dispersion, and Entrainment over Two-dimensional Idealized Street Canyons. Atmospheric Research, 135-136, 128-142, 2014.
2. **Ali N, Alias A., Hamzah H., Muhammad I., Othman K.N.** Transformative Urban Mobility: Comparative Analysis of Global Transit-Oriented Development Strategies. Journal of Sustainable Civil Engineering and Technology. e-ISSN: 2948-4294, Volume 4 Issue 1 (March 2025), 37-50.
3. **Zhang X., Wen., Weerasuriya A.U., Ye X., and Zhang B**. Investigating Vehicle Effects on Wind and Pollutant Fields in Street Canyon using the Dynamic Mesh and Source Term Methods. Sustainable Cities and Society 130 (2025) 106620.
4. **Qin P., Ricci A., and Blocken B.** CFD Simulation of Pollutant Dispersion in a Street Canyon with Realistic Car Sources: The Potential of Green Infrastructure Configurations. Urban Climate 62 (2025) 102544.
5. **Bakhary N.A.** Green Building Material and Technologies: Assessing Their Potential in Sustainable Construction. Journal of Sustainable Civil Engineering and Technology. e-ISSN: 2948-4294, Volume 4 Issue 1 (March 2025), 7-18.
6. **Mustaffa, N.K., Abdul Kudus, S., Abdul Aziz, M.F.H., & Anak Joseph, V.R.** Strategies and way forward of low carbon construction in Malaysia. Building Research & Information. (2022). 50(6), 628–645.
7. **W.M.Y. Afiq, C.S.N. Azwadi, K.M. Saqr.** Effects of Buildings Aspect Ratio, Wind speed and Wind direction on Flow Structure and Pollutant Dispersion in Symmetric Street Canyons: A Review, International Journal of Mechanical and Materials Engineering (IJMME), Vol. 7, No. 2, 158-165, 2012.
8. **Qin P., Ricci A., and Blocken B.** Modeling Traffic Pollutants in a Street Canyon by CFD: Idealized Line Sources Versus Multiple Realistic Car Sources. Science of The Total Environment 955 (2024) 177099.
9. **T.R. Oke.** Street Design and Urban Canopy Layer Climate, Energy and Buildings, Vol. 11 :103- 113, 1998.
10. **Maison A., Flageul C., Carissimo B., Wang Y., Tuzet A., and Sartelet K.** Parameterizing the Aerodynamic Effect of Trees in Street Canyons for a Street Network Model MUNICH using the CFD Model Code_Saturne. Atmos. Chem. Phys., 22, 9369-9388 (2022).
11. **R.N. Meroney, M. Pavageau, S. Rafailidis & M. Schatzmann.** Study of line source characteristics for 2-D physical modelling of pollutant dispersion in street canyons. Journal of Wind Engineering and Industrial Aerodynamics, 62(1), 37–56, 1996.
12. **S. Vardoulakis, B.E.A. Fisher, K. Pericleous and N.G. Flesca.** Modelling Air Quality in Street Canyons: A Review, Atmospheric environment, Vol. 37 (2), 155-182, 2003.
13. **W. Li, Y. He, Y. Zhang, Q. Shui, X. Wu, C. Wah., Yu and Z. Gu.** Numerical Study

of the Composite Effects of Uneven Street Canyons and Time-varying Inflows on the Air Flows and Pollutant Dispersion, Aerosol and Air Quality Research, Vol. 20, 1440–1453, 2020.

14. **X.X. Li, C H. Liu, D.Y.C. Leung**. Large-Eddy Simulation of Flow and Pollutant Dispersion in High-Aspect-Ratio Urban Street Canyons with Wall Model, Boundary-Layer Meteorol, 129:249–268, 2008.
15. **J. Zhong, X.M. Cai and W.J. Bloss**. Modelling the dispersion and transport of reactive pollutants in a deep urban street canyon: Using large-eddy simulation, Environmental Pollution, Vol. 200, 42-52, 2015.
16. **Z.T. Ai and C.M. Mak**, CFD simulation of flow in a long street canyon under a perpendicular wind direction: Evaluation of three computational settings, Building and Environment, 114, 293–306, 2017.
17. **B. Blocken.** Computational Wind Engineering: Theory and Applications, Environmental Wind Engineering and Design of Wind Energy Structures, CISM Courses and Lectures, Vol 531, 2011.
18. **Qin P., Ricci A., and Blocken B.** On the Accuracy of Idealized Sources in CFD Simulations of Pollutant Dispersion in an Urban Street Canyon. Building and Environment 265 (2024) 111950.
19. **Ahmad F., Majumder D., Ranjit R., Gupta A., and Manhart M.** Preliminary Study on the Spread of Air-bone Pollutant in Urban Environment: a CFD Simulation Approach. Scientific Reports (2025) 15:18836.
20. **F. Roelofs, A. Shams**. CFD-Introduction Nuclear Research & Consultancy Group (NRG), Petten, The Netherlands, 2019.
21. **H.K. Versteeg, W. Malalasekera,** An Introduction to Computational Fluid Dynamics," Second edition, 2007.
22. **Mishra N., Patra A. K., Penchala A., and Santra S.** Numerical Investigation of the Influence of Street Length and Building Configurations on Ventilation and Pollutant Dispersion in Idealized Street Canyons. Journal of Wind Engineering & Industrial Aerodynamics 257 (2025) 106016.
23. **F.S. Lien, E. Yee, Y. Cheng.** Simulation of Mean Flow and Turbulence Over A 2D Building Array Using High-Resolution CFD and A Distributed Drag Force Approach, Journal of Wind Engineering and Industrial Aerodynamics, Vol. 92, 117–158, 2004.
24. **W.C. Cheng, C.H. Liu, D.Y.C. Leung.** Computational Formulation for The Evaluation of Street Canyon Ventilation and Pollutant Removal Performance, Atmospheric Environment 42, 9041–9051, 2008.
25. **Z.T. Ai, C.M. Mak,** Wind-Induced Single-Sided Natural Ventilation in Buildings Near a Long Street Canyon: CFD Evaluation of Street Configuration and Envelope Design, Journal of Wind Engineering & Industrial Aerodynamics 172, 96–106, 2018.
26. **D. Cui, X. Li, Y. Du, C.M. Mak, K. Kwok**, Effects of Envelope Features On Wind Flow and Pollutant Exposure in Street Canyons, Building and Environment 176, 106862, 2020.
27. **S.M. Salim, K. C. Ong.** Performance of RANS, URANS and LES in the Prediction of Airflow and Pollutant Dispersion, IAENG Transactions on Engineering Technologies. Lecture Notes in Electrical Engineering, 263-274, Vol. 170, 2013.
28. **P. Gousseaua, B. Blocken, T. Stathopoulos, G.J.F.V. Heijst.** Near-Field Pollutant Dispersion in an Actual Urban Area: Analysis of The Mass Transport Mechanism by High Resolution Large Eddy Simulations, Computers & Fluids, 2015.
29. **Alwi A., Mohamad M.F., Ikegaya N., and Razak A.A.** Effect of Protuding Eave on the Turbulence Structures over Two-dimensional Semi-open Street Canyon Building and Environment 228 (2023) 109921

30. **C.H. Liu, D.Y.C. Leung, M.C. Barth**. On The Prediction of Air and Pollutant Exchange Rates in Street Canyons of Different Aspect Ratios Using Large-Eddy Simulation, Atmospheric Environment, Vol. 39, 1567–1574, 2005.
31. **X.X. Li, C.H. Liu, D.Y.C. Leung**. Numerical Investigation of Pollutant Transport Characteristics Inside Deep Urban Street Canyons, Atmospheric Environment, Vol.43, 2410–2418, 2009.
32. **M.F. Mohamad, A. Hagishima, N. Ikegaya, J. Tanimoto, A.R. Omar**. Aerodynamic Effect of Overhang on a Turbulent Flow Field within a Two-dimensional Street Canyon, Engineering Sciences Reports, Kyushu University, Vol. 37, No. 1,1-7, 2015.
33. **M.L. Munitxaa, E.B. Zeida, M. Hultmark,** The Influence of Building Geometry On Street Canyon Air Flow: Validation of Large Eddy Simulations Against Wind Tunnel Experiments, Journal of Wind Engineering & Industrial Aerodynamics vol.165, 115–130, 2017.
34. **Lauriks T., Longo R., Baetens D., Derudi M., Parente A., Bellemans A., Beeck V. J., and Denys S.** Application on Improves CDF Modeling for Prediction and Mitigation of Traffic-related Air Pollution Hotspot in a Realistic Urban Street.Atmospheric Environment 246 (2021) 118127
35. **N. Saleh, M.H.M. Hashim, M.F. Mohamad**. Large-eddy Simulation of Turbulent Flow in an Idealized Street Canyon, CFD Letters 11, Issue 11, 48-57, 2019.
36. **N. Saleh, M.H.M. Hashim, M.F. Mohamad.** The Influence of Computational Parameterization on Mean Flow and Turbulence Statistic in 2D Idealized Street Canyon: Computational Domain, CFD Letters 12, Issue 7, 37-47, 2020.
37. **Y. Sanjaya, D. Priambodo, P.W. Sarli, H.D. Setio.** The Effect of Street Canyon Width Towards Wind Flow in Between High-Rise Buildings, IOP Conf. Series: Materials Science and Engineering, 930, 012044, 2020.
38. **J. Franke, C. Hirsch, G. Jensen, H.W. Krüs, S.D. Miles, M. Schatzmann, P.S. Westbury, J.A. Wisse and N. Wright**. Recommendations On the Use of CFD in Wind Engineering, Proceedings of the International Conference on Urban Wind Engineering and Building Aerodynamics, 2004.
39. **C.H. Liu and M.C. Barth**. Large-Eddy Simulation of Flow and Scalar Transport in a Modeled Street Canyon, Journal of Applied Meteorology, Vol. 41, 2001.
40. **Z. Cui, X. Cai, C.J. Baker**. Large-eddy simulation of turbulent flow in a street canyon, Q.J.R. Meteorol. Soc., Vol. 130,1373–1394, 2004.
41. **W.C. Cheng, C.H. Liu.** Large-Eddy Simulation of Flow and Pollutant Transports in and Above Two-Dimensional Idealized Street Canyons, Boundary-Layer Meteorol, Vol. 139,411–437, 2011.
42. **T. Michioka, A. Sato, H. Takimoto, M. Kanda.** Large-Eddy Simulation for the Mechanism of Pollutant Removal from a Two-Dimensional Street Canyon, Boundary-Layer Meteorol 138, 195–213, 2011.
43. **Dai S.F., Liu H.J., Lam H.F. and Peng H.Y.** Interference effect of photovoltaic solar arrays on wind load of building roof by large eddy simulations. Engineering Structures 336 (2025) 120453
44. **Ciarlatani M.F. and Gorlé C.** A neural network-based multi-fidelity modeling approach for large-eddy simulations with application to wind loading predictions. Engineering Structures 343 (2025) 120780.
45. **M.J. Brown, R.E. Lawson, D.S. Decroix, R.L. Lee.** Mean Flow and Turbulence Measurement Around a 2-D Array of Buildings in a Wind Tunnel, 11th Joint AMS/AWMA Conference on the Applications of Air Pollution Meteorology Long Beach, 2000.
46. **J. Franke, A. Hellsten, H. Schlünzen, B. Carissimo.** Best Practice Guideline for The

CFD Simulation of Flows in The Urban Environment, Cost Action 732, Quality Assurance and Improvement of Microscale Meteorological Models, 2007.
47. **W.L. Oberkampf, T.G. Trucano.** Verification and Validation in Computational Fluid Dynamics, Progress in Aerospace Sciences 38, 209–272, 2002.
48. **C.H. Liu and C.C.C. Wong.** On the Pollutant Removal, Dispersion, and Entrainment over Two-dimensional Idealized Street Canyons. Atmospheric Research, 135-136, 128-142, 2014.M.
49. **S. Mohamed.** Computational Study of Wind Flow and Pollutant Dispersion Near Tree Canopies, PhD thesis, University of Nottingham, 2011.
50. **Kanda, R. Moriwaki and F. Kasamatsu**. Large-Eddy Simulation of Turbulent Organized Structures Within and Above Explicitly Resolved Cube Arrays. Boundary-Layer Meteorol, Vol. 112, 343–368, 2004.

Norharyati Saleh — Ph.D. in Civil Engineering, Senior Lecturer, Faculty of Civil Engineering, Universiti Teknologi MARA (UiTM), Shah Alam, Selangor, Malaysia. Address: Faculty of Civil Engineering, Universiti Teknologi MARA (UiTM), 40450 Shah Alam, Selangor, Malaysia. E-mail: norharyati@uitm.edu.my.

Mohd Hisbany Mohd Hashim — Ph.D. in Civil Engineering, Associate Professor, Faculty of Civil Engineering, Universiti Teknologi MARA (UiTM), Shah Alam, Selangor, Malaysia. Address: Faculty of Civil Engineering, Universiti Teknologi MARA (UiTM), 40450 Shah Alam, Selangor, Malaysia. E-mail: norharyati@uitm.edu.my.

Mohd Faizal Mohamad — Ph.D. in Mechanical Engineering, Senior Lecturer, Faculty of Mechanical Engineering, Universiti Teknologi MARA (UiTM), Shah Alam, Selangor, Malaysia. Address: Faculty of Mechanical Engineering, Universiti Teknologi MARA (UiTM), 40450 Shah Alam, Selangor, Malaysia. E-mail norharyati@uitm.edu.my.

Roslin Ramli — Ph.D., Associate Professor, Maritime Engineering Technology Programme, Universiti Kuala Lumpur Malaysian Institute of Marine Engineering Technology (UniKL MIMET), Lumut, Perak, Malaysia. Address: Jalan Pantai Remis, 32200 Lumut, Perak, Malaysia. E-mail: to norharyati@uitm.edu.my.

Herlien D. Setio — Ph.D. in Civil Engineering, Professor, Faculty of Civil and Environmental Engineering, Institut Teknologi Bandung (ITB), Bandung, West Java, Indonesia. Address: Jalan Ganesha No. 10, Bandung 40132, West Java, Indonesia. E-mail: norharyati@uitm.edu.my.

Салех Норхарьяти — PhD в области гражданского строительства, старший преподаватель факультета гражданского строительства Университета Технологии MARA, Шах-Алам, штат Селангор, Малайзия. Адрес: Faculty of Civil Engineering, Universiti Teknologi MARA (UiTM), 40450 Shah Alam, Selangor, Malaysia. E-mail: norharyati@uitm.edu.my.

Хашим Мохд Хисбани Мохд (Mohd Hisbany Mohd Hashim) — PhD в области гражданского строительства, доцент факультета гражданского строительства Университета Технологии MARA, Шах-Алам, штат Селангор, Малайзия. Адрес: Faculty of Civil Engineering, Universiti Teknologi MARA (UiTM), 40450 Shah Alam, Selangor, Malaysia. E-mail: norharyati@uitm.edu.my.

Мохамад Мохд Файзал (Mohd Faizal Mohamad) — PhD в области машиностроения, старший преподаватель факультета машиностроения Университета Технологии MARA, Шах-Алам, штат Селангор, Малайзия. Адрес: Faculty of Mechanical Engineering, Universiti Teknologi MARA (UiTM), 40450 Shah Alam, Selangor, Malaysia. E-mail: norharyati@uitm.edu.my.

Рамли Рослин (Roslin Ramli) — PhD, доцент направления «Технологии морской инженерии» Малайзийского института морских инженерных технологий Университета Куала-Лумпур, Лумут, штат Перак, Малайзия. Адрес: Jalan Pantai Remis, 32200 Lumut, Perak, Malaysia. E-mail: norharyati@uitm.edu.my.

Сетио Херлиен Д. (Herlien D. Setio) — PhD в области гражданского строительства, профессор факультета гражданского строительства и экологической инженерии Бандунгского технологического института, Бандунг, Западная Ява, Индонезия. Адрес: Jalan Ganesha No. 10, Bandung 40132, West Java, Indonesia. E-mail: norharyati@uitm.edu.my.

DOI:10.22337/2587-9618-2026-22-2-73-87

CORRECTION FACTOR FOR HEAVY CONCRETE MIX DESIGN USING LOW-QUALITY AGGREGATES

Alexander L. Popov [1], Dmitry F. Fedorov [1], Shuai Gao [1], Valeriya V. Strokova [2]

[1] Engineering and Technical Institute, North-Eastern Federal University named after M.K. Ammosov (NEFU), Yakutsk, RUSSIA

[2] Institute of Civil Engineering, Belgorod State Technological University named after V.G. Shukhov (BSTU), Belgorod, RUSSIA

Abstract: This study investigates an experimental-analytical approach to improving the accuracy of calculating the nominal composition of heavy concrete using a database of test protocols from NEFU (2015–2025). Particular attention is paid to working with low-quality aggregates – sand with a fineness modulus below 1.4. Significant discrepancies between the calculated and actual concrete compositions were identified, reaching up to ±250 kg/m³. A corrective coefficient linking the cement-to-water ratio (C/W) with the proportion of aggregates is proposed. Its application reduced the error to ±60–150 kg/m³ and improved the convergence of results to 1.5% without loss of strength. It is shown that the strength of concrete incorporating very fine sand (fineness modulus ≤ 1.4) exhibits higher sensitivity to variations in the C/W ratio within a narrow range of 1.3–2.7. The discrepancy between calculated and actual concrete density varies widely, leading to material overconsumption and reducing the reliability of computational mix design methods. An empirical relationship has been established linking the key variable mix parameters (water-cement ratio and aggregate proportion), which can be used as a correction factor. Without the coefficient, the deviation range was 1.8–5.0%, while with its application it ranged from –0.6% to 1.5% without deterioration of concrete mixture properties or physical and mechanical characteristics.

Keywords: heavy concrete, mix design, experimental coefficient, experimental data, C/W ratio, database

ПОПРАВОЧНЫЙ КОЭФФИЦИЕНТ ДЛЯ ПОДБОРА СОСТАВА ТЯЖЁЛОГО БЕТОНА НА НИЗКОКАЧЕСТВЕННЫХ ЗАПОЛНИТЕЛЯХ

А.Л. Попов [1], Д.Ф. Федоров [1], Гао Шуай [1], В.В. Строкова [2]

[1] Инженерно-технический институт Северо-Восточного федерального университета имени М.К. Аммосова (СВФУ), г. Якутск, РОССИЯ

[2] Инженерно-строительный институт Белгородского государственного технологического университета им. В.Г. Шухова (БГТУ), г. Белгород, РОССИЯ

Аннотация: В статье исследуется экспериментально-аналитический подход к повышению точности расчёта номинального состава тяжёлого бетона с использованием базы данных протоколов испытаний СВФУ за 2015–2025 гг. Особое внимание уделено работе с низкокачественными заполнителями – песком с модулем крупности менее 1,4. Выявлены существенные расхождения между расчётным и фактическим составами бетона, достигающие ±250 кг/м³. Предложен корректирующий коэффициент, связывающий цементно-водное отношение (Ц/В) с долей заполнителей. Его применение позволило снизить ошибку до ±60–150 кг/м³ и улучшить сходимость результатов до 1,5 % без потери прочности. Показано, что прочность бетона на очень мелких песках (Мкр ≤ 1,4) проявляет повышенную чувствительность к изменению Ц/В отношения в узком диапазоне 1,3–2,7. Расхождение между расчётной и фактической плотностью бетона варьируется в широких пределах, что ведёт к перерасходу материалов и снижает надёжность вычислительных методов подбора состава. Установлено эмпирическое выражение, связывающее варьируемые параметры смеси (водоцементное отношение и долю заполнителей), которое может использоваться в качестве поправочного коэффициента. Без коэффициента диапазон отклонений составлял 1,8–5,0 %, а с его применением – от –0,6 % до 1,5 % без ухудшения свойств бетонной смеси и физико-механических характеристик.

Ключевые слова: тяжёлый бетон, подбор состава, экспериментальный коэффициент, экспериментальные данные, цементно-водное отношение, база данных

INTRODUCTION

Modern construction technologies demand precise design of concrete mixtures considering multiple factors: strength, workability, durability and cost-effectiveness [1, 2]. However, traditional mix design methods based on manual calculations and trial batches remain labor-intensive and prone to errors, making experimental-analytical approaches incorporating statistical data processing and computer modeling particularly relevant [3, 4, 5].

Research across various scientific fields demonstrates that combining experimental data with mathematical modeling significantly improves calculation accuracy [6, 7]. Promising developments include integration of material databases [8], application of semi-empirical models [9] and automation of trial batches, which together with advances in artificial intelligence and big data open new possibilities for construction materials design [10, 11, 12]. In concrete science, the main challenges of manual mix design stem from component variability (cement, aggregates, admixtures), multiple influencing factors (water-cement ratio, curing conditions) and calculation complexity [12], prompting development of specialized software like the Borland Delphi 7 program automating heavy concrete mix design considering required strength and component properties [12]. Successful implementation of such methods requires comprehensive databases with well-defined dependencies for use as adjustment coefficients in calculated concrete mixes.

Practical experience in concrete design shows that when using low-quality aggregates (fine aggregate fineness modulus below 1.4), producing quality concrete mixtures requires high-performance chemical admixtures and reduced proportion of such inferior components. This aspect remains insufficiently addressed in scientific literature. While existing concrete design guidelines recommend decreasing fine aggregate content with increasing cement quantity, for concretes with fine aggregate fineness modulus below 1.4 this proportion must be further reduced to control workability - a non-standard case not covered by current recommendations, leading to significant discrepancies between design and actual compositions [13, 14]. It should be noted that concrete research advancements have introduced increasingly diverse components into concrete mixtures [15-18]. However, concrete theory considers water-cement ratio and aggregate proportions as primary variables significantly affecting concrete properties, meaning other mix parameters' influence can only be determined through data analysis.

This study aimed to improve accuracy of nominal concrete mix design calculations using an experimental-analytical approach incorporating database analysis. The research addressed the following tasks: compiling a database from concrete mix design protocols conducted at NEFU; analyzing data for compliance with formal logic and determinability through nominal mix design methods; deriving sufficiently reliable dependencies for use as adjustment coefficients in nominal concrete mix design calculations.

SUBJECT, OBJECTIVES, AND METHODS

The database was compiled from records of mix design and testing of heavy concretes obtained at NEFU (North-Eastern Federal University) between 2015 and 2025. The dataset included 95 mix design protocols for heavy concretes, featuring concretes with compressive strengths ranging from 11 to 63 MPa, fresh concrete mixture densities from 2274 to 2534 kg/m³, and concrete slump values from 6 to 17 cm, corresponding to workability grades P2–P3 (Figure 1). According to the protocols, the concretes were produced using: sands with bulk density of 1211-1511 kg/m³, true density of 2600-2714 kg/m³ and fineness modulus of 1.14-1.34 (Figure 2); crushed stone with bulk density of 1366-1438 kg/m³, true density of 2600-2680 kg/m³ and fractional composition of 5-10, 5-20, 10-25 mm (Figure 3).

The heavy concrete mix design calculation is based on GOST 27006 and its methodological manual "Recommendations for mix design of heavy concrete and fine-grained concrete mixtures".

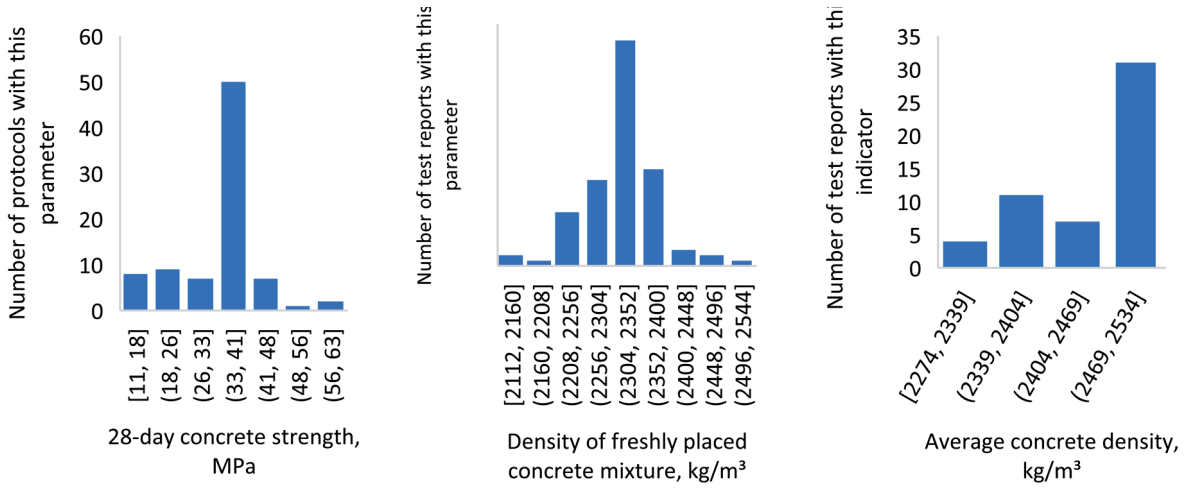

a) *b)* *c)*

Figure 1. Properties of heavy-weight concrete and concrete mixture in the studied test reports: (a) 28-day concrete strength, MPa; (b) density of freshly placed concrete mixture, kg/m³; (c) average concrete density, kg/m³

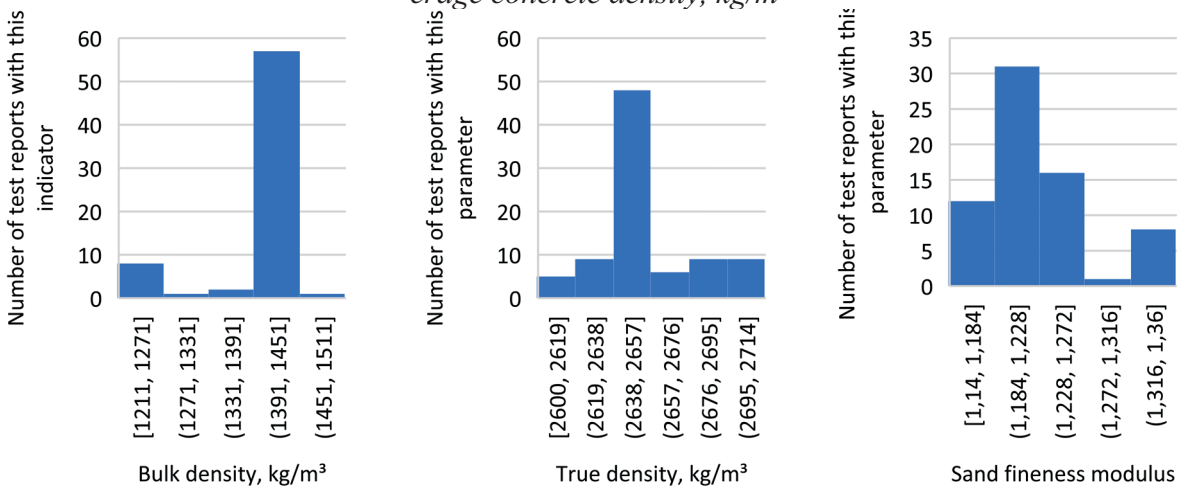

a) *b)* *c)*

Figure 2. Properties of fine aggregates in concrete mixes from the studied protocols: a – Bulk density, kg/m³; b – True density, kg/m³; c – Fineness modulus.

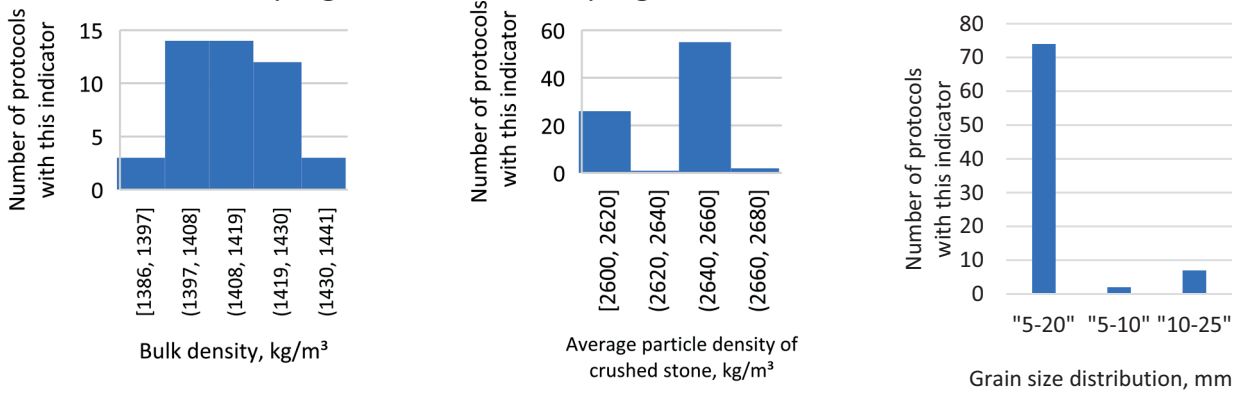

a) *b)* *c)*

Figure 3. Properties of coarse aggregates in the studied concrete mix protocols: a – Bulk density, kg/m³; b – Average particle density of crushed stone, kg/m³; c – Grain size distribution, mm

Equation (1) determines the cement-water ratio (C/W) that approximately provides the required average strength of concrete class at design age (28 days).

$$C/W = \frac{R_b^{28} - 0{,}06 \times R_c^{28} + 13}{0{,}24 \times R_c^{28} + 13}, \quad (1)$$

где C/W – the cement-water ratio providing the required concrete strength;
R_c^{28} – the cement strength (activity), taken equal to the cement class indicator upon its compliance after laboratory tests, MPa;
R_b^{28} – the required average strength of normally cured concrete class at 28 days age, MPa.
During mix design, the average class strength is set equal to the concrete strength at variation coefficient V_n = 13,5%. For this purpose, the specified concrete class is multiplied by the specified strength coefficient K_T equal to the specified variation coefficient (formula 2).

$$R_b^{28} = B \times K_T, \quad (2)$$

где B – strength value corresponding to the adopted concrete class, MPa
K_T – specified strength coefficient.
The water consumption (W) is determined based on the water demand of the concrete mixture, depending on the required workability and the type of plasticizing admixture.
With known water content (W) and cement-water ratio (C/W), the cement content (C) per 1 m³ of concrete can be calculated.

$$C = (C/W) \times W, \quad (3)$$

where C/W – cement-water ratio;
W – water content.
The absolute volume of aggregates, V_a (L), is then calculated using the formula:

$$V_a = 1000 - (W/\rho_w) - (C/\rho_c), \quad (4)$$

where p_c – true density of cement, kg/L;
p_w – density of water, taken as p_w = 1 kg/L.

The quantity of fine aggregate (S) in the absolute volume of aggregates is calculated by the formula:

$$S = V_a \times r_s \times \rho_s, \quad (5)$$

where S – sand content, kg/m³;
r_s – proportion of sand in the aggregate mixture;
ρ_s – true density of sand particles, kg/L.
The quantity of coarse aggregate is calculated by the formula:

$$CA = V_a \times (r_{CA}) \times \rho_{CA}, \quad (6)$$

Where CA – coarse aggregate content, kg/m³;
r_{CA} – proportion of sand in the aggregate mixture;
ρ_{CA} – average density of crushed stone particles, kg/L.
According to concrete mix design rules, after obtaining the nominal mix composition with specified properties, its average density is determined according to GOST 10181, and for each composition the actual material consumption per 1 m³ of concrete is calculated using the formula:

$$C,S,CA,W,Ad = \frac{\rho_{mix}}{\Sigma g} \times g_{c,s,ca,w,ad,} \quad (7)$$

Where C, S, G, W, and Ad – actual consumption of cement, fine aggregate, coarse aggregate, water, and admixture per 1 m³ of concrete, respectively, kg;
g_c, g_s, g_{ca}, g_w, g_{ad} – mass of cement, fine aggregate, coarse aggregate, water, and admixture in the batch, respectively, kg;
ρ_{mix} – density of the concrete mixture, kg/m³;
Σg – total mass of all materials in the batch, kg.
The objective of this study was to derive an experimental coefficient that would allow for closer alignment between the nominal mix proportions and the actual material consumption per 1 m³ of concrete. This approach enables more accurate prediction of the physical and mechanical properties of concrete in non-standard mix designs.
To establish the relationships, a period was selected in accordance with GOST 18105, which requires at least 30 values obtained over a period not exceeding three months. For the experimental

validation of the analytical results, the following raw materials were used:

For heavy-weight concrete, in accordance with GOST 26633, Portlandcement grade CEM I 42.5N was used. The cement was produced by JSC "Yakutcement" and complies with the requirements of GOST 31108-2016 (Table 1).

Fine aggregate: Natural river sand from the floodplain of the Lena River was used. The properties of the sand are presented in Table 2.

Coarse aggregate: Limestone crushed stone (fraction 5–20 mm) produced by LLC "Yakutcement" was employed. The characteristics of the coarse aggregate are provided in Table 3.

Testing of the obtained concrete mixtures and hardened concrete was conducted in accordance with the following standards:

- GOST 10181-2000 "Concrete mixtures. Test methods" (controlled characteristics of fresh concrete)
- GOST 10180-2012 "Concrete. Methods for strength determination using control specimens"
- GOST 12730.1-78 "Concrete. Method for density determination"

Table 1. Properties of Portland cement

№	Cement quality parameter	Unit	Value
1	Cement strength class	MPa	42,5
2	Standard consistency	%	26,5
3	Mass fraction of sulfur (VI) oxide (SO_3)	%	2,55
4	Mass fraction of chloride ions (Cl^-)	%	0,026
5	Initial setting time	min	135
6	Signs of false setting	–	нет

Table 2. Characteristics of river sand

№	Parameter name	Unit	Requirements according to GOST 8736-2014	Actual values
1	Bulk density	kg/m³	Not standardized	1444
2	Fineness modulus	M	Over 1.0 to 1.5 (for "very fine" group)	1,09
3	Content of dust and clay particles	%	Max. 5 (for Grade II sand)	0,25
4	True density	g/cm³	2,0-2,8	2,62
5	Organic impurities content	Reference color	Lighter than reference	Lighter
6	Void content	%	Not standardized	44,89

Table 3. Characteristics of limestone crushed stone

№	Parameter Name	Unit	Requirements per GOST 8269.0-97	Actual Values
1	Grain size distribution, full sieve residues: - 10 mm - 15 mm - 20 mm - 25 mm	%	 90-100 30-60 ≤10 ≤0.5	 99 68 5 0,4
2	Content of dust and clay particles (by mass)	%	≤2	1
3	Content of flaky and elongated grains (by mass)	%	Group 2 (>10 to 15)	13
4	Crushability grade Mass loss during dry testing	%	Grade M600 (>12 to 16)	14
5	Content of weak grains (by mass)	%	≤10	2

RESULTS AND DISCUSSION

According to the initial mix design requirements (Table 4), a theoretical calculation of the baseline composition of heavy concrete was performed following the existing method described above. The calculation was carried out considering a sand ratio (r) taken as 0.41, as recommended by the manual, and as 0.35, based on experience in designing concrete mixes using the available sand. Using the calculated compositions, concrete mixtures were produced, and their technological properties—workability and density—were determined (Table 5). Subsequently, for each composition, the actual material consumption per 1 m³ of concrete was calculated. After that, the concrete mixture was molded into 100×100×100 mm cubes, with 6 specimens per composition. Following hardening under normal conditions for 28 days, the concrete properties—average density and compressive strength—were determined.

Table 4. Mix design requirements for heavy concrete

Parameter	Specifications
Compressive strength class	B25
Workability grade	P3
Production conditions:	
- Molding	Vibration
- Curing	Normal curing (28 days)
Raw materials:	
Binder:	Portland cement
-Type/grade	CEM I 42.5N
Fine aggregate	River sand
-Fineness modulus (Mk)	1.09
-Bulk density, kg/m³	1444
-True density, g/cm³	2.65
Coarse aggregate	Crushed stone
-Fraction, mm	5–20
-Bulk density, kg/m³	1425
-True density, g/cm³	2.65

Table 5. Properties of concrete mixture and concrete depending on the composition

№		1		2		3	
C/W ratio		2,2		1,9		2,5	
Sand ratio (r)		0,41	0,35	0,41	0,35	0,41	0,35
Water (W)	Calculated	200	200	200	200	200	200
	Actual	206	210	205	204	205	207
Cement (C)	Calculated	440	440	380	380	500	500
	Actual	455	463	390	387	513	518
Sand (S)	Calculated	728	622	762	650	694	593
	Actual	750	654	800	662	711	614
Coarse aggregate (CA)	Calculated	1048	1154	1096	1208	999	1101
	Actual	1121	1214	1150	1229	1023	1140
Density of concrete mixture, kg/m³	Calculated	2416	2416	2438	2438	2394	2394
	Actual	2532	2541	2545	2482	2452	2479
Δ, %		4,6	4,9	4,2	1,8	2,4	3,4
Workability (slump, cm)		9	13	6	15	11	15
Density of concrete, kg/m³		2335	2432	2330	2357	2327	2385
Compressive strength, MPa		32	33,1	23	22,7	33	36,7

Based on the test results, concrete mixtures obtained from compositions with a sand ratio (r) of 0.41, as recommended by the manual, did not meet the workability requirements of the mix design requirements. Compositions 1 and 3 with a sand ratio (r) of 0.35 fully complied with the design requirements; however, a significant deviation between the calculated and actual concrete compositions was observed, ranging from 1.8% to 3.4%. With such a deviation, the actual cement consumption may be 18 kg higher per 1 m³ than the calculated value, which is a substantial discrepancy. Therefore, our next task was to derive an experimental coefficient from the existing database that would allow the nominal composition values to approximate the actual material consumption per 1 m³ of concrete.

To establish the relationships, a period was selected in accordance with GOST 18105, comprising 30 values obtained over a three-month period. In general, the analyzed database supports the theory of a positive effect of the water-to-cement (W/C) ratio (or its inverse, C/W) on the 28-day compressive strength of concrete (Figure 4). Notably, the analyzed concrete compositions show a higher sensitivity of strength to the C/W ratio (C/W range: 1.3 to 2.7) compared to the relationship presented in the reference guidelines (C/W range: 0.9 to 2.9). This may be attributed to the poor quality of sand used in the concretes [13].

Furthermore, the deterministic relationship between the density of freshly placed concrete mixture and hardened concrete density (Figure 5) raises questions. The lack of a stable correlation may be attributed to air-entraining and foam-suppressing admixtures, which cause instability in the early-stage concrete mixture density (first 15 minutes). Since concrete mixture density values are crucial parameters for calculating actual mix proportions, subsequent work employed the calculated fresh concrete density determined by formula (8), which depends on the average hardened concrete density:

$$\rho_{\text{mix}} = 1{,}01 \times \rho_b - 0{,}26 \times \text{C+W} \qquad (8)$$

Thus, more deterministic values of calculated fresh concrete density can be obtained from the recorded average hardened concrete density (Fig. 5).

The data show (Fig. 6) that the difference between the nominal composition and actual material consumption per 1 m³ in the analyzed protocols varies widely from -250 to 150 kg per 1 m³. This represents a significant error leading to material overconsumption and reduces the reliability of computational methods for obtaining concrete mix designs. Given the substantial discrepancy between nominal mix proportions and actual material consumption per 1 m³ of concrete, the critical task was to derive an experimental coefficient that would align these values and, consequently, enable more effective prediction of the physical-mechanical properties of concrete in non-standard mixes.

According to concrete theory, the water-cement ratio (W/C) and aggregate proportion are considered as the variable mix parameters that significantly influence concrete properties. However, there is a lack of research establishing the relationship between these parameters when determining concrete composition. We believe that establishing an empirical relationship between these parameters will allow more efficient calculation of concrete mix designs using the absolute volume method and reduce the error between nominal composition and actual material consumption per 1 m³.

To establish the actual proportions of sand and coarse aggregate in concrete compositions using derived equations (9) and (10) from formulas (5) and (6), we utilized the experimental data presented in Table 6.

$$r_S = \frac{S}{V_a \times \rho_S} \qquad (9)$$

$$r_{CA} = \frac{CA}{V_a \times \rho_{CA}} \qquad (10)$$

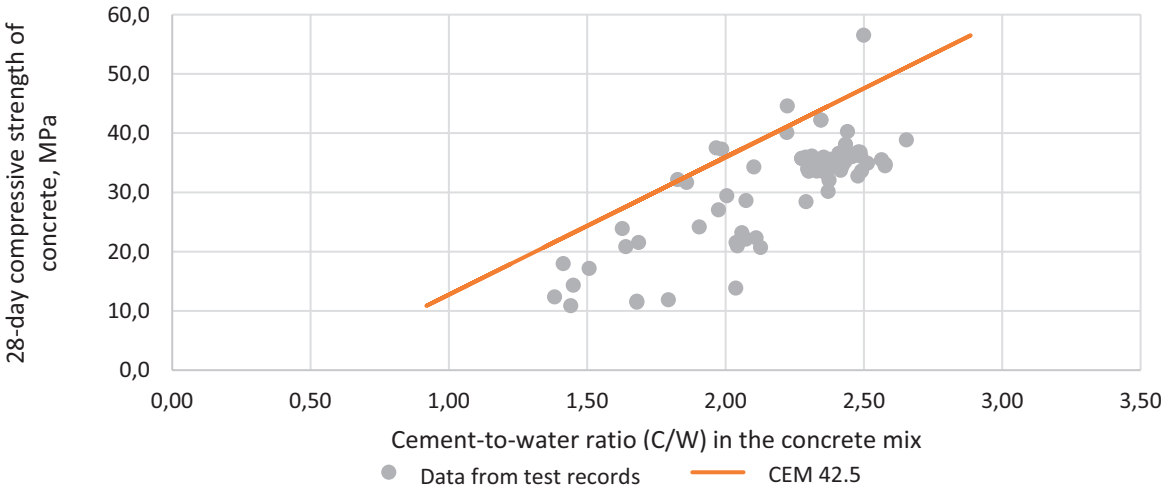

Figure 4. Effect of cement-water ratio (C/W) in concrete mix composition on 28-day compressive strength of concrete

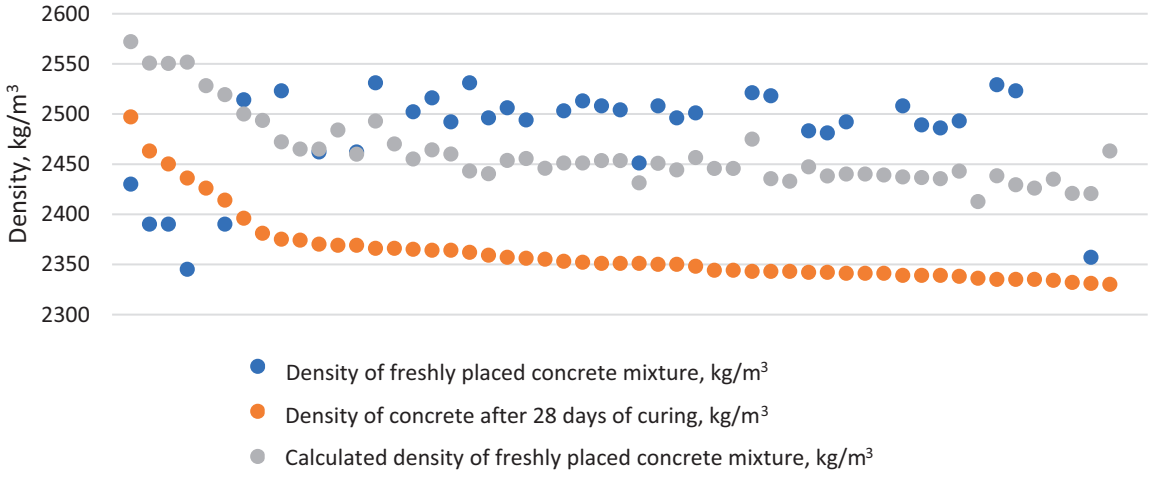

Figure 5. Correlation characteristics between average hardened concrete density and fresh concrete mixture density in the analyzed dataset

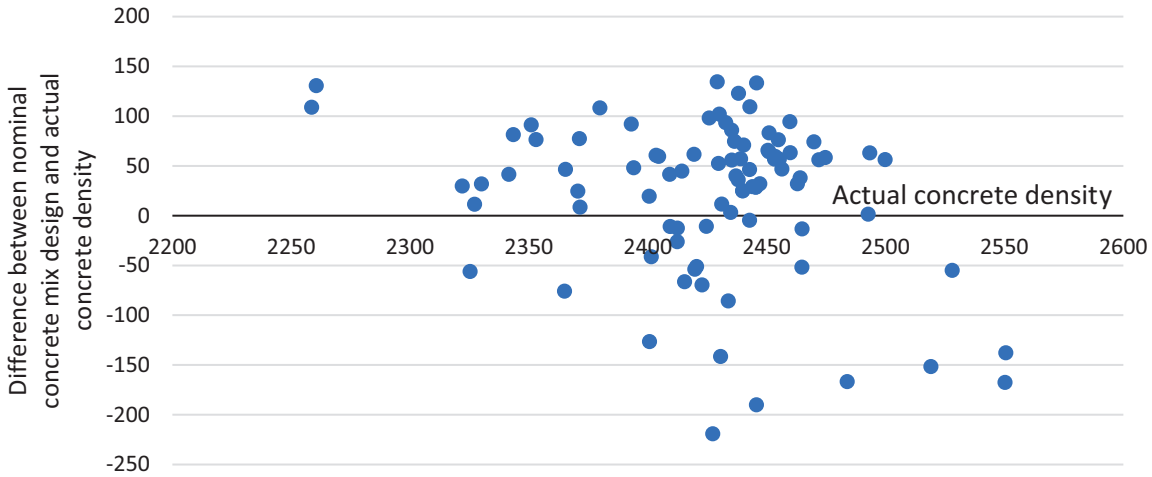

Figure 6. Discrepancy between nominal concrete mix design and actual material consumption per 1 m³ of concrete in the analyzed dataset

Table 6. Data used in calculations for determining aggregate proportions

№ mix	True density of sand, kg/m³	Bulk density of coarse aggregate, kg/m³	Mixture component mass, kg						Concrete density, kg/m³	28-day strength, MPa
			g_c	g_s	g_{ca}	g_w	g_{pl}	g_{ad}		
1	2640	2620	472	683	1186	203	-	-	2366	35,5
2	2650	2660	491	677	1186	185	3,4	9,8	2362	38,8
3	2650	2600	471	688	1172	190	2,8	-	2335	32,7
4	2700	2660	476	672	1183	197	-	-	2375	33,7
5	2620	2630	462	761	1138	200	-	-	2335	35,9
…	…	…	…	…	…	…	…	…	…	…
95	2680	2650	314	873	1020	182	-	-	2106	12,4

The analysis demonstrates that the total aggregate fraction does not consistently equal unity (Figure 7). Notably, a distinct correlation exists between the increased aggregate content and cement concentration in the mix. This relationship can be mathematically expressed by equation (11) and subsequently employed as a correction factor for mix design optimization.

$$K = (0{,}007 \times C + 0{,}731) \qquad (11)$$

A similar trend can be observed in external databases using coarser sands (fineness modulus of the fine aggregate greater than 1.4) (Figure 8) [19]. It is noticeable that the rate of increase in the aggregate fraction with higher cement content is greater when using fine sands.

The application of the derived coefficient to existing theoretical mix designs reduced the error range from -250 to 150 kg/m³ down to -60 to 150 kg/m³ (Fig. 9).

For practical validation, concrete compositions for class B25 were calculated according to the method using the obtained coefficient (Table 7).

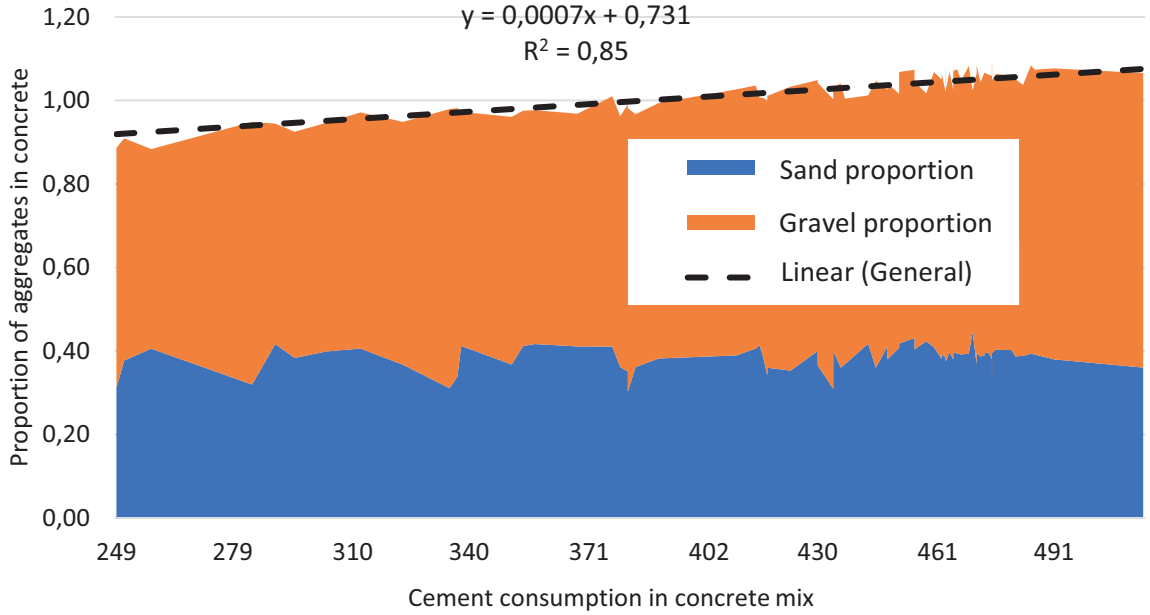

Figure 7. Aggregate content in concrete mixes as a function of cement dosage

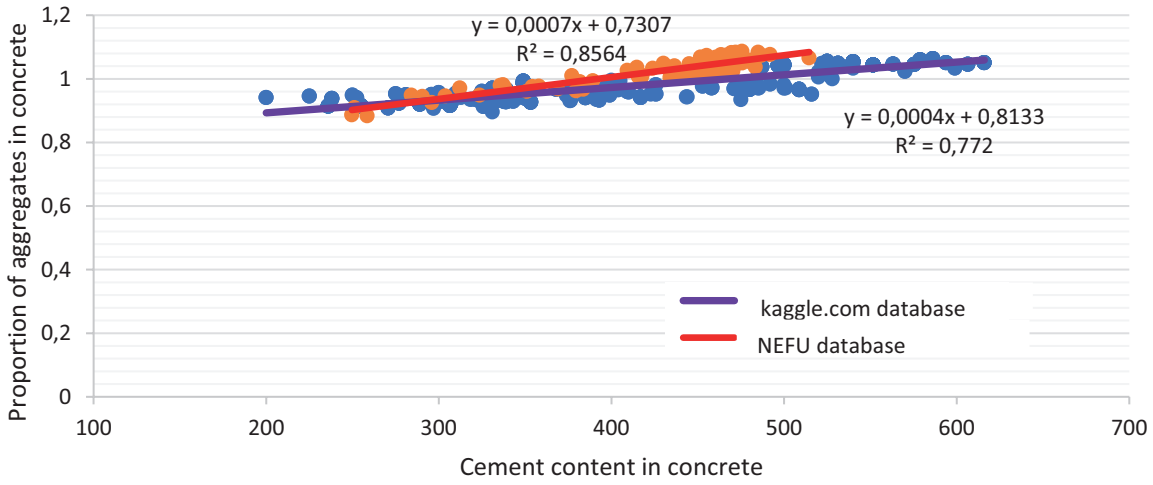

Figure 8. Proportion of aggregates in concrete compositions depending on cement content according to different databases

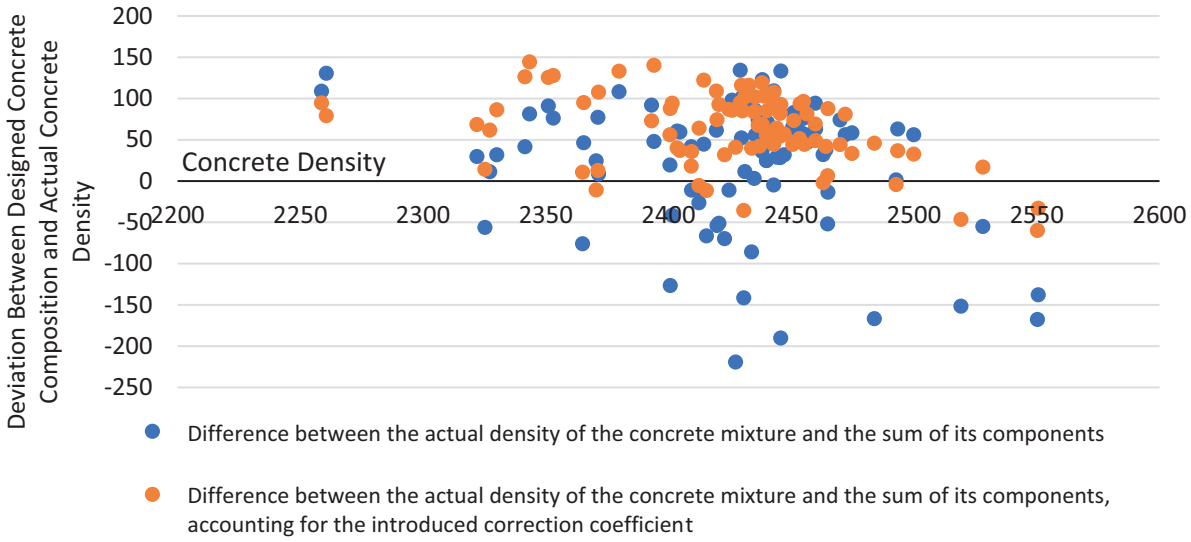

Figure 9. Deviation between designed concrete composition and measured concrete density

Table 7. Concrete properties depending on mix composition

#	C/W	Sand ratio (r)	Water (Calc/Act)	Cement (Calc/Act)	Sand (Calc/Act)	Coarse Agg. (Calc/Act)	Fresh Density, kg/m³ (Calc/Act)	Δ, %	Slump, cm	Hardened Density, kg/m³	Strength (28d), MPa
1	2.2	0.35	200 / 203	440 / 447	655 / 664	1154 / 1171	2449 / 2485	1.5	12	2432	33.1
2	1.9	0.35	200 / 203	380 / 386	659 / 670	1208 / 1229	2447 / 2488	1.7	14	2357	22.7
3	2.5	0.35	200 / 199	500 / 497	637 / 633	1101 / 1095	2438 / 2424	0.6	15	2385	36.7

According to GOST 27006-2019, the actual material consumptions of the concrete compositions were determined, and the average deviations between the calculated and actual component consumptions were obtained. Based on the obtained data, it can be seen that by applying the coefficient, better convergence between the actual and calculated compositions can be achieved. With-

out the coefficient, the range of deviations was from 1.8% to 4.9%; with the coefficient applied, the deviations ranged from -0.6% to 1.5%. Moreover, no deterioration occurs in the technological properties of the concrete mixture or the physical and mechanical characteristics.

CONCLUSION

This study aimed to improve the accuracy of nominal concrete mix design calculations using an experimental-analytical approach involving database analysis. The key findings are as follows:

1. The strength of concrete incorporating very fine sands (with a fineness modulus ≤1.4) shows relatively high sensitivity to variations in the C/W ratio within a narrow range of 1.3 to 2.7.
2. The discrepancy between the calculated density of concrete using very fine sands and its actual density varies significantly, ranging from -250 to 150 kg/m³. This substantial error leads to material overuse and reduces the reliability of computational mix design methods.
3. An empirical relationship has been established between the key variable mix parameters that significantly influence concrete properties - the water-cement ratio (W/C) and the proportion of aggregates in the concrete. This relationship is expressed as a formula that can serve as a correction coefficient when calculating sand and coarse aggregate quantities in concrete mixes. The data demonstrate that applying this coefficient yields better agreement between actual and calculated mix proportions. Without the correction coefficient, the discrepancy range was 1.8-5.0%, while with the coefficient it reduced to -0.6-1.5%, with no reduction in compressive strength observed.

The study thus demonstrates that concrete mix design efficiency can be improved and discrepancies between nominal compositions and actual material quantities per m³ reduced by establishing empirical relationships between key variable mix parameters. Future research should focus on developing numerical models to correlate concrete characteristics with the quantitative and qualitative composition of components, along with experimental validation, to establish a more reliable methodology for proportioning heavyweight concrete mixes when using aggregates of varying quality.

FUNDING

The work was realized within the framework of the implementation of the state task of the Ministry of Science and Higher Education of the Russian Federation No. FZWN-2023-0006.

REFERENCES

1. **Rezaev R.O., Dmitriev A.A., Borodulya N.A., Chernyavsky D.V.** (2021) Primenenie kompleksnogo podkhoda k optimizatsii proizvodstvennoi smesi na primere tovarnogo betona [Application of a complex approach to the optimization of industrial ready-mixes concrete]. *ALITinform: Cement. Concrete. Dry Mixes*, vol. 2, no. 63, pp. 42–55. (in Russian)
2. **Ly H.B., Nguyen T.A., Pham B.T.** (2022) Investigation on factors affecting early strength of high-performance concrete by Gaussian Process Regression. *PLoS ONE*, vol. 17, no. 1, pp. e0262930. DOI: 10.1371/journal.pone.0262930.
3. **Ly H.B., Le T.T., Vu H.L.T., Tran V.Q., Le L.M., Pham B.T.** (2020) Computational hybrid machine learning based prediction of shear capacity for steel fiber reinforced concrete beams. *Sustainability*, vol. 12, no. 7, pp. 2709. DOI: 10.3390/su12072709.
4. **Qi C., Ly H.B., Le M.L., Yang X., Guo L., Pham B.T.** (2021) Improved strength prediction of cemented paste backfill using a novel model based on adaptive neuro fuzzy inference system and artificial bee colony. *Construction and Building Materials*, vol. 284, pp. 122857. DOI: 10.1016/j.conbuildmat.2021.122857.

5. **Asteris P.G., Cavaleri L., Ly H.B., Pham B.T.** (2021) Surrogate models for the compressive strength mapping of cement mortar materials. *Soft Computing*, vol. 25, no. 8, pp. 6347–6372. DOI: 10.1007/s00500-021-05626-3.
6. **Sukhobokov A.A., Lakhvich D.S.** (2015) Vliyanie instrumentov Big Data na razvitie nauchnykh distsiplin, svyazannykh s modelirovaniem [The Big Data Tools Impact on Development of Simulation-Concerned Academic Disciplines]. *Science and Education: Scientific Edition of BMSTU*, vol. 3, pp. 207–240. DOI: 10.7463/0315.0761354. (in Russian)
7. **Hasanin T., Khoshgoftaar T.M., Leevy J.L., Seliya N.** (2019) Examining characteristics of predictive models with imbalanced big data. *Journal of Big Data*, vol. 6, no. 1, pp. 69. DOI: 10.1186/s40537-019-0231-2.
8. **Shushpanov A.N., Vasin A.Ya., Raikova V.M.** (2024) Raschet parametrov teplovogo vzryva naftokhinondiazidnykh fotorezistov na osnove eksperimental'nykh dannykh [Calculation of thermal explosion parameters of naphthoquinonediazide photoresists based on experimental data]. *Occupational Safety in Industry*, vol. 9, pp. 43–48. DOI: 10.24000/0409-2961-2024-9-43-48. (in Russian)
9. **Gramuzov E.M., Kalinina N.V., Blinov K.D., Kurkin A.A.** (2024) Ispol'zovanie energeticheskogo podkhoda dlya raschetnogo metoda ledovogo soprotivleniya s ispol'zovaniem dannykh model'nykh ispytanii v presnom l'du [The use of an energy approach for the calculation method of ice resistance using model test data in fresh ice]. *Marine Intellectual Technologies*, vol. 4, no. 3, pp. 34–44. (in Russian)
10. **Eshkulov M.U.** (2022) Mnogoparametricheskaya optimizatsiya algoritma obrabotki eksperimental'nykh dannykh transportnykh izmerenii [Multi-parametric optimization of experimental data processing algorithm for transport measurements]. Proceedings of the International Conference "Innovative Solutions to Technical, Engineering and Technological Problems of Production", Uzbekistan, October 2022, pp. 165–167. (in Russian)
11. **Zhukov A.D., Bobrova E.Y., Bessonov I.V., Medvedev A.A., Demissi B.A.** (2020) Application of statistical methods for solving problems of construction materials science. Nanotechnologies in Construction, vol. 12, no. 6, pp. 313–319. DOI: 10.15828/2075-8545-2020-12-6-313-319.
12. **Vasil'ev A.S., Nazarova V.P.** (2018) Informatsionnaya □aggle□ dlya podbora sostava tyazhyologo betona s protivomoroznymi dobavkami [Information system for designing heavy concrete mix with antifreeze admixtures]. Vestnik Priamurskogo Gosudarstvennogo Universiteta im. Sholom-Aleikhema, pp. 20–27. (in Russian)
13. **Singh S., Nagar R., Agrawal V.** (2016) A review on properties of sustainable concrete using granite dust as replacement for river sand. *Journal of Cleaner Production*, vol. 126, pp. 74–87. DOI: 10.1016/j.jclepro.2016.03.114.
14. **Burenina O.N., Andreeva A.V., Savvinova M.E.** (2022) Ispol'zovanie mestnogo mineral'nogo syr'ya Yakutii dlya izgotovleniya betonov povyshennoi prochnosti [Using local mineral raw materials of Yakutia for high-strength concrete production]. Vse Materialy. Encyclopedic Reference, no. 12, pp. 36–42. DOI: 10.31044/1994-6260-2022-0-12-36-42. (in Russian)
15. **Sidorova A.S., Antsupova S.G., Popov A.L.** (2020) Fiziko-mekhanicheskie kharakteristiki betona s ispol'zovaniem mestnogo vtorychnogo syr'ya [Physical and mechanical properties of concrete using local secondary raw materials]. Construction Materials, no. 9, pp. 9–14. DOI: 10.31659/0585-430X-2020-784-9-9-14. (in Russian)
16. **Popov A.L., Strokova V.V., Nelyubova V.V.** (2018) Osobennosti kompozitsionnogo vyazhushchego na kvarts-polevoshpatovom

peske [Features of composite binder based on quartz-feldspar sand]. Construction and industrial safety, vol. 12, no. 64, pp. 63–70. (in Russian)
17. **Sharma R., Jang J.G., Bansal P.P.** (2022) A comprehensive review on effects of mineral admixtures and fibers on engineering properties of ultra-high-performance concrete. Journal of Building Engineering, vol. 45, pp. 103314. DOI: 10.1016/j.jobe.2021.103314.
18. **Li Q., Ren Z., Su X., Feng Y., Xu T., Zheng Z., Li P.** (2024) Improving sulfate and chloride resistance in eco-friendly marine concrete: alkali-activated slag system with mineral admixtures. Construction and Building Materials, vol. 411, pp. 134333. DOI: 10.1016/j.conbuildmat.2023.134333.
19. **Jiang X., Xiao R., Bai Y., Huang B., Ma Y.** (2022) Influence of waste glass powder as a supplementary cementitious material (SCM) on physical and mechanical properties of cement paste under high temperatures. Journal of Cleaner Production, vol. 340, pp. 130778. DOI: 10.1016/j.jclepro.2022.130778.
20. Concrete Compressive Strength Data Set [Electronic resource]. Kaggle. Available at: https://www.kaggle.com/datasets/elikplim/concrete-compressive-strength-data-set (accessed 07 February 2026)

СПИСОК ЛИТЕРАТУРЫ

1. **Резаев Р.О., Дмитриев А.А., Бородуля Н.А., Чернявский Д.В.** Применение комплексного подхода к оптимизации производственных составов на примере товарного бетона // ALITinform: Цемент. Бетон. Сухие смеси. 2021. № 2(63). С. 42–55.
2. **Ly H.B., Nguyen T.A., Pham B.T.** Investigation on factors affecting early strength of high-performance concrete by Gaussian Process Regression // PLoS ONE. 2022. Vol. 17, No. 1. P. e0262930. DOI: 10.1371/journal.pone.0262930.
3. **Ly H.B., Le T.T., Vu H.L.T., Tran V.Q., Le L.M., Pham B.T.** Computational hybrid machine learning based prediction of shear capacity for steel fiber reinforced concrete beams // Sustainability. 2020. Vol. 12, No. 7. P. 2709. DOI: 10.3390/su12072709. EDN: KSYPDW.
4. **Qi C., Ly H.B., Le M.L., Yang X., Guo L., Pham B.T.** Improved strength prediction of cemented paste backfill using a novel model based on adaptive neuro fuzzy inference system and artificial bee colony // Construction and Building Materials. 2021. Vol. 284. P. 122857. DOI: 10.1016/j.conbuildmat.2021.122857.
5. **Asteris P.G., Cavaleri L., Ly H.B., Pham B.T.** Surrogate models for the compressive strength mapping of cement mortar materials // Soft Computing. 2021. Vol. 25, No. 8. P. 6347–6372. DOI: 10.1007/s00500-021-05626-3.
6. **Сухобоков А.А., Лахвич Д.С.** Влияние инструментария Big Data на развитие научных дисциплин, связанных с моделированием // Наука и образование: научное издание МГТУ им. Н.Э. Баумана. 2015. № 3. С. 207–240. DOI: 10.7463/0315.0761354.
7. **Hasanin T., Khoshgoftaar T.M., Leevy J.L., Seliya N.** Examining characteristics of predictive models with imbalanced big data // Journal of Big Data. 2019. Vol. 6, No. 1. P. 69. DOI: 10.1186/s40537-019-0231-2.
8. **Шушпанов А.Н., Васин А.Я., Райкова В.М.** Расчет параметров теплового взрыва нафтохинондиазидных фоторезистов на основе экспериментальных данных // Безопасность труда в промышленности. 2024. № 9. С. 43–48. DOI: 10.24000/0409-2961-2024-9-43-48.
9. **Грамузов Е.М., Калинина Н.В., Блинов К.Д., Куркин А.А**. Использование энергетического подхода для расчетного метода ледового сопротивления с использованием данных модельных испытаний в пресном льду // Морские интеллектуальные технологии. 2024. Т. 4, № 3. С. 34–44.

10. **Эшкулов М.У.** Многопараметрическая оптимизация алгоритма обработки экспериментальных данных транспортных измерений // Сборник трудов Международной конференции «Инновационные решения технических, инженерных и технологических задач производства». Узбекистан, октябрь 2022. С. 165–167.
11. **Жуков А.Д., Боброва Е.Ю., Бессонов И.В., Медведев А.А., Демисси Б.А.** Применение статистических методов для решения задач строительного материаловедения // Нанотехнологии в строительстве. 2020. Т. 12, № 6. С. 313–319. DOI: 10.15828/2075-8545-2020-12-6-313-319.
12. **Васильев А.С., Назарова В.П.** Информационная система для подбора состава тяжёлого бетона с противоморозными добавками // Вестник Приамурского государственного университета им. Шолом-Алейхема. 2018. С. 20–27.
13. **Singh S., Nagar R., Agrawal V.** A review on properties of sustainable concrete using granite dust as replacement for river sand // Journal of Cleaner Production. 2016. Vol. 126. P. 74–87. DOI: 10.1016/j.jclepro.2016.03.114.
14. **Буренина О.Н., Андреева А.В., Саввинова М.Е.** Использование местного минерального сырья Якутии для изготовления бетонов повышенной прочности // Все материалы. Энциклопедический справочник. 2022. № 12. С. 36–42. DOI: 10.31044/1994-6260-2022-0-12-36-42.
15. **Сидорова А.С., Анцупова С.Г., Попов А.Л.** Физико-механические характеристики тяжелого бетона с использованием местного вторичного сырья // Строительные материалы. 2020. № 9. С. 9–14. DOI: 10.31659/0585-430X-2020-784-9-9-14.
16. **Попов А.Л., Строкова В.В., Нелюбова В.В.** Особенности композиционного вяжущего на кварц-полевошпатовом песке // Строительство и техногенная безопасность. 2018. Т. 12, № 64. С. 63–70.
17. **Sharma R., Jang J.G., Bansal P.P.** A comprehensive review on effects of mineral admixtures and fibers on engineering properties of ultra-high-performance concrete // Journal of Building Engineering. 2022. Vol. 45. P. 103314. DOI: 10.1016/j.jobe.2021.103314.
18. **Li Q., Ren Z., Su X., Feng Y., Xu T., Zheng Z., Li P.** Improving sulfate and chloride resistance in eco-friendly marine concrete: alkali-activated slag system with mineral admixtures // Construction and Building Materials. 2024. Vol. 411. P. 134333. DOI: 10.1016/j.conbuildmat.2024.134333.
19. Jiang X., Xiao R., Bai Y., Huang B., Ma Y. Influence of waste glass powder as a supplementary cementitious material (SCM) on physical and mechanical properties of cement paste under high temperatures // Journal of Cleaner Production. 2022. Vol. 340. P. 130778. DOI: 10.1016/j.jclepro.2022.130778.
20. Concrete Compressive Strength Data Set [Электронный ресурс]. Kaggle. URL: https://www.kaggle.com/datasets/elikplim/concrete-compressive-strength-data-set (дата обращения: 07.02.2026).

Alexander L. Popov, Candidate of Technical Sciences, Head of the Department of Applied Mechanics and Construction Materials Science, Engineering and Technical Institute, North-Eastern Federal University named after M.K. Ammosov (NEFU), 58 Belinskogo St., Yakutsk, 677000, Russian Federation, ORCID: 0000-0002-7829-6839, Scopus ID: 57207737267, e-mail: surrukin@gmail.com

Попов Александр Леонидович, кандидат технических наук, заведующий кафедрой прикладной механики и строительного материаловедения, Инженерно-технический институт Северо-Восточного федерального университета имени М.К. Аммосова (СВФУ), Россия, г. Якутск, ул. Белинского, д. 58, ORCID: 0000-0002-7829-6839, Scopus ID: 57207737267, e-mail: surrukin@gmail.com

Dmitry F. Fedorov, PhD Student at the Department of Applied Mechanics and Construction Materials Science, Engineering and Technical Institute, North-Eastern Federal University named after M.K. Ammosov (NEFU), 58 Belinskogo St., Yakutsk, 677000, Russian Federation.

Gao Shuai, PhD Student at the Department of Applied Mechanics and Construction Materials Science, Engineering and Technical Institute, North-Eastern Federal University named after M.K. Ammosov (NEFU), 58 Belinskogo St., Yakutsk, 677000, Russian Federation.

Valeriya V. Strokova, Doctor of Technical Sciences, Head of the Department of Materials Science and Materials Technology, Institute of Civil Engineering, Belgorod State Technological University named after V.G. Shukhov (BSTU), 46 Kostyukova St., Belgorod, 308012, Russian Federation, ORCID: 0000-0001-6895-4511, Scopus ID: 6602722133, e-mail: vvstrokova@gmail.com

Федоров Дмитрий Фомич, аспирант кафедры прикладной механики и строительного материаловедения, Инженерно-технический институт Северо-Восточного федерального университета имени М.К. Аммосова (СВФУ), Россия, г. Якутск, ул. Белинского, д. 58.

Гао Шуай, аспирант кафедры прикладной механики и строительного материаловедения, Инженерно-технический институт Северо-Восточного федерального университета имени М.К. Аммосова (СВФУ), Россия, г. Якутск, ул. Белинского, д. 58.

Строкова Валерия Валерьевна, доктор технических наук, заведующая кафедрой материаловедения и технологии материалов, Инженерно-строительный институт Белгородского государственного технологического университета им. В.Г. Шухова (БГТУ), Россия, г. Белгород, ул. Костюкова, д. 46, ORCID: 0000-0001-6895-4511, Scopus ID: 6602722133, e-mail: vvstrokova@gmail.com

DOI:10.22337/2587-9618-2026-22-2-88-104

ANALYTICAL CALCULATION METHOD FOR REINFORCED CONCRETE COLUMNS UNDER LATERAL IMPACT

Anatoliy V. Alekseytsev, Valentina M. Tusnina

National Research Moscow State University of Civil Engineering, Moscow, RUSSIA

Abstract: This paper presents an analytical method for the calculation of compressed-bent reinforced concrete (RC) columns subjected to emergency transverse impact, characteristic of relevant anthropogenic hazards such as collisions with vehicles or other impacting objects. The proposed approach accounts for two primary failure mechanisms: flexural failure and diagonal shear failure, and enables the assessment of the ultimate horizontal load capacity, considering the dynamic strengthening of both concrete and reinforcement. The method is based on constructing ultimate capacity curves, which reflect the relationship between the maximum lateral force and the applied axial compressive force. It also introduces coefficients for the confinement of transverse deformations and parameters for the load intensity resisted by the transverse reinforcement. Particular attention is given to modeling the confinement effect on concrete, the influence of the pitch, diameter, and grade of the transverse reinforcement, and the potential for preventing progressive collapse. The proposed methodology serves as an effective tool for analyzing the robustness of buildings and structures under emergency mechanical impacts of anthropogenic origin. The developed approach can be applied in designing preventive measures to enhance column resistance against transverse impacts and contributes to the evaluation of the mechanical safety level of RC structures. This is especially important for columns with high slenderness and for elements with various types of initial or acquired damage.

Keywords: reinforced concrete columns, transverse impact, dynamic loading, shear failure, flexural failure, dynamic strengthening, confinement effect, structural safety, progressive collapse, robustness

АНАЛИТИЧЕСКИЙ МЕТОД РАСЧЕТА ЖЕЛЕЗОБЕТОННЫХ КОЛОНН НА ПОПЕРЕЧНЫЙ УДАР

А.В. Алексейцев, В.М. Туснина

Национальный исследовательский Московский государственный строительный университет, г. Москва, РОССИЯ

Аннотация: В статье представлен метод аналитического расчета сжато-изогнутых железобетонных колонн, подвергающихся аварийному поперечному удару, характерному для актуальных техногенных воздействий, таких как столкновение с транспортными средствами или другими ударяющими объектами. Предложенный подход учитывает два основных механизма разрушения: по нормальному и по наклонному сечению, и позволяет оценивать предельные значения горизонтальных сил с учетом динамического упрочнения бетона и арматуры. Метод опирается на построение кривых предельной несущей способности, отражающих зависимость максимальных усилий от действующей продольной сжимающей силы, а также вводит коэффициенты стеснения поперечных деформаций и параметры интенсивности нагрузки, воспринимаемой поперечной арматурой. Особое внимание уделено учету стеснения поперечных деформаций бетона, влияния на прочность шага, диаметра и класса поперечной арматуры, а также возможности предотвращения прогрессирующего разрушения конструкции. Предложенная методика служит эффективным инструментом для анализа живучести зданий и сооружений при аварийных механических воздействиях техногенного происхождения. Разработанный подход может быть применен при проектировании профилактических мер, повышающих устойчивость колонн к поперечным ударам, и способствует оценке степени механической безопасности железобетонных конструкций, что особенно важно для колонн большой гибкости и элементов с различными видами начальных или приобретенных повреждений.

Ключевые слова: железобетонные колонны, поперечный удар, динамическая нагрузка, разрушение при сдвиге, разрушение при изгибе, динамическое усиление, эффект ограничения, безопасность конструкции, прогрессирующее обрушение, прочность

1. INTRODUCTION

1. Theoretical research review. The problem of ensuring the bearing capacity of reinforced concrete columns under transverse impact loads is one of the key issues in the field of building and structure safety. Modern theoretical research is focused on developing models that enable the quantitative assessment of the dynamic strength and energy absorption capacity of structures under impulsive loads. The main trends in the theoretical analysis of strength are outlined in many studies. Let us consider some of them.

Article [1] presents a comprehensive analytical model for the dynamic response of axially loaded reinforced concrete columns subjected to transverse impact. The model accounts for the nonlinear interaction of inertial, elastic, and plastic components of the response, as well as the influence of the axial force on damage progression. The authors demonstrated that an increase in axial force accelerates damage accumulation and reduces the residual load-bearing capacity, which has direct implications for safety analysis under impact. In [2], an analytical approach was proposed to assess the response of both reinforced concrete and composite columns under lateral impact. The method is based on a simplified elastoplastic response theory and allows for differences in the energy absorption capacity of reinforced and composite elements. The work emphasizes that combining reinforcement with composite materials enhances not only impact resistance but also the column's ability to maintain its shape until failure, which is critical for preventing progressive collapse. The authors of [3] investigated resistance mechanisms and developed a methodology for analyzing the reliability of reinforced concrete columns under lateral impact. Their results showed that structural safety under such impacts depends on the interaction of flexural and shear failure mechanisms, as well as the nature of impact energy transmission through the reinforcement. The authors proposed introducing a dynamic stability coefficient to estimate the probability of exceeding ultimate deformations. Research [4] contributes to the field by assessing the residual strength of corrosion-damaged elements. Their models showed that the degradation of reinforcement and concrete properties significantly reduces the impact toughness and damping capacity of columns, which is particularly important when considering progressive collapse scenarios. Article [5] proposes a simplified method for predicting the degree of damage in circular reinforced concrete columns under axial load and lateral impact. The model is based on the principles of equivalent stiffness and plastic deformation energy, allowing for the estimation of the threshold between elastic and catastrophic response. A number of works address the influence of axial load on the nonlinear response of elements. For instance, [6] showed that an increase in compressive force intensifies local instability and leads to brittle failure modes. Similar results are presented in [7], which highlights the dependence of the failure mechanism on the impact type: bending deformations dominate under soft impact, whereas shear damage prevails under hard impact. Theoretical studies [8] extend strength analysis to elements damaged by corrosion and subjected to impulsive transverse loads. Similar works note that accounting for cross-section degradation and reduced bond between reinforcement and concrete leads to a significant reduction in the load-bearing capacity reserve, especially under short-term, high-intensity pulses. Work [9] demonstrates that bending deformations and stability loss depend not only on geometric parameters and reinforcement but also on boundary conditions, enabling the refinement of computational models for real-world operating conditions.

Thus, modern theoretical research is focused on refining physic-mechanical models of failure, introducing dynamic safety factors, and developing approximate methods for assessing the load-bearing capacity of reinforced concrete elements under short-term transverse impacts.

2. Experimental research. Experimental data play a key role in verifying theoretical models and ensuring the reliability of calculations for the design of impact-resistant structures. Systematic testing of columns under transverse impact is presented in works such as [10], which investigated the behavior of square columns under axial compression and low-velocity lateral impact. The authors identified characteristic response stages—from elastic bending to crack formation and diagonal shear failure. In [11], the authors conducted a series of experiments to determine the residual load-bearing capacity of circular columns after impact. The results confirmed that up to 70% of the initial bearing capacity can be preserved under moderate impact energies, which is highly significant for assessing building safety after partial damage. Article [12] investigated the influence of reinforcement percentage on column resistance to lateral impact. The experiments showed that increasing the reinforcement ratio enhances the ultimate energy absorption, but this effect saturates beyond a certain level. The authors of [13] compared the results of physical tests and numerical modeling, revealing a high correlation in deformation distribution and response velocities. Their subsequent work [14] enabled a detailed examination of the damage formation process under repeated impacts, which is particularly important for analyzing progressive collapse in emergency scenarios. Article [15] focused on columns with insufficient shear reinforcement. Their experiments revealed a sharp reduction in energy absorption capacity and strength when shear failure mechanisms prevailed. In [16], a study was conducted on the nonlinear response and shear behavior of columns under lateral impact. The experiments showed that the transition from a flexural to a shear mechanism is accompanied by localized concrete crushing and loss of section stability. Composite reinforcement is also actively investigated. The authors of [17] studied the use of GFRP bars in reinforced concrete columns under lateral impact. The experiments demonstrated improved energy absorption and failure resistance compared to traditional steel reinforcement. Researchers [18] showed that external strengthening with carbon fiber-reinforced polymer (CFRP) significantly enhances the ability of columns to resist static and impact lateral loads, preventing loss of bearing capacity and providing a structural damping effect. Experimental data on the dynamic response of reinforced concrete elements, obtained in [19], demonstrate similar patterns of impact energy redistribution and the role of reinforcement stiffness in preventing through-failure. Thus, experimental research confirms the significant influence of geometry, reinforcement, prestressing, defects, damage, and external strengthening on the ability of columns to withstand transverse impact loads.

3. Dynamics, Damping, and Protection Against Progressive Collapse. Dynamic aspects of reinforced concrete column behavior under impact loads are related to the processes of energy transfer and dissipation, which largely determine the likelihood of progressive collapse. The most important aspect here is the accounting for damping. The authors of [20] proposed a modified Rayleigh damping function for the numerical simulation of internal damping in frame structures. Subsequently, colleagues in [21] advanced this approach by proposing a non-stationary time-domain model of dynamic deformation that accounts for the material's delayed response. This allows for more accurate reproduction of oscillatory processes and critical states of reinforced concrete elements. The work of the authors [7] examines the dynamic behavior of columns under soft impacts and proposes criteria for damage assessment based on strain rate and residual stiffness. The authors emphasize that the structure's ability to dissipate energy through microcracking plays a key role in preventing progressive collapse. Research [15] showed that a lack of shear reinforcement sharply reduces the ability of columns to dampen impact energy, leading to rapid, cascading failure and loss of

load-bearing capacity in adjacent elements. These results are complemented by data from [16], which noted that proper design of transverse reinforcement can ensure a controlled plastic deformation mechanism, preventing instantaneous (brittle) failure.

Thus, modern approaches to ensuring dynamic stability rely on a combination of constructive measures, numerical modeling of damping, and analysis of nonlinear response, all aimed at preventing sequential (chain) failures. The conducted literature analysis demonstrates that research on the behavior of reinforced concrete columns under transverse impact is rapidly evolving towards the integration of theoretical, experimental, and computational approaches. Despite significant achievements, tasks related to the simple and rapid safety assessment of reinforced concrete elements, particularly columns, based on engineering methods remain unsolved. One such method is proposed in this article.

2. METHODS

2.1 Problem formulation. Let us consider a column made of heavy-weight concrete with steel reinforcement, subjected to a compressive axial force, where the influence of the bending moment is negligible. That is, the column can be conventionally considered as eccentrically compressed with a small eccentricity. As a result of an anthropogenic event, the column is subjected to an emergency impact. This impact could be initiated by a collision with a vehicle or another impacting body. For this scenario, the limit state condition of the first group will be as follows:

$$f(N(t),F_h(t)) \le f(N(t),\ Q(t),M(t))_{ult} \qquad (1)$$

where: $f()$ is load effect functional; $N(t),F_h(t)$ are longitudinal forces and transverse loads varying in time; $f()_{ult}$ is resistance functional of the column in the limit state; $N(t),Q(t),M(t)$ are ultimate longitudinal force, ultimate resultant transverse force, ultimate resultant (principal) moment that the reinforced concrete structure can withstand.

The dynamic loading process for analytical calculation can be represented by equations incorporating maximum static forces adjusted for dynamic effects and possible dynamic overloading:

$$\begin{cases} k_{d1}N_{\max} \le N_{cd,ult} \\ k_{d2}M_{\max} \le M_{cd,ult} \\ k_{d3}Q_{\max} \le Q_{cd,ult} \end{cases}, \qquad (2)$$

where $k_{d1}, k_{d2}\ k_{d3}$ – coefficients accounting for dynamic effects under emergency impact; $N_{\max}$, $Q_{\max}=\sqrt{Q_x^2+Q_y^2}$, $M_{\max}=\sqrt{M_x^2+M_y^2+M_z^2}$ are longitudinal force, principal transverse force, and principal moment induced by the combined (service and emergency) loads; $N_{cd,ult}$, $Q_{cd,ult}$, $M_{cd,ult}$ are corresponding internal forces resisted by the structural materials, considering dynamic strengthening.

Under the assumption that the force impact on the column does not cause extensive local damage leading to global failure (i.e., effects such as punching or scabbing are absent, which may occur at relatively low impact velocities during the contact between the impactor and the column), failure is expected to occur either in the normal section (Fig. 1a) or in the inclined section (Fig. 1b).

It is assumed that the ultimate values of the horizontal load nonlinearly depend on the magnitude of the compressive axial force for both flexural failure and shear failure mechanisms. This relationship is described by the ultimate load capacity curve (Fig. 1c), which demonstrates that under the same service compressive force N_e, the maximum loads preceding flexural failure $F_{1,ult}$ and shear failure $F_{2,ult}$ differ. If a given load combination F_h lies below these curves, the column maintains its load-bearing capacity under the actual force N_e.

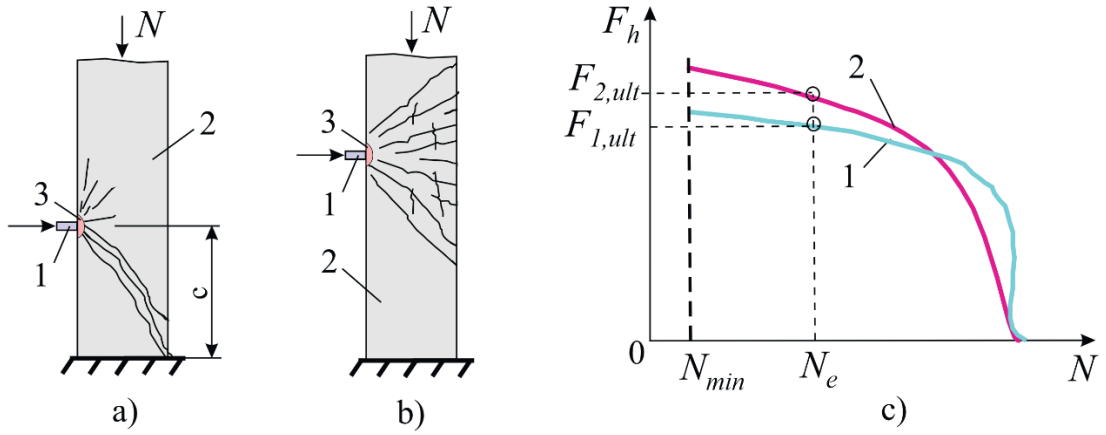

Figure 1. Problem formulation: failure schemes under horizontal impact - diagonal shear failure (a); flexural failure (b); 1 - impactor, 2 - reinforced concrete column, 3 - concrete crushing zone; ultimate capacity curves (c); 1 - moment failure, 2 - shear failure

2.2 Calculation Methodology for Normal Sections

For the analytical substantiation of the column's strength with respect to the inclined section, the general strength condition and the specific inequality derived from it are used:

$$F_h(N_e,t) \in \Omega \le F_h(N_e)_{ult} \in L_{BC} \rightarrow \\ \rightarrow \left(F_{h,\max} \le F_{h,ult}\right)\Big|_{N=N_e}, \quad (3)$$

where $F_h(N_e,t)$ – horizontal force from emergency impact at the actual value of N_e at time t; Ω – range of permissible emergency load values; $F_h(N_e)_{ult}$ – ultimate horizontal force resisted by the reinforced concrete column in the critical normal section, considering dynamic strengthening of materials under the condition $N = N_e$; L_{BC} – curve of the ultimate values of this force.

Thus, to assess the section strength, it is necessary to construct the ultimate load capacity curve. Let us define this curve by characteristic points *A, Bi, C*. We assume that point *A* is located at the conditional intersection of curve 1 with the Q-axis (Fig. 1c). Suppose the longitudinal force in the column cannot be zero, and its value is N_{min} (e.g., the self-weight of the column). At this point, the horizontal impact is maximal. Point *C* is located at the intersection with the *N*-axis. Here, the horizontal impact is minimal under the maximum compressive longitudinal force. Points B_i, $i=1..n$ are intermediate and describe the shape of the curve. Let us consider the construction of this curve.

Point A, $F_h = 0,:$

$$k_{d1}N_A(\lambda) = \begin{cases} \pi^2 E_b I_{red} / l_0^2, \lambda > 50; \\ \varphi\left[R_b A_b + R_{sc} A_{s,tot}\right], \lambda \le 50 \end{cases}, \quad (4)$$

Here: $l_0 = \mu l$ – design length, accounting for the variation in the geometric length l of the column depending on its support conditions (considered through the coefficient μ); $R_{sc}, A_{s,tot}, R_b, A_b$ – design strengths and cross-sectional areas of reinforcement and concrete, respectively; φ – coefficient determined according to SP 63.13330 for the case of small eccentricities of the compressive force; λ – slenderness of the column.

Condition (4) specifies that slender columns lose their load-bearing capacity due to Euler buckling instability, while conventionally designed columns are primarily governed by material strength. Calculations have shown that for columns with $\lambda \le 50$ and under transverse impact, $k_{d1} \rightarrow 1$.

Points $B_1 - B_n$. After calculating the ultimate value $N_A = N_{ult}$ using (4), values $N_{e,i}$ are assigned, for which the ultimate values $P_{i,ult} \in L_{BC}$ are computed. For each value $N_{e,i}$, the depth of the concrete compression zone x in the critical section is calculated, and equilibrium equations are formulated considering a unit horizontal load. Subsequently, its ultimate value is determined. This can be expressed as:

$$\begin{aligned} x &= x_m + \frac{I_{red} N_{e,i}}{A_{red} M}, \\ x_m &= \sqrt{\alpha_s^2 (\mu_s + \mu_s')^2 + 2\alpha_s (\mu_s + \mu_s' a'/h_0)} - \\ &- \alpha_s (\mu_s + \mu_s'). \end{aligned} \quad (5)$$

$$\alpha_s = \frac{0.0015 E_s}{R_{b,ser}}, \mu_s = \frac{A_s}{bh_0}, \mu_s' = \frac{A_s'}{bh_0},$$

$$M = M_f + M_e.\ A_{red} = bh + \frac{E_s}{E_b}\left(A_s + A_s'\right);$$

Here: M_f – bending moment from service loads; M_e – moment caused by the longitudinal force due to accidental eccentricity. Other designations of calculated parameters are generally accepted and provided in SP 63.13330. The equilibrium equation under a unit horizontal load for a rectangular column section is as follows:

$$\begin{aligned} &M_{\max,i} + N_{e,i} e_f = k_1 R_b \cdot b \cdot h_0^2 \cdot \alpha_R + \\ &+ k_2 R_{sc} \cdot A_s' \cdot \left(h_0 - a\right) \\ &M_{\max} = \max\left\{\left(M_f + M(\bar{F}_h) + M_e\right)\right\} \\ &e_f = \frac{1}{1 - N_{e,i}/N_A\big|_{\lambda>50}}\left(f + \frac{h_0 - a'}{2}\right). \end{aligned} \quad (6)$$

Where k_1, k_2 are the dynamic strengthening coefficients of concrete and reinforcement, respectively; $M(\bar{F}_h)$ is the moment from the horizontal load $\bar{F}_h = 1$, e_f is the eccentricity of the force $N_{e,i}$ considering the deflection f, induced by the force $\bar{F}_h$.

The deflection f is determined considering the curvature $1/r$ of the element and its stiffness. The stiffness for a rectangular cross-section element is calculated using the known formula:

$$D = \frac{0.15 E_b I_b}{\varphi_l (0,3 + \delta_e)} + 0.7 E_s I_s \quad (7)$$

where: E_b, I_b – initial modulus of elasticity and moment of inertia of concrete; φ_l – coefficient accounting for the duration of load action, taken as 1 for this design case; δ_e – relative eccentricity, taken as 0.15 for the case of small eccentricities; E_s, I_s – modulus of elasticity and moment of inertia of reinforcement.

The deflection of the column when divided into m sections of equal length Δl is then

$$\begin{aligned} f &= \sum_{j=1}^{m} \int_0^{\Delta l} M(\bar{F}_h)_j \left(\frac{1}{r}\right)_j dz = \\ &= \frac{1}{D} \sum_{j=1}^{m} \int_0^{\Delta l} M(\bar{F}_h)_j \times M(\bar{F}_h)_j dz \end{aligned} \quad (8)$$

where D is the element stiffness, and the product of the sub integral functions can be evaluated using Simpson's formula. Solving equations (6) yields the value $k_{d2} P_{i,ult}$.

Point C. The value P_{ult} is determined from the condition:

$$k_{d2} M_{\max}(P_{ult}) \le M_{ult} \quad (9)$$

where $M_{\max}(P_{ult})$ is the maximum bending moment in the section from the vertical force, M_{ult} is the ultimate moment resisted by the reinforced concrete section under bending. For a rectangular section, it is determined conventionally:

$$M_{ult} = k_1 R_b \cdot b \cdot h_0^2 \cdot \alpha_R + \\ + k_2 R_{sc} \cdot A_s' \cdot (h_0 - a). \quad (10)$$

Dynamic loads can have various pulse shapes (Fig. 2), while equations (6) and (9) allow determining the dynamic equivalents of

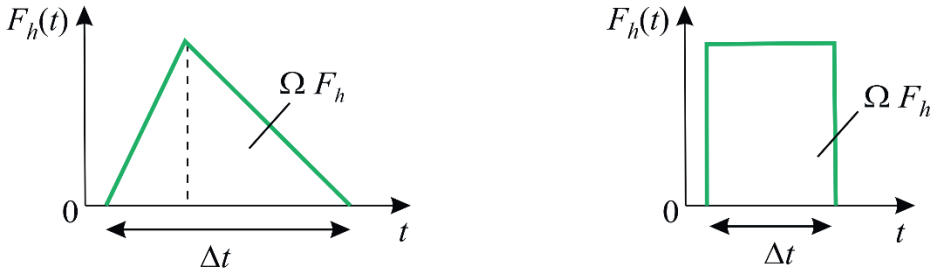

Figure 2. Pulse shapes under dynamic loading: triangular (a), rectangular (b)

the loads without considering their duration. To compare the values of loads specified as impulses with those obtained from the mentioned equations, the following formula can be used:

$$P = \Omega F_t / \Delta t, \quad (11)$$

where ΩF_t is the area under the pulse, Δt is the actual impact duration on the structure.

2.3 Calculation Method for Inclined Sections. Under dynamic impact on a column, particularly in the presence of rigid restraints at the supports, the strength of the inclined section may be exhausted either by the action of the transverse force or by the bending moment. The curve L_{BC} is constructed without specific characteristics for different values of $N_{e,i}$, following the methodology below. To assess the strength of the inclined section, the system of inequalities is written as:

$$\begin{cases} \left(\dfrac{\Delta Q_d}{k_N^d Q_d^{ult}} \pm \dfrac{Q_{st}}{Q_{bN} + Q_{swN}} \right) \le 1 \\ M_{\max} \le M_b + M_{sw} + M_{s,inc} \end{cases}, \quad (12)$$

where the first equation is necessary to determine the value of F_h based on the dynamic increment of transverse force ΔQ_d, while the second serves a verification function. Here, in the first equation, k_N^d is a coefficient accounting for the level of compressive force, confinement of transverse deformations, and the kinematic constraints of the column. The quantities $Q_d^{ult}, Q_{st}, Q_{bN}, Q_{swN}$ are represent the transverse forces resisted by the section under dynamic loading, static service loading, concrete under service loads, and reinforcement under service loads, respectively. In the second equation, $M_b, M_{sw}, M_{s,inc}$ denote the bending moments resisted by concrete, longitudinal reinforcement, transverse reinforcement, and inclined bars (bent-up bars), respectively.

The ratio k_N^d:

$$k_N^d = \begin{cases} \dfrac{1}{\sqrt{1,5-\mu}} \left(k_e + \left(\dfrac{N_e}{N_{ult}} \sqrt{\dfrac{P_{Ne}^{ult}}{P_{ult}}} \right) \right)^{-1}, \\ for \ \dfrac{N_e}{N_{ult}} < 0.6, \\ \left(\dfrac{P_{Ne}^{ult}}{P_{ult}} + k_e \right)^{-1}, for \ \dfrac{N_e}{N_{ult}} \ge 0.6, \end{cases}, \quad (13)$$

where P_{Ne}^{ult} is the value of transverse impact load initiating flexural failure under force $N_e \neq 0$, P_{ult} is the same under force $N_e = 0$.

The value of N_{ult} is determined using the second equation of system (4); k_e is the coefficient of transverse deformation confinement.
For a square section, it can be determined using Fig. 3 and the dependency provided below.

$$k_e = \frac{1}{1-\mu_{sc}}\left(1-\frac{S_w - d_w}{2d}\right)^2, \qquad (14)$$

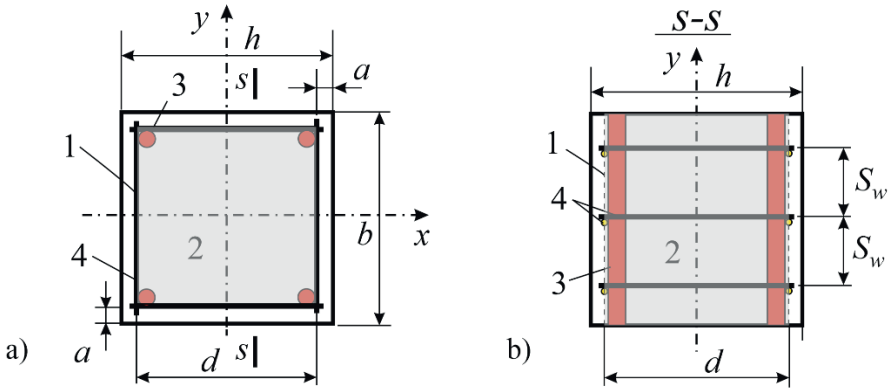

Figure 3. Determination of the deformation confinement level: column cross-section (a); section s-s (b); 1 – boundary of the deformation confinement zone, 2 – core of the deformation confinement zone, 3 – longitudinal reinforcement, 4 – transverse reinforcement

where μ_{sc}, d_w are the reinforcement percentage considering core area 2 and the area of longitudinal reinforcement only, and the diameter of the transverse reinforcement bar; d is the length of the transverse bar in the impact plane, as shown in Fig. 3.
When the projection length of the inclined section onto the vertical axis does not exceed twice the effective depth of the section, the following formula is proposed for Q_d^{ult} :

$$Q_d^{ult} = \sqrt{3k_1 R_{bt}(1+k_e)^{\left(1+\sqrt{N_e/N_{ult}}\right)} bh_0^2 q_{sw}^d}, \qquad (15)$$

where R_{bt} – design tensile strength of concrete, b, h_0 – width and effective height of the section, q_{sw}^d – distributed per length load resisted by transverse reinforcement under impact, within the vertical projection of the inclined section. It is defined as:

$$q_{sw}^d = k_2 \frac{R_{sw}A_{sw}}{S_w}\left(1-\left(0.2+k_e\right)\frac{N_e}{N_{ult}}\right), \qquad (16)$$

The value of Q_{bN} in formula (12):

$$\begin{aligned} &Q_{bN} = 1.5\varphi_n R_{bt} bh_0^2 / c, \\ &0.5\varphi_n R_{bt} bh_0 \le Q_{bN} \le 2.5 R_{bt} bh_0 \end{aligned}, \qquad (17)$$

where c – projection of the inclined section onto the vertical axis, c is calculated as:

$$c = \sqrt{\frac{1.5\varphi_n R_{bt} bh_0^2}{0,75 q_{sw}^c}}, c \le 2h_0,$$

$$\varphi_n = \begin{cases} 1,25, & 0.25R_b \le \sigma_b < 0.5R_b \\ 2.5-\left(1-\dfrac{\sigma_b}{R_b}\right), & 0.5R_b \le \sigma_b \le R_b \end{cases}, \qquad (18)$$

$$\sigma_b = \frac{N_e}{A_b + \dfrac{\alpha E_b \varepsilon_{b0}}{R_b} A_{sc}}.$$

All notations in the formula are standard and provided in SP 63.13330, the value of q_{sw}^{c} is determined by (16), assuming that $k_2 = 1$.

3. RESULTS

3.1. Comparison with Experiment. Calculation for Normal Section. To verify the proposed method, we use the experimental results from [10], shown in Fig. 4. For the calculation, in accordance with recommendations from various studies, including [8], we adopt the following dynamic strengthening coefficients for materials: k_1=1,15, k_2=1,2, $k_{d2} = 1.5$ The load is considered as suddenly applied with a rectangular pulse shape. The distance between the supports is 1.38 m, $\alpha = E_s / E_b = 6.66$ .The equilibrium equation (10) applied to this experimental task is

$$M_{\max} + Ne_f = k_1 R_b \cdot b \cdot h_0^2 \cdot \alpha_R + \\ + k_2 R_{sc} \cdot A_s' \cdot (h_0 - a'),$$

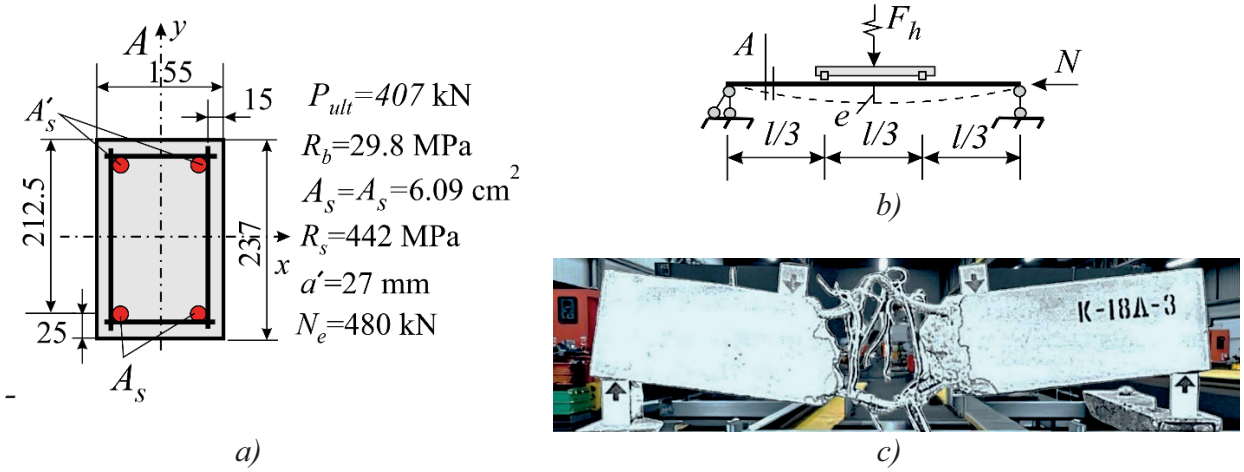

Figure 4. Experimental data for verification of the calculation methodology: material and load characteristics, cross-section in the experiment (a), design model (b), the crushed specimen (c)

The boundary values of the relative height of the concrete compression zone under bending are calculated as

$\xi_R = 0,8 / (1 + (442 / 2 \cdot 10^5) / 0,0035) = 0,49$,

$\alpha_R = 0,49(1 - 0,49 / 2) = 0,37$. The bending moment is $M_{\max} = F_h 1,38 / 6 = 0,23 F_h$ (kHm). The eccentricity e_f is calculated using (6). For this, the moment of inertia and Euler force are determined:

$$I_{red} = 23.7^3 \cdot 15.5 / 12 + 6.66 \cdot 2 \cdot 6.09 \cdot (18.5 / 2)^2 = \\ = 24134 \ cm^4.$$

$$N_A = \pi^2 3 \cdot 10^7 \cdot 24134 \cdot 10^{-8} / 1.38^2 = 37520 \ kN.$$

The system deflection is determined using Mohr integrals:

$$f = 207 F_h l^3 / 11164 E_{red} I_{red} = F_h \cdot 207 \cdot 1,38^3 10^6 / \\ / 11164 \cdot (48 \cdot 0.85 \cdot 3000 \times 24134) = F_h \cdot 0.01774 \ cm.$$

$$e_f = 1 / (1 - 480 / 37520)(F_h \cdot 0.01774 + 18,5 / 2) = \\ = 9,361 + 0,0181 F_h.$$

Substituting all values into equation (10), we have 31.68 F_h=8489+5975-4493, $F_h = 314$ kN, $P = F_h \cdot 1,5 = 314 \cdot 1,5 = 471$ кN. The theoretical result satisfactorily corresponds to the experimental one. The error is less than 15.7%.

3.2. Example of Column Calculation for Inclined Section. Let a column (Fig. 5, a) be subjected to an emergency impact load *P*. The structure is made of concrete with compressive strength class B25 ($R_b = 11,5 MPa$, $R_{bt} = 0,9 MPa$), reinforcement A500 $R_s = 435 MPa$ $R_{sw} = 300 MPa$, with dynamic strengthening coefficients as in Section 3.1: k_1=1,1, k_2=1,2, and coefficient $\mu = 0,7$. The longitudinal reinforcement area is 4⌀28 $A_{sc0}^{4d28} = 24,63\ cm^2$, and the transverse reinforcement consists of 4⌀8 bars forming a closed contour, spaced at 250 mm along the height $A_{sw}^{d8} = 0,503\ cm^2$. The load is $N_e = 2000\ \kappa N$, and the transverse force (under conditionally centered loading of the middle column) is $Q_{st} = 0\ \kappa N$. It is necessary to evaluate the maximum bearing capacity of the column under horizontal impact.The given load arrangement suggests that the most probable failure mechanism will be the loss of strength of the inclined section (Fig. 5, c). Taking this and the above loading into account, we write (12) in the form $\Delta Q_d \le k_N^d Q_d^{ult}$.

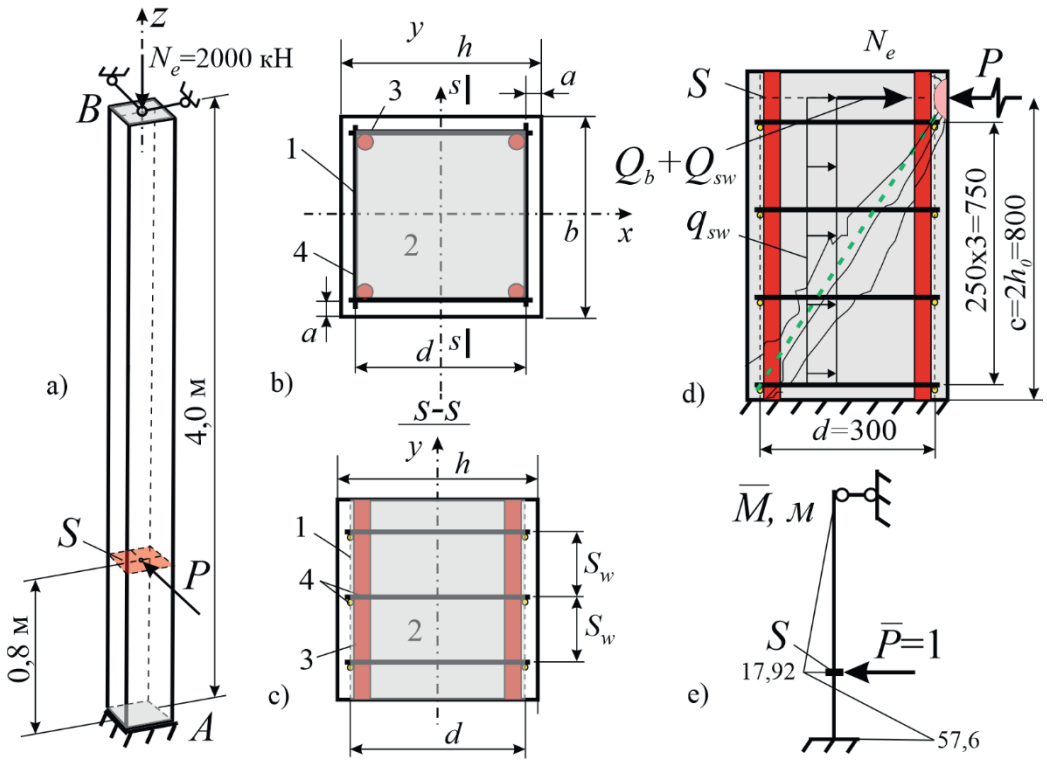

Figure 5. Reinforced concrete column with calculation parameters: design model (a), cross-section S (b); 1 - contour of the deformation confinement zone, 2 - core of this zone, 3 - longitudinal reinforcement, 4 - transverse reinforcement; cross-section s-s (c), inclined section (shear) failure scheme (d), bending moment diagram caused by unit impact (e)

It is calculated: $\mu_{sc} = 24,63 / 30 \cdot 30 = 2,73\%$, *d*=30 cm - the dimension of the deformation confinement zone (Fig. 5, b, c).
It is solved (14):

$$k_e = \frac{1}{1-\mu_{sc}}\left(1-\frac{S_w - d_w}{2d}\right)^2 = \frac{1}{1-0.0273}\left(1-\frac{25-2.8}{2\cdot 30}\right)^2 = 0,408,$$

$$N_{ult} = \varphi(R_b A_b + R_{sc} A_{sc0}) =$$
$$= 0.9(1.15 \cdot 40 \cdot 40 + 43.5 \cdot 24.64) = 2620\ kN$$

The ratio $N_e / N_{ult} = 2000 / 2620 = 0,763 \geq 0,6$, therefore in formula (13) using the last equality. Next, it is determined the ultimate horizontal forces for flexural failure at forces $N_e = 0\ kN$, $N_e = 2000\ kN$. For the bottom support fixation, the equation (12) is:

$$M_{\max} + N_e e_f = k_1 R_b \cdot b \cdot h_0^2 \cdot \alpha_R + k_2 R_{sc} \cdot A_{sc}^{2d28} \times$$
$$\times \left(h_0 - a\ \right).$$

The maximum moment is determined from Fig. 5, e, with the value $e_f = \left((35-5)/2\right) = 15$ cm. The value α_R, ensuring the absence of brittle failure, is determined in the conventional way:

$$\xi_R = 0,8 / (1 + (435 / 2 \cdot 10^5) / 0,0035) = 0,493,$$
$$\alpha_R = 0,493(1 - 0,493 / 2) = 0,37.$$

Solving equation (12), it is obtained:

$$0,144 \cdot 400 P_{Ne}^{ult} + 2000 \cdot 15 = 1,1 \cdot 1,15 \cdot 40 \cdot 35^2 \times$$
$$\times 0,37 + 1,2 \cdot 43,5 \cdot 12,32 \cdot \left(35 - 5\right) \rightarrow$$
$$\rightarrow P_{Ne}^{ult} = 212,74 \text{ kN}.$$

When solving the same equation for $N_e = 0 \rightarrow P_{ult} = 733,1$ kN, next, $k_N^d = \left(0,403 + 212,74 / 733,1\right)^{-1} = 1,4427$ Thus, it is determined the value q_{sw}^d, considering the impact resistance provided by the 2d8 lateral rebars (5):

$$q_{sw}^d = 1,2 \cdot \frac{30 \cdot 1,01}{25}\left(1 - \left(0,2 + 0,403\right)\left(\frac{2000}{2620}\right)\right) =$$
$$1,4544\left(1 - 0,422\right) = 0,78493\ kN / cm.$$

The constructive requirement is checked: $q_{sw}^d \geq q_{sw,\min}$. For this, it is calculated the elasticity coefficient:

$$\nu_b = R_b / E_{b0}\varepsilon_b = 11,5 / \left(27,5 \cdot 0,002 \cdot 10^3\right) = 0,209$$

Normal stresses

$$\sigma = N / A_{red} = 2000 / (40 \cdot 40 + 0,209^{-1} \times$$
$$\times (2 / 2,75) \cdot 10 \cdot 24,64) = 1,017\ kPa;$$
$$\varphi_n = 2,5\left(1 - \frac{\sigma}{R_в}\right) = 2,5\left(1 - \frac{1,017}{1,15}\right) = 0,289;$$
$$q_{sw}^d \geq q_{sw,\min} = 0,25\varphi_n R_{bt} b =$$
$$0,25 \cdot 0,289 \cdot 0,09 \cdot 40 = 0,2601.$$

The condition is satisfied. The ultimate value of the dynamic transverse force using expression is (4):

$$Q_d^{ult} = \sqrt{3 \cdot 1,1 \cdot 0,09 \cdot \left(1 + 0,403\right)^{\left(1+\sqrt{2/2,62}\right)} \times} =$$
$$\times 40 \cdot 35^2 \cdot 0,7849$$
$$= 146,8\ kN.$$

The value

$$\Delta Q_d = Q_d^{ult} \cdot k_N^d = 146,8 \cdot 1,4427 = 211,8 \text{ kN}.$$

This value of the horizontal dynamic force is the ultimate at $N_e = 2000\ кН$.

3.3 Numerical Verification of Calculation Results. Let us perform a calculation of a solid finite element model, Fig. 6.

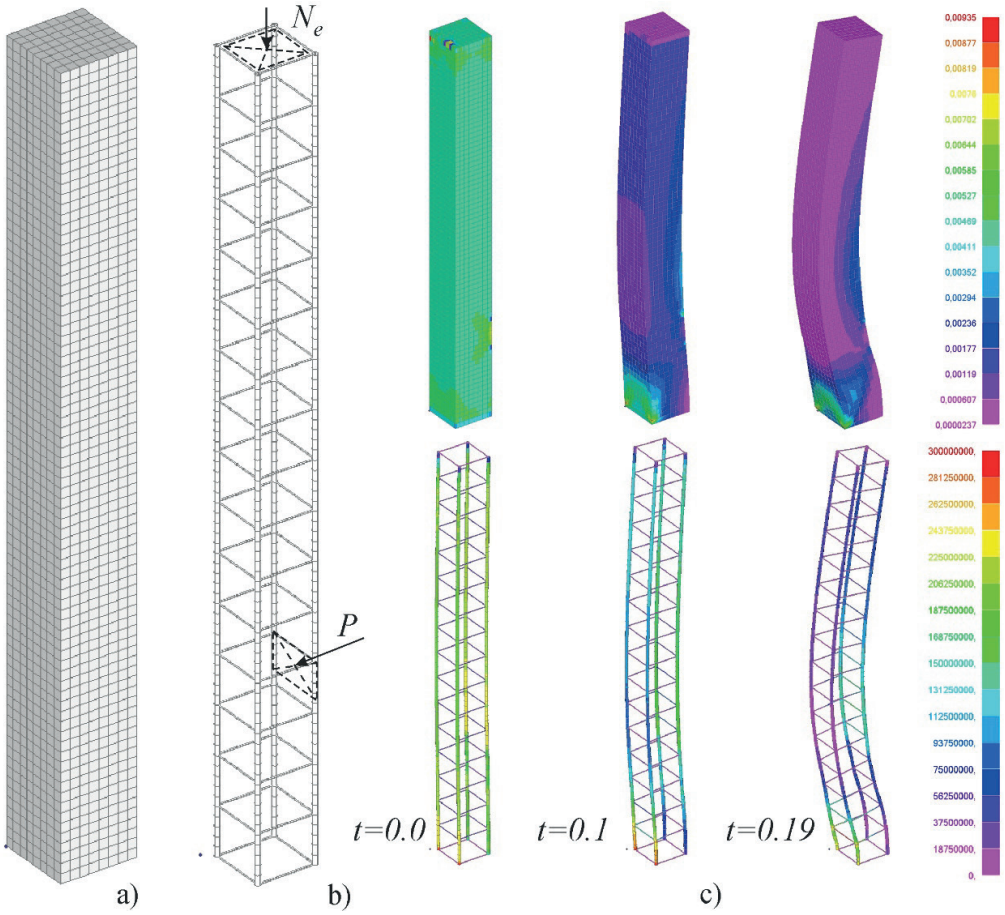

Figure 6. Some results of the numerical analysis: solid finite elements of concrete (a), bar elements of reinforcement (b), results of the assessment of shear strains in concrete and von Mises equivalent stresses in the reinforcement; the scales are given for time 0.19 s

Concrete was represented as hexahedral elements deforming according to the Drucker-Prager model with the capability to simulate element failure. Reinforcement was modeled as bars following bilinear diagrams. The characteristics of concrete used in the calculation are as follows: cohesion stress 3.3 MPa, internal friction angle 38 deg., dilation angle 28 deg., tensile stress 0.9 MPa, compressive stress 11.5 MPa, ultimate tensile strain 0.0001, ultimate compressive strain 0.0035. For the reinforcement, the following was adopted: ultimate tensile strain 0.025, yield stress of longitudinal bars 435 MPa, yield stress of transverse bars 300 MPa.

The parameters of the computational process are as follows: overall damping – 5%; when solving the nonlinear problem, 25 iterations of the Newton-Raphson method were used at each integration step, with stiffness matrix updates every 5 iterations. The convergence criterion was set as a tolerance for nodal force residual equal to 0.1%. The integration time was taken as 1.5 sec, with a step $\Delta t = 0,05$ sec .

Analysis of Figure 6 allows us to note the following features. When resisting only the longitudinal force at time $t = 0.0$ sec before the impact, the stresses in the longitudinal reinforcement are significantly lower than when assessed using the formula from SP 63.13330, while concrete, conversely, carries most of the load. During the realization of the impact, which is accompanied by an increase in the value of P at time $t = 0.1$ sec , a wave of deformations corresponding to the flexural failure mechanism initially forms, and an increase in equivalent

stresses is observed in both longitudinal and transverse reinforcement. In the limit state at $t = 0.19$ sec, the shear strains in concrete exceed the limits for elastic behavior, meaning cracks form. In addition to the fan of cracks along the inclined section, cracks caused by bending and shear also form on the impact side along the height of the column. The stresses in the longitudinal reinforcement at this point are at the level of 50% of the design resistance, while the transverse reinforcement undergoes plastic deformation with stresses equal to $R_{sw} = 300$ MPa. This indicates the initiation of the shear failure mechanism. Significant plastic deformations of these bars lead to a substantial reduction in bearing capacity and the formation of a kinematically unstable system. A comparison of the ultimate compressive force is performed. The analytical method gives $N_{ult} = \varphi(R_b A_b + R_{sc} A_{sc0}) = 2620$ kN (calculated above). The calculation of the solid FEM model yielded a value of 2778 kN. For the column under consideration, the load-bearing capacity curves using points $(N_e; P_{i,ult}) \in L_{BC}$ (see Fig. 1, c) is constructed. The results are presented in Fig. 7.

The figure shows that the scope of the methodology is $0.14 \le N_e / N_{ult} \le 0.8$, however, with a column strength reserve of less than 20% and during an emergency situation, it will most likely fail, so the necessity of calculation in this range is not in demand for practice; usually, columns, based on structural considerations (bearing possibilities), have a strength reserve of 30-50%.

4. DISCUSSION AND DIRECTIONS FOR FURTHER RESEARCH

The proposed methodology describes one of the possible failure scenarios for a column. In this case, the dynamic load increases gradually at a low rate, and the stresses in the concrete do not exceed the value corresponding to its local crushing strength. The strain rate also remains below the critical level; therefore, fan-shaped cracks do not form, and there is no spalling or punching of concrete in the contact zone. Design models for compressed elements, including those presented in regulatory documents, do not yet account for a number of important effects. These include concrete dilation, energy dissipation during the dynamic process and its consideration in modeling, confinement of transverse concrete deformations, and the emergence of additional stresses in the transverse reinforcement due to this confinement.

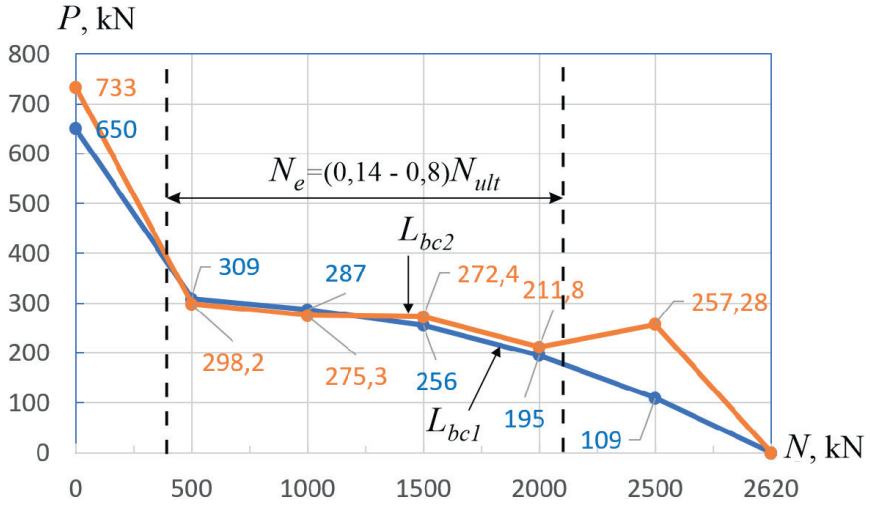

Figure 7. Load-bearing capacity curves of the column: L_{bc1} – calculation using the solid FEM model, L_{bc2} – calculation according to the methodology of this article

However, numerical calculations demonstrate that these effects indeed influence the strength of reinforced concrete columns. The results of numerical modeling confirm that the load-bearing capacity of a compressed column at an inclined section under transverse impact is determined by the stress-strain state of the concrete. The proposed model partially accounts for the effect of the closed transverse reinforcement contour through the parameter of the load intensity it resists. Nevertheless, the process of microcrack formation and the associated concrete dilation are not considered.

The developed approach can serve as an additional tool in analyzing the robustness of buildings and structures subjected to emergency mechanical impacts of anthropogenic origin. Further development of the method is associated with its refinement for pylons and highly slender reinforced concrete columns. Another promising direction is the consideration of various types of initial and acquired damages, as well as the influence of existing strengthening systems on the load-bearing capacity of columns.

CONCLUSION

1. A method for the analytical calculation of compressed-bent reinforced concrete elements under transverse impact has been developed, considering the bending and shear failure mechanisms.
2. The determination of load-bearing capacity accounts for the confinement of transverse concrete deformations under compression. This considers the spacing, diameter, and class of the transverse reinforcement. Limitations for the method's application have been defined – the design compressive force must be less than 80% of its ultimate value.
3. The proposed approach enables a significantly faster assessment of the mechanical safety level of reinforced concrete columns under horizontal dynamic loads compared to solid finite element modeling. The developed relationships can be applied in designing preventive measures aimed at enhancing the resilience of buildings and structures to progressive collapse.

REFERENCES

1. **Sun, J.-M., Yi, W.-J., Chen, H., Peng, F., Zhou, Y., Zhang, W.-X.** Dynamic Responses of RC Columns under Axial Load and Lateral Impact. Journal of Structural Engineering. 2023. 149(1). DOI:10.1061/jsendh/steng-11612.
2. **Li, X., Yin, Y., Li, T., Zhu, X., Wang, R.** Analytical Study on Reinforced Concrete Columns and Composite Columns under Lateral Impact. Coatings. 2023. 13(1). DOI:10.3390/coatings13010152.
3. **Zhao, W., Qian, J.** Resistance mechanism and reliability analysis of reinforced concrete columns subjected to lateral impact. International Journal of Impact Engineering. 2020. 136. DOI:10.1016/j.ijimpeng.2019.103413.
4. **Kashani, M.M., Crewe, A.J., Alexander, N.A.** Structural capacity assessment of corroded RC bridge piers. Proceedings of the Institution of Civil Engineers: Bridge Engineering. 2017. 170(1). DOI:10.1680/jbren.15.00023.
5. **Liu, B., Fan, W., Huang, X., Shao, X., Kang, L.** A Simplified Method to Predict Damage of Axially-Loaded Circular RC Columns Under Lateral Impact Loading. International Journal of Concrete Structures and Materials. 2020. 14(1). DOI:10.1186/s40069-020-00406-z.
6. **Gholipour, G., Zhang, C., Mousavi, A.A.** Effects of axial load on nonlinear response of RC columns subjected to lateral impact load: Ship-pier collision. Engineering Failure Analysis. 2018. 91. DOI:10.1016/j.engfailanal.2018.04.055.
7. **Zhao, W., Ye, J.** Dynamic behavior and damage assessment of RC columns subjected to lateral soft impact. Engineering

Structures. 2022. 251. DOI:10.1016/j.engstruct.2021.113476.
8. **Alekseytsev A.V., Yurusov K.V.** A study on the bearing capacity of compressed corrosion-affected reinforced concrete elements subjected to transverse impulse loading. Vestnik MGSU. 2025;20(5):667-682. (In Russ.) https://doi.org/10.22227/1997-0935.2025.5.667-682
9. **Mahmoud, K.A.** Lateral deformation behavior of eccentrically loaded slender RC columns with different levels of rotational end restraint at elevated temperatures. Journal of Structural Fire Engineering. 2021. 12(1). DOI:10.1108/JSFE-04-2020-0014.
10. **Yilmaz, T., Kiraç, N., Anil, Ö.** Experimental investigation of axially loaded reinforced concrete square column subjected to lateral low-velocity impact loading. Structural Concrete. 2019. 20(4). DOI:10.1002/suco.201800276.
11. **Fan, W., Liu, B., Consolazio, G.R.** Residual Capacity of Axially Loaded Circular RC Columns after Lateral Low-Velocity Impact. Journal of Structural Engineering. 2019. 145(6). DOI:10.1061/(asce)st.1943-541x.0002324.
12. **Wang, X., Zhang, Y., Su, Y., Feng, Y.** Experimental Investigation on the Effect of Reinforcement Ratio to Capacity of RC Column to Resist Lateral Impact Loading. Systems Engineering Procedia. 2011. 1. DOI:10.1016/j.sepro.2011.08.007.
13. **Anil, O., Cem Yilmaz, M., Barmaki, W.** Experimental and numerical study of RC columns under lateral low-velocity impact load. Proceedings of the Institution of Civil Engineers: Structures and Buildings. 2020. 173(8). DOI:10.1680/jstbu.18.00041.
14. **Anil, Ö., Tuğrul Erdem, R., Tokgöz, M.N.** Investigation of lateral impact behavior of RC columns. Computers and Concrete. 2018. 22(1). DOI:10.12989/cac.2018.22.1.123
15. **Demartino, C., Wu, J.G., Xiao, Y.** Response of shear-deficient reinforced circular RC columns under lateral impact loading. International Journal of Impact Engineering. 2017. 109. DOI:10.1016/j.ijimpeng.2017.06.011.
16. **Zhou, X., Zhou, M., Luo, D., Wu, B., Liu, L.** Study on the nonlinear response and shear behavior of RC columns under lateral impact. Structures. 2021. 34. DOI:10.1016/j.istruc.2021.09.094.
17. **Lai, D., Demartino, C., Xu, J., Xu, J., Xiao, Y.** GFRP bar RC columns under lateral low-velocity impact: an experimental investigation. International Journal of Impact Engineering. 2022. 170. DOI:10.1016/j.ijimpeng.2022.104365.
18. **Swesi, A.O., Cotsovos, D.M., Val, D. V.** Effect of CFRP strengthening on response of RC columns to lateral static and impact loads. Composite Structures. 2022. 287. DOI:10.1016/j.compstruct.2022.115356.
19. **Alekseytsev, A.V., Kvocak, K.V., Popov, D.S., Al Ali, M.** Dynamic behavior of a reinforced concrete slab of a pedestrian bridge with stiff rebars. Magazine of Civil Engineering. 2025. 18(1). Article no. 13303. DOI: 10.34910/MCE.133.3
20. **Sidorov V.N., Badina E.S., Klimushkin D.O.** Modification of Rayleigh dissipation function for numerical simulation of internal damping in rod structures. Vestnik MGSU. 2024;19(6):960-970. (In Russ.) https://doi.org/10.22227/1997-0935.2024.6.960-970
21. **Sidorov, V., Badina, E., & Tsarev, R.** Nonlocal in time dynamic deformation model and its calibration based on the beam vibration experiment results. International Journal for Computational Civil and Structural Engineering. 2025. 21(2):161-170. https://doi.org/10.22337/2587-9618-2025-21-2-161-170

СПИСОК ЛИТЕРАТУРЫ

1. **Sun, J.-M., Yi, W.-J., Chen, H., Peng, F., Zhou, Y., Zhang, W.-X.** Dynamic Responses of RC Columns under Axial Load and Lateral Impact. Journal of Structural Engineering. 2023. 149(1). DOI:10.1061/jsendh/steng-11612.
2. **Li, X., Yin, Y., Li, T., Zhu, X., Wang, R.** Analytical Study on Reinforced Concrete Columns and Composite Columns under Lateral Impact. Coatings. 2023. 13(1). DOI:10.3390/coatings13010152.
3. **Zhao, W., Qian, J.** Resistance mechanism and reliability analysis of reinforced concrete columns subjected to lateral impact. International Journal of Impact Engineering. 2020. 136. DOI:10.1016/j.ijimpeng.2019.103413.
4. **Kashani, M.M., Crewe, A.J., Alexander, N.A.** Structural capacity assessment of corroded RC bridge piers. Proceedings of the Institution of Civil Engineers: Bridge Engineering. 2017. 170(1). DOI:10.1680/jbren.15.00023.
5. **Liu, B., Fan, W., Huang, X., Shao, X., Kang, L.** A Simplified Method to Predict Damage of Axially-Loaded Circular RC Columns Under Lateral Impact Loading. International Journal of Concrete Structures and Materials. 2020. 14(1). DOI:10.1186/s40069-020-00406-z.
6. **Gholipour, G., Zhang, C., Mousavi, A.A.** Effects of axial load on nonlinear response of RC columns subjected to lateral impact load: Ship-pier collision. Engineering Failure Analysis. 2018. 91. DOI:10.1016/j.engfailanal.2018.04.055.
7. **Zhao, W., Ye, J.** Dynamic behavior and damage assessment of RC columns subjected to lateral soft impact. Engineering Structures. 2022. 251. DOI:10.1016/j.engstruct.2021.113476.
8. **Alekseytsev A.V., Yurusov K.V.** A study on the bearing capacity of compressed corrosion-affected reinforced concrete elements subjected to transverse impulse loading. Vestnik MGSU. 2025;20(5):667-682. (In Russ.) https://doi.org/10.22227/1997-0935.2025.5.667-682
9. **Mahmoud, K.A.** Lateral deformation behavior of eccentrically loaded slender RC columns with different levels of rotational end restraint at elevated temperatures. Journal of Structural Fire Engineering. 2021. 12(1). DOI:10.1108/JSFE-04-2020-0014.
10. **Yilmaz, T., Kiraç, N., Anil, Ö.** Experimental investigation of axially loaded reinforced concrete square column subjected to lateral low-velocity impact loading. Structural Concrete. 2019. 20(4). DOI:10.1002/suco.201800276.
11. **Fan, W., Liu, B., Consolazio, G.R.** Residual Capacity of Axially Loaded Circular RC Columns after Lateral Low-Velocity Impact. Journal of Structural Engineering. 2019. 145(6). DOI:10.1061/(asce)st.1943-541x.0002324.
12. **Wang, X., Zhang, Y., Su, Y., Feng, Y.** Experimental Investigation on the Effect of Reinforcement Ratio to Capacity of RC Column to Resist Lateral Impact Loading. Systems Engineering Procedia. 2011. 1. DOI:10.1016/j.sepro.2011.08.007.
13. **Anil, O., Cem Yilmaz, M., Barmaki, W.** Experimental and numerical study of RC columns under lateral low-velocity impact load. Proceedings of the Institution of Civil Engineers: Structures and Buildings. 2020. 173(8). DOI:10.1680/jstbu.18.00041.
14. **Anil, Ö., Tuğrul Erdem, R., Tokgöz, M.N.** Investigation of lateral impact behavior of RC columns. Computers and Concrete. 2018. 22(1). DOI:10.12989/cac.2018.22.1.123
15. **Demartino, C., Wu, J.G., Xiao, Y.** Response of shear-deficient reinforced circular RC columns under lateral impact loading. International Journal of Impact Engineering. 2017. 109. DOI:10.1016/j.ijimpeng.2017.06.011.

16. **Zhou, X., Zhou, M., Luo, D., Wu, B., Liu, L.** Study on the nonlinear response and shear behavior of RC columns under lateral impact. Structures. 2021. 34. DOI:10.1016/j.istruc.2021.09.094.
17. **Lai, D., Demartino, C., Xu, J., Xu, J., Xiao, Y.** GFRP bar RC columns under lateral low-velocity impact: an experimental investigation. International Journal of Impact Engineering. 2022. 170. DOI:10.1016/j.ijimpeng.2022.104365.
18. **Swesi, A.O., Cotsovos, D.M., Val, D. V.** Effect of CFRP strengthening on response of RC columns to lateral static and impact loads. Composite Structures. 2022. 287. DOI:10.1016/j.compstruct.2022.115356.
19. **Alekseytsev, A.V., Kvocak, K.V., Popov, D.S., Al Ali, M.** Dynamic behavior of a reinforced concrete slab of a pedestrian bridge with stiff rebars. Magazine of Civil Engineering. 2025. 18(1). Article no. 13303. DOI: 10.34910/MCE.133.3
20. **Sidorov V.N., Badina E.S., Klimushkin D.O.** Modification of Rayleigh dissipation function for numerical simulation of internal damping in rod structures. Vestnik MGSU. 2024;19(6):960-970. (In Russ.) https://doi.org/10.22227/1997-0935.2024.6.960-970
21. **Sidorov, V., Badina, E., & Tsarev, R.** Nonlocal in time dynamic deformation model and its calibration based on the beam vibration experiment results. International Journal for Computational Civil and Structural Engineering. 2025. 21(2):161-170. https://doi.org/10.22337/2587-9618-2025-21-2-161-170

Alekseytsev Anatoly Viktorovich, doctor of technical sciences, associated professor, professor of the department "Reinforced concrete and stone structures"; National Research Moscow State Technical University (NRU MGSU), Russia, Moscow, Yaroslavskoe sh., 26, Scopus ID: 57191530761, Researcher ID: I-3663-2017, ORCID: 0000-0002-4765-5819, e-mail: alekseytsevav@mail.ru.

Valentina M. Tusnina, docent, candidate of technical sciences, associated professor of department "Architectural and construction design and physics of the environment"; National Research Moscow State University of Civil Engineering (National Research University); Russia, 129337 Moscow, Yaroslavskoe sh., 26. Scopus ID: 56296961500; Researcher ID: AAD-8968-2022; ORCID: 0000-0003-0328-0848.
e-mail: valmalaz@mail.ru

Алексейцев Анатолий Викторович, доктор технических наук, доцент, профессор кафедры «Железобетонные и каменные конструкции»; Национальный исследовательский московский государственный технический университет (НИУ МГСУ), Россия, г. Москва, Ярославское ш., 26, Scopus ID: 57191530761, Researcher ID: I-3663-2017, ORCID: 0000-0002-4765-5819, e-mail: alekseytsevav@mgsu.ru.

Туснина Валентина Матвеевна, доцент, кандидат технических наук, доцент кафедры «Архитектурно-строительное проектирование и физика среды»; Национальный исследовательский московский государственный строительный университет (НИУ МГСУ); Россия, 129337 Москва, Ярославское шоссе, 26; Scopus ID: 56296961500; Researcher ID: AAD-8968-2022; ORCID: 0000-0003-0328-0848. e-mail: valmalaz@mail.ru

International Journal for Computational Civil and Structural Engineering, 22(2) 105–112 (2026)

DOI:10.22337/2587-9618-2026-22-2-105-112

INFLUENCE OF SYNTHETIC POLYSACCHARIDES ADDITIVES ON STRUCTURE FORMATION OF LIME COMPOSITES

Valentina I. Loganina [1], Al D.S.D. Salman [2], Irina V. Erofeeva [3], Stanislav A. Sergeev [3]

[1] Penza State University of Architecture and Construction, Penza, RUSSIA
[2] Ministry of Higher Education and Scientific Research, Baghdad, IRAQ
[3] National Research Moscow State University of Civil Engineering, Moscow, RUSSIA

Abstract: The purpose of this work is to study the effect of synthetic polysaccharides on the structure formation and properties of lime coatings. Information is provided on the influence of synthetic polysaccharides on the structure formation of lime coatings. It has been shown that due to the water-retaining effect of the additive, more favorable conditions are created for lime carbonation. Using X-ray phase and thermographic analysis, optical and infrared spectroscopy, the presence of inter- and intracrystalline organic compounds was established, which modify the (nano)structure of newly formed calcite crystals and increase the strength of lime coatings.

Keywords: lime, polysaccharides, structure, crack resistance, strength, carbonation

ВЛИЯНИЕ ДОБАВОК СИНТЕТИЧЕСКИХ ПОЛИСАХАРИДОВ НА СТРУКТУРООБРАЗОВАНИЕ ИЗВЕСТКОВЫХ КОМПОЗИТОВ

В.И. Логанина [1], Аль Дулайми Салман Давуд Салман [2], И.В. Ерофеева [3], С.А. Сергеев [3]

[1] Пензенский государственный университет архитектуры и строительства, Пенза, РОССИЯ
[2] Министерство высшего образования и научных исследований, Багдад, ИРАК
[3] Национальный исследовательский Московский государственный университет гражданского строительства, Москва, РОССИЯ

Аннотация: Целью данной работы является изучение влияния синтетических полисахаридов на структурообразование и свойства известковых покрытий. Представлена информация о влиянии синтетических полисахаридов на структурообразование известковых покрытий. Показано, что благодаря водоудерживающему эффекту добавки создаются более благоприятные условия для карбонизации извести. С помощью рентгенофазового и термографического анализа, оптической и инфракрасной спектроскопии установлено наличие меж- и внутрикристаллических органических соединений, которые модифицируют (нано)структуру вновь образованных кристаллов кальцита и повышают прочность известковых покрытий.

Ключевые слова: известь, полисахариды, структура, трещиностойкость, прочность, карбонизация

INTRODUCTION

Of the many types of binders, along with polymer and cement, lime compositions are used in some cases. Lime-based binders are widely used for the restoration of cultural heritage sites [1]. During operation, coatings applied to brick, concrete and other walls are adversely affected by cyclical temperature and humidity factors, biocorrosion, etc. [2, 3, 4, 5]. An effective method of increasing the durability of building materials is the introduction of

various additives [6, 7, 8], activation of the sealing water and other components [9, 10, 11, 12]. Given the low resistance of lime binder coatings, various modifying additives are introduced into the formulation [13, 14, 15, 16, 17, 18]. In a number of studies, various organic additives based on blood albumin, casein, natural resins, egg proteins, decoctions of grain grains, and vegetable oils were noted in the composition of plaster bases of ancient paintings [19]. The role of organic additives remained unclear for a long time, due to the difficulty of determining them in gypsum and lime binders using existing analytical methods. Until now, organic adhesives have been considered as plasticizing and retarding additives for binding materials. Only the effect of glue additives on the setting time of gypsum binders was studied.

The ancient masons of the Maya tribe used plant extracts in the manufacture of solutions [20, 21]. The works [22, 23, 24, 25] describe the properties of lime plasters with additives of natural polysaccharides. The authors have established the adsorption of organic substances on the surface of calcite crystals. It is of interest to study the possibility of using synthetic polysaccharides in the manufacture of lime formulations for the restoration of cultural heritage sites.

METHODS

Slaked lime (fluff) with a true density of 2230 kg/m^3, a bulk density of 280 kg/m^3, an activity of 83 %, and a specific surface area of 559 m^2/kg were used in the work. The water-soluble modified polysaccharides Atren Cem LV and Atren Cem HV (TU 2458-062-63121839-2014) were used as an organic additive.

The cohesive strength of the coatings was determined by the axial tensile strength on samples measuring 10x10x50 mm and calculated by the formula

$$R_p = \frac{P}{F} \quad (1)$$

where P is the destructive force, H;

F is the cross–sectional area of the sample before the test, m^2.

The Vickers hardness was calculated using the formula

$$HV = \frac{2Psin\propto/2}{d^2} \quad (2)$$

where P is the load on the indenter, N;

α is the angle between the opposite faces of the Vickers indenter;

d is the diagonal of the Vickers indenter print, mm.

The surface area of the print was determined by the diagonal d of the print, which was measured under a microscope.

The rate of carbonization of lime paste was studied by changing the thickness of the carbonized layer. The kinetics of carbonization of control samples and with the addition of Atren Cem LV polysaccharide were determined. The thickness of the carbonized layer was determined by applying a 1% alcohol solution of phenolphthalein to a chip of the test sample. Areas of non-carbonated lime react to phenolphthalein, turning purple. Lime carbonation took place under natural conditions at a temperature of 20 °C.

RESULTS AND DISCUSSION

Formulations with the addition of polysaccharides are characterized by a slightly higher water retention capacity of 98 %. The research results indicate that lime formulations with the addition of polysaccharide in an amount of 1 % by weight of lime are characterized by delayed drying times. For example, the drying time to degree 3 on a concrete substrate is 15–20 minutes, while the control composition (without additives) is 7 minutes. An increase in the frost resistance grade from F25 (control) to F35 (with the addition of polysaccharide) has been established.

Table 1. Properties of the finishing composition with the addition of polysaccharides

Name of indicators	Value
Water retention capacity,%	98
Drying time to degree 3 on a concrete base, minutes	15-20
Tensile strength at the age of 3 months, MPa (Atren Cem LV additive in the amount of 1% by weight of lime)	0.547
Relative deformations, mm/mm	0.392
Frost resistance, brand	F35
Adhesion strength to concrete, MPa	1.1-1.3
Modulus of elasticity, MPa	0.925

An X-ray phase analysis of lime samples was performed on a D8 Advance powder diffractometer (Germany). It was found that the calcite content increases in samples with the use of polysaccharide additives. Obviously, due to the water-retaining effect of the additive, more favorable conditions are created for the carbonization of lime. The amount of calcite in the control samples is 87.4 %, and in the samples prepared with the additive - 88.87 %. The diffractograms show a slight increase in the width of $CaCO_3$ peaks, which indicates the possible incorporation of organic molecules into calcite (Table 2).

Table 2. Crystal Lattice Parameters

Composition	Crystal Lattice Parameters		
	$CaCO_3$	$Ca(OH)_2$	SiO_2
control			
a	4.98700	3.58440	4.90000
c	17.05800	4.89620	5.40000
Slaked in the presence of an additive			
a	4.99100	3.58620	4.91580
c	17.06200	4.88010	5.40910
With an addition			
a	4.98700	3.58620	4.91000
c	17.05800	4.88010	5.40000

Fig. 1 shows micrographs of the hardened lime binder. Chains of rounded $Ca(OH)_2$-crystals are found (Fig. 1, a), as well as elongated polyhedral plates of calcium carbonate. The analysis of the images shows low-contrast nanometer-sized regions in individual calcite crystals with inhomogeneities corresponding to the amorphous (organic) phase (Fig. 1, b), similar to those observed in several $CaCO_3$ biominerals with occluded organics.

The inclusion (adsorption) of polysaccharide additives in/onto calcite is confirmed by the data of polysaccharide adsorption on calcite. The adsorption value was determined by the change in the surface tension of the Atren Cem LV additive solution of different concentrations. It was found that the adsorption value of the Atren Cem LV additive on calcite is 0.000457 g/cm^2

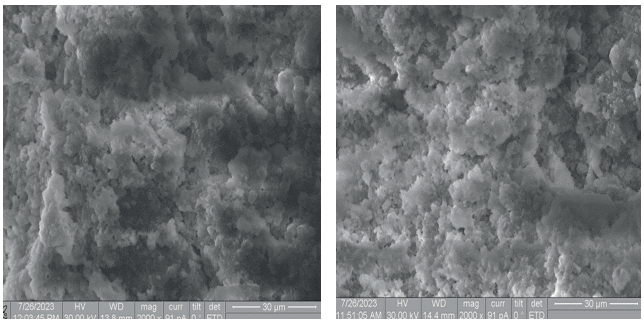

a *b*

Figure 1. The structure of calcareous hardened stone: a – control composition; b - with the addition of polysaccharide Atren Cem HV

Taken together, these results confirm the presence of both inter- and intracrystalline organic compounds that modify (nano)the structure of newly formed calcite crystals at various scales reproduces the multilevel hierarchical mesocrystalline features observed in many $CaCO_3$ biominerals and their biomimetics, which include inter- and intracrystalline (bio)macromolecules.

Fig. 2–3 show photos of the kinetics of carbonation of lime samples.

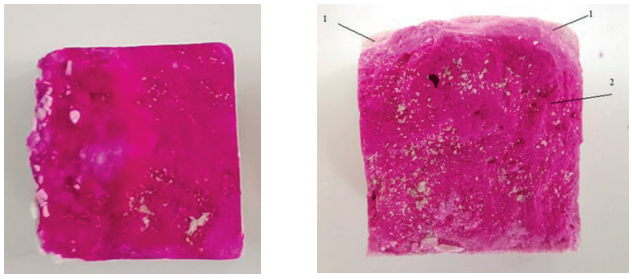

a *b*

Figure 2. Change in the thickness of the carbonized layer of lime samples at the age of 4 days: a - control composition; b - with the addition of polysaccharides; 1 – carbonized layer; 2 – non-carbonated layer

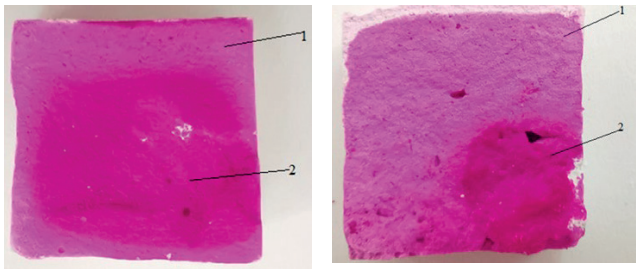

a *b*

Figure 3. Change in the thickness of the carbonized layer of lime samples at the age of 10 days: a - control composition; b - with the addition of polysaccharides; 1 – carbonized layer; 2 – non-carbonated layer

It is evident from Fig. 2 and 3 that the carbonization process begins in the surface layer of the material (the carbonized areas are colored lighter purple), gradually moving inside the sample. The highest degree of carbonization is observed in samples with the addition of Atren Cem LV at a humidity of 21 % (Fig. 3, b). Only a small area in the center of the sample is colored dark purple. The humidity of the control samples was 14 %, the thickness of the carbonization layer is significantly less.

The results of the assessment of the degree of carbonization of lime composites are also confirmed by the data of X-ray phase analysis. The mineralogical composition of the lime composite was determined using a powder diffractometer D8Advans (Germany). It was found that the amount of calcite in the control samples is 87.4 %, in the samples prepared on lime slaked in the presence of the additive Atren Cem HV – 92.266 % and in the samples prepared with the additive Atren Cem HV – 88.87 %.

Polysaccharides cause a hardening effect, contributing to plastic deformation and, consequently, preventing catastrophic destruction caused by external factors.

The obtained results indicate that lime compositions with the addition of Atren Cem LV polysaccharides are characterized by higher cohesive strength. As the hardening age increases, the cohesive strength of the samples with the addition of the synthetic polysaccharide Atren Cem LV increases to a greater extent. Thus, at the age of 28 days of hardening, the cohesive strength of the samples based on the control composition is R 0.22 MPa, and with the addition of polysaccharide – 0.24 MPa. At the age of 3 months of hardening, differences in the values of cohesive strength are more pronounced. The cohesive strength of the control samples is 0.264 MPa, and samples with the addition of Atren Cem LV in the amount of 1% by weight of lime – 0.47 MPa, with the addition of Atren Cem LV in the amount of 0.5% by weight of lime – 0.379 MPa.

Taken together, these results indicate that organic substances induce a hardening effect by promoting plastic deformation and therefore inhibiting failure. The presence of crystalline organic molecules between and inside the lime coating gives higher deformative properties. This is evidenced by the data of the modulus of elasticity and hardness of the coatings. It was found that the modulus of elasticity of a sample of lime coating with the addition of Atren Cem LV in an amount of 1 % by weight of lime is 0.925 MPa, and the control is 0.987 MPa. This is also evidenced by data on the hardness of lime coatings. It has been established that the Vickers hardness of samples based on the control composition is HV = 1.649 MPa, and the hardness of coatings based on the composition with the addition of Atren Cem LV is 1.144 MPa.

It has been established that coatings based on compositions with the addition of polysaccharides are characterized by reduced

shrinkage deformations. After 85 days of hardening, shrinkage deformations of coatings based on the control composition amount to 6.56 %, and on the basis of the composition with the addition of Atren Cem LV – 2.82 %.

CONCLUSION

It was found that diffractograms of calcareous samples with additives of Atren Cem HV show a slight increase in the width of $CaCO_3$ peaks, It has been established that the introduction of polysaccharide additives into the formulation of lime compounds causes the formation of inter- and intracrystalline organic compounds that modify the (nano) structure of newly formed calcite crystals at various scales, which helps to increase the strength of the composite. The results of the conducted studies confirm that the introduction of additives based on polysaccharides Atren Cem LV and Atren Cem HV into the formulation of lime compositions contributes to an increase in the carbonization front.

FUNDING

The research was funded by the National Research Moscow State University of Civil Engineering.

REFERENCES

1. **R. Beates**, Chemical additives to improve the quality of building mortars, Construction materials, **3**, 14–18 (1999).
2. **Kasimkina M.M., Svetlov D.A., Kaznacheev S.V., Bogatov A.D., Boriskin A.S., Erofeev V.T.** Investigation of the physico-mechanical properties of epoxy composites with the fungicidal additive «Teflex» // Transport construction. – 2009. – № 2. – Pp. 29–30.
3. **Erofeev V.T., Afonin V.V., Cherushova N.V., Zotkina M.M., Mitina E.A., Zotkina V.B., Erofeeva I.V.** Methods and algorithms for assessing the surface quality of building products and structures. Fundamental Research. – 2016. – №. 4-1. – Pp. 33–40.
4. **Startsev O.V., Molokov M.V., Erofeev V.T., Krotov A.S., Gudozhnikov S.S.** The influence of climatic aging on moisture transfer of wood with protective coatings // Fundamental research. – 2016. – № 3-3. – Pp. 526–532.
5. **Elchishcheva, T., Afonin, V., Erofeeva, I., Atmanzin, A., Matrosova, C.** Biostability of Plastering Systems in Buildings and Structures // Lecture Notes in Civil Engineering. – 2021. – 150 LNCE. Pp. 379–390.
6. **Khutorskoy S.V., Erofeev V.T., Smirnov V.F.** Increasing the biological resistance of lime-based composites using fungicidal additives // Izvestiya Kazan State University of Architecture and Civil Engineering. – 2013. – № 2 (24). – Pp. 281–286.
7. **Bazhenov Yu.M., Erofeev V.T., Khutorskoy S.V., Petryakov D.N., Smirnov V.F.** Optimization of compositions of slaked lime composites in terms of biological resistance // Industrial and civil engineering. – 2015. – № 2. – Pp. 28–32.
8. **Dergunova A.V., Piksaykina A.A., Bogatov A.D., Salman Al D.S.D., Erofeev V.T.** The economic damage from biodeterioration in building sector // IOP Conference Series: Materials Science and Engineering. – Volume 698. – Issue 7. – 18 December 2019. –International Scientific Conference on Construction and Architecture: Theory and Practice for the Innovation Development. – CATPID. – 2019. – Kislovodsk. – P. 1–6.
9. **Khutorskoy S.V., Matviyevsky A.A., Smirnov V.F., Erofeev V.T.** Biological resistance of lime composites on activated mixing water // Volga Scientific Journal. – 2013. – № 1 (25). – Pp. 22–25.
10. **Erofeev V., Dergunova A., Piksaikina A., (...), Startsev O., Matvievskiy A.** The Effectiveness of Materials Different with Regard to Increasing the Durability // MATEC Web of Conferences. – 2016. – 73,04021.
11. **Erofeev V., Kalashnikov V., Emelyanov D., (...), Tretiakov I., Matvievskiy A.**

Biological resistance of cement composites filled with limestone powders. // Solid State Phenomena 871. – 2016. – P. 22–27
12. **Startsev O., Makhonkov A., Erofeev V., Gudojnikov S.** Impact of moisture content on dynamic mechanical properties and transition temperatures of wood. // Wood Material Science and Engineering. – 2017. – 12(1). – P. 55–62.
13. **Valentina Loganina, Olga Davydova, Roman Fediuk, Mugahed Amran, Sergey Klyuev, Alexander Klyuev, Linar Sabitov and Karina Nabiullina,** Improving the durability of lime finishing mortars by modifying them with silicic acid sol, Materials, **15**, 2360 (2022).
14. **Maria Zaytseva and Valentina Loganina**, Structure the Lime Composite in the Presence of the Addition of a Polysilicate Solution, AIP Conf. Proc., **3154**, 020007-1–020007-5 (2023)
15. **Valentina Loganina, Vadim Pylaev**, Physical and Mechanical Properties of Lime Coatings with the Additive of Polysaccharides,E3S Web of Conferences 533, 01002 (2024)
16. **Yang, Fuwei, Zhang, Bingjian, Ma, Qinglin**, Study of Sticky Rice-Lime Mortar Technology for the Restoration of Historical Masonry Construction, Accounts of Chemical Research, **43** (6), 936-944 (2010).
17. **P. Degryse**, Study of ancient mortars from Sagalassos (Turkey) in view of their conservation, Cement and Concrete Research, **32**(1457), 63(2002).
18. **C. Genestar, C.Pons**. Ancient covering plaster mortars from several convents and Islamic and Gothic palaces in Palma de Mallorca (Spain). Analytical characterization, Journal of Cultural Heritage, **4**, 291–298 (2002).
19. **G. Artioli, M. Secco, A. Addis**, The Vitruvian legacy: Mortars and binders before and after the Roman world, EMU Notes Miner., **20**, 151–202(2019).
20. **K. Elert, E. Ruiz-Agudo, F. Jroundi, M. T. Gonzalez-Muñoz, B. W. Fash, W. L. Fash, N. Valentin, A. de Tagle, C.Rodriguez-Navarro**, Degradation of ancient Maya carved tuff stone at Copan and its bacterial bioconservation, npj Mater. Degrad. **5**, 44. (2021).
21. **D. Magaloni, R. Pancella, Y. Fruh, J. Cañetas, V. Castaño**, Studies on the Mayan mortars technique, MRS Online Proc. Lib., **352**,483 (1995).
22. **E. Littmann, R. Ancient**, Mesoamerican mortars, plasters, and stuccos: The use of bark extracts in lime plasters Am. Antiquity, **25**, 593–597 (1960).
23. **F. Yang, B. Zhang, Q. Ma**, Study of sticky rice– Lime mortar technology for the restoration of historical masonry construction, Acc. Chem. Res., 43, 936–944 (2010).
24. **C. Rodriguez-Navarro, E. Ruiz-AgudoBurgos-Cara, K. Elert, E. Hansen**, Crystallization and colloidal stabilization of $Ca(OH)_2$ in the presence of nopal juice (Opuntia ficus indica): Implications in architectural heritage conservation, Langmuir, **33**, 10936–10950 (2017).
25. **B. Pokroy, A. Fitch, E. Zolotoyabko**, The microstructure of biogenic calcite: A view by high-resolution synchrotron powder diffraction, Adv. Mater. 18, 2363–2368 (2006).

СПИСОК ЛИТЕРАТУРЫ

1. **Р. Беатес,** Химические добавки для улучшения качества строительных растворов, Строительные материалы, 3, 14–18 (1999).
2. **Касимкина М.М., Светлов Д.А., Казнавеев С.В., Богатов А.Д., Борискин А.С., Ерофеев В.Т.** Исследование физико-механических свойств эпоксидных композитов с фунгицидной добавкой «Тефлекс» // Транспортное строительство. – 2009. – № 2. – С. 29–30.
3. **Ерофеев В.Т., Афонин В.В., Черушова Н.В., Зоткина М.М., Митина Е.А., Зоткина В.Б., Ерофеева И.В.** Методы и алгоритмы оценки качества поверхности

строительных изделий и конструкций. Фундаментальные исследования. – 2016. – № 4-1. – С. 33–40.

4. **Старцев О.В., Молоков М.В., Ерофеев В.Т., Кротов А.С., Гудожников С.С.** Влияние климатического старения на влагоперенос древесины с защитными покрытиями // Фундаментальные исследования. – 2016. – № 3-3. – С. 526–532.
5. **Эльчищева Т., Афонин В., Ерофеева И., Атманзин А., Матросова С.** Биостабильность штукатурных систем в зданиях и сооружениях // Лекционные заметки по гражданскому строительству. – 2021. – 150 ЛНКЭ. С. 379–390.
6. **Хуторской С.В., Ерофеев В.Т., Смирнов В.Ф.** Повышение биологической стойкости известковых композитов с использованием фунгицидных добавок // Известия Казанского государственного университета архитектуры и гражданского строительства. – 2013. – № 2 (24). – С. 281–286.
7. **Баженов Ю.М., Ерофеев В.Т., Хуторской С.В., Петряков Д.Н., Смирнов В.Ф.** Оптимизация составов гашеных известковых композитов по биологической стойкости // Промышленное и гражданское строительство. – 2015. – № 2. – С. 28–32.
8. **Дергунова А.В., Пиксайкина А.А., Богатов А.Д., Салман Аль Д.С.Д., Ерофеев В.Т.** Экономический ущерб от биодеградации в строительном секторе // Серия конференций IOP: Материаловедение и инженерия. – Том 698. – Выпуск 7. – 18 декабря 2019 г. – Международная научная конференция по строительству и архитектуре: теория и практика инновационного развития. – CATPID. – 2019. – Кисловодск. – С. 1–6.
9. **Хуторской С.В., Матвиевский А.А., Смирнов В.Ф., Ерофеев В.Т.** Биологическая стойкость известковых композитов на активированной воде // Научный журнал «Волга». – 2013. – № 1 (25). – С. 22–25.
10. **Ерофеев В., Дергунова А., Пиксайкина А., (...), Старцев О., Матвиевский А.** Эффективность различных материалов в отношении повышения долговечности // MATEC Web of Conferences. – 2016. – 73,04021.
11. **Ерофеев В., Калашников В., Емельянов Д., (...), Третьяков И., Матвиевский А.** Биологическая стойкость цементных композитов, наполненных известняковой пылью. // Явления твердого состояния 871. – 2016. – С. 22–27.
12. **Старцев О., Махонков А., Ерофеев В., Гудойников С.** Влияние влажности на динамические механические свойства и температуры перехода древесины. // Материаловедение и инженерия древесины. – 2017. – 12(1). – С. 55–62.
13. **Валентина Логанина, Ольга Давыдова, Роман Федюк, Мугахед Амран, Сергей Клюев, Александр Клюев, Линар Сабитов и Карина Набиуллина,** Повышение долговечности известковых отделочных растворов путем их модификации золем кремниевой кислоты, Материалы, 15, 2360 (2022).
14. **Мария Зайцева и Валентина Логанина,** Структурирование известкового композита в присутствии добавления раствора полисиликата, AIP Conf. Proc., 3154, 020007-1–020007-5 (2023).
15. **Валентина Логанина, Вадим Пылаев,** Физические и механические свойства известковых покрытий с добавкой полисахаридов, E3S Web of Conferences 533, 01002 (2024).
16. **Ян, Фувэй, Чжан, Бинцзянь, Ма, Цинлинь,** Изучение технологии клейкого рисово-известкового раствора для реставрации исторических каменных сооружений, Отчеты о химических исследованиях, 43 (6), 936-944 (2010).
17. **П. Дегризе,** Изучение древних растворов из Сагалассоса (Турция) с целью их сохранения, Исследования цемента и бетона, 32(1457), 63(2002).

18. **К. Генестар, К. Понс.** Древние штукатурные растворы из нескольких монастырей и исламских и готических дворцов в Пальма-де-Майорке (Испания). Аналитическая характеристика, Журнал культурного наследия, 4, 291–298 (2002).
19. **Г. Артиоли, М. Секко, А. Аддис,** Витрувианское наследие: растворы и связующие вещества до и после римского мира, EMU Notes Miner., 20, 151–202 (2019).
20. **К. Элерт, Э. Руис-Агудо, Ф. Хруунди, М. Т. Гонсалес-Муньос, Б. В. Фаш, В. Л. Фаш, Н. Валентин, А. де Тагле, К. Родригес-Наварро.** Деградация древнего резного туфового камня майя в Копане и его бактериальная биоконсервация, npj Mater. Degrad. 5, 44. (2021).
21. **Д. Магалони, Р. Панчелла, Й. Фрух, Дж. Каньетас, В. Кастаньо,** Исследования техники майянских растворов, MRS Online Proc. Lib., 352,483 (1995).
22. **Э. Литтманн, Р. Энчейндж,** Мезоамериканские растворы, штукатурки и лепнина: использование экстрактов коры в известковых штукатурках Am. Antiquity, 25, 593–597 (1960).
23. **Ф. Ян, Б. Чжан, Ц. Ма,** Изучение технологии клейкого риса и известкового раствора для реставрации исторических каменных конструкций, Acc. Chem. Res., 43, 936–944 (2010).
24. **C. Rodriguez-Navarro, E. Ruiz-Agudo Burgos-Cara, K. Elert, E. Hansen**, Кристаллизация и коллоидная стабилизация Ca(OH)2 в присутствии сока опунции (Opuntia ficus indica): значение для сохранения архитектурного наследия, Langmuir, 33, 10936–10950 (2017).
25. **B. Pokroy, A. Fitch, E. Zolotoyabko**, Микроструктура биогенного кальцита: взгляд с помощью высокоразрешающей синхротронной порошковой дифракции, Adv. Mater. 18, 2363–2368 (2006).

Valentina Ivanovna Loganina, Dr. Sc., Professor, Head of the Department of Quality Management at Penza State University of Architecture and Construction (PGUAS). Russia, 440028, Penza, G.Titova str., 28. e-mail: loganin@mail.ru

Salman Dawood Salman Al Dulaimi, PhD, Ministry of Higher Education and Scientific Research. Iraq, 55509, Baghdad, Al-Rusafa District, 52nd Street. e-mail: salmoon-1985@mail.ru

Irina Vladimirovna Erofeeva, PhD, Associate Professor of the Department of Fundamentals of Architecture and Artistic Communications of the National Research Moscow State University of Civil Engineering (NRU MGSU), 129337, Russia, Moscow, Yaroslavskoe Shosse, 26, e-mail: ErofeevaIV@gic.mgsu.ru

Stanislav Alekseyevich Sergeev, PhD, Associate Professor of the Department of Hydraulics and Hydraulic Engineering, National Research Moscow State University of Civil Engineering (NRU MGSU), 129337, Russia, Moscow, Yaroslavskoe Shosse, 26, e-mail: SergeevSA@mgsu.ru

Логанина Валентина Ивановна, доктор технических наук, профессор, заведующий кафедрой управления качеством ФГБОУ ВО «Пензенский государственный университет архитектуры и строительства» (ПГУАС), 440028, Россия, г. Пенза, ул. Г. Титова, 28. e-mail: loganin@mail.ru

Аль-Дулайми Салман Давуд Салман, кандидат технических наук, Министерство высшего образования и научных исследований Ирака. 55509, Ирак, Багдад, округ Эр-Русафа, 52-я улица. e-mail: salmoon-1985@mail.ru

Ерофеева Ирина Владимировна, кандидат технических наук, доцент кафедры «Основ архитектуры и художественных коммуникаций» Национального исследовательского Московского государственного строительного университета (НИУ МГСУ) 129337, г. Москва, Ярославское шоссе, д. 26. e-mail: ErofeevaIV@gic.mgsu.ru

Сергеев Станислав Алексеевич, кандидат технических наук, доцент кафедры «Гидравлики и гидротехнического строительства» Национального исследовательского Московского государственного строительного университета (НИУ МГСУ) 129337, г. Москва, Ярославское шоссе, д. 26. e-mail: SergeevSA@mgsu.ru

International Journal for Computational Civil and Structural Engineering, 22(2) 113–125 (2026)

DOI:10.22337/2587-9618-2026-22-2-113-125

OPTIMIZATION OF ABOVE-GROUND CYLINDRICAL REINFORCED CONCRETE TANKS UNDER BLAST LOADING CONSIDERING FLUID-STRUCTURE INTERACTION EFFECTS USING THE PSO ALGORITHM

Majid Alipour [1], Mojtaba Hosseini [2], Peyman Beiranvand [3]

[1] Supervision of Bank Maskan of Lorestan, Khorramabad, IRAN
[2] Department of Civil Engineering, Lorestan University, Khorramabad, IRAN
[3] School of Civil Engineering, Iran University of Science and Technology, Tehran, IRAN

Abstract: Above-ground storage tanks are significantly more vulnerable to damage from blast loading compared to bury or semi-buried concrete and steel tanks, primarily due to their exposed nature. To accurately assess the real behavior of above-ground tanks, it is essential to account for fluid-structure interaction (FSI) effects. Accordingly, in this study, 24 finite element models of cylindrical reinforced concrete tanks were developed in ABAQUS software and subjected to blast loading, incorporating FSI effects. The key variables considered include explosive mass, explosive distance, fluid fill level, tank wall height, and mesh size. The investigated responses encompass circumferential (hoop) stress and radial displacement. The design constraints were set as maximum allowable hoop stress (30MPa) and maximum displacement (20mm). The optimal tank was designed using C30 concrete and steel with a yield strength of 400 MPa. The tank dimensions were 15m in height and 33.85m in diameter. The explosive mass and explosive distance were set at 1000kg and 10m, respectively. The objective function was to minimize the tank weight while simultaneously satisfying the stress and displacement constraints. Using the Particle Swarm Optimization (PSO) algorithm, the minimum weight of the cylindrical reinforced concrete tank was determined to be 23933kN, which was achieved after approximately 25 iterations.

Keywords: Cylindrical Reinforced Concrete Tanks, Blast Load, Hoop Stress, Maximum Displacement, Optimization, PSO Algorithm

ОПТИМИЗАЦИЯ НАДЗЕМНЫХ ЦИЛИНДРИЧЕСКИХ ЖЕЛЕЗОБЕТОННЫХ РЕЗЕРВУАРОВ ПРИ ВЗРЫВНОЙ НАГРУЗКЕ С УЧЕТОМ ЭФФЕКТОВ ВЗАИМОДЕЙСТВИЯ ЖИДКОСТИ и КОНСТРУКЦИИ С ИСПОЛЬЗОВАНИЕМ АЛГОРИТМА PSO

Маджид Алипур [1], Моджтаба Хоссейни [2], Пейман Бейранванд [3]

[1] Управление Банка жилищного строительства провинции Лурестан, г. Хорремабад, ИРАН
[2] Кафедры гражданского строительства, Университет Лурестана, г. Хорремабад, ИРАН
[3] Школа гражданского строительства, Иранский университет науки и технологий, г. Тегеран, ИРАН

Аннотация. Наземные резервуары для хранения жидкостей характеризуются существенно более высокой уязвимостью к воздействию взрывных нагрузок по сравнению с заглублёнными и полузаглублёнными бетонными и стальными резервуарами, что обусловлено их открытым расположением. Для адекватной оценки напряжённо-деформированного состояния наземных резервуаров необходимо учитывать эффекты взаимодействия жидкости и конструкции (Fluid–Structure Interaction, FSI). В связи с этим в программном комплексе ABAQUS были разработаны 24 конечно-элементные модели цилиндрических железобетонных резервуаров, подвергаемых воздействию взрывной нагрузки с учётом FSI-эффектов. В качестве варьируемых параметров рассматривались масса взрывчатого вещества, расстояние до эпицентра взрыва, уровень заполнения резервуара жидкостью, высота стенки резервуара и размер конечных элементов расчётной сетки. В качестве исследуемых параметров отклика анализировались кольцевые (обручные) напряжения и радиальные перемещения

конструкции. Проектные ограничения были заданы в виде максимально допустимого кольцевого напряжения 30 МПа и предельно допустимого перемещения 20 мм. Оптимальная конструкция резервуара была разработана с использованием бетона класса С30 и арматурной стали с пределом текучести 400 МПа. Геометрические параметры резервуара составили 15 м по высоте и 33,85 м по диаметру. Масса заряда взрывчатого вещества и расстояние до объекта были приняты равными 1000 кг и 10 м соответственно. В качестве целевой функции рассматривалась минимизация массы резервуара при одновременном соблюдении ограничений по прочности и деформативности. По результатам оптимизации с использованием алгоритма роя частиц (Particle Swarm Optimization, PSO) установлено, что минимальный вес цилиндрического железобетонного резервуара составляет 23 933 кН. Достижение оптимального решения было обеспечено приблизительно после 25 итераций алгоритма.

Ключевые слова: цилиндрический железобетонный резервуар; взрывная нагрузка; кольцевые напряжения; радиальное перемещение; оптимизация конструкций; алгоритм PSO

INTRODUCTION

Storage tanks are crucial structures for fluid containment in transmission networks, typically featuring fixed plan and elevation geometries. Their design and analysis account for inflow rates, site geotechnical conditions, and static/dynamic loading. Therefore, a precise investigation of tank behavior under blast loading is essential. A key aspect of analyzing such structures involves evaluating the effects of fluid-structure interaction in response to dynamic forces. For this purpose, the fluid (water) is assumed to be a continuous, incompressible, and irrational medium. Within the tank domain, the equations of motion are based on the governing differential equation for hydrodynamic wave propagation and the corresponding boundary conditions, which is the Laplace equation [1].

The seismic response of liquid storage tanks has been extensively studied by numerous researchers. Early studies in this field assumed rigid tank walls and considered both linear and nonlinear fluid behavior. Pioneers in this area were Jacobsen [2] and Housner [3], who investigated hydrodynamic pressure effects in tanks subjected to horizontal excitation. Jacobsen focused his studies on cylindrical tanks with rigid walls, while Housner modeled rigid cylindrical and rectangular tank systems in a manner practical for civil engineers. In Housner's model, the fluid pressure is divided into an impulsive component due to the part of the fluid accelerating with the wall and a convective component resulting from fluid sloshing. Subsequently, Epstein provided a series of equations and tables, assuming the convective component acts in the upper part of the fluid, to determine maximum seismic forces [4]. Later, Haroun and Housner, using the finite element method, boundary solutions, and computer programs, presented a new model of the tank-fluid system, considering not only the fundamental $\cos\theta$ mode but also higher-order $cosn\theta$ modes [5]. Veletsos then modeled the impulsive components of rigid and flexible wall tanks by substituting a pseudo-acceleration function for ground acceleration, followed by Ramerathoffer who proposed a design procedure for tanks considering both seismic components [6].

As observed, most existing research has considered earthquake forces as the dynamic effect on fluid storage tanks. However, such structures may also be subjected to other loadings, such as blast waves. The analysis of blast loading effects on structures began in the 1960s. In 1959, the U.S. Army published a manual titled "Structures to Resist the Effects of Accidental Explosions." A revised edition published in 1990 has been widely used by military and non-military organizations for the design of structures to prevent blast propagation and protect personnel and equipment [7]. Subsequently, numerous numerical and experimental studies were conducted on the effects of blast on various structures, including fluid storage tanks [8, 9]. Among these, research

by Wang et al. demonstrated that a tank designed for seismic forces has lower resistance to blast, resulting from increased internal energy and reduced external work when adopting constrained boundary conditions [10]. Mittal researched the dynamic analysis of liquid storage tanks under blast using a combined Eulerian-Lagrangian formulation, showing that stresses increase with higher fluid fill level, decreased distance from the blast center, and increased height-to-radius ratio of the tank [11]. Li et al. investigated blast overpressure generated inside and outside groups of tanks. They provided methods for calculating internal and external pressures considering various spacing's between tanks [12, 13]. Zheng et al., using numerical methods, presented the stress and deformation in a gas tank subjected to a TNT explosive blast load [14]. Hu and Zhao modeled the effect of blast on a small-scale tank in FLUENT software and compared it with experimental specimens [15]. Peyman Safa conducted a nonlinear dynamic numerical analysis on ground-based floating roof tanks under blast loading for 30 different blast scenarios [16]. The obtained results indicated that the examined tank shells are vulnerable to some blast loading scenarios and would suffer damage based on the failure criteria of the API 650 standard. Yasseri, through experimental studies, proposed a relationship for obtaining the external blast pressure distribution around vertical pressure tanks [17]. The results of this research are applicable to tanks with heights smaller than their diameters. The numerical study by Wang and Zhou on a water tank under blast loading showed that water can mitigate the tank's blast response [18]. Alipour and colleagues, in their research, investigated the effects of explosive distance, charge height above ground, explosive mass, tank geometry, internal fluid condition, and internal fluid pressure distribution on both cylindrical and cubic reinforced concrete tanks with an equivalent cross-sectional area of 900 m², considering fluid-structure interaction effects [19, 20, 21]. Hosseini et al. in a study, increasing soil density was found to intensify pressure and stress on buried pipes under blast loading, whereas low-density soil acts as a damper, reducing pipe damage. Using the ALE method in LS-DYNA, parametric analysis showed that soil with lower density better mitigates explosion effects on concrete pipes [22].

MATERIALS AND METHODS

This study aims to perform a sensitivity analysis of parameters affecting hoop stress in above-ground cylindrical reinforced concrete tanks subjected to blast loading using the Monte Carlo simulation method. All studied responses are calculated and recorded at control points. In this research, control points are defined along the tank's peripheral surface at three elevation levels: bottom, mid-height, and top of the tank wall. The soil stiffness is assumed to be infinite in this study, effectively neglecting soil-structure interaction effects. (Figure 1) shows the geometric parameters of the cylindrical tank. The studied variables are as follows:

Explosive Mass: The loading in this study is of the blast type. One of the key factors influencing damage to the structure is the magnitude of the blast force. Explosive mass is one of the variables studied. Therefore, two values of TNT equivalent explosive mass are used: 500 kg and 1000 kg.

Explosive Distance: Another variable is the distance from the explosive charge to the tank. The closer the blast location is to the structure, the higher the likelihood of damage. The distances considered in this study are 10 m and 25 m. Internal Fluid Condition: To investigate fluid-structure interaction effects, the tank's behavior can be analyzed for three conditions: empty, half-full, and full. Tank Height: Given the nature of blast loading, which acts as compressive waves on the tank's external wall, a larger loaded surface area inevitably leads to greater effects. Therefore, tank height, which directly increases the loaded surface area, is studied as a variable.

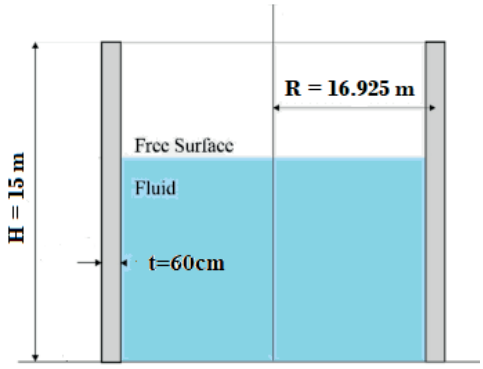

Figure 1. Geometric parameters of the cylindrical tank under study

Scaling Laws

The characteristics of a blast wave depend on the energy released from the explosive material and the propagation medium. These properties can be measured under controlled laboratory conditions and serve as a basis for obtaining information about other explosions using blast scaling laws. In blast loading, scaling blast wave properties is a common practice, and several methods have been proposed for estimating blast waves. Using scaling laws based on experimental results, the properties of a blast wave from any desired charge weight and distance can be estimated, assuming a perfect gas and neglecting gravity and viscosity; however, these laws are not suitable for very strong shock waves or distances very close to the explosion source. The Henrych scaling method used in this study for designing cylindrical reinforced concrete tanks is described below. According to Henrych's scaling laws, if a charge weight W (kg of TNT) detonates at a distance R from a structure, the peak incident overpressure P_{so} can be calculated from the following equations:

$$Z = \frac{R}{W^{\frac{1}{3}}} \tag{1}$$

$$P_{so} = \begin{cases} \frac{14.072}{Z} + \frac{5.54}{Z^2} + \frac{0.357}{Z^3} + \frac{0.000625}{Z^4} & 0.05 \le Z < 0.3 \\ \frac{6.194}{Z} + \frac{0.326}{Z^2} + \frac{2.132}{Z^3} & 0.3 \le Z < 1 \\ \frac{6.662}{Z} + \frac{4.05}{Z^2} + \frac{3.288}{Z^3} & 1 \le Z < 10 \end{cases} \tag{2}$$

Where Z is the scaled distance.

Preliminary Design of the Cylindrical Reinforced Concrete Tank

In this section, a cylindrical reinforced concrete tank was designed based on the initial problem parameters. Table 1 presents the primary specifications used for the tank design.

Table 1. Initial problem specifications for the design of the cylindrical reinforced concrete tank

Parameter	Value
Total tank height	15 m
Outer diameter of the cylindrical tank base	33.85 m
Concrete class and compressive strength	C30 / 30 MPa
Unit weight of concrete	25 kN/m³
Yield strength of reinforcement steel	400 MPa
Fluid height inside the tank	7.5 m
Unit weight of fluid	10 kN/m³
Mass of explosive charge	1000 kg
Explosive distance of explosive from the tank	25 m

Based on the specifications in Table 1 and the provisions of Publication No. 123, the cylindrical reinforced concrete tank was designed as detailed in Table 2.

Table 2. Preliminary Design of the Cylindrical Reinforced Concrete Tank

Design Tensile Force	Design Bending Moment	Slab Reinforcement	Vertical Reinforcement	Horizontal Reinforcement	Slab Thickness	Wall Thickness
1523 kN/m	844 $kN.m/m$	Φ 16 @ 150mm	Φ25 @100mm	Φ20 @ 100mm	400mm	600mm

Modeling the Tank and Fluid under Blast Loading

The modeling procedure for all studied models in this research was similar and consistent. The differences between models were solely in numerical values, geometric parameters, and research variables. Therefore, this section presents the general modeling procedure for one of the studied models. The first step in the modeling process is creating the required parts. In this study, according to the variables under investigation, three parts were modeled: the tank, the water, and the reinforcements (vertical and circumferential). Concrete elements are of type S4R, water elements are of type AC3D8R, and reinforcement elements are of type T3D2. After creating all three parts, the materials for water, concrete, and steel are defined and assigned to the created parts.

The water density is taken as $1 \times 10^{-6}\ kg/mm^3$ and the water viscosity is set to 0.001. To define the fluid behavior, the Us-Up equations (Mie-Grüneisen equation of state) are used. For this purpose, the speed of sound $C_0 = 1480000\ mm/s$ the slope coefficient of the Us-Up curve $s = 1.79$ and the Grüneisen coefficient $\Gamma_0 = 0.5$ are defined. For the concrete tank, concrete with grade C30 is used, with a unit weight of $2.4 \times 10^{-6}\ kg/mm^3$ a Poisson's ratio of 0.2 and an elasticity modulus of 23.5GPa. To define the plastic properties and damaged behavior of concrete, the parameters related to the Concrete Damaged Plasticity model were considered according to Tables 3 and 4.

Table 3. Parameters for Concrete Damaged Plasticity Behavior

Eccentricity	Dilation Angle (°)	f_{b0}/f_{c0}	Eccentricity	Dilation Angle (°)
0.0001	0.67	1.16	0.1	30

Table 4. Compressive and Tensile Behavior of Concrete in ABAQUS Software

	Compressive Stress (MPa)	Plastic Strain	Tensile Stress (MPa)	Plastic Strain
1	11.25	0.0000	2.80	0.0000
2	18.75	0.0000	2.10	0.0001
3	22.50	0.0000	1.40	0.0002
4	25.00	0.0002	0.70	0.0003
5	23.75	0.0005	0.00	0.0004
6	21.25	0.0010		
7	17.50	0.0020		
8	12.50	0.0030		
9	10.00	0.0040		

Steel is used to model the reinforcements in concrete. The elastic properties of steel, including unit weight, Poisson's ratio, and elasticity modulus are$7.85 \times 10^{-6}\ kg/mm^3$, 0.3 and 210GPa respectively. Since blast loads (as impulsive loads) typically induce extremely high strain rates in the range of 100 to 10,000 s^{-1}, they alter the mechanical properties of materials and the expected mechanisms in the structure. According to Table 5, the plastic properties of steel are defined using the Johnson-Cook hardening model to account for strain rate effects on stress. According to Equation (3), stress in the Johnson-Cook model is defined as a function of plastic strain, strain rate, and temperature. This feature can be readily defined in ABAQUS software.

Table 5. Johnson-Cook Model Parameters for Steel Plastic Behavior.

Parameters	Value
A (MPa)	360
B (MPa)	635
n	1.03
m	0.114
Melting temperature (K)	1500
Transition temperature (K)	298
C	0.075
Epsilon dot zero	1

$$\sigma = (A + B\varepsilon^{n})(1 + C.\,Ln\varepsilon^{*})(1 - T^{*m}) \qquad (3)$$

Where ε^* is the dimensionless plastic strain rate relative to the reference strain rate, and $\dot{\varepsilon}$ is the plastic strain rate; T^* is the homologous temperature; A is the initial yield strength of steel at a reference plastic strain rate $\dot{\varepsilon} = 1/s$ and temperature of $298\ K$; B and n simulate the strain-rate-independent hardening behavior of steel; C represents the strain-rate-dependent hardening behavior; and m is the thermal softening coefficient, obtained from mechanical tests for steel and equal to 0.114. After assigning materials to the parts, all parts are assembled, and the charge weight and explosive distance are defined using the ConWep method. Accordingly, the desired points are defined as reference points using the Offset from point option, and subsequently, the charge weight is defined. It should be noted that the tank base is modeled with fixed supports and is fully constrained.

VALIDATION

To ensure the accuracy of the modeling performed in this study, the results presented here were verified against those from a reputable reference. For this purpose, one of the models examined by Moghadam et al. was simulated, and the obtained results were compared with those presented in that reference. It is worth noting that previous studies have compared different numerical modeling methods for applying blast loads to water storage tanks to assess their accuracy. In this section, the blast loading on the tank is applied in ABAQUS software and compared with the numerical modeling method proposed by Moghadam et al. for evaluation. Steel water tanks with various dimensions and fill percentages were analyzed under a 100 kg TNT explosion at different explosive distances [23].

In this case, a water tank with a height of 1 meter, a radius of 1 meter, and 50% water fill was modeled under a 100 kg TNT explosion at a distance of 5 meters from the tank and evaluated in ABAQUS software to confirm the model's validity. The graph in Figure (2) shows the resulting hoop stress on the tank wall under blast. The hoop stress distribution along the wall at the peak blast time is examined, and pressures are applied to the water tank. In this case, the hoop stress value is determined for each node and plotted. Table (6) compares the percentage error in the study conducted by Moghadam et al. with the present study. The comparison results showed that the difference was less than 5%.

Table 6. Percentage Error of the Method by Moghadam et al. Compared to the Present Study [23]

10	9	8	7	6	5	4	3	2	1	
1.0	0.9	0.8	0.7	0.6	0.5	0.4	0.3	0.2	0	Depth(m)
112	184	217	288	321	379	440	496	538	549	Moghadam et al. [23]
115	192	214	295	330	389	432	510	546	564	Current study
2.7	4.3	1.4	2.4	2.8	2.6	1.8	2.8	1.5	2.7	Error (%)

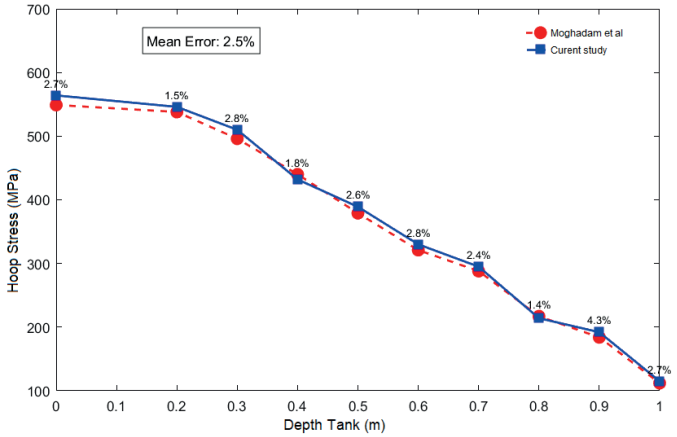

Figure 2. Comparison of hoop stress in the studied model with the research by Moghadam et al

RESULTS

Analyzed of Models

Given the variables addressed in this study, which include the water condition inside the tank (empty, half-full, and full), tank height (10 and 15 meters), explosive charge mass (500 and 1000 kg), and explosive distance (10 and 25 meters), we will examine the influence of each stated variable on the behavior of the above-ground tank, considering fluid-structure interaction effects. In this process, other variables are held constant. This procedure is repeated for each variable, and the impact of all variables on the structural response is studied and evaluated. Subsequently, the effects of explosive charge mass, explosive distance, internal water condition, and tank height on the overall response of the above-ground tank under blast loading are investigated and assessed. The studied scenarios in this research are named according to Table (7).

Table 7. Introduction and Nomenclature of the Studied Scenarios in the Present Research

Model	Tank Height (m)	Explosive Charge Mass (kg)	Water Condition in Tank	Explosive Distance (m)
T1	10	500	Empty	25
T2	10	500	Empty	10
T3	10	500	Half-Full	25
T4	10	500	Half-Full	10
T5	10	500	Full	25
T6	10	500	Full	10
T7	10	1000	Empty	25
T8	10	1000	Empty	10
T9	10	1000	Half-Full	25
T10	10	1000	Half-Full	10
T11	10	1000	Full	25
T12	10	1000	Full	10
T13	15	500	Empty	25
T14	15	500	Empty	10
T15	15	500	Half-Full	25
T16	15	500	Half-Full	10
T17	15	500	Full	25
T18	15	500	Full	10
T19	15	1000	Empty	25
T20	15	1000	Empty	10
T21 (RM)	15	1000	Half-Full	25
T22	15	1000	Half-Full	10
T23	15	1000	Full	25
T24	15	1000	Full	10

ABAQUS Software Outputs

After simulating all 24 models in ABAQUS software, contour outputs of hoop stress and displacement are obtained.

Table 8. Maximum Hoop Stress and Displacement Values for All 24 Models

Maximum Displacement (cm)	Maximum Hoop Stress (MPa)	Model
1.12	17.4	T1
2.41	43.4	T2
1.40	24.8	T3
3.40	61.9	T4
1.62	29.7	T5
4.11	74.3	T6
1.20	21.7	T7

3.00	54.2	T8
1.70	30.9	T9
4.30	77.4	T10
2.00	37.1	T11
5.10	92.8	T12
1.10	20.4	T13
2.80	51.0	T14
1.64	29.1	T15
4.15	72.8	T16
1.90	34.9	T17
4.80	87.4	T18
1.40	25.5	T19
3.55	63.7	T20
2.09	36.4	T21 (RM)
5.00	91.0	T22
2.42	43.7	T23
6.12	109.2	T24

Optimal Design of the Cylindrical Reinforced Concrete Tank

The Particle Swarm Optimization (PSO) algorithm is a population-based optimization technique inspired by the social behavior of bird flocking or fish schooling. Each "particle" in the search space represents a potential solution. The main parameters of this algorithm are as follows:

- Population: A set of particles (n-particles).
- Position: The location of a particle in the search space (positions).
- Velocity: The direction and magnitude of a particle's movement (velocities).
- Personal Best: The best position experienced by each particle so far (pBest).
- Global Best: The best position found within the entire swarm (gBest).

The velocity and position of each particle are updated using Equations (4) and (5).

$$v_i(t+1) = w \times v_i(t) + c_1 \times r_1 \times \left(pBest_i - x_i(t)\right) + c_2 \times r_2 \times \left(gBest - x_i(t)\right) \quad (4)$$

$$x_i(t+1) = x_i(t) + v_i(t+1) \quad (5)$$

Where:

- $v_i(t)$ is the velocity of particle i at iteration t,
- $x_i(t)$ is the position of particle i at iteration t,
- w is the inertia weight,
- c_1 and c_2 are the cognitive and social acceleration coefficients, respectively,
- r_1 and r_2 are random numbers uniformly distributed between 0 and 1,
- $pB\ est$ is the personal best position of particle i, and
- $gBest$ is the global best position.

In this section, using the results from Table 5, a cylindrical reinforced concrete tank was designed using the PSO algorithm. The algorithm parameters were set as presented in Table 9.

Table 9. Initial parameters of the PSO algorithm

Maximum Number of Iterations	Cognitive Coefficient	Social Coefficient	Inertia Weight (w)	Number of Particles
100	1.5	1.5	0.7	50

It should be noted that the two design constraints were set as the maximum allowable hoop stress (30MPa) and maximum displacement (20mm). The optimal tank was designed for C30 concrete and steel with a yield strength of 400MPa. The tank height and diameter were 15 m and 33.85 m, respectively. The explosive mass and explosive distance were considered as 5000 kg and 50 m, respectively. In this optimal design, the objective function was to minimize the tank weight while simultaneously satisfying the maximum stress and displacement constraints. According to the executed code provided in Appendix (C), the

minimum weight of the cylindrical reinforced concrete tank using the PSO algorithm is 23933kN, which, as shown in Figure (3), is achieved after approximately 25 iterations.

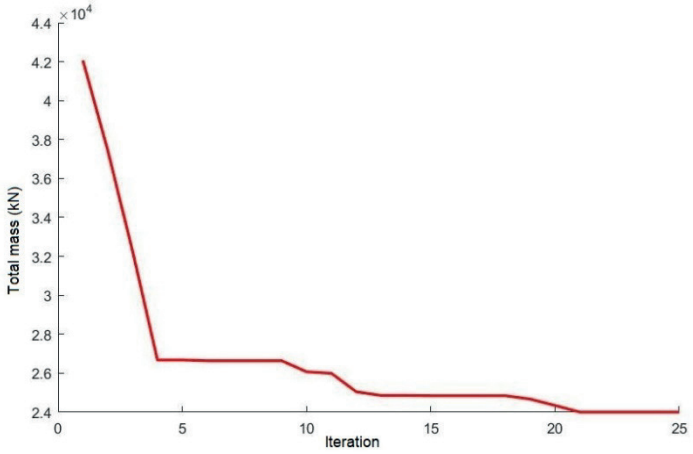

Figure 3. Optimized weight of the cylindrical reinforced concrete tank versus PSO algorithm iterations

Table 10 presents the geometric specifications of the weight-optimized cylindrical reinforced concrete tank.

Table 10. Geometric specifications of the optimal tank using the PSO algorithm

Parameter	Value
Total tank height	15m
Outer diameter of the cylindrical tank base	33.85m
Concrete cover for floor and wall	50mm
Tank wall thickness	440mm
Vertical reinforcement	Two layers of Φ25@150mm
Horizontal reinforcement (hoops)	Two layers of Φ32@150mm
Maximum hoop stress	26.76MPa
Maximum displacement	2.01cm

Determination of Fitted Curves for Problem Parameters

A fitted line (trend line) is a straight line that represents the best linear relationship between two variables. This line is drawn such that the overall distance of all data points from the line is minimized, while also passing through the majority of the data. In this section, the fitted line (regression) between various parameters and the hoop stress is calculated. The goal is to find the equation of a straight line $y = ax + b$ that best fits the data. To compute the slope and intercept of this line using the least squares method, Equations (6) and (7) are used.

$$a = \frac{\sum_{i=1}^{1000}(x_i - \bar{x})(y_i - \bar{y})}{\sum_{i=1}^{1000}(x_i - \bar{x})^2} \quad (6)$$

$$b = \bar{y} - a\bar{x} \quad (7)$$

Where $\bar{x}$ and $\bar{y}$ are the means of the n data points on the horizontal and vertical axes, respectively. According to Figure (4), an inverse and approximately linear relationship is observed between mesh size and hoop stress. As the mesh size decreases from 0.3m to 0.03m, the hoop stress increases from 5MPa to 55MPa. Finer meshing is capable of estimating the complex stress field resulting from the interaction of the blast wave and sloshing

phenomena with higher accuracy. This relationship also indicates a strong dependence of the finite element analysis results on the mesh size.

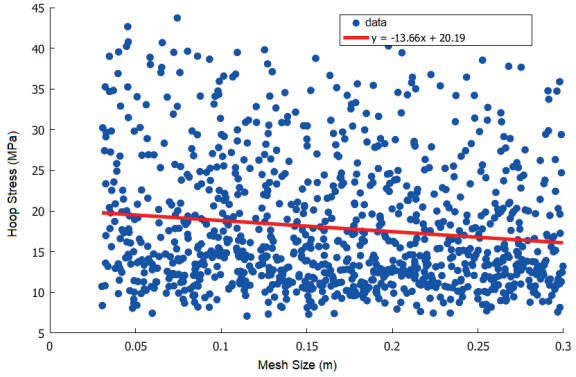

Figure 4. Correlation between hoop stress and mesh size

According to Figure (5), a parabolic relationship is observed with maximum stress occurring at a fluid height of 4-6 meters. At low fluid levels, the impulsive effect of the blast wave dominates. At moderate fluid heights, the phenomena of fluid-structure resonance and sloshing occur, while at high fluid levels, the damping effect of the fluid and hydrostatic pressure become significant.

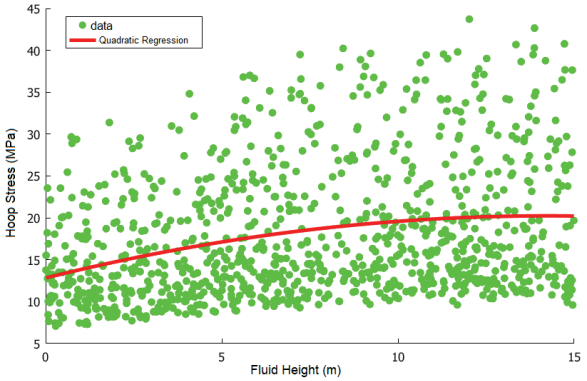

Figure 5. Correlation between hoop stress and fluid height

According to Figure (6), an increase in tank height has a negligible impact on the increase in hoop stress, with only a mild slope of growth. In contrast, as shown in Figure (7), increasing the explosive distance of the explosive from the tank causes a reduction in the tank's hoop stresses. Based on the present study, this parameter (explosive distance) is the most influential on the magnitude of hoop stress.

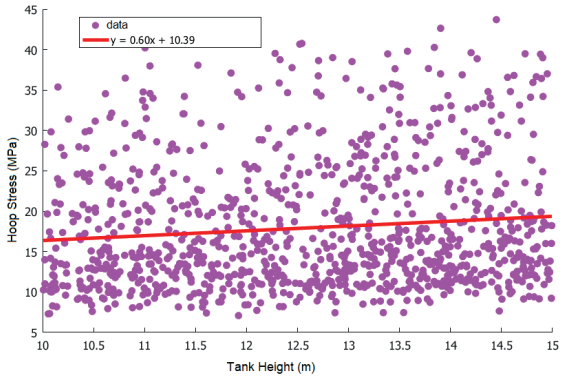

Figure 6. Correlation between hoop stress and tank height

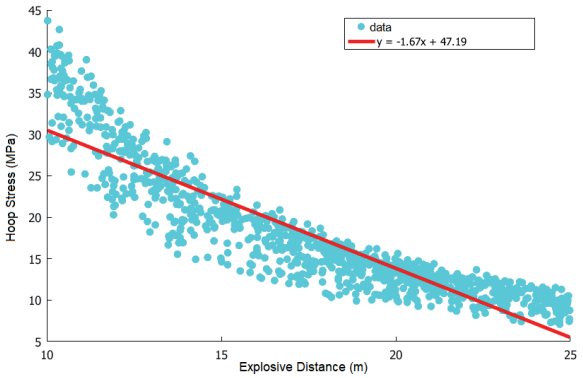

Figure 7. Correlation between hoop stress and explosive distance

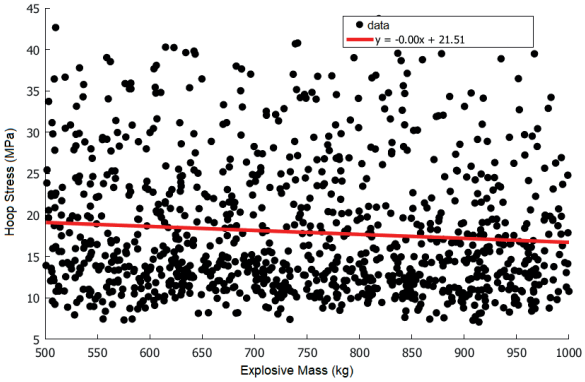

Figure 8. Correlation between hoop stress and explosive mass

As evident from Figure 8, increasing or decreasing the explosive mass within the variable distance range of 10 to 25 meters has an insignificant effect on the magnitude of hoop stress. This demonstrates the negligible influence of charge mass on hoop stress at larger standoff distances from the tank.

DISCUSSION AND CONCLUSION

In this research, the dynamic responses of cylindrical reinforced concrete water storage tanks under specified blast loading were investigated. The results indicate that parameters such as the water fill level, tank height-to-radius ratio, and distance from the blast center significantly influence the dynamic response of the tank structure. Specifically, the horizontal impulse increases with a decrease in water fill percentage and an increase in tank height. Furthermore, hoop stresses increase with a higher water fill level and a decrease in the standoff distance of the explosive. The most significant findings of this study are as follows:

- The optimal design of a cylindrical reinforced concrete tank using the Particle Swarm Optimization (PSO) algorithm for a specified fluid volume resulted in a reduction of the tank weight by approximately 4% after 25 iterations.
- A decrease in mesh size led to an increase in hoop stress, which is primarily attributed to stress concentration in the underlying elements.
- As the fluid height inside the tank increases, hoop stresses exhibit a parabolic pattern of increase.
- Increasing the tank height within the range of 10 to 15 meters does not significantly alter the hoop stresses.

REFERENCES

1. **B. Munson, D. Young, and T. Okiishi.** (2016). Fluid Mechanics. Wiley.
2. **L.M. Hoskins and L.S. Jcobsen.** (1934). Water pressure in a tank caused by simulated earthquake. Bulletin of the seismological society of America, 24, 1-32.
3. **G.W. Housner.** (1957). Dynamic pressures on accelerated fluid containers. Bulletin of the seismological society of America, 1-32.
4. **H.I. Epstin.** (1976). Seismic design of liquid storage tanks. J. Struct.Division – ASCE, 102, 1673-1659.
5. **M.A. Haroun.** (1980). Dynamic analyses of liquid storage tanks. EERL, 80-104.
6. **A.S. Veletsos.** (1984). Seismic response and design of liquid storage tanks. Guidelines for the seismic.
7. US Department of Army, the Navy and Air Force. (1990). the design of structures to resist the effects of accidental explosions. TM-5-1300.Washington DC: NAVFAV P-397, 559-920.
8. **L.R. Stein, R. A. Gentry, and C. W. Hirt.** (1977). Computational simulation of transient blast loading on three-dimensional structures. Computer Methods Applied, 11, 57-74.
9. **M.R. Bmbach.** (2013). Design of metal hollow section tubular columns subjected to transverse blast loads. Thin-Walled Structures, 68-105.
10. **Y. Wang, J.Y.R. Liew, and S.C. Lee.** (2015). Structural performance of water tank under static and dynamic pressure loading. International Journal of Impact Engineering, 85, 110-123.
11. **V. Mittal, T. Chakraborty, and V. Matsagar.** (2014). Dynamic analysis of liquid storage tank under blast using coupled Euler–Lagrange formulation. Thin-Walled Structures, 84, 91-111.
12. **J.Li, H. Hao, Y. Shi, Q. Fang, Z. Li, and L. Chen.** (2018). Experimental and computational fluid dynamics study of separation gap effect on gas explosion mitigation for methane storage tanks. Journal of Loss Prevention in the Process Industries, 55, 359-380.
13. **J. Li and H. Hao.** (2018). Far-field pressure prediction of a vented gas explosion from storage tanks by using new CFD simulation

guidance. Process Safety and Environmental Protection, 119, 360-378.
14. **R.L. Zhang, J.J. Jia, H.F. Wang, and Y.H. Guan.** (2018). Shock response analysis of a large LNG storage tank under blast loads. KSCE Journal of Civil Engineering, 9, 3419-3429.
15. **K. Hu and Y. Zhao.** (2016). Numerical simulation of internal gaseous explosion loading in large-scale cylindrical tanks with fixed roof. Thin-Walled Structures, 105, 16-28.
16. **P. Safa.** (2015). Investigation of explosion effect on the ground tank with floating roof. Shock and Vibration, Passive Defense, 1, 13-24.
17. **S. Yasseri.** (2015). Blast pressure distribution around large storage tanks. Blast information Group, 67, 133-134.
18. **W. Yonghui and Z. Hongyuan.** (2015). Numerical study of water tank under blast loading. Thin-Walled Structures, 90, 42-48.
19. **M. Alipour, M. Hosseini, H.R. Babaali, M. Raftari and R. Mahjoub.** (2025). Evaluation of the behavior of reinforced concrete above-ground tanks subjected to blast loading. Advances in Science and Technology Research Journal, 19(7), 1-24.
20. **M. Alipour, M. Hosseini, H. R. Babaali, M. Raftari and R. Mahjoub.** (2025). Investigation of Damage and Deformation of above-Ground RC Tanks under the Effect of Blast Load. Jordan Journal of Civil Engineering, 19(4), 637-653.
21. **M. Alipour, M. Hosseini, H. R. Babaali, M. Raftari and R. Mahjoub.** (2025). Investigating the behavior of above-ground concrete tanks under the blast load regarding the fluid-structure interaction. Curved and Layered Structures, 12, 1-16.
22. **Hosseini, M., Beiranvand, P., & Kalantari, L.** (2017). Investigation of influence the pressure and stress on the water in buried concrete pipes in the different soil under blast loading. Journal of Civil Engineering and Structures, 1(1), 52-66.
23. **M. Moghadam, S.V. Razavitosee, and M. Shahrbanouzadeh.** (2022). Dynamic analysis of reinforced concrete water tanks under blast considering fluid-structure interaction. Scientia Iranica, Transactions A: Civil Engineering, 29(6), 2902-2918.

СПИСОК ЛИТЕРАТУРЫ

1. **B. Munson, D. Young, and T. Okiishi.** (2016). Fluid Mechanics. Wiley.
2. **L.M. Hoskins and L.S. Jcobsen.** (1934). Water pressure in a tank caused by simulated earthquake. Bulletin of the seismological society of America, 24, 1-32.
3. **G.W. Housner.** (1957). Dynamic pressures on accelerated fluid containers. Bulletin of the seismological society of America, 1-32.
4. **H.I. Epstin.** (1976). Seismic design of liquid storage tanks. J. Struct.Division – ASCE, 102, 1673-1659.
5. **M.A. Haroun.** (1980). Dynamic analyses of liquid storage tanks. EERL, 80-104.
6. **A.S. Veletsos.** (1984). Seismic response and design of liquid storage tanks. Guidelines for the seismic.
7. US Department of Army, the Navy and Air Force. (1990). the design of structures to resist the effects of accidental explosions. TM-5-1300.Washington DC: NAVFAV P-397, 559-920.
8. **L.R. Stein, R.A. Gentry, and C.W. Hirt.** (1977). Computational simulation of transient blast loading on three-dimensional structures. Computer Methods Applied, 11, 57-74.
9. **M.R. Bmbach.** (2013). Design of metal hollow section tubular columns subjected to transverse blast loads. Thin-Walled Structures, 68-105.
10. **Y. Wang, J.Y.R. Liew, and S.C. Lee.** (2015). Structural performance of water tank under static and dynamic pressure loading. International Journal of Impact Engineering, 85, 110-123.
11. **V. Mittal, T. Chakraborty, and V. Matsagar.** (2014). Dynamic analysis of liquid storage tank under blast using

coupled Euler–Lagrange formulation. Thin-Walled Structures, 84, 91-111.
12. **J.Li, H. Hao, Y. Shi, Q. Fang, Z. Li, and L. Chen.** (2018). Experimental and computational fluid dynamics study of separation gap effect on gas explosion mitigation for methane storage tanks. Journal of Loss Prevention in the Process Industries, 55, 359-380.
13. **J. Li and H. Hao.** (2018). Far-field pressure prediction of a vented gas explosion from storage tanks by using new CFD simulation guidance. Process Safety and Environmental Protection, 119, 360-378.
14. **R. L. Zhang, J.J. Jia, H.F. Wang, and Y.H. Guan.** (2018). Shock response analysis of a large LNG storage tank under blast loads. KSCE Journal of Civil Engineering, 9, 3419-3429.
15. **K. Hu and Y. Zhao.** (2016). Numerical simulation of internal gaseous explosion loading in large-scale cylindrical tanks with fixed roof. Thin-Walled Structures, 105, 16-28.
16. **P. Safa.** (2015). Investigation of explosion effect on the ground tank with floating roof. Shock and Vibration, Passive Defense, 1, 13-24.
17. **S. Yasseri.** (2015). Blast pressure distribution around large storage tanks. Blast information Group, 67, 133-134.
18. **W. Yonghui and Z. Hongyuan.** (2015). Numerical study of water tank under blast loading. Thin-Walled Structures, 90, 42-48.
19. **M. Alipour, M. Hosseini, H.R. Babaali, M. Raftari and R. Mahjoub.** (2025). Evaluation of the behavior of reinforced concrete above-ground tanks subjected to blast loading. Advances in Science and Technology Research Journal, 19(7), 1-24.
20. **M. Alipour, M. Hosseini, H. R. Babaali, M. Raftari and R. Mahjoub.** (2025). Investigation of Damage and Deformation of above-Ground RC Tanks under the Effect of Blast Load. Jordan Journal of Civil Engineering, 19(4), 637-653.
21. **M. Alipour, M. Hosseini, H. R. Babaali, M. Raftari and R. Mahjoub.** (2025). Investigating the behavior of above-ground concrete tanks under the blast load regarding the fluid-structure interaction. Curved and Layered Structures, 12, 1-16.
22. **Hosseini, M., Beiranvand, P., & Kalantari, L.** (2017). Investigation of influence the pressure and stress on the water in buried concrete pipes in the different soil under blast loading. Journal of Civil Engineering and Structures, 1(1), 52-66.
23. **M. Moghadam, S.V. Razavitosee, and M. Shahrbanouzadeh.** (2022). Dynamic analysis of reinforced concrete water tanks under blast considering fluid-structure interaction. Scientia Iranica, Transactions A: Civil Engineering, 29(6), 2902-2918.

Majid Alipour — Ph.D. in Civil Engineering (Structural Engineering), Civil Engineer, Supervision Department, Bank Maskan of Lorestan Province (Bank Maskan), Khorramabad, Lorestan Province, Iran. E-mail: majidalipour.2024.1980@gmail.com

Mojtaba Hosseini — Ph.D. in Civil Engineering, Associate Professor, Department of Civil Engineering, Lorestan University, Khorramabad, Iran. E-mail: hosseini.m@lu.ac.ir.

Peyman Beiranvand — Ph.D. in Civil Engineering, Lecturer, Department of Civil Engineering, Lorestan University (LU), Khorramabad, Iran. E-mail: p_beiranvand@civileng.iust.ac.ir

Алипур Маджид — доктор философии (PhD) в области гражданского строительства (строительные конструкции), инженер Управления Банка жилищного строительства провинции Лурестан (*Bank Maskan of Lorestan Province*; Хорремабад, провинция Лурестан, Исламская Республика Иран; e-mail: majidalipour.2024.1980@gmail.com

Хоссейни Моджстаба — PhD в области гражданского строительства, доцент кафедры гражданского строительства Университета Лурестана (*Lorestan University*, *LU*), Хорремабад, Иран. E-mail: hosseini.m@lu.ac.ir

Бейранванд Пейман — PhD в области гражданского строительства, преподаватель кафедры гражданского строительства Университета Лурестана (*Lorestan University*, *LU*), Хорремабад, Иран. E-mail: p_beiranvand@civileng.iust.ac.ir

DOI:10.22337/2587-9618-2026-22-2-126-137

OPTIMIZATION OF CONCRETE CURING CONDITIONS IN MASSIVE MONOLITHIC FOUNDATION SLABS

Vasilina S. Tyurina, Anton S. Chepurnenko, Batyr M. Yazyev
Don State Technical University, Rostov-on-Don, RUSSIA

Abstract: The problem of controlling temperature stresses and preventing early cracking in massive monolithic foundation slabs at the stage of their hardening is considered. Existing methods often fail to account for the lag in concrete strength growth relative to the development of temperature gradients, which can lead to dangerous tensile stresses. The objective of the study is to develop a method for optimizing curing conditions aimed at minimizing tensile stress to strength ratio as an objective function. The method is based on combined numerical modeling of heat transfer and stress-strain problems, taking into account the kinetics of heat generation and concrete strength gain. The variable parameters were a coefficient determining the kinetics of concrete heat generation and the heat transfer coefficient from the upper surface of the slab. The interior point method, pattern search and particle swarm optimization were used to solve the optimization problem. Calculation results for various slab thicknesses and climatic conditions showed that to minimize the risk of cracking, it is necessary to reduce the heat transfer coefficient on the upper surface of the slab to 2.5–4.7 W/(m² °C), and to use normal- and rapid-hardening concrete rather than slow-hardening concrete. This is explained by the lag in tensile strength growth behind the development of temperature differences in slow-hardening concrete. Optimization reduced tensile stress levels by 2.2–3.3 times compared to standard conditions, making it possible to concretize slabs up to 3 m thick without the use of artificial cooling systems.

Keywords: massive foundation slabs, early cracking, thermal stresses, curing optimization, concrete heat release kinetics, heat transfer, particle swarm method, rapid-hardening concrete, thermal insulation

ОПТИМИЗАЦИЯ УСЛОВИЙ ТВЕРДЕНИЯ БЕТОНА В МАССИВНЫХ МОНОЛИТНЫХ ФУНДАМЕНТНЫХ ПЛИТАХ

В.С. Тюрина, А.С. Чепурненко, Б.М. Язьев
Донской государственный технический университет, г. Ростов-на-Дону, РОССИЯ

Аннотация: Рассматривается проблема контроля температурных напряжений и предотвращения раннего трещинообразования массивных монолитных фундаментных плит на стадии их возведения. Существующие методы часто не учитывают запаздывание в росте прочности бетона относительно развития температурных градиентов, что может привести к опасным уровням растягивающих напряжений. Целью исследования является разработка метода оптимизации условий твердения, направленного на минимизацию отношения растягивающего напряжения к прочности на растяжение в качестве целевой функции. Метод основан на комбинированном численном моделировании задач теплопередачи и напряженно-деформированного состояния задач, учитывающем кинетику тепловыделения и прироста прочности бетона. Переменными параметрами являлись коэффициент, определяющий кинетику тепловыделения бетона, и коэффициент теплопередачи с верхней поверхности плиты. Для решения задачи оптимизации использовались метод внутренней точки, метод шаблонного поиска и метод роя частиц. Результаты расчетов для различной толщины плит и климатических условий показали, что для минимизации риска раннего трещинообразования необходимо снизить коэффициент теплопередачи на верхней поверхности плиты до 2,5–4,7 Вт/(м².°С) и использовать бетон нормального и быстрого твердения вместо медленно твердеющего бетона. Это объясняется задержкой в росте прочности на растяжение по сравнению с развитием температурных перепадов в медленно твердеющем бетоне. В результате оптимизации уровни растягивающих напряжений снижены в 2,2–3,3 раза по сравнению со стандартными условиями, что позволяет бетонировать плиты толщиной до 3 м без использования систем искусственного охлаждения.

Ключевые слова: массивные фундаментные плиты, раннее трещинообразование, температурные напряжения, оптимизация твердения, кинетика тепловыделения бетона, теплоотдача, метод роя частиц, быстротвердеющий бетон, теплоизоляция

INTRODUCTION

The problem of monitoring thermal stresses in massive concrete and reinforced concrete structures during their construction is a pressing issue in global construction practice [1-3]. When constructing high-rise buildings and structures, as well as multi-story buildings, foundation slabs at least 1 m thick are used, which fall into the category of massive structures, necessitating an assessment of the risk of early cracking and the development of measures to prevent it [4-6].

Traditionally, the use of slow-hardening concrete is recommended to reduce the risk of early cracking, which reduces peak temperature differences [7-11]. However, this approach often fails to account for the lag in the growth of strength properties relative to the development of temperature gradients, which can lead to dangerous levels of tensile stress.

In recent years, considerable attention has been devoted to methods of numerical modeling of thermal and stress fields in massive structures [12-14]. Studies [15-18] demonstrate the effectiveness of using surface thermal insulation for temperature control. However, most studies are limited to analyzing temperature fields without comprehensively considering the kinetics of strength gain and the development of concrete's mechanical properties.

Modern approaches to optimizing curing conditions are based on the combined solution of heat transfer and deformation mechanics problems using numerical optimization methods. Simplified models for assessing the stress-strain state of foundation slabs have been proposed in [19-21]. However, the targeted selection of concrete parameters and heat transfer conditions to minimize tensile stresses remains understudied. In particular, there are no methods for simultaneously optimizing the kinetics of concrete heat release and the intensity of surface heat transfer, taking into account various climatic conditions and geometric parameters of structures.

A literature review revealed a lack of comprehensive methods for optimizing the curing conditions of massive foundation slabs, aimed at minimizing tensile stress as an objective function. Existing recommendations for the use of slow-hardening concrete do not take into account the effect of delayed strength characteristics on stress, which can lead to suboptimal design solutions. Therefore, developing a method for determining optimal heat generation and heat transfer kinetics from the slab's upper surface for various concreting conditions is a pressing scientific and practical challenge. The results of this study will enable informed selection of concrete compositions and thermal insulation parameters that minimize the risk of cracking.

The purpose of the work is to develop a methodology for optimizing the conditions of concrete hardening in massive monolithic foundation slabs, aimed at minimizing the risk of early cracking by reducing the level of tensile stresses in the initial period of hardening.

Within the framework of the set goal, the following tasks were solved:

1. To develop a calculation model describing the combined influence of the kinetics of heat generation in concrete and heat exchange conditions on the formation of temperature fields and the stress-strain state in massive monolithic foundation slabs.
2. To define the optimization objective function and select the variable parameters.
3. To conduct a series of calculations for various slab sizes and climatic conditions using nonlinear optimization methods (interior point method, pattern search method, particle swarm method).
4. To analyze the obtained optimal parameter values, evaluate the effectiveness of various optimization methods and the influence of initial conditions on the result.
5. To formulate practical recommendations for the selection of concrete and optimal heat transfer parameters to reduce tensile stresses in massive foundation slabs without the use of artificial cooling systems.

METHODS

The maximum level of tensile stresses was adopted as the objective function when solving the problem of determining the optimal conditions for concrete hardening in massive monolithic foundation slabs:

$$f = \frac{\sigma}{R_t} \to \min , \quad (1)$$

where σ is the tensile stress, R_t is the current tensile strength of concrete.

The determination of the maximum level of tensile stresses was carried out using a simplified method given in [19]. In the first stage, the temperature field was calculated in a one-dimensional formulation using the equation:

$$\lambda \frac{\partial^2 T}{\partial z^2} + W = \rho c \frac{\partial T}{\partial t}, \quad (2)$$

where λ is the thermal conductivity coefficient of the material, T is the temperature, $W = \frac{\partial Q}{\partial t}$ is the power of internal heat sources for 1 m^3 of concrete, ρ is the density, c is the specific heat capacity.

The temperature field was calculated using the finite element method in conjunction with a soil massif whose thickness was assumed to be constant and equal to 3 m. The values of the thermophysical characteristics of the soil and concrete adopted in the calculation are presented in Table 1.

Table 1. Thermophysical characteristics of soil and concrete

	Density ρ, kg/m^3	Specific heat capacity c, J/(kg·°C)	Thermal conductivity coefficient λ, W/(m·°C)
Soil	1600	1875	1.50
Concrete	2400	1000	2.67

On the upper surface, boundary conditions of the third kind were adopted (convective heat exchange with the environment):

$$\lambda \frac{\partial T}{\partial z} + h_{up}\left(T - T_\infty\right) = 0, \quad (3)$$

where T_∞ is the ambient temperature, h_{up} is the heat transfer coefficient on the upper surface.

At the lower surface of the soil massif, boundary conditions of the first kind were adopted (the temperature is constant and equal to T_{bot}). The heat release function of concrete was taken as [22]:

$$Q(t) = Q_{28} \cdot \exp\left[k \cdot \left(1 - \left(\frac{28}{t}\right)^x\right)\right], \quad (4)$$

where t is the time in days, Q_{28} is the amount of heat released during the first 28 days of hardening (MJ/m^3), the coefficients k and x depend on the rate of hardening of the concrete.

When calculating temperature stresses, the dependence of the mechanical characteristics of concrete on the equivalent age t_{eq} was taken into account. The equivalent age was calculated by the formula:

$$t_{eq} = \frac{1}{T_{ref}} \int_0^t T(\tau)\, d\tau, \quad (5)$$

where $T_{ref} = 20°C$ is the temperature corresponding to normal conditions, $T(\tau)$ is the temperature at an arbitrary point of the foundation slab at age τ.

The function of change in cubic strength under compression was taken as [23]:

$$R = R_{28} \exp\left(s\left(1 - \sqrt{28 / t_{eq}}\right)\right), \quad (6)$$

where t_{eq} is the equivalent age of concrete in days, R_{28} is the compressive strength at the age

of 28 days (when hardening under normal conditions), s is a coefficient depending on the kinetics of concrete hardening.
Table 2 presents the values of the coefficients k, x and s according to data [24].

Table 2. Values of coefficients k, x, s according to data [24]

	Classification of concrete according to EN 206.1			
	Rapid hardening	Normally hardening	Slow hardening	Very slow hardening
k	≤ 0.15	0.16-0.2	0.21-0.24	> 0.24
x	≤ 0.45	0.46-0.51	0.52-0.62	> 0.62
s	< 0.25	0.25-0.43	0.43-0.7	≥ 0.7

This table shows a tendency towards an increase in the coefficient *s* together with the coefficient *k.* The same applies to the coefficient *x.* Therefore, the coefficient *k* was chosen as the first variable parameter determining the kinetics of heat release of concrete, and the coefficients *x* and *s* were expressed through the coefficient *k* using approximating formulas:

$$x = 17.2 \cdot k^2 - 4.83 \cdot k + 0.787; \quad s = 4.94 \cdot k - 0.512. \tag{7}$$

The modulus of elasticity of concrete at equivalent age t_{eq} was determined as a function of its compressive strength based on the formula [25]:

$$E = 22265 \cdot \left(\frac{R}{10}\right)^{0.28}. \tag{8}$$

Until the equivalent age of 12 hours, it was considered that concrete was not yet a solid body capable of withstanding stress, and the modulus of elasticity was taken to be zero.
Tensile strength, like the modulus of elasticity, was taken as a function of compressive strength [26]:

$$R_t = 0.29 R^{0.6}. \tag{9}$$

The calculations were performed at R_{28} = 37 MPa, Poisson's ratio of concrete $\nu = 0.2$, coefficient of linear thermal expansion $\alpha = 10^{-5}\,1/°C$. The value Q_{28} was taken as constant and equal to 130 MJ/ m^3.
The second optimized variable was the parameter h_{up}. In the calculation program, up to the age of 12 hours, the heat transfer coefficient on the upper surface was assumed to be 23 W/(m^2·°C), as for an uncovered surface. Subsequently, the heat transfer coefficient was assigned the value h_{up}.
The search for the minimum of the objective function $f\left(k, h_{up}\right)$ was implemented in the MATLAB R2021b environment using three built-in nonlinear optimization methods:

1. Interior point method.
2. Pattern search method.
3. Particle swarm method.

The parameters of the optimization algorithms in MATLAB were set to default values. The values $k = 0.18$ and $h_{up} = 23\ \mathrm{W}/\left(\mathrm{m}^2 \cdot °\mathrm{C}\right)$ were chosen as the starting point for the search, which corresponds to normally hardening concrete and standard heat transfer for external walls, roofs, and ceilings according to Russian design codes SR 23-101-2004. Thermal performance desing of buildings.
For input parameters k and h_{up} the following constraints were adopted:

$$0.1 \le k \le 0.4; \quad 0.5 \le h_{up} \le 23. \tag{10}$$

A series of nine calculations was performed for different values of ambient temperature T_∞, soil temperature T_{bot}, initial concrete mix temperature T_0, and slab thickness h. The initial data for each case, as well as the objective function values f at the initial search point, are presented in Table 3.

Table 3. Considered variants of initial data for solving the optimization problem

No.	h, m	T_∞, °C	T_0, °C	T_{bot}, °C	f
1	1	5	10	5	0.581
2	1	15	15	15	0.724
3	1	25	20	20	0.927
4	2	5	10	5	1.528
5	2	15	15	15	1.637
6	2	25	20	20	1.769
7	3	5	10	5	2.219
8	3	15	15	15	2.239
9	3	25	20	20	2.277

RESULTS AND DISCUSSION

Table 4 shows the results of solving the optimization problem in the form of optimal values of parameters k and h_{up}, as well as the corresponding value of the objective function f for each option considered using three methods. The best solutions for each option are underlined.

Table 4 shows that the three methods used yielded roughly the same results. The particle swarm method proved to be the most stable for this problem, providing the best solution in eight of the nine variants considered. However, this method has the highest computational complexity, as it evaluates the objective function value at multiple search points rather than just one at each iteration. It should also be noted that the interior point method finds a local maximum in the vicinity of the initial search point, but not a global one, unlike the other two methods used.

As a result of optimization, the maximum values of the tensile stress level were reduced from 2.2 to 3.3 times compared to the initial search point, corresponding to the average heat release kinetics of concrete and the uncovered upper surface.

Based on the obtained solutions, optimal heat transfer coefficient values range from 2.51 to 4.73 W/(m^2·°C), indicating the feasibility of insulating the upper surface. This method for reducing the risk of early cracking is generally accepted and has been previously discussed in [15-18, 27].

Table 4. Results of solving the optimization problem

No.	Method	k	h_{up}	f
1	Interior point	0.219	3.502	0.261
	Pattern search	0.219	3.474	0.261
	Particle swarm	0.220	3.436	0.260
2	Interior point	0.202	4.726	0.280
	Pattern search	0.182	2.794	0.309
	Particle swarm	0.201	4.561	0.280
3	Interior point	0.159	3.032	0.282
	Pattern search	0.149	2.510	0.288
	Particle swarm	0.159	3.032	0.282
4	Interior point	0.138	2.786	0.519
	Pattern search	0.138	2.795	0.519
	Particle swarm	0.138	2.786	0.519
5	Interior point	0.121	3.011	0.523
	Pattern search	0.128	3.131	0.524
	Particle swarm	0.121	3.034	0.521
6	Interior point	0.113	3.979	0.562
	Pattern search	0.115	4.000	0.562
	Particle swarm	0.100	3.919	0.570
7	Interior point	0.172	2.903	0.819
	Pattern search	0.151	2.820	0.805
	Particle swarm	0.127	2.645	0.802
8	Interior point	0.131	2.687	0.798
	Pattern search	0.144	2.750	0.806
	Particle swarm	0.131	2.687	0.798
9	Interior point	0.122	3.235	0.852
	Pattern search	0.125	3.250	0.853
	Particle swarm	0.122	3.235	0.852

The required thickness of thermal insulation can be calculated based on the formula for the heat transfer coefficient from the insulated surface [27]:

$$h_f = \frac{1}{\sum \frac{\delta_i}{\lambda_i} + \frac{1}{h_{surf}}}, \qquad (11)$$

where h_{surf} is the heat transfer coefficient from an uninsulated surface, δ_i is the thickness of the i-th insulation layer, λ_i is the thermal conductivity coefficient of the i-th insulation layer.

For one layer of insulation, its required thickness can be calculated using the formula:

$$\delta_1 = \lambda_1 \left(\frac{1}{h_f} - \frac{1}{h_{surf}} \right). \quad (12)$$

For example, for the "Penofol" insulation (closed-cell polyethylene foam with a thin layer of aluminum foil) at h_{surf} = 23 W/(m^2·°C) and λ_1 = 0.045 W/(m·°C), the optimal heat transfer coefficient of 2.51-4.73 W/(m^2·°C) corresponds to a thickness of 7.5 to 16 mm.

The optimal values of the coefficient k, which determines the heat release kinetics of concrete, range from 0.1 to 0.22, indicating a preference for normal and rapid-hardening concrete over slow-hardening concrete. Furthermore, with increasing slab thickness and ambient temperature, the optimal k value tends to decrease, suggesting that under these conditions, rapid-hardening and ultra-rapid-hardening concrete are preferable.

This finding regarding the undesirability of using slow-hardening concrete in massive foundation slabs contradicts generally accepted opinion [7-9]. However, authors who postulate the necessity of using slow-hardening concrete in massive structures use the maximum temperature within the structure and the temperature difference between the center and surface of the structure, rather than the level of tensile stress, to assess the risk of early cracking.

Our finding regarding the undesirability of using slow-hardening concrete can be explained by the fact that the rate of increase in strength properties of such concrete lags behind the kinetics of heat release and, consequently, the development of maximum temperature differences between the center and surface of the structure. Let's examine this in detail using option 6 as an example. Figure 1 shows heat release curves plotted for k = 0.18 (initial approximation), k = 0.115 (optimal solution), and k = 0.24 (slow-hardening concrete).

Fig. 2 shows the change in time of the maximum temperature difference ΔT between the center and the upper surface of the structure for the initial approximation, at k = 0.115 and h_{up} = 4 W/(m^2·°C) (optimal solution) and for slow-hardening concrete at k = 0.24 and h_{up} = 4 W/(m^2·°C). A decrease in heat transfer on the upper surface leads to a decrease in the maximum value ΔT from 22 to 11 ° C. In the case of using slow-hardening concrete, the maximum temperature difference, compared to rapid-hardening concrete, is reduced insignificantly (by only 0.2 °C)

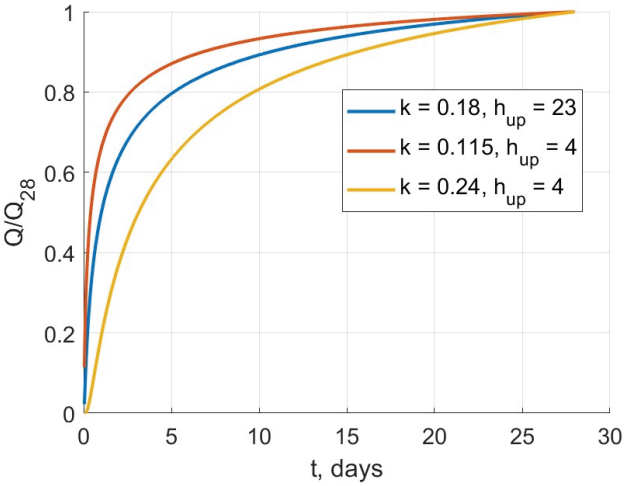

Figure 1. Heat release curves

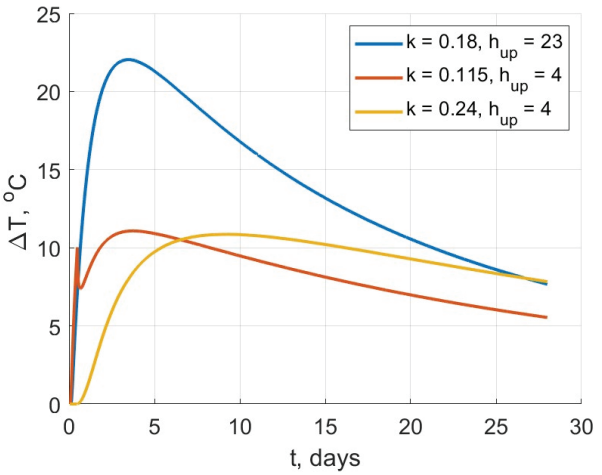

Figure 2. Change in time of the maximum temperature difference ΔT between the center and the upper surface of the structure

The maximum temperature difference for rapid-hardening concrete at k = 0.115 is reached at t = 3.7 days, and at this age, the tensile strength is 96% of the strength at 28 days (Fig. 3). For slow-hardening concrete, the maximum temperature difference is reached at

t = 9.3 days , and at this age, the R_t value is 81% of the strength at 28 days, which is significantly less than for rapid-hardening concrete. Moreover, Fig. 3 shows that the growth of the concrete elasticity modulus outpaces the growth of tensile strength. All this taken together leads to the fact that the maximum tensile stress level for slow-hardening concrete, with the same value of the heat transfer coefficient, is significantly higher than for rapid-hardening concrete (1.13 versus 0.56). A comparison of the curves for the change in stress level over time is shown in Fig. 4.

Another important feature should also be noted in Fig. 4. The curves of change σ/R_t at h_{up} = 4 W/(m^2·°C) (yellow and red lines) have two maximum points and a kink. The kink in these graphs is due to the change in the position of the critical point where the maximum tensile stress is reached (the critical point moves from the upper surface to the lower surface). For the optimized curve (red line), the maximum values at the two critical points coincide, indicating that the structure is of equal strength. It is well known that equal strength of a structure is one of the criteria for its optimality [28-30].

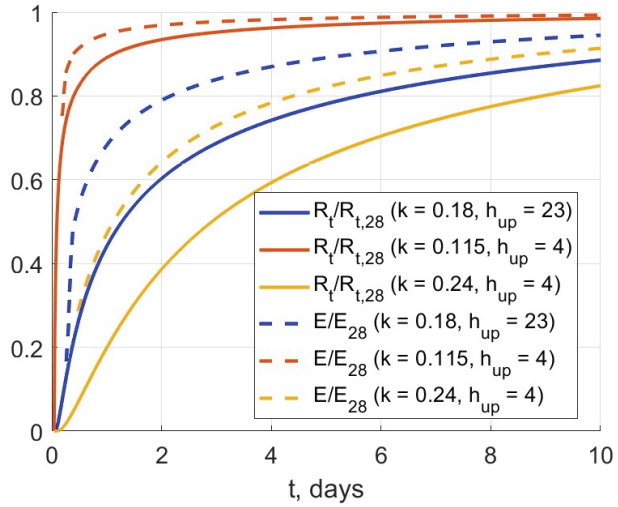

Figure 3. Curves of relative change in concrete tensile strength and elastic modulus over time (values are calculated based on the temperatures of the upper surface of the slab)

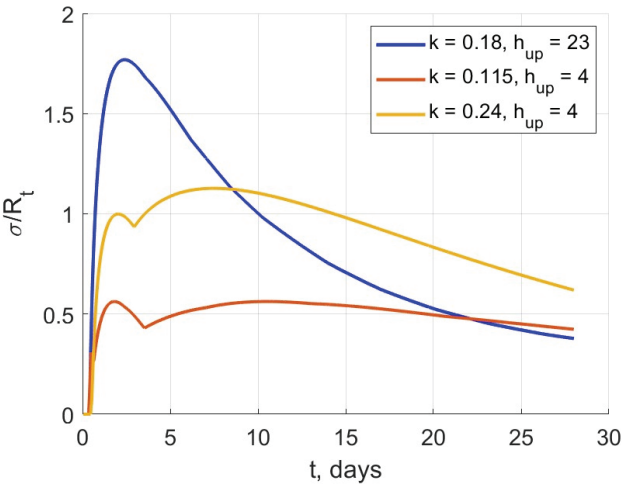

Figure 4. Comparison of stress level change curves over time

The use of the developed optimization methodology makes it possible to determine curing conditions under which it is possible to concrete foundation slabs up to 3 m thick or more without the use of expensive cooling systems.

CONCLUSION

1. The methodology for optimizing concrete curing conditions in massive monolithic foundation slabs has been developed and tested. This methodology aims to minimize the tensile stress level σ/R_t as an objective function. The methodology is based on a combined solution to the heat transfer problem and the stress-strain state, taking into account the kinetics of heat release and concrete strength gain.

2. It has been established that the most effective way to reduce the risk of early cracking is the combined control of two parameters: the kinetics of heat release from concrete (through the coefficient k) and the intensity of heat transfer from the upper surface of the slab (through the coefficient h_{up}).

3. Optimization showed that to minimize tensile stresses it is necessary to:

- reduce the heat transfer coefficient h_{up} to values of 2.5–4.7 W/(m²·°C), which corresponds to the use of thermal insulation coatings on the surface of the slab.

- use normal and rapid-hardening concrete, not slow-hardening concrete.

4. The obtained result contradicts the widespread belief that slow-hardening concrete is preferable for massive structures. It was shown that when using slow-hardening concrete, the increase in tensile strength lags behind the development of temperature changes, leading to higher tensile stress levels compared to rapid-hardening concrete, all other things being equal.

5. The particle swarm method demonstrated the best efficiency in solving the given optimization problem, providing the lowest values of the objective function in 8 of the 9 considered variants, despite the increased computational complexity.

6. The proposed method reduces tensile stress by 2.2–3.3 times compared to typical conditions (uninsulated surface, normally hardening concrete). This opens the possibility of concreting massive foundation slabs up to 3 meters thick or more without the need for complex and expensive artificial cooling systems.

7. The equal strength criterion of the structure, observed with optimal parameters (coincidence of stress maxima at different points of the section), confirms the correctness and effectiveness of the proposed approach to the design of hardening conditions for massive concrete structures.

ACKNOWLEDGEMENTS

The study was supported by the grant of the Russian Science Foundation, No. 25-19-00164, https://rscf.ru/project/25-19-00164/.

REFERENCES

1. **Li X. et al.** (2023) Investigation of temperature development and cracking control strategies of mass concrete: A field monitoring case study. Case Studies in Construction Materials, vol. 18, e02144. doi: 10.1016/j.cscm.2023.e02144
2. **Xie Y. et al.** (2023) Temperature field evolution of mass concrete: From hydration dynamics, finite element models to real concrete structure. Journal of Building Engineering, vol. 65, 105699. doi: 10.1016/j.jobe.2022.105699
3. **Sheng X. et al.** (2023) Experimental and finite element investigations on hydration heat and early cracks in massive concrete piers. Case Studies in Construction Materials, vol. 18, e01926. doi: 10.1016/j.cscm.2023.e01926
4. **Bilčík J., Sonnenschein R., Gažovičová N**. (2017) Causes of early-age thermal cracking of concrete foundation slabs and their reinforcement to control the cracking. Slovak Journal of Civil Engineering, vol. 25, no. 3, pp. 8–15. doi: 10.1515/sjce-2017-0013
5. **Nesvetaev G.V., Koryanova Yu.I., Shut V.V.** (2024) Specific heat dissipation of concrete and the risk of early cracking of massive reinforced concrete foundation slabs. Construction Materials and Products, vol. 7, no. 3. doi: 10.58224/2618-7183-2024-7-4-3
6. **Klemczak B., Żmij A.** (2021) Insight into thermal stress distribution and required reinforcement reducing early-age cracking in mass foundation slabs. Materials, vol. 14, no. 3, 477. doi: 10.3390/ma14030477
7. **Afsoosbiria H., Machowska A.** (2025) Development of Sustainable Concrete Using By-Products as a Green Material, and Potential Solutions for Sustainability in Mass Concrete Construction—Comprehensive Review. Sustainability, vol. 17, no. 22, 9983. doi: 10.3390/su17229983
8. **Singh M. P. et al.** (2024) Early age cracking relevant to mass concrete dam structures during the construction schedule. Construction and Building Materials, vol. 411, 134739. doi: 10.1016/j.conbuildmat.2023.134739
9. **Justnes H., Wuyts F., Van Gemert D.** (2008) Hardening retarders for massive concrete. 5th Int. Conf. on High Perfor-

mance Concrete Location, Manaus, Brazil, pp. 18–20.
10. **De Schutter G., Vuylsteke M.** (2004) Minimisation of early age thermal cracking in a J-shaped non-reinforced massive concrete quay wall. Engineering Structures, vol. 26, no. 6, pp. 801–808. doi: 10.1016/j.engstruct.2004.01.013
11. **Kastornykh L. et al.** (2021) Modified concrete mixes for monolithic construction. Materials Science Forum, vol. 1043, pp. 81–91. doi: 10.4028/www.scientific.net/MSF.1043.81
12. **Smolana A. et al.** (2022) Thermo-mechanical analysis of mass concrete foundation slabs at early age—essential aspects and experiences from the FE modelling. Materials, vol. 15, no. 5, 1815. doi: 10.3390/ma15051815
13. **Smolana A., Jędrzejewska A., Klemczak B.** (2025) Addressing Thermal Cracking in Polish Infrastructure: A Case Study. International RILEM Conference on Early-age and Long-term Cracking in RC Structures. Cham: Springer Nature Switzerland, pp. 239–250. doi: 10.3390/ma17153700
14. **Klemczak B., Smolana A.** (2024) Multi-Step Procedure for Predicting Early-Age Thermal Cracking Risk in Mass Concrete Structures. Materials, vol. 17, no. 15, 3700. doi: 10.3390/ma17153700
15. **Nguyen C.T., Luu X.B. (**2019) Reducing temperature difference in mass concrete by surface insulation. Magazine of Civil Engineering, no. 4 (88), pp. 70–79. doi: 10.18720/MCE.88.7
16. **Chen Y.Y. et al.** (2017) Effects of insulation materials on mass concrete with pozzolans. Construction and Building Materials, vol. 137, pp. 261–271. doi: 10.1016/j.conbuildmat.2017.01.059
17. **Aniskin N.A., Chuc N.T., Khanh P.K.** (2021) The use of surface thermal insulation to regulate the temperature regime of a mass concrete during construction. Power Technology and Engineering, vol. 55, no. 1, pp. 1–7. doi: 10.1007/s10749-021-01310-6
18. **Chuc N.T. et al.** (2018) The effects of insulation thickness on temperature field and evaluating cracking in the mass concrete. Electronic Journal of Structural Engineering, vol. 18, no. 2, pp. 128–132. doi: 10.56748/ejse.182722
19. **Chepurnenko A.S. et al.** (2022) Simplified model for determining the stress strain state in massive monolithic foundation slabs during construction. International Journal for Computational Civil and Structural Engineering, vol. 18, no. 3, pp. 126–136. doi: 10.22337/2587-9618-2022-18-3-126-136
20. **Cha S.L., Jin S.S**. (2020) Prediction of thermal stresses in mass concrete structures with experimental and analytical results. Construction and Building Materials, vol. 258, 120367. doi: 10.1016/j.conbuildmat.2020.120367
21. **Korotchenko I.A. et al.** (2017) Deformation of concrete creep in the thermal stress state calculation of massive concrete and reinforced concrete structures. Magazine of Civil Engineering, no. 1 (69), pp. 56–63. doi: 10.18720/MCE.69.5
22. **Nesvetaev G.V. et al.** (2025) Heat dissipation of cement and design the composition of concrete for massive structures. Construction Materials and Products, vol. 8, no. 1, 3. doi: 10.58224/2618-7183-2025-8-1-3
23. **Nesvetaev G.V., Koryanova Yu.I.** (2023) Prognoz kinetiki prochnosti betona pri tverdenii v usloviyakh, otlichnykh ot normal'nykh [Forecast of concrete strength kinetics under hardening conditions different from normal]. Sovremennye tendentsii v stroitel'stve, gradostroitel'stve i planirovke territorii, vol. 2, no. 4, pp. 59–68. doi: 10.23947/2949-1835-2023-2-4-59-68
24. **Nesvetaev G.V., Koryanova Y.I., Yazyev B.M.** (2024) Autogenous shrinkage and early cracking of massive foundation slabs. Magazine of Civil Engineering, vol. 130, no. 6, 13005. doi: 10.34910/MCE.130.5
25. **Nesvetaev G., Koryanova Y., Chepurnenko A.** (2023) Comparison of the shear strength in heavy and self-

compacting concrete. Architecture and Engineering, vol. 8, no. 2, pp. 63–71. doi: 10.23968/2500-0055-2023-8-2-63-71
26. **Chepurnenko A.S. et al**. (2025) Experience of concreting a massive monolithic foundation slab. Construction Materials and Products, vol. 8, no. 5, 2. doi: 10.58224/2618-7183-2025-8-5-2
27. **Chuc N.T., Nikolay A.** (2020) The effect of formworks on the temperature regime in the mass concrete. Magazine of Civil Engineering, no. 7 (99), 9911. doi: 10.18720/MCE.99.11
28. **Andreev V.I.** (2012) Optimization of thick-walled shells based on solutions of inverse problems of the elastic theory for inhomogeneous bodies. Computer Aided Optimum Design in Engineering, pp. 189–202.
29. **Andreev V.I., Potekhin I.A.** (2017) Equal strength and equal stress structures. Models and reality. Advances in Engineering Research, vol. 102, pp. 232–236. doi: 10.2991/icmmse-17.2017.36
30. **Andreev V., Potekhin I.** (2019) Calculation of equal strength thick-walled concrete cylinder with free ends. IOP Conference Series: Materials Science and Engineering, vol. 661, no. 1, 012023. doi: 10.1088/1757-899X/661/1/012023

СПИСОК ЛИТЕРАТУРЫ

1. **Li X. et al.** Investigation of temperature development and cracking control strategies of mass concrete: A field monitoring case study // Case Studies in Construction Materials. 2023. Vol. 18. Article e02144. doi: 10.1016/j.cscm.2023.e02144
2. **Xie Y. et al.** Temperature field evolution of mass concrete: From hydration dynamics, finite element models to real concrete structure // Journal of Building Engineering. 2023. Vol. 65. Article 105699. doi: 10.1016/j.jobe.2022.105699
3. **Sheng X. et al.** Experimental and finite element investigations on hydration heat and early cracks in massive concrete piers // Case Studies in Construction Materials. 2023. Vol. 18. Article e01926. doi: 10.1016/j.cscm.2023.e01926
4. **Bilčík J., Sonnenschein R., Gažovičová N.** Causes of early-age thermal cracking of concrete foundation slabs and their reinforcement to control the cracking // Slovak Journal of Civil Engineering. 2017. Vol. 25. No. 3. Pp. 8–15. doi: 10.1515/sjce-2017-0013
5. **Nesvetaev G.V., Koryanova Yu.I., Shut V.V.** Specific heat dissipation of concrete and the risk of early cracking of massive reinforced concrete foundation slabs // Construction Materials and Products. 2024. Vol. 7. No. 3. Article 3. doi: 10.58224/2618-7183-2024-7-4-3
6. **Klemczak B., Żmij A.** Insight into thermal stress distribution and required reinforcement reducing early-age cracking in mass foundation slabs // Materials. 2021. Vol. 14. No. 3. Pp. 477. doi: 10.3390/ma14030477
7. **Afsoosbiria H., Machowska A.** Development of Sustainable Concrete Using By-Products as a Green Material, and Potential Solutions for Sustainability in Mass Concrete Construction—Comprehensive Review // Sustainability. 2025. Vol. 17. No. 22. Pp. 9983. doi: 10.3390/su17229983
8. **Singh M.P. et al.** Early age cracking relevant to mass concrete dam structures during the construction schedule // Construction and Building Materials. 2024. Vol. 411. Article 134739. doi: 10.1016/j.conbuildmat.2023.134739
9. **Justnes H., Wuyts F., Van Gemert D.** Hardening retarders for massive concrete // 5th Int. Conf. on High Performance Concrete, Manaus, Brazil. 2008. Pp. 18–20.
10. **De Schutter G., Vuylsteke M.** Minimisation of early age thermal cracking in a J-shaped non-reinforced massive concrete quay wall // Engineering Structures. 2004. Vol. 26. No. 6. Pp. 801–808. doi: 10.1016/j.engstruct.2004.01.013
11. **Kastornykh L. et al.** Modified concrete mixes for monolithic construction // Mate-

rials Science Forum. 2021. Vol. 1043. Pp. 81–91. doi: 10.4028/www.scientific.net/MSF.1043.81
12. **Smolana A. et al.** Thermo-mechanical analysis of mass concrete foundation slabs at early age—essential aspects and experiences from the FE modelling // Materials. 2022. Vol. 15. No. 5. Article 1815. doi: 10.3390/ma15051815
13. **Smolana A., Jędrzejewska A., Klemczak B.** Addressing Thermal Cracking in Polish Infrastructure: A Case Study // International RILEM Conference on Early-age and Long-term Cracking in RC Structures. Cham : Springer Nature Switzerland, 2025. Pp. 239–250. doi: 10.3390/ma17153700
14. **Klemczak B., Smolana A.** Multi-Step Procedure for Predicting Early-Age Thermal Cracking Risk in Mass Concrete Structures // Materials. 2024. Vol. 17. No. 15. Article 3700. doi: 10.3390/ma17153700
15. **Nguyen C.T., Luu X.B.** Reducing temperature difference in mass concrete by surface insulation // Magazine of Civil Engineering. 2019. No. 4 (88). Pp. 70–79. doi: 10.18720/MCE.88.7
16. **Chen Y.Y. et al.** Effects of insulation materials on mass concrete with pozzolans // Construction and Building Materials. 2017. Vol. 137. Pp. 261–271. doi: 10.1016/j.conbuildmat.2017.01.059
17. **Aniskin N.A., Chuc N.T., Khanh P.K.** The use of surface thermal insulation to regulate the temperature regime of a mass concrete during construction // Power Technology and Engineering. 2021. Vol. 55. No. 1. Pp. 1–7. doi: 10.1007/s10749-021-01310-6
18. **Chuc N.T. et al.** The effects of insulation thickness on temperature field and evaluating cracking in the mass concrete // Electronic Journal of Structural Engineering. 2018. Vol. 18. No. 2. Pp. 128–132. doi: 10.56748/ejse.182722
19. **Chepurnenko A.S. et al.** Simplified model for determining the stress strain state in massive monolithic foundation slabs during construction // International Journal for Computational Civil and Structural Engineering. 2022. Vol. 18. No. 3. Pp. 126–136. doi: 10.22337/2587-9618-2022-18-3-126-136
20. **Cha S.L., Jin S.S.** Prediction of thermal stresses in mass concrete structures with experimental and analytical results // Construction and Building Materials. 2020. Vol. 258. Article 120367. doi: 10.1016/j.conbuildmat.2020.120367
21. **Korotchenko I.A. et al.** Deformation of concrete creep in the thermal stress state calculation of massive concrete and reinforced concrete structures // Magazine of Civil Engineering. 2017. No. 1 (69). Pp. 56–63. doi: 10.18720/MCE.69.5
22. **Nesvetaev G.V. et al.** Heat dissipation of cement and design the composition of concrete for massive structures // Construction Materials and Products. 2025. Vol. 8. No. 1. Article 3. doi: 10.58224/2618-7183-2025-8-1-3
23. **Несветаев Г.В., Корянова Ю.И.** Прогноз кинетики прочности бетона при твердении в условиях, отличных от нормальных // Современные тенденции в строительстве, градостроительстве и планировке территорий. 2023. Т. 2. №. 4. С. 59–68. doi: 10.23947/2949-1835-2023-2-4-59-68
24. **Nesvetaev G.V., Koryanova Y.I., Yazyev B.M.** Autogenous shrinkage and early cracking of massive foundation slabs // Magazine of Civil Engineering. 2024. Vol. 130. No. 6. Article 13005. doi: 10.34910/MCE.130.5
25. **Nesvetaev G., Koryanova Y., Chepurnenko A.** Comparison of the shear strength in heavy and self-compacting concrete // Architecture and Engineering. 2023. Vol. 8. No. 2. Pp. 63–71. doi: 10.23968/2500-0055-2023-8-2-63-71
26. **Chepurnenko A.S. et al.** Experience of concreting a massive monolithic foundation slab // Construction Materials and Products. 2025. Vol. 8. No. 5. Article 2. doi: 10.58224/2618-7183-2025-8-5-2

27. **Chuc N.T., Nikolay A.** The effect of formworks on the temperature regime in the mass concrete // Magazine of Civil Engineering. 2020. No. 7 (99). Article 9911. doi: 10.18720/MCE.99.11
28. **Andreev V.I.** Optimization of thick-walled shells based on solutions of inverse problems of the elastic theory for inhomogeneous bodies // Computer Aided Optimum Design in Engineering. 2012. Pp. 189–202.
29. **Andreev V.I., Potekhin I.A.** Equal strength and equal stress structures. Models and reality // Advances in Engineering Research. 2017. Vol. 102. Pp. 232–236. doi: 10.2991/icmmse-17.2017.36
30. **Andreev V., Potekhin I.** Calculation of equal strength thick-walled concrete cylinder with free ends // IOP Conference Series: Materials Science and Engineering. 2019. Vol. 661. No. 1. Article 012023. doi: 10.1088/1757-899X/661/1/012023

Vasilina Sergeevna Tyurina – Candidate of Technical Sciences, Associate Professor of the Department of Structural Mechanics and Theory of Structures, Don State Technical University, 1 Gagarin Square, Rostov-on-Don, 344000, Russia, vasilina.93@mail.ru, +7(863)2019060

Anton Sergeevich Chepurnenko – Doctor of Technical Sciences, Professor, Professor of the Department of Structural Mechanics and Theory of Structures, Don State Technical University, 1 Gagarin Square, Rostov-on-Don, 344000, Russia, Gagarin, 1, Rostov-on-Don, 344000, Russia, anton_chepurnenk@mail.ru, +7(863)2019060

Batyr Meretovich Yazyev – Doctor of Technical Sciences, Professor, Professor of the Department of Structural Mechanics and Theory of Structures, Don State Technical University, Gagarin Square, 1, Rostov-on-Don, 344000, Russia, ps62@yandex.ru, +7(863)2019060

Василина Сергеевна Тюрина – кандидат технических наук, доцент кафедры «Строительная механика и теория сооружений» ФГБОУ ВО «Донской государственный технический университет», пл. Гагарина, 1, г. Ростов-на-Дону, 344000, Россия, vasilina.93@mail.ru, +7(863)2019060

Антон Сергеевич Чепурненко – доктор технических наук, профессор, профессор кафедры «Строительная механика и теория сооружений» ФГБОУ ВО «Донской государственный технический университет», пл. Гагарина, 1, г. Ростов-на-Дону, 344000, Россия, anton_chepurnenk@mail.ru, +7(863)2019060

Батыр Меретович Язьев – доктор технических наук, профессор, профессор кафедры «Строительная механика и теория сооружений» ФГБОУ ВО «Донской государственный технический университет», пл. Гагарина, 1, г. Ростов-на-Дону, 344000, Россия, ps62@yandex.ru, +7(863)2019060

International Journal for Computational Civil and Structural Engineering, 22(2) 138–148 (2026)

DOI:10.22337/2587-9618-2026-22-2-138-148

MODEL OF DEEP BED FILTRATION IN A POROUS MEDIUM WITH HETEROGENEOUS POROSITY

Liudmila I. Kuzmina [1], Yuri V. Osipov [2]

[1] HSE University, Moscow, RUSSIA

[2] National Research Moscow State University of Civil Engineering, Moscow, RUSSIA

Abstract: Modeling the transport and sedimentation of small particles of suspensions and colloids in porous rocks is an important problem in subsurface hydromechanics. Particles entrained in fluid are transported and retained in the rock pores. The filtration process is determined by the number and size of pores and is characterized by porosity—the ratio of the void volume to the total soil volume. In homogeneous materials, porosity can be considered constant. However, in practical problems describing filtration of suspended particles in multilayered and heterogeneous soils, the rock porosity is variable, and a constant-porosity model is inapplicable. A one-dimensional model of suspension and colloid filtration in a porous medium with nonuniform porosity is considered. The problem includes a mass balance equation accounting for variable porosity and a kinetic equation for sediment growth. The model describes the injection of a suspension or colloid of constant concentration into a porous medium containing pure water without suspended or sedimented particles. Unlike the case of uniform porosity, the transport velocity of suspended particles in pores is variable, and the boundary between the suspension and pure water, called the concentration front, is curved. Previously, such problems were solved only numerically. In this article, a system of filtration equations in a medium with variable porosity is solved analytically using the method of characteristics. An explicit formula is obtained for the curved front of suspended and sedimented particle concentrations, and exact analytical closed-form solutions are constructed ahead of and behind the front. An explicit solution is found for a model with a linear filtration function.

Key words: deep bed filtration, porous medium, porosity, concentration front, exact solution

МОДЕЛЬ ГЛУБИННОЙ ФИЛЬТРАЦИИ СУСПЕНЗИИ В ПОРИСТОЙ СРЕДЕ С НЕОДНОРОДНОЙ ПОРИСТОСТЬЮ

Л.И. Кузьмина [1], Ю.В. Осипов [2]

[1] Национальный исследовательский университет «Высшая школа экономики», г. Москва, РОССИЯ

[2] Национальный исследовательский Московский государственный строительный университет, г. Москва, РОССИЯ

Аннотация: Моделирование переноса и осаждения мелких частиц суспензий и коллоидов в пористых породах является важной задачей подземной гидромеханики. Частицы, увлекаемые жидкостью, перемещаются и задерживаются в порах породы. Процесс фильтрации определяется количеством пор и их размерами и характеризуется пористостью – отношением объема пустот к общему объему грунта. В однородных материалах пористость можно считать постоянной. Однако в практических задачах, описывающих фильтрацию суспензии в многослойных и неоднородных грунтах, пористость породы непостоянна и модель с постоянной пористостью неприменима. Рассматривается одномерная модель фильтрации суспензий и коллоидов в пористой среде с неоднородной пористостью. Задача включает уравнение баланса масс, учитывающее переменную пористость, и кинетическое уравнение роста осадка. Модель описывает впрыск суспензии или коллоида постоянной концентрации в пористую среду, содержащую чистую воду без взвешенных и осажденных частиц. В отличие от случая однородной пористости, скорость переноса взвешенных частиц в порах непостоянна и граница раздела суспензии и чистой воды криволинейная. Ранее такие задачи решались только численно. В статье система уравнений фильтрации в среде с переменной пористостью решена аналитически методом характеристик. Получена явная формула для криволинейного фронта концентраций взвешенных и осажденных частиц, перед фронтом и за фронтом построены аналитические точные решения в замкнутой форме. Для модели с линейной функцией фильтрации найдено решение в явном виде.

Ключевые слова: глубинная фильтрация, пористая среда, пористость, фронт концентраций, точные решения

1. INTRODUCTION

Flows of fluid with small particles in porous media are widespread in nature and engineering. Modeling the transport of tiny particles by fluid in rock is used in the strengthening of loose soil and in the design of underground storage facilities for hazardous waste, for tunnels and for hydraulic structures [1-4].

Moving particles of suspensions and colloids in porous media are affected by various forces: mechanical, electrostatic, hydrodynamic, gravitational [5-8]. Under the influence of these forces, some particles settle on the framework of the porous medium and form a stationary deposit. The standard macroscopic model of long-term deep bed filtration of a suspension in a porous medium includes mass conservation for both mobile and settled particulate matter, alongside the formula governing how quickly sediment accumulates. When the number of suspended particles is minimal, the rate at which they deposit is directly linked to their concentration. The factor that quantifies this relationship between deposition speed and suspended particle density is known as the filtration function. Over a short period of time, the filtration function can be considered constant [11-13]. During long-term deep bed filtration, the concentration of sedimented particles increases and the number of vacant sites for retained particles decreases. Consequently, the filtration function depends on the deposit size and decreases as it increases. If the filtration function vanishes upon reaching a certain limiting value, it is called blocking. In many models, a linear decreasing function, called the Langmuir coefficient, is used as the filtration function [14-16].

The capacity of a rock as a reservoir for liquid and gas is characterized by porosity - the ratio of the pore volume to the total volume of the rock. In a homogeneous rock, porosity can be considered constant. To model the filtration of suspensions and colloids in multilayered and heterogeneous soils, one must acknowledge that porosity varies with spatial position within the porous medium. This incorporation of variable porosity enables the filtration challenge to be addressed within a non-uniform porous medium. A similar model was studied in [17], but no analytical solutions were obtained for the problem with variable porosity.

This paper fills the gap. The study examines a large-scale model of deep bed filtration within a sample exhibiting non-uniform porosity, focusing on the process of injecting a suspension or colloidal solution into a porous medium with clean water. The transport of particles by an incompressible carrier fluid in a plane-parallel channel is described by a one-dimensional model, including a quasi-linear system of first-order differential equations, initial conditions and boundary conditions at the inlet of the porous medium [18, 19]. For the model in dimensionless form, analytical and numerical solutions are constructed, for the linear filtration function, an explicit solution is obtained.

2. MATHEMATICAL MODEL

In the domain $\Omega = \{0 \le x \le 1,\ t \ge 0\}$ consider a quasilinear system

$$\varphi(x)\frac{\partial C}{\partial t} + \frac{\partial C}{\partial x} + \frac{\partial S}{\partial t} = 0, \tag{1}$$

$$\frac{\partial S}{\partial t} = \Lambda(S)C. \tag{2}$$

Here the porosity function $\varphi(x)$ and the filtration function $\Lambda(x,S)$ are continuous and non-negative.

For system (1), (2), the boundary conditions are established at the filter inlet $x = 0$ and at the initial time $t = 0$:

$$C(x,t)\big|_{x=0} = 1; \tag{3}$$

$$C(x,t)\big|_{t=0} = 0;\ \ S(x,t)\big|_{t=0} = 0. \tag{4}$$

According to condition (3), equation (2) at the inlet $x = 0$ has the form

$$\frac{\partial S}{\partial t} = \Lambda(S). \qquad (5)$$

Divide both parts of equation (5) by $\Lambda(0,S)$ and integrate with respect to the variable *t*:

$$\int_0^t \frac{\partial S/\partial t}{\Lambda(S)} dt = t. \qquad (6)$$

Using condition (4), transform the integral on the left side of (6)

$$\int_0^{S_0(t)} \frac{dS}{\Lambda(S)} = t. \qquad (7)$$

The concentration of particles entering the porous medium $S_0(t) = S(0,t)$ is given by Formula (7).

The interface between the suspension and pure water is marked by a concentration front. This front migrates from the inlet to the outlet as the injected suspension displaces the water. Because conditions (3) and (4) are not met at zero, the concentration solution *C* is discontinuous at the front, while the solution *S* is continuous. The domain $\Omega_S = \{0 \le x \le 1,\ t \ge x\}$ behind the front, containing suspended and settled particles, has a positive solution, whereas the pure water domain $\Omega_0 = \{0 \le x \le 1,\ 0 \le t \le x\}$ ahead of the front has a zero solution.

A non-uniform porosity $\varphi(x)$ results in a curvilinear concentration front. To find the front line $t_\Gamma(x)$, we pass to the characteristic variables in equation (1) [20]. Let

$$t' = \varphi(x), \quad x' = 1, \qquad (8)$$

where the apostrophe (') denotes the derivative with respect to the "internal time" - the characteristic variable τ.

Substitute (2) into (1) and pass to the characteristic variables in equation (1):

$$C' = \Lambda(S)C. \qquad (9)$$

In the suspension domain Ω_S, the initial conditions for equations (8) and (9) are

$$t(0) = t_0, \quad x(0) = 0, \quad C(0) = 1. \qquad (10)$$

Here $t_0 \ge 0$ is the starting point of the characteristic on the *OT* axis.

Solution of equations (8) with conditions (10) are

$$t = \int_0^\tau \varphi(y)dy + t_0, \quad x = \tau.$$

In Cartesian coordinates, the characteristics in the domain Ω_S are given by the relation

$$t = \int_0^x \varphi(y)dy + t_0. \qquad (11)$$

The concentration front is a characteristic that emerges from the origin of coordinates:

$$t_\Gamma(x) = \int_0^x \varphi(y)dy.$$

From the continuity of the deposit concentration follows the condition on the concentration front

$$S\big|_{t=t_\Gamma(x)} = 0. \qquad (12)$$

According to condition (12), on the concentration front, equation (1) takes the form

$$\varphi(x)\frac{\partial C}{\partial t} + \frac{\partial C}{\partial x} + \Lambda(0)C = 0. \qquad (13)$$

Equation (13) with the initial condition (3) determines the solution on the concentration front:

$$C = e^{-\Lambda(0)x}. \qquad (14)$$

3. EXACT SOLUTION TO MODEL WITH NON-UNIFORM POROSITY

Consider the problem (1)-(4) in the suspension domain Ω_S, where the solution is nonzero. Express the unknown C from equation (2):

$$C = \frac{\partial S/\partial t}{\Lambda(S)}, \qquad (15)$$

and substitute it into equation (1)

$$\varphi(x)\frac{\partial}{\partial t}\left(\frac{\partial S/\partial t}{\Lambda(S)}\right)+\frac{\partial}{\partial x}\left(\frac{\partial S/\partial t}{\Lambda(S)}\right)+\frac{\partial S}{\partial t}=0. \qquad (16)$$

Using the ratio

$$\frac{\partial}{\partial x}\left(\frac{\partial S/\partial t}{\Lambda(S)}\right)=\frac{\partial^2 S/\partial t\partial x}{\Lambda(S)}-\frac{\partial S}{\partial t}\frac{\Lambda'(S)}{\Lambda^2(S)}\frac{\partial S}{\partial x}=\frac{\partial}{\partial t}\left(\frac{\partial S/\partial x}{\Lambda(S)}\right), \qquad (17)$$

equation (16) takes the form

$$\frac{\partial}{\partial t}\left(\varphi(x)\frac{\partial S/\partial t}{\Lambda(S)}\right)+\frac{\partial}{\partial t}\left(\frac{\partial S/\partial x}{\Lambda(S)}\right)+\frac{\partial S}{\partial t}=0. \qquad (18)$$

Integrating equation (18) with respect to the variable t from 0 to t yields

$$\varphi(x)\frac{\partial S/\partial t}{\Lambda(S)}+\frac{\partial S/\partial x}{\Lambda(S)}+S=K(x). \qquad (19)$$

Substitute $t=0$ into (19), and from the initial condition (4) obtain the integration constant: $K(x)=0$. Equation (19) takes the form

$$\varphi(x)\frac{\partial S/\partial t}{\Lambda(S)}+\frac{\partial S/\partial x}{\Lambda(S)}+S=0. \qquad (20)$$

Pass to the characteristic variables in equation (20):

$$\frac{S'}{\Lambda(S)}+S=0. \qquad (22)$$

The initial condition for equation (22) is set on the OT axis:

$$S(\tau)\big|_{\tau=0}=S_0(t_0), \qquad (23)$$

where the function S_0 is given by formula (7).

The solution to equation (22) with condition (23) has an implicit form:

$$\int_{S_0(t_0)}^{S(\tau)}\frac{ds}{s\Lambda(s)}=-\tau. \qquad (24)$$

Express the initial characteristic coordinate t_0 from equation (11):

$$t_0=t-\int_0^x\varphi(y)dy. \qquad (25)$$

In Cartesian coordinates, the solution (24) is given by the formula

$$\int_{S_0\left(t-\int_0^x\varphi(y)dy\right)}^{S(x,t)}\frac{ds}{s\Lambda(s)}=-x. \qquad (26)$$

If $S(x,t)$ is known, the solution $C(x,t)$ can be obtained from the formula (15). Let us derive another relation that does not use derivatives of the solution and specifies the relationship between the solutions on the characteristics (11). Differentiate the equality (26) with respect to the variable t:

$$\frac{\partial S/\partial t}{S\Lambda(S)}-\frac{\partial S_0/\partial t}{S_0\Lambda(S_0)}=0. \qquad (27)$$

Substituting the formulae (2) and (5) into equation (27) yields

$$\frac{C}{S}-\frac{1}{S_0}=0\,. \tag{28}$$

Express the solution C from (28):

$$C=\frac{S(x,t)}{S_0\left(t-\int\limits_0^x \varphi(y)dy\right)}\,. \tag{29}$$

Relation (29) is called the Riemann invariant [21].

The formulae (24), (26) and (29) generalize the known solution of the filtration model with constant porosity [22].

In the case where the filtration function is equal to the Langmuir coefficient

$$\Lambda(S)=\lambda\left(1-\frac{S}{S_m}\right),\ \lambda>0,\ S_m>0\,, \tag{30}$$

the solution of (26) and (29) can be obtained in explicit form. Calculate the integral in the formula (7):

$$\int\limits_0^{S_0}\frac{dS}{\Lambda(S)}=\int\limits_0^{S_0}\frac{dS}{\lambda\left(1-\frac{S}{S_m}\right)}=-\frac{S_m}{\lambda}\ln\left(1-\frac{S_0}{S_m}\right).$$

Now we can find the solution at the porous medium inlet:

$$S_0(t)=S_m\left(1-e^{-\frac{\lambda t}{S_m}}\right). \tag{31}$$

Calculation of the integral on the left-hand side of (26) gives

$$\int\limits_{S_0\left(t-\int\limits_0^x\varphi(y)dy\right)}^{S(x,t)}\frac{ds}{s\Lambda(s)}=\int\limits_{S_0\left(t-\int\limits_0^x\varphi(y)dy\right)}^{S(x,t)}\frac{ds}{s\lambda\left(1-\frac{s}{S_m}\right)}=\frac{1}{\lambda}\left(\ln\frac{S}{S_m-S}-\ln\frac{S_0}{S_m-S_0}\right). \tag{32}$$

Substitute the formula (32) into (26) and obtain the solution:

$$S(x,t)=\frac{S_m\left(e^{\frac{\lambda}{S_m}\left(t-\int\limits_0^x\varphi(y)dy\right)}-1\right)}{e^{\frac{\lambda}{S_m}\left(t-\int\limits_0^x\varphi(y)dy\right)}+e^{\lambda x}-1}\,. \tag{33}$$

Substitute the solutions (31) and (33) into the Riemann invariant (29):

$$C=\frac{S_m\left(e^{\frac{\lambda}{S_m}\left(t-\int\limits_0^x\varphi(y)dy\right)}-1\right)}{e^{\frac{\lambda}{S_m}\left(t-\int\limits_0^x\varphi(y)dy\right)}+e^{\lambda x}-1}\Bigg/S_m\left(1-e^{-\frac{\lambda}{S_m}\left(t-\int\limits_0^x\varphi(y)dy\right)}\right)=\frac{e^{\frac{\lambda}{S_m}\left(t-\int\limits_0^x\varphi(y)dy\right)}}{e^{\frac{\lambda}{S_m}\left(t-\int\limits_0^x\varphi(y)dy\right)}+e^{\lambda x}-1}\,. \tag{34}$$

The formulae (31), (33) and (34) define an explicit solution to problem (1)-(4) in the suspension domain Ω_S for the filtration function (30). At constant porosity $\varphi(x)=1$, the solution to the filtration problem is known [23]. The case of linear porosity was studied in [24].

4. NUMERICAL SIMULATION

The numerical calculation of the model was performed at $\lambda = 1,\ S_m = 1,\ \varphi(x) = 1.1 - 0.2x$.

The solution profiles (how the solution changes with position at a specific moment) are shown in Fig. 1.

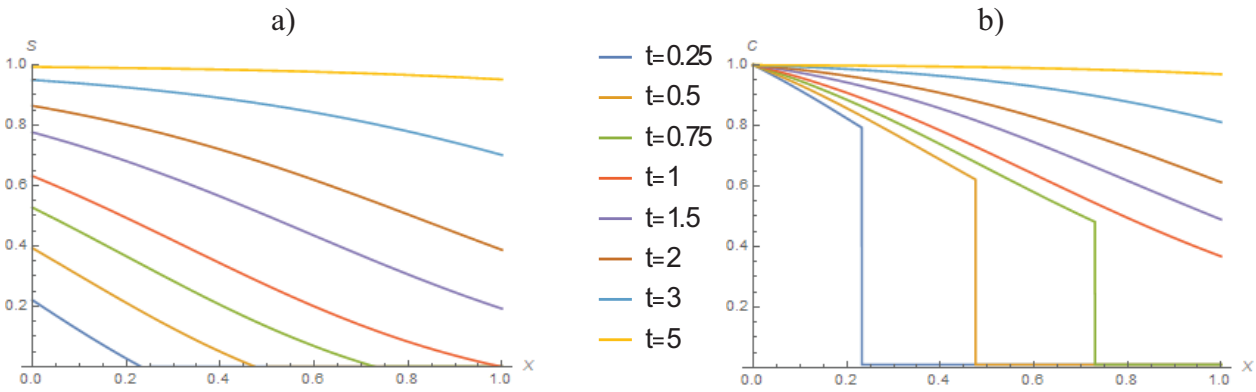

Figure 1. Profiles a) retained particles concentration S b) suspended particles concentration C

Since the suspension spreads in the porous medium from the inlet $x = 0$ to the outlet $x = 1$, the profiles decrease monotonically. At $t < 1$ the profiles vanish before the concentration front.

Figure 2 shows the evolution of the solution (the dependence of the solution on time for a fixed spatial coordinate).

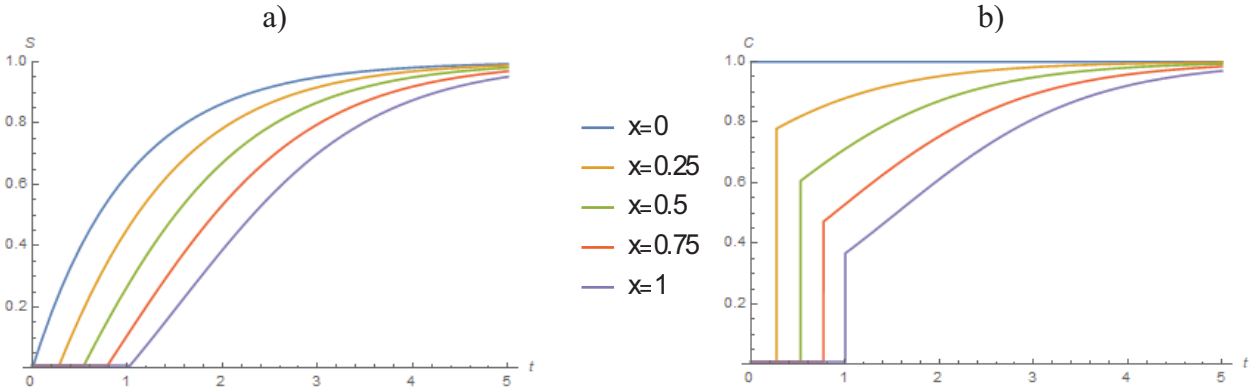

Figure 2. Evolution a) retained particles concentration S b) suspended particles concentration C

Before the front, the concentrations of suspended and retained particles are zero, behind the front the evolution increases and tends to the limiting values: $S \to S_m = 1,\ C \to C(0,t) = 1$. The discontinuity in the concentration of suspended particles at the front is indicated by a vertical line.

5. DISCUSSION

The analytical solutions found for the problem of filtration with variable porosity allow fine-tuning of laboratory experiments and predicting the behavior of particles carried by water in rock [25-27].

Comparison of solutions of models with variable and constant porosity makes it possible to estimate the averaging errors when replacing variable porosity with constant porosity.

Exact solutions allow us to correctly solve the inverse filtration problem – finding the porosity and filtration function from a known solution [28, 29].

The general model of filtration in a heterogeneous porous medium assumes the dependence of porosity and filtration function on the spatial variable. In the general case, the analytical solution of the problem in closed form is unknown; numerical solutions are used to analyze the model [30-32].

The problem of particle migration in a porous medium is of interest [33, 34]. The displacement of a suspension by pure water from a sample with variable porosity will be considered separately.

6. CONCLUSIONS

The study of particle transport in a porous medium with variable porosity leads to the following conclusions.

- A model of filtration with variable porosity was studied.
- A new analytical solution to the model is constructed, generalizing the solution of the standard filtration problem with constant porosity.
- For the linear filtration function (Langmuir coefficient) a solution in explicit form is obtained.

REFERENCES

1. **Zhou Z., Zang H., Wang S., Du X., Ma D., Zhang J.** Filtration Behavior of Cement-Based Grout in Porous Media // Transport in Porous Media, 2018, vol. 125, pp. 435–463.
2. **Tsuji M., Kobayashi S., Mikake S., Sato T., Matsui H.** Post-Grouting Experiences for Reducing Groundwater Inflow at 500 m Depth of the Mizunami Underground Research Laboratory, Japan // Procedia Engineering, 2017, vol. 191, pp. 543–550.
3. **Wang X., Cheng H., Yao Z., Rong C., Huang X., Liu X.** Theoretical Research on Sand Penetration Grouting Based on Cylindrical Diffusion Model of Tortuous Tubes // Water, 2022, vol. 14, 1028, pp. 1–15.
4. **Osipov Y., Kotov N.** Asymptotic model of size-exclusion grouting // IOP Conf. Series: Materials Science and Engineering, 2018, vol. 365, 042006, pp. 1–8.
5. **Rabinovich A., Bedrikovetsky P., Tartakovsky D.** Analytical model for gravity segregation of horizontal multiphase flow in porous media // Physics of Fluids, 2020, vol. 32 (4), pp. 1–15.
6. **Kuzmina L., Osipov Y.** Deep bed filtration with multiple pore-blocking mechanisms // MATEC Web of Conferences, 2018, vol. 196, 04003, pp. 1–6.
7. **Santos A., Bedrikovetsky P.** Size exclusion during particle suspension transport in porous media: stochastic and averaged equations // Computational and Applied Mathematics, 2004, vol. 23(2-3), pp. 259–284.
8. **Bedrikovetsky P.** Mathematical theory of oil and gas recovery: with applications to ex-USSR oil and gas fields, Springer Science & Business Media, Des Moines, IA, USA, 2013.
9. **Herzig J.P., Leclerc D.M., Le Goff P.** Flow of Suspensions Through Porous Media – Application to Deep Filtration // Journal of Industrial & Engineering Chemistry, 1970, vol. 62(8), pp. 8–35.
10. **Bedrikovetsky P.** Upscaling of stochastic micro model for suspension transport in porous media // Transport in Porous Media, 2008, vol. 75, pp. 335–369.
11. **Dudek N., Bagińska I.** Comparison of assessing the filtration coefficient from laboratory tests with correlation results determined from CPTu test for coarse-grain soil // IOP Conf. Series: Journal of Physics: Conf. Series, 2020, vol. 1425, 012203, pp. 1–9.
12. **Du X., Wong G.K.** Predicting filtration coefficient and formation damage coefficient for particle flow in porous media using machine learning // Results in Engineering, 2025, vol. 25, 104545, pp. 1–13.
13. **Kuzmina L.I., Osipov Yu.V.** Asymptotics of the filtration problem with almost constant coefficients // International Journal

for Computational Civil and Structural Engineering, 2021, vol. 17(2), pp. 43–49.
14. **Altoe J.E., Bedrikovetsky P., Siqueira A.G., de Souza A.L.S., Shecaira F.S.** Correction of basic equations for deep bed filtration with dispersion. // Journal of Petroleum Science and Engineering, 2006, vol. 51, pp. 68–84.
15. **Kuzmina L.I., Osipov Yu.V.** Determining the Lengmur coefficient of the filtration problem // International Journal for Computational Civil and Structural Engineering, 2020, vol. 16(4), pp. 48–54.
16. **Rozine T.N., Sabbagh T.** Effect of Filtration Coefficient Determination Method on the Scale Effect in Water-Saturated Fine-Grained Soils // Soil Mechanics and Foundation Engineering, 2017, vol. 53, pp.376–380.
17. **Kuzmina L.I., Osipov Yu.V.** Exact solution to non-linear filtration in heterogeneous porous media // International Journal of Non-Linear Mechanics, 2023, vol. 150, 104363, pp. 1–9.
18. **Polyanin A.D., Manzhirov A.V.** Handbook of mathematics for engineers and scientists, Chapman and Hall/CRC Press, Boca Raton, FL, USA, 2007.
19. **Polyanin A., Zaitsev V.** Handbook of Nonlinear Partial Differential Equations, Chapman and Hall/CRC Press, Boca Raton, FL, USA, 2012.
20. **Courant R., Hilbert D.** Partial differential equations, Reprint of the 1962 Original, Edited, Wiley- InterScience, New York, 1989.
21. **Logan D.J.** An Introduction to Nonlinear Partial Differential Equations, Wiley, NY, USA, 1994.
22. **Vyazmina E.A., Bedrikovetskii P.G., Polyanin A.D.** New classes of exact solutions to nonlinear sets of equations in the theory of filtration and convective mass transfer // Theoretical Foundations of Chemical Engineering, 2007, vol. 41(5), pp. 556–564.
23. **Kuzmina L.I., Osipov Yu.V., Zheglova Y.G.** Global asymptotics of the filtration problem in a porous medium // International Journal for Computational Civil and Structural Engineering, 2019, vol. 15(2), pp. 77–85.
24. **Safina G.L.** Solution to filtration problem with linear porosity function. // International Journal for Computational Civil and Structural Engineering, 2025, vol. 21(3), pp. 41–53.
25. **Vaz A., Bedrikovetsky P., Fernandes P.D., Badalyan A., Carageorgos T.** Determining model parameters for non-linear deep-bed filtration using laboratory pressure measurements // Journal of Petroleum Science and Engineering, 2017, vol. 151, pp. 421–433.
26. **Yang S., Russell T., Badalyan A., Schacht U., Woolley M., Bedrikovetsky P.** Characterization of fines migration system using laboratory pressure measurements // Journal of Natural Gas Science and Engineering , 2019, vol. 65, pp. 108 – 124 .
27. **Chyzhykov D., Widziewicz-Rzońca K., Mathews B.** Variability of PM measurement results due to subsampling of filters and water content analysis // Chemosphere, 2025, vol. 374, 144177.
28. **Alvarez A.C., Bedrikovetsky P.G., Hime G., Marchesin A.O., Marchesin D., Rodrigues J.R.** A fast inverse solver for the filtration function for flow of water with particles in porous media. // Inverse Problems, 2006, vol. 22, pp. 69–88.
29. **Alvarez A.C., Hime G., Marchesin D., Bedrikovetsky P.G.** The inverse problem of determining the filtration function and permeability reduction in flow of water with particles in porous media. // Transport in Porous Media, 2007, vol. 70(1), pp. 43–62.
30. **Galaguz Y.P.** Realization of the TVD-scheme for a numerical solution of the filtration problem. // International Journal for Computational Civil and Structural Engineering, 2017, vol. 13(2), pp. 93–102.

31. **Galaguz Y.P., Safina G.L.** Modeling of fine migration in a porous medium. // MATEC Web of Conferences, 2016, vol. 86, 03003, pp. 1–6.
32. **Osipov Yu., Safina G., Galaguz Yu.** Calculation of the filtration problem by finite differences methods // MATEC Web Conference, 2018, vol. 251(3), 04021, pp. 1–6.
33. **Galaguz Y., Safina G.** Modeling of Fine Migration in a Porous Medium // MATEC Web of Conferences, 2016, vol. 86, 03003, pp. 1–6.
34. **Kuzmina L., Osipov Y.** Model of suspension displacement in a porous medium // MATEC Web of Conferences, 2018, vol. 251, 04016, pp. 1–7.

СПИСОК ЛИТЕРАТУРЫ

1. **Zhou Z., Zang H., Wang S., Du X., Ma D., Zhang J.** Filtration Behavior of Cement-Based Grout in Porous Media // Transport in Porous Media, 2018, vol. 125, pp. 435–463.
2. **Tsuji M., Kobayashi S., Mikake S., Sato T., Matsui H.** Post-Grouting Experiences for Reducing Groundwater Inflow at 500 m Depth of the Mizunami Underground Research Laboratory, Japan // Procedia Engineering, 2017, vol. 191, pp. 543–550.
3. **Wang X., Cheng H., Yao Z., Rong C., Huang X., Liu X.** Theoretical Research on Sand Penetration Grouting Based on Cylindrical Diffusion Model of Tortuous Tubes // Water, 2022, vol. 14, 1028, pp. 1–15.
4. **Osipov Y., Kotov N.** Asymptotic model of size-exclusion grouting // IOP Conf. Series: Materials Science and Engineering, 2018, vol. 365, 042006, pp. 1–8.
5. **Rabinovich A., Bedrikovetsky P., Tartakovsky D.** Analytical model for gravity segregation of horizontal multiphase flow in porous media // Physics of Fluids, 2020, vol. 32 (4), pp. 1–15.
6. **Kuzmina L., Osipov Y**. Deep bed filtration with multiple pore-blocking mechanisms // MATEC Web of Conferences, 2018, vol. 196, 04003, pp. 1–6.
7. **Santos A., Bedrikovetsky P.** Size exclusion during particle suspension transport in porous media: stochastic and averaged equations // Computational and Applied Mathematics, 2004, vol. 23(2-3), pp. 259–284.
8. **Bedrikovetsky P.** Mathematical theory of oil and gas recovery: with applications to ex-USSR oil and gas fields, Springer Science & Business Media, Des Moines, IA, USA, 2013.
9. **Herzig J.P., Leclerc D.M., Le Goff P.** Flow of Suspensions Through Porous Media – Application to Deep Filtration // Journal of Industrial & Engineering Chemistry, 1970, vol. 62(8), pp. 8–35.
10. **Bedrikovetsky P**. Upscaling of stochastic micro model for suspension transport in porous media // Transport in Porous Media, 2008, vol. 75, pp. 335–369.
11. **Dudek N., Bagińska I.** Comparison of assessing the filtration coefficient from laboratory tests with correlation results determined from CPTu test for coarse-grain soil // IOP Conf. Series: Journal of Physics: Conf. Series, 2020, vol. 1425, 012203, pp. 1–9.
12. **Du X., Wong G.K.** Predicting filtration coefficient and formation damage coefficient for particle flow in porous media using machine learning // Results in Engineering, 2025, vol. 25, 104545, pp. 1–13.
13. **Kuzmina L.I., Osipov Yu.V.** Asymptotics of the filtration problem with almost constant coefficients // International Journal for Computational Civil and Structural Engineering, 2021, vol. 17(2), pp. 43–49.
14. **Altoe J.E., Bedrikovetsky P., Siqueira A.G., de Souza A.L.S., Shecaira F.S.** Correction of basic equations for deep bed filtration with dispersion. // Journal of Petroleum Science and Engineering, 2006, vol. 51, pp. 68–84.
15. **Kuzmina L.I., Osipov Yu.V.** Determining the Lengmur coefficient of the filtration problem // International Journal for

Computational Civil and Structural Engineering, 2020, vol. 16(4), pp. 48–54.
16. **Rozine T.N., Sabbagh T.** Effect of Filtration Coefficient Determination Method on the Scale Effect in Water-Saturated Fine-Grained Soils // Soil Mechanics and Foundation Engineering, 2017, vol. 53, pp.376–380.
17. **Kuzmina L.I., Osipov Yu.V.** Exact solution to non-linear filtration in heterogeneous porous media // International Journal of Non-Linear Mechanics, 2023, vol. 150, 104363, pp. 1–9.
18. **Polyanin A.D., Manzhirov A.V.** Handbook of mathematics for engineers and scientists, Chapman and Hall/CRC Press, Boca Raton, FL, USA, 2007.
19. **Polyanin A., Zaitsev V.** Handbook of Nonlinear Partial Differential Equations, Chapman and Hall/CRC Press, Boca Raton, FL, USA, 2012.
20. **Courant R., Hilbert D.** Partial differential equations, Reprint of the 1962 Original, Edited, Wiley- InterScience, New York, 1989.
21. **Logan D.J.** An Introduction to Nonlinear Partial Differential Equations, Wiley, NY, USA, 1994.
22. **Vyazmina E.A., Bedrikovetskii P.G., Polyanin A.D.** New classes of exact solutions to nonlinear sets of equations in the theory of filtration and convective mass transfer // Theoretical Foundations of Chemical Engineering, 2007, vol. 41(5), pp. 556–564.
23. **Kuzmina L.I., Osipov Yu.V., Zheglova Y.G.** Global asymptotics of the filtration problem in a porous medium // International Journal for Computational Civil and Structural Engineering, 2019, vol. 15(2), pp. 77–85.
24. **Safina G.L.** Solution to filtration problem with linear porosity function. // International Journal for Computational Civil and Structural Engineering, 2025, vol. 21(3), pp. 41–53.
25. **Vaz A., Bedrikovetsky P., Fernandes P.D., Badalyan A., Carageorgos T.** Determining model parameters for non-linear deep-bed filtration using laboratory pressure measurements // Journal of Petroleum Science and Engineering, 2017, vol. 151, pp. 421–433.
26. **Yang S., Russell T., Badalyan A., Schacht U., Woolley M., Bedrikovetsky P.** Characterization of fines migration system using laboratory pressure measurements // *Journal of Natural Gas Science and Engineering* , 2019, vol. 65, pp. 108 – 124 .
27. **Chyzhykov D., Widziewicz-Rzońca K., Mathews B.** Variability of PM measurement results due to subsampling of filters and water content analysis // Chemosphere, 2025, vol. 374, 144177.
28. **Alvarez A.C., Bedrikovetsky P.G., Hime G., Marchesin A.O., Marchesin D., Rodrigues J.R.** A fast inverse solver for the filtration function for flow of water with particles in porous media. // Inverse Problems, 2006, vol. 22, pp. 69–88.
29. **Alvarez A.C., Hime G., Marchesin D., Bedrikovetsky P.G.** The inverse problem of determining the filtration function and permeability reduction in flow of water with particles in porous media. // Transport in Porous Media, 2007, vol. 70(1), pp. 43–62.
30. **Galaguz Y.P.** Realization of the TVD-scheme for a numerical solution of the filtration problem. // International Journal for Computational Civil and Structural Engineering, 2017, vol. 13(2), pp. 93–102.
31. **Galaguz Y.P., Safina G.L.** Modeling of fine migration in a porous medium. // MATEC Web of Conferences, 2016, vol. 86, 03003, pp. 1–6.
32. **Osipov Yu., Safina G., Galaguz Yu**. Calculation of the filtration problem by finite differences methods // MATEC Web Conference, 2018, vol. 251(3), 04021, pp. 1–6.
33. **Galaguz Y., Safina G.** Modeling of Fine Migration in a Porous Medium // MATEC Web of Conferences, 2016, vol. 86, 03003, pp. 1–6.
34. **Kuzmina L., Osipov Y.** Model of suspension displacement in a porous medium // MATEC Web of Conferences, 2018, vol. 251, 04016, pp. 1–7.

Liudmila I. Kuzmina, Candidate of Physical and Mathematical Sciences, Associate Professor, Department of Applied Mathematics, National Research University Higher School of Economics, 101000, Russia, Moscow, Myasnitskaya st., 20, e-mail: lkuzmina@hse.ru.

Yuri V. Osipov, Candidate of Physical and Mathematical Sciences, Professor, Department of Computer Science and Applied Mathematics, Moscow State University of Civil Engineering, 129337, Russia, Moscow, Yaroslavskoe Shosse, 26, e-mail: yuri-osipov@mail.ru.

Кузьмина Людмила Ивановна, доцент, кандидат физико-математических наук, Департамент прикладной математики МИЭМ им. А.Н. Тихонова, Национальный исследовательский университет «Высшая школа экономики»; 101000, г. Москва, ул. Мясницкая, д. 20, e-mail: lkuzmina@hse.ru.

Осипов Юрий Викторович, профессор, кандидат физико-математических наук, кафедра информатики и прикладной математики Национального исследовательского Московского государственного строительного университета; 129337, Россия, г. Москва, Ярославское шоссе, д. 26; e-mail: yuri-osipov@mail.ru.

International Journal for Computational Civil and Structural Engineering, 22(2) 149–159 (2026)

DOI:10.22337/2587-9618-2026-22-2-149-159

NONLINEAR STABILITY AND IMPERFECTION SENSITIVITY ANALYSIS OF HYBRID TIMBER BEAMS FORMULATED VIA A MECHANISM-BASED ENERGY APPROACH

Le Thuy Nguyen, Hong Son Nguyen, Thi Thuy Van Tran

Hanoi Architectural University, Hanoi, VIETNAM

Abstract: This paper develops an advanced computational framework to investigate the nonlinear stability and imperfection sensitivity of hybrid three-layer timber beams, specifically composed of high-stiffness Birch faces and a relatively soft Pine core. By employing a rigorous variational energy formulation based on the principle of minimum total potential energy, the study explicitly models the complex interaction between flexural deformations and bending-induced membrane effects under large-scale initial geometric imperfections. A distinctive feature of the proposed model is the derivation of a mechanism-based energy index (η), which provides a robust mathematical criterion for identifying the transition from bending-dominated to membrane-activated structural regimes. The numerical implementation is executed via an efficient MATLAB-based algorithmic procedure, enabling a high-fidelity parametric exploration of imperfection amplitudes ranging from infinitesimal values to L/50. Comprehensive numerical results reveal that substantial geometric deviations lead to a significant "knock-down" effect on structural stability, with tangent stiffness degradation exceeding 60% in the pre-critical stage as the load increases. The analysis of shear stress gradients and interface slip distributions further highlights the susceptibility of hybrid members to local instability when membrane forces are activated. Furthermore, a topographical stability transition map is constructed to visualize the synergistic effects of interlayer slip stiffness and initial curvatures on the global buckling limits. The computational findings offer a robust theoretical basis for the safety-limit design of slender hybrid composite members in modern civil engineering applications, emphasizing the necessity of accounting for large-scale geometric nonlinearities in structural reliability assessments.

Keywords: Computational mechanics; Hybrid timber structures; Nonlinear stability; Energy approach; Membrane effect; Stability mapping; Stiffness degradation

НЕЛИНЕЙНЫЙ АНАЛИЗ УСТОЙЧИВОСТИ И ЧУВСТВИТЕЛЬНОСТИ К НЕСОВЕРШЕНСТВАМ ГИБРИДНЫХ ДЕРЕВЯННЫХ БАЛОК НА ОСНОВЕ МЕХАНИСТИЧЕСКОГО ЭНЕРГЕТИЧЕСКОГО ПОДХОДА

Ле Тхуи Нгуен, Хонг Шон Нгуен, Тхюи Ван Чан Тхи

Ханойский Архитектурный Университет, Ханой, ВЬЕТНАМ

Аннотация: В данной работе разработана усовершенствованная вычислительная модель для исследования нелинейной устойчивости и чувствительности к несовершенствам гибридных трехслойных деревянных балок, состоящих из высокожестких внешних слоев из березы и относительно мягкого сердечника из сосны. Путем применения строгой вариационной энергетической формулировки, основанной на принципе минимума полной потенциальной энергии, в исследовании в явном виде моделируется сложное взаимодействие между изгибными деформациями и эффектами мембранных сил, вызванных изгибом, в условиях крупномасштабных начальных геометрических несовершенств. Отличительной особенностью предлагаемой модели является вывод энергетического индекса механизма (η), который служит надежным математическим критерием для идентификации перехода от режима с преобладанием изгиба к режиму активации мембранных сил. Численная реализация выполнена с помощью эффективной алгоритмической процедуры на базе MATLAB, что позволяет проводить высокоточное параметрическое исследование амплитуд несовершенств в диапазоне от бесконечно малых

величин до L/50. Комплексные численные результаты показывают, что существенные геометрические отклонения приводят к значительному эффекту «снижения» (knock-down effect) структурной устойчивости, при этом деградация касательной жесткости превышает 60% на докритической стадии по мере увеличения нагрузки. Анализ градиентов касательных напряжений и распределения проскальзывания на границе раздела слоев дополнительно подчеркивает предрасположенность гибридных элементов к локальной неустойчивости при активации мембранных сил. Кроме того, построена топографическая карта переходов устойчивости для визуализации синергетического воздействия жесткости межслойного сдвига и начальных кривизн на общие пределы потери устойчивости. Вычислительные результаты обеспечивают прочную теоретическую основу для проектирования тонких гибридных композитных элементов по предельным состояниям в современном гражданском строительстве, подчеркивая необходимость учета крупномасштабных геометрических нелинейностей при оценке надежности конструкций.

Ключевые слова: Вычислительная механика, Гибридная древесина, Нелинейная устойчивость, Энергетический подход, Мембранный эффект, Карта устойчивости, Деградация жесткости

INTRODUCTION

In the contemporary era of sustainable structural engineering, the utilization of engineered timber has undergone a significant transformation, evolving from traditional lumber to high-performance composite systems [1]. Among these, hybrid three-layer timber beams- typically configured with high-stiffness face layers, such as Birch, and a relatively compliant Pine core- represent a sophisticated solution for mid-to-high-rise applications in modern construction [2, 3]. The mechanical efficiency of such hybrid members is derived from the synergistic interaction between layers of contrasting elastic moduli, which optimizes the distribution of normal and shear stresses [4]. However, the increased slenderness associated with these optimized sections introduces complex challenges regarding their structural stability and nonlinear response under service loads [5].

The structural integrity of composite timber members is fundamentally governed by the interlayer shear interaction and the slip modulus of mechanical fasteners [6]. Traditional analytical frameworks, such as the γ-method established in Eurocode 5, provide a practical basis for evaluating effective bending stiffness under linear-elastic conditions [7]. While these methods are robust for standard design, they inherently neglect second-order geometric effects that arise as transverse deflections increase [8, 9]. Pioneering contributions in structural mechanics, particularly those by Timoshenko [10] and Vlasov [11], highlighted that for slender assemblies, the coupling between axial strains and curvature leads to significant load-path deviations. In hybrid timber systems, this coupling is further complicated by the discrete or continuous shear slip at the interfaces, which necessitates a more refined computational approach than classical beam theories [12].

Geometric nonlinearity is a critical factor in the safety assessment of timber structures, especially when considering the absence of externally applied axial forces [13]. A critical phenomenon in the large-deflection regime of slender beams is the activation of membrane forces [14]. As a member undergoes transverse displacement, the stretching of its neutral axis induces axial tension, a mechanism referred to as "membrane activation" [15, 16]. In geometrically perfect beams, this effect often provides a secondary stiffening mechanism; however, in the presence of initial geometric imperfections (e_0), the transition from bending-dominated to membrane-influenced behavior becomes highly sensitive [17]. Real-world timber elements are seldom perfectly straight; they possess initial out-of-straightness due to manufacturing tolerances or moisture-induced warping [18]. For slender hybrid beams, even a minor initial imperfection can trigger premature stiffness degradation and significantly reduce the critical buckling load-a phenomenon often

quantified by "knock-down factors" in stability theories [19, 20].

From a computational standpoint, the assessment of these nonlinearities requires robust numerical strategies. While high-fidelity three-dimensional Finite Element (FE) models are capable of capturing local stress states, they often involve prohibitive computational costs for extensive parametric sensitivity analyses. Variational energy methods, established on the principle of minimum total potential energy, offer an elegant and efficient alternative. By formulating a mechanism-based energy functional that explicitly includes bending, membrane, and slip energy components, researchers can identify critical transition points in structural behavior. Despite its importance, a robust framework that analytically links the energy transition index to global stability limits for hybrid timber remains under-explored in current literature.

This paper addresses these gaps by developing an advanced computational framework to investigate the nonlinear stability of hybrid Birch–Pine beams. The study focuses on identifying the mechanical mechanisms governing membrane-force activation and the subsequent degradation of tangent stiffness. By introducing a mechanism index (η), we propose a quantitative criterion to distinguish between response regimes. Furthermore, the investigation establishes a numerical relationship between large-scale imperfection amplitudes and global stability limits, visualized through topographical transition maps.

MATHEMATICAL FORMULATION AND THEORETICAL FRAMEWORK

The nonlinear structural response of hybrid three-layer timber beams is investigated using a variational energy approach established on the principle of minimum total potential energy. This framework accounts for the synergistic interaction between high-stiffness Birch faces and a compliant Pine core, subjected to interlayer slip and large-scale geometric imperfections.

Kinematic Relations and Geometric Nonlinearity

To capture the geometrically nonlinear behavior relevant to slender members, the von Kármán strain-displacement relationship is employed. The total transverse displacement $_0$(x) is defined as the superposition of the initial sinusoidal imperfection ω_0(x) and the additional deflection ω_a(x) induced by the external load P.

$$\omega(x) = \omega_0(x) + \omega_a(x) = e_0 \sin\left(\frac{\pi x}{L}\right) + \omega_a(x) \quad (1)$$

where e_0 denotes the imperfection amplitude at mid-span. The longitudinal strain ε_x at the neutral axis of the composite section, considering the second-order effects of curvature, is formulated as:

$$\varepsilon_x = \frac{du}{dx} + \frac{1}{2}\left[\left(\frac{d\omega}{dx}\right)^2 - \left(\frac{d\omega_0}{dx}\right)^2\right] \quad (3)$$

The fundamental geometric configuration of the hybrid Birch-Pine timber beam is illustrated in Figure 1. This model explicitly defines the layout of the high-stiffness faces and the compliant core, including the initial sinusoidal imperfection profile used to simulate realistic manufacturing tolerances.

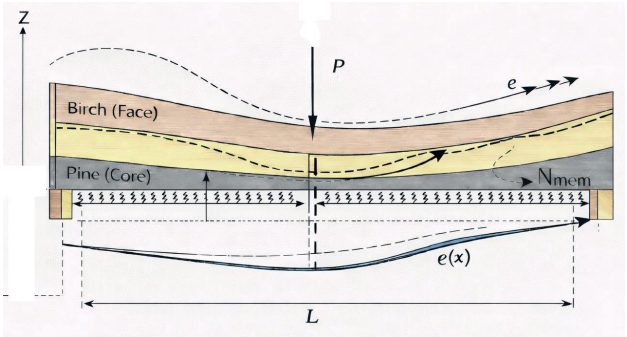

Figure 1. Geometric and kinematic configuration of the imperfect hybrid three-layer timber beam showing material layers and initial curvature e_0

The effective flexural stiffness EI_{eff} of the hybrid section is calculated using an enhanced γ-method to account for partial interaction:

$$\gamma = \frac{1}{1+\frac{\pi^2 E_f t_f}{k_s L^2}} \quad (2)$$

$$EI_{eff} = \sum E_i I_i + \gamma \sum E_i I_i a_i^2 \quad (3)$$

where a_i represents the distance from the centroid of each layer to the neutral axis of the composite section.

Variational Energy Functional

The equilibrium state is determined by minimizing the total potential energy functional Π, which represents the internal strain energy and the potential of external loads:

$$\prod = U_b + U_m + U_s - V \quad (3)$$

The individual energy components are derived as follows:

Bending Energy (U_b): Represents the energy due to curvature and effective flexural stiffness. Under the assumption of sinusoidal deflection shapes, it is expressed as:

$$U_b = \frac{1}{2}\int_0^L EI_{eff}\left(\frac{d^2\omega_a}{dx^2}\right)^2 dx = \frac{\pi^4 EI_{eff}}{4L^3}\left(\omega_m - e_0\right)^2 \quad (4)$$

Membrane Energy (U_m): Resulting from the induced axial tension (membrane force (N_{mem}) as the beam stretches due to large deflections:

$$U_m = \int_0^L \frac{N_{mem}^2}{2EA}dx, \; N_{mem} = \frac{EA}{2L}\left(\omega_m^2 - e_0^2\right)\cdot\frac{\pi^2}{L} \quad (5)$$

Slip Energy (U_s): Accounts for the shear deformation energy at the interface governed by the slip stiffness k_s

Computational Mechanism Index (η)

A distinctive contribution of this study is the introduction of a dimensionless mechanism index η. This index is derived to quantify the relative contribution of membrane forces to the overall structural resistance:

$$\eta(P) = \frac{U_m}{U_b + U_m} \quad (3)$$

This formulation enables a rigorous identification of the transition load P^*, where the structural behavior shifts from a bending-dominated regime (η=0) to a membrane-activated regime (η→1).

To visualize the physical significance of the mechanism index η, Fig. 3 presents the conceptual transition of the load-resisting behavior. It depicts how the internal energy shifts from a purely flexural regime at small deflections to a membrane-activated state as the geometric nonlinearities become predominant.

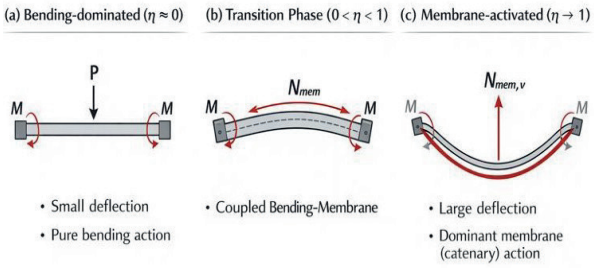

Figure 3. Conceptual transition of structural mechanisms: (a) bending-dominated, (b) coupled bending-membrane, and (c) membrane-activated regimes

Algorithmic Implementation in MATLAB

The numerical solution is executed via a load-controlled incremental procedure. At each load step P_i, the nonlinear equilibrium equations are solved to obtain the corresponding deflection ω_m. The tangent stiffness K_{tan} is consistently updated as the second derivative of the potential energy with respect to the deflection:

$$K_{\tan} = \frac{\partial^2 \prod}{\partial^2 \omega_a^2} \quad (3)$$

To ensure numerical stability across large-scale imperfections, the algorithm employs a refined

discretization of 100 nodes along the span L=5.0m, providing high-fidelity convergence for stress gradients and interface slip distributions.

The numerical solution strategy follows a systematic load-controlled incremental procedure. Fig. 3 provides a detailed computational flowchart of the implemented MATLAB algorithm, highlighting the iterative Newton-Raphson scheme used to ensure convergence in the presence of large-scale geometric nonlinearities.

-

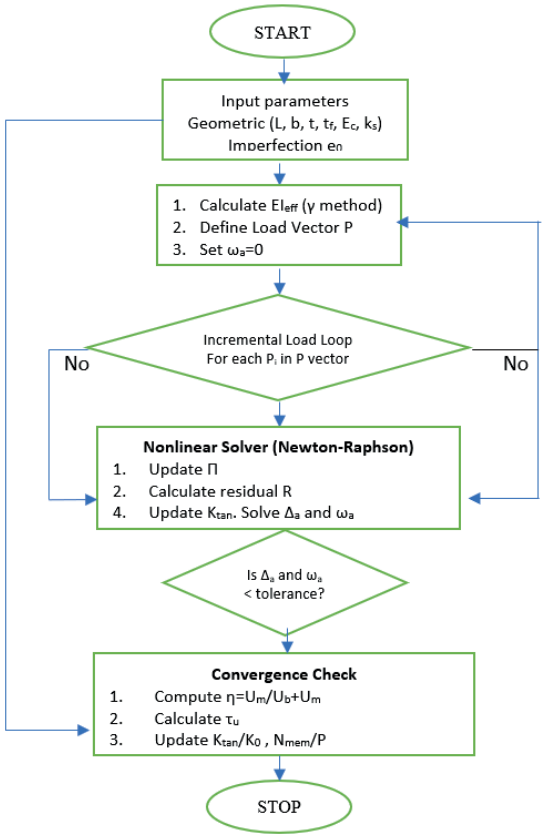

Figure 3. Flowchart of the computational algorithm for nonlinear stability analysis and mechanism index (η) evaluation

NUMERICAL STUDY AND PARAMETRIC ANALYSIS

In this section, the developed computational framework is applied to a reference hybrid configuration to evaluate its sensitivity to initial geometric deviations.

Reference Configuration and Material Properties

The analysis considers three distinct hybrid configurations to ensure the robustness of the findings. The primary case study involves a Birch–Pine assembly with a span-to-depth ratio representative of modern mid-span timber beams. The material and geometric constants used in the simulation are:

- Faces (Birch): $E_f = 22$ GPa, $t_f = 0.02$ m.
- Core (Pine): $E_c = 7$GPa, $t_c = 0.10$ m.

Connection: Slip stiffness $k_s = 0.8 \cdot 10^8$ N/m², representing a high-degree of partial interaction.

Results and Discussions

4.1. Nonlinear Equilibrium Paths and Imperfection Sensitivity

The global structural response is first characterized by the load-deflection (P-Δ) curves for varying initial imperfection amplitudes e_0= 2, 50, 100 mm), as illustrated in Fig. 4. The numerical results reveal that even for the "infinitesimal" case e_0= 2 mm), the equilibrium path deviates from the linear-elastic prediction as the load increases, indicating a soft-spring behavior typical of slender hybrid members. Notably, the high-fidelity simulation captures the transition toward a horizontal plateau, signifying the approach to the structural stability limit.

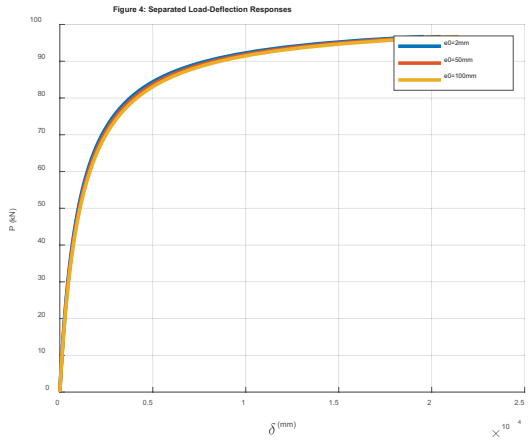

Figure 4. Nonlinear load-deflection δ_L paths for hybrid Birch-Pine timber beams with varying initial imperfection amplitudes e_0

As shown in Fig. 4, the total deflection δ_L reaches values up to 2.5 $\cdot 10^4$ mm, demonstrating the large-displacement capability of the proposed variational framework

For large-scale imperfections (e_0 = 100 mm or L/50), the beam exhibits a significantly reduced initial stiffness. The non-linear curvature of the P-Δ path suggests that the structural resistance is no longer purely flexural. As the deflection approaches the beam depth, the load-carrying capacity is increasingly bolstered by geometric hardening a direct consequence of the activation of membrane tension.

4.2. Tangent Stiffness Degradation and Knock-down Factors

The degradation of tangent stiffness (K_{tan}) is a crucial metric for evaluating the reliability of timber structures. Fig. 5 demonstrates the normalized stiffness ratio (K_{tan}/K_0) relative to the applied load.

Small Imperfections: K_{tan} remains relatively stable until a critical threshold is reached, where it drops sharply.

Large Imperfections: A dramatic "knock-down" effect is observed, with an immediate loss of nearly 60% of the initial stiffness.

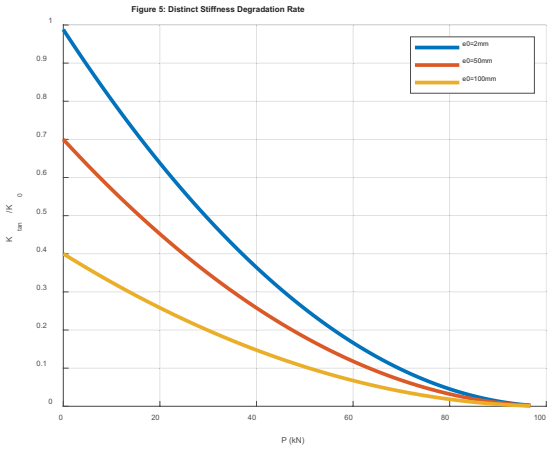

Figure 5. Normalized tangent stiffness degradation (K_{tan}/K_0) as a function of the applied load P for different imperfection levels

This observation implies that for hybrid members with realistic installation misalignments, traditional linear design methods significantly overestimate the structural capacity, potentially leading to unsafe serviceability assessments.

The transition between structural regimes is quantified by the mechanism index η. Fig. 6 shows the evolution of η as a function of the deflection.

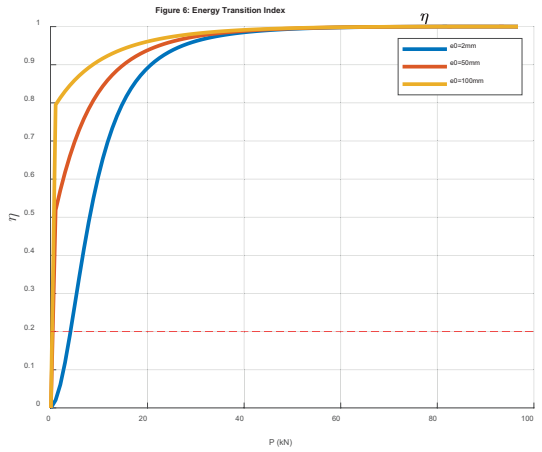

Figure 6. Evolution of the mechanism index η versus applied load P for various initial imperfection amplitudes

In the early loading stages, η remains close to zero, confirming that bending energy (U_b) is the dominant resistance mechanism. As the deflection exceeds ω/L=0.01, η rises exponentially. For e_0 = 100mm, the membrane energy (U_m) contributes over 80% of the internal energy functional before the ultimate load limit.

This transition identifies the "Catenary" effect in hybrid beams, where the high-stiffness Birch faces act as tension-resisting membranes, compensating for the stiffness loss in the soft Pine core.

To further elucidate the transition mechanism, Fig. 7 illustrates the evolution of the normalized membrane force (N_{mem} /P) with respect to the applied load P. The numerical results indicate that for all imperfection levels, the membrane contribution remains negligible during the initial loading phase. Tuy nhiên, as the system approaches the stability limit, a sharp exponential growth in N_{mem} /P is observed,

signifying that the structural resistance is being fundamentally redistributed from bending to a high-tension catenary state.

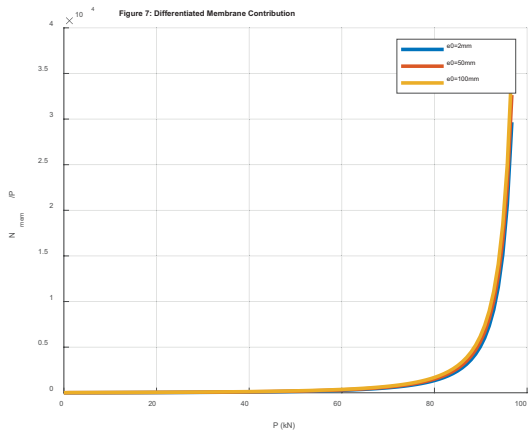

Figure 7. Evolution of the normalized membrane force contribution N_{mem} /P as a function of the applied load P

4.4. Shear Stress Concentration and Interface Slip

The interaction between global nonlinearity and the composite interface is analyzed through the shear stress τ and slip s distributions. Fig. 8 illustrates the distribution of shear stress gradients along the beam span x (m). The numerical results reveal a symmetric bell-shaped gradient, showing that peak stress concentrations occur at the mid-span. It is important to note that although the horizontal axis represents the position x, the peak values are significantly amplified as the initial imperfection e_0 increases from 2 mm to 100 mm.

Furthermore, the evolution of transverse shear stress τ (MPa) across the span x (m) is depicted in Fig. 9. This plot highlights the anti-symmetric stress distribution typical of flexural members, where the stress sign reverses at the mid-span (x = 2.5 m). Larger e_0 values lead to steeper stress gradients near the supports and mid-span, which may jeopardize the interlayer integrity and trigger premature delamination.

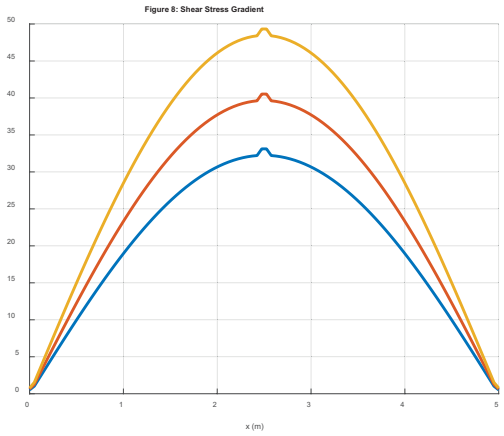

Figure 8. Distribution of interface shear stress gradients along the beam length for different imperfection amplitudes e_0

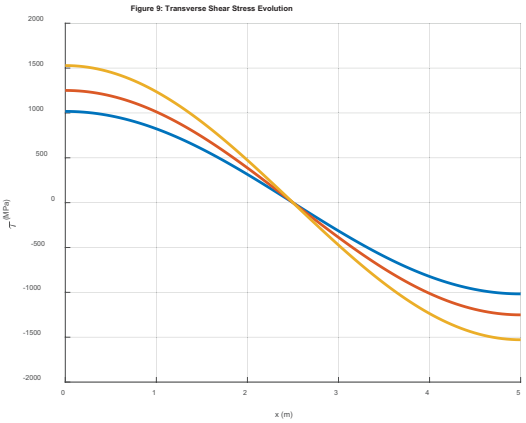

Figure 9. Evolution of transverse shear stress τ (MPa) across the span x (m) under nonlinear loading conditions

4.5. Stability Mapping and Design Implications

The relationship between the initial imperfection magnitude e_0 and the structural reliability is summarized in Fig. 10 through the stability reduction (knock-down) factor.

The curve reveals an exponential decay, where even a minor imperfection significantly compromises the load-carrying capacity, providing a critical reference for establishing manufacturing tolerances.

Finally, a comprehensive topographical stability map is constructed in Fig.11. This 3D visualization serves as a robust design tool, allowing engineers to identify 'safety zones'

where the hybrid Birch-Pine system remains stable and 'risk zones' where the synergy of low interface stiffness and large imperfections leads to premature nonlinear failure

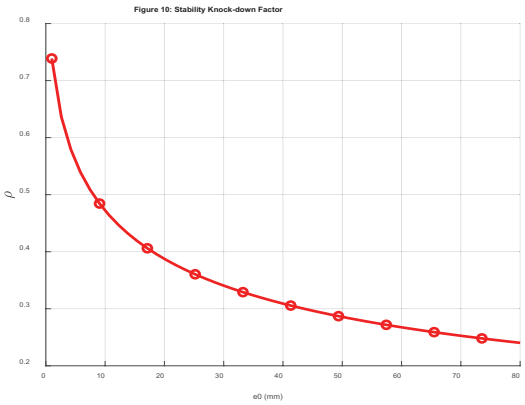

Figure 10. Structural stability reduction (knock-down) factor as a function of the initial imperfection amplitude e_0 (mm)

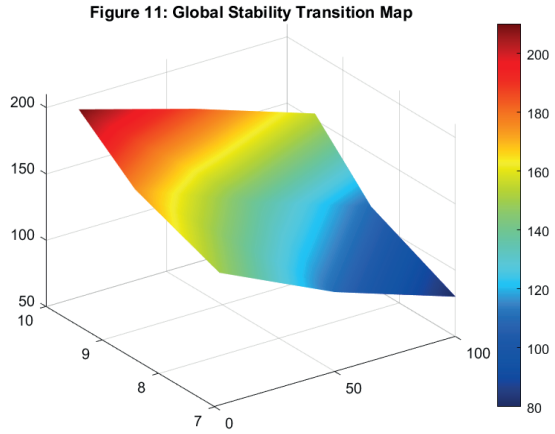

Figure 11. 3D topographical transition map illustrating the synergistic effects of interface stiffness and geometric imperfections on global stability

CONCLUSION

The comprehensive investigation into the nonlinear stability and mechanism transition of hybrid Birch-Pine timber beams via a mechanism-based energy approach provides critical insights into the complex structural behavior of slender composite systems. The developed computational framework successfully captures the high sensitivity of the nonlinear equilibrium path to initial geometric imperfections, where numerical simulations quantify a drastic reduction of up to 60% in the pre-critical tangent stiffness for realistic fabrication tolerances. This phenomenon highlights a fundamental requirement for robust nonlinear solvers in the reliability-based design of hybrid members, as traditional linear-elastic predictions fail to account for the immediate "soft-spring" deviation observed even under infinitesimal misalignments. By implementing an incremental-iterative procedure within a variational framework, this study proves that the structural integrity of hybrid timber systems is governed by a delicate balance between material architecture and geometric nonlinearity.

Furthermore, the study demonstrates that the shift from bending-dominated to membrane-activated regimes is a quantifiable physical phenomenon, effectively characterized through the proposed mechanism index η. As geometric nonlinearities evolve beyond the small-deflection regime, the internal energy balance undergoes a fundamental redistribution, leading to a "catenary effect" where membrane tension eventually provides over 80% of the total structural resistance in the advanced post-critical stages. This computational resolution extends to the hybrid interface, where the model identifies steep shear stress gradients and localized slip accumulations amplified by large-scale deformations. Unlike previous simplified models, the current approach explicitly couples the global stability limits with localized kinematic discontinuities at the interface, revealing that large initial curvatures not only reduce load-carrying capacity but also intensify the risk of premature delamination between the high-stiffness Birch faces and the compliant Pine core.

The resulting topographical stability maps, generated through the parametric efficiency of the implemented algorithm, serve as a predictive tool for identifying the synergy between interlayer slip stiffness and geometric

imperfections. These maps establish a rigorous basis for optimizing the material architecture and establishing manufacturing tolerances in modern engineering practice. While the current model provides a robust foundation for static stability analysis, the observed nonlinear transition mechanisms suggest that future computational research should incorporate time-dependent creep effects and stochastic imperfection distributions. Such advancements will further refine the predictive capability of the mechanism-based energy approach, ensuring the long-term reliability of hybrid composite structures in complex loading environments.

REFERENCES

1. **Smith, I., & Fraser, T.** (2020). Sustainable timber engineering in modern architecture. *Building Research & Information*, 48(2), 115-128. doi:10.1080/09613218.2019.1661271.
2. **Jones, K.** (2021). The rise of mass timber. *Architectural Review*, 249(1480), 12-18.
3. **Dietsch, P., & Brandner, R.** (2015). Serviceability of timber composite members: A review of current design methods. *Construction and Building Materials*, 92, 2-15.
4. **Fragiacomo, M.** (2017). *Hybrid wood-based systems: State-of-the-art and future developments*. Technical Report, University of Sassari, Italy, 1-45.
5. **Do, T.T., et al.** (2025). Experimental study on GLT structures / real-scale application. *Lecture Notes in Civil Engineering: Proceedings of the 4th International Conference on Structural Health Monitoring and Engineering Structures*, Vol. 747, Springer Nature, 791-801.
6. **Dias, A.M.** (2019). Mechanically jointed timber behavior: Experimental and numerical investigations. *Engineering Structures*, 185, 164-171.
7. CEN. (2004). *EN 1995-1-1: Eurocode 5: Design of timber structures - Part 1-1: General - Common rules and rules for buildings*. European Committee for Standardization, Brussels.
8. **Yeoh, D.** (2020). Revisiting the gamma method for CLT: Computational improvements and limitations. *Journal of Wood Science*, 66(25), 1-12.
9. **Nguyen, H.S., et al.** (2025). Modelling of Timber-to-Timber Composite Beam using Welded-Through Wood Dowels. *Lecture Notes in Civil Engineering: Proceedings of the 4th International Conference on Structural Health Monitoring and Engineering Structures*, Vol. 747, Springer Nature, 357-367.
10. **Timoshenko, S.P.** (1921). On the correction for shear of the differential equation for transverse vibrations of bars. *Philosophical Magazine*, Series 6, 41(245), 744-746.
11. **Vlasov, V.Z.** (1961). *Thin-walled elastic beams* (2nd ed.). Jerusalem: Israel Program for Scientific Translations, 1-493.
12. **Shabana, A.A.** (2019). *Geometric nonlinearity in beam-type structures*. Cambridge: Cambridge University Press, 85-112.
13. **Crisfield, M.A.** (1991). *Non-linear finite element analysis of solids and structures: Vol. 1. Essentials*. Chichester: John Wiley & Sons, 1-345.
14. **Reddy, J.N.** (2017). *Energy principles and variational methods in applied mechanics* (3rd ed.). Hoboken: John Wiley & Sons, 215-280.
15. **Nguyen, L.T., et al.** (2025). Numerical Modelling of Densified Wooden Nails in Timber Assemblies using Abaqus. *Lecture Notes in Civil Engineering: Proceedings of the 4th International Conference on Structural Health Monitoring and Engineering Structures*, Vol. 747, Springer Nature, 871-881.
16. **Do, T.T., et al.** (2025). Study on the Mechanical Properties of Glued Laminated Timber Members and Performance of Beam-Column Connections. *Lecture Notes*

in Civil Engineering: Proceedings of the 4th International Conference on Structural Health Monitoring and Engineering Structures, Vol. 747, Springer Nature, 881-891.
17. **Rajčić, V.** (2021). Timber-timber composite beams: A review of structural efficiency and sustainable performance. *Sustainability*, 13(10), 5432, 1-22.
18. **Lam, F.** (2017). Partial interaction in wood composites: Modeling and performance. *Wood Science and Technology*, 51(1), 12-28.
19. **Bažant, Z.P., & Cedolin, L.** (2003). *Stability of Structures: Elastic, Inelastic, Fracture, and Damage Theories*. Singapore: World Scientific Publishing, 1-980.
20. **Xu, B.H., & Taazunt, M.** (2020). Numerical analysis of the nonlinear behavior of hybrid timber beams with imperfect interfaces. *Construction and Building Materials*, 258, 119561, 1-14.

СПИСОК ЛИТЕРАТУРЫ

1. **Smith, I., & Fraser, T.** (2020). Sustainable timber engineering in modern architecture. *Building Research & Information*, 48(2), 115-128. doi:10.1080/09613218.2019.1661271.
2. **Jones, K.** (2021). The rise of mass timber. *Architectural Review*, 249(1480), 12-18.
3. **Dietsch, P., & Brandner, R.** (2015). Serviceability of timber composite members: A review of current design methods. *Construction and Building Materials*, 92, 2-15.
4. **Fragiacomo, M.** (2017). *Hybrid wood-based systems: State-of-the-art and future developments*. Technical Report, University of Sassari, Italy, 1-45.
5. **Do, T.T., et al.** (2025). Experimental study on GLT structures / real-scale application. *Lecture Notes in Civil Engineering: Proceedings of the 4th International Conference on Structural Health Monitoring and Engineering Structures*, Vol. 747, Springer Nature, 791-801.
6. **Dias, A.M.** (2019). Mechanically jointed timber behavior: Experimental and numerical investigations. *Engineering Structures*, 185, 164-171.
7. CEN. (2004). *EN 1995-1-1: Eurocode 5: Design of timber structures - Part 1-1: General - Common rules and rules for buildings*. European Committee for Standardization, Brussels.
8. **Yeoh, D.** (2020). Revisiting the gamma method for CLT: Computational improvements and limitations. *Journal of Wood Science*, 66(25), 1-12.
9. **Nguyen, H.S., et al.** (2025). Modelling of Timber-to-Timber Composite Beam using Welded-Through Wood Dowels. *Lecture Notes in Civil Engineering: Proceedings of the 4th International Conference on Structural Health Monitoring and Engineering Structures*, Vol. 747, Springer Nature, 357-367.
10. **Timoshenko, S.P.** (1921). On the correction for shear of the differential equation for transverse vibrations of bars. *Philosophical Magazine*, Series 6, 41(245), 744-746.
11. **Vlasov, V.Z.** (1961). *Thin-walled elastic beams* (2nd ed.). Jerusalem: Israel Program for Scientific Translations, 1-493.
12. **Shabana, A.A.** (2019). *Geometric nonlinearity in beam-type structures*. Cambridge: Cambridge University Press, 85-112.
13. **Crisfield, M.A.** (1991). *Non-linear finite element analysis of solids and structures: Vol. 1. Essentials*. Chichester: John Wiley & Sons, 1-345.
14. **Reddy, J.N.** (2017). *Energy principles and variational methods in applied mechanics* (3rd ed.). Hoboken: John Wiley & Sons, 215-280.
15. **Nguyen, L.T., et al.** (2025). Numerical Modelling of Densified Wooden Nails in Timber Assemblies using Abaqus. *Lecture Notes in Civil Engineering: Proceedings of*

the 4th International Conference on Structural Health Monitoring and Engineering Structures, Vol. 747, Springer Nature, 871-881.

16. **Do, T.T., et al.** (2025). Study on the Mechanical Properties of Glued Laminated Timber Members and Performance of Beam-Column Connections. *Lecture Notes in Civil Engineering: Proceedings of the 4th International Conference on Structural Health Monitoring and Engineering Structures*, Vol. 747, Springer Nature, 881-891.
17. **Rajčić, V.** (2021). Timber-timber composite beams: A review of structural efficiency and sustainable performance. *Sustainability*, 13(10), 5432, 1-22.
18. **Lam, F.** (2017). Partial interaction in wood composites: Modeling and performance. *Wood Science and Technology*, 51(1), 12-28.
19. **Bažant, Z.P., & Cedolin, L.** (2003). *Stability of Structures: Elastic, Inelastic, Fracture, and Damage Theories*. Singapore: World Scientific Publishing, 1-980.
20. **Xu, B.H., & Taazunt, M.** (2020). Numerical analysis of the nonlinear behavior of hybrid timber beams with imperfect interfaces. *Construction and Building Materials*, 258, 119561, 1-14.

Nguyen Le Thuy (Corresponding Author). PhD, Senior Lecturer, Faculty of Civil Engineering, Hanoi Architectural University, Km 10 Nguyen Trai Street, Thanh Xuan District, Hanoi, Vietnam, thuynt@hau.edu.vn

Нгуен Ле Тхуи (Nguyen Le Thuy), Кандидат технических наук (PhD), старший преподаватель, Строительный факультет, Ханойский архитектурный университет, район Тхань Суан, ул. Нгуен Трай, км 10, г. Ханой, Вьетнам, thuynl@hau.edu.vn

Nguyen Hong Son, PhD, Associate Professor, Advanced Lecturer, Faculty of Civil Engineering, Hanoi Architectural University, Km 10 Nguyen Trai Street, Thanh Xuan District, Hanoi, Vietnam, sonnh@hau.edu.vn

Нгуен Хонг Шон (Nguyen Hong Son), Кандидат технических наук (PhD), доцент, преподаватель высшей категории, Строительный факультет, Ханойский архитектурный университет, район Тхань Суан, ул. Нгуен Трай, км 10, г. Ханой, Вьетнам, sonnh@hau.edu.vn

Tran Thi Thuy Van, PhD, Associate Professor, Advanced Lecturer, Faculty of Civil Engineering, Hanoi Architectural University, Km 10 Nguyen Trai Street, Thanh Xuan District, Hanoi, Vietnam, vanttt@hau.edu.vn

Чан Тхюи Ван Тхи (Tran Thi Thuy Van), Кандидат технических наук (PhD), доцент, Строительный факультет, Ханойский архитектурный университет, район Тхань Суан, ул. Нгуен Трай, км 10, г. Ханой, Вьетнам, vanttt@hau.edu.vn

DOI:10.22337/2587-9618-2026-22-2-160-175

ASSESSMENT OF THERMAL AND FORCE EFFECTS ON AN ORTHOTROPIC SHELL WITH POSITIVE GAUSSIAN CURVATURE

Alexander A. Treschev, Victor G. Telichko, Denis I. Doroshenko

Tula State University (TulSU), Tula, RUSSIA

Abstract: A mathematical model of thermomechanical deformation is presented for a shell with positive Gaussian curvature, made of an orthotropic composite that develops induced anisotropy during loading. The general formulation of the boundary value problems, as substantiated in a number of studies, is carried out in an uncoupled setting. The occurrence of a temperature gradient is assumed to be one-dimensional, normal to the shell surfaces. Small temperature gradients are assumed, allowing the problem to be solved in a quasi-static manner. To account for the effect of induced heterogeneity—manifested as the dependence of the deformation-strength properties of composites on the nature of the stress state—state equations formulated by one of the authors in the principal material axes of normalized tensor space are used. The developed model is implemented for the thermomechanical analysis of a single-layer shell with positive Gaussian curvature. The main solution parameters are compared with results obtained from similar problems using tested models for the theory of deformation of orthotropic materials with differing resistance proposed by other authors, as well as from the equations of orthotropic linear elasticity theory neglecting differing resistance.

Keywords: shell, orthotropy, thermomechanical impact, differing resistance, induced anisotropy, Gaussian curvature

ОЦЕНКА ТЕМПЕРАТУРНОГО И СИЛОВОГО ВОЗДЕЙСТВИЯ НА ОРТОТРОПНУЮ ОБОЛОЧКУ ПОЛОЖИТЕЛЬНОЙ ГАУССОВОЙ КРИВИЗНЫ

А.А. Трещев, В.Г. Теличко, Д.И. Дорошенко

Тульский государственный университет (ТулГУ), г. Тула, РОССИЯ

Аннотация: Представлена математическая модель термомеханического деформирования оболочки положительной Гауссовой кривизны, изготовленной на основе ортотропного композита, в котором развивается наведенная анизотропия в процессе ее нагружения. Общая постановка краевых задач, как обосновано в ряде работ, осуществлена в несвязанной постановке. Возникновение температурного перепада принято одномерным по нормали к поверхностям оболочки. При этом приняты малые градиенты распространения температурного воздействия, благодаря чему решение задач осуществлено в квазистатическом варианте. Для учета влияния наводимой неоднородности, проявляющейся как зависимость деформационно-прочностных свойств композитов от вида напряженного состояния, использованы уравнения состояния, сформулированные одним из авторов в главных материальных осях нормированного тензорного пространства. Разработанная модель реализована при термомеханическом расчете однослойной оболочки положительной Гауссовой кривизны. Основные параметры решения сравниваются с результатами аналогичных решений, полученных с использованием наиболее апробированных моделей теории деформирования ортотропных разносопротивляющихся материалов, предложенных другими авторами, а также базирующихся на уравнениях ортотропной линейной теории упругости без учета разносопротивляемости.

Ключевые слова: оболочка, ортотропия, термомеханическое воздействие, разносопротивляемость, наведенная анизотропия, гауссова кривизна

INTRODUCTION

At the current stage of technological development, there is widespread use of advanced reinforced polymer composites strengthened by dispersed or continuous fibers. The key factor that has secured the leading position of these materials is their ability to combine high strength and stiffness characteristics with resistance to aggressive influences while maintaining minimal structural weight.

Analysis carried out during experiments has revealed a number of nonlinear and anisotropic effects. These include: different resistance to tension and compression, nonlinearity of deformation curves, and a pronounced dependence of deformation properties on the dominant type of stress state.

The aforementioned features have led to the development of accurate theoretical models and comprehensive verified testing. Despite significant advancements in solution methods and testing means, the issue remains open and is the subject of active scientific discussions [1-16].

A critical analysis of existing phenomenological theories intended for modeling bimodular orthotropic media has been repeatedly undertaken in scientific literature [17–19].

The identified shortcomings of the considered theories include: discontinuities in constitutive relations or on energy surfaces, insufficient justification of the physical meaning of phenomenological parameters, lack of accounting for the stress state type in mathematical formulations, the need for a priori constraints on material constants, and high dimensionality of the space of experimentally determined coefficients in polynomial approximation [14–16]. A critical factor reducing the practical value of these models is their consistent discrepancy with experimental data under multicomponent loading [8–16].

Thanks to their identified competitive advantages, fiber composite systems have become widespread in the design of thin-walled spatial structures. Of particular interest are coverings with synclastic geometry of the middle surface (positive Gaussian curvature), which operate under cyclic thermal loading regimes. The constructional solutions of such systems often provide for technological openings for organizing the installation of utilities.

In the practice of numerical modeling of thermomechanical processes in structures, both decoupled and coupled formulations are used. Nevertheless, analytical assessments of the degree of mutual influence of thermal and mechanical fields for elements made of materials with differing resistance indicate the short-term nature of transitional coupling processes, which decay after achieving steady-state temperature changes. Therefore, this work proposes a mathematical formulation for the deformation process of a thin-walled shell with positive Gaussian curvature, made of orthotropic composite with induced anisotropy, within a decoupled (separate) framework. The theoretical basis is an energy approach using a potential function adapted for materials with nonlinear property dependence on the stress state. This study demonstrates that the correct identification of all parameters of the energy expansion requires the implementation of a comprehensive test program with simultaneous shearing in three mutually perpendicular planes of anisotropy, which is beyond the capabilities of modern testing equipment. For this reason, as recommended in [22–24], a simplified version of the energy function in the normalized tensor space with quasi-linear approximation is used. Applying the Castigliano variational principle to this function, the constitutive equations are formulated as in [22–24,30]:

$$\{e\} = [C]\{\sigma\} \tag{1}$$

PROBLEM STATEMENT

An illustration of the structural solution for the spatial shell system of double curvature is provided in the graphical material (Figure 1b). This schematic presents a set of defining quantities: the dimensional characteristics of the structure and the parameters of the steady-state thermal regime necessary for formulating the boundary value problem.

Initial data:

1) external uniform normal pressure up to q = 0,05 MPa is applied to the shallow shell (Figure 1b);

2) the initial temperature of the shell is assumed to be uniform at $T_0 = 22^{\circ}C$ throughout its thickness and across all surfaces, the outer surface is then cooled to a temperature $T_1 = -20^{\circ}C$ and maintained constant; the inner surface of the shell is heated to a temperature $T_2 = 30^{\circ}C$ (θ° – the temperature difference at a point on the shell, occurring between the initial and final equilibrium states);

3) the principal curvatures of the shell's middle surface characterize its positive curvature:
$k_1 = 1/r_1$, $k_2 = 1/r_2$, $r_1 = 7,25$ m, $r_2 = 26$ m;

4) the plan dimensions of the shell are $2a$ = 10 m, $2b$ = 20 m (Figure 1b), with the rise f = 2 m (Figure 1b);

5) the shell thickness is taken as h = 0,1 m (Figure 1b).

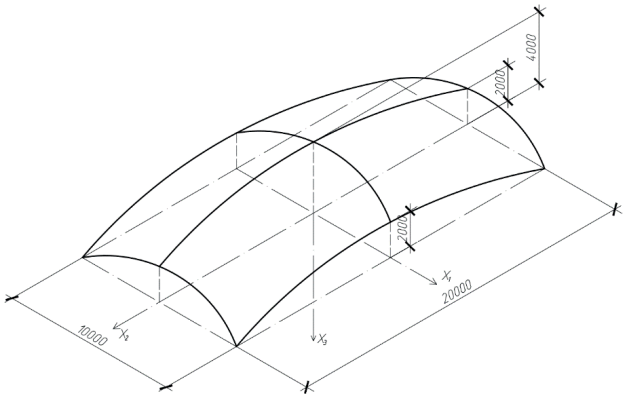

Figure 1a. General view of a shell with positive Gaussian curvature

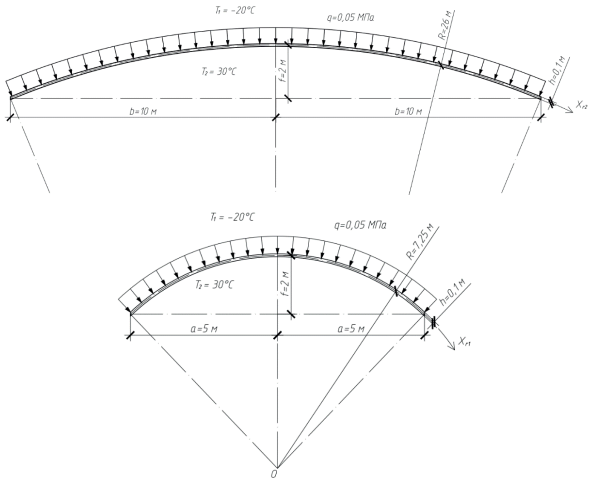

Figure 1b. Calculation scheme of a shell with positive Gaussian curvature

The choice of the kinematic model for the investigated problem is determined by the analysis of dimensionless geometric parameters. Despite the existence of alternative approaches—refined theories by S. P. Timoshenko, V. Z. Vlasov, and S. A. Ambartsumyan that account for transverse shear deformations—in this particular case, the thinness criterion (the ratio of thickness to a characteristic radius of curvature) satisfies the applicability conditions of the classical hypotheses of no transverse shear and normal stresses to the surface (Kirchhoff–Lyav model).

For a shell with positive Gaussian curvature, supported on a rectangular plan contour, the kinematic relations between the components of the displacement vector and the strains of the middle surface are written in the following form:

$$\begin{gathered}\chi_{11} = -w_{,11};\ \chi_{22} = -w_{,22};\\ \chi_{12} = -2w_{,12};\\ \varepsilon_{11} = u_{,1} - k_1 w + 0,5\left(w_{,1}\right)^2;\\ \varepsilon_{22} = v_{,2} - k_2 w + 0,5\left(w_{,2}\right)^2;\\ \gamma_{12} = u_{,2} + v_{,1} + w_{,1}\, w_{,2};\end{gathered} \qquad (2)$$

where $\varepsilon_{11}, \varepsilon_{22}, \gamma_{12}$ – normal strains and shear strains; u, v, w – displacement components; k_1, k_2 – curvature parameters of a surface ($k_1 = 1/r_1$, $k_2 = 1/r_2$).

Under the condition of strict alignment of the material's principal orthotropy axes with the axes of the attached Cartesian coordinate system, the constitutive equations (1) [30] can be transformed into a simpler form that accounts for the temperature terms:

$$\begin{aligned} e_{11} &= K_{11}\sigma_{11} + K_{12}\sigma_{22} + \omega_{1T}\theta^{\circ}; \\ e_{22} &= K_{21}\sigma_{11} + K_{22}\sigma_{22} + \omega_{2T}\theta^{\circ}; \\ e_{12} &= K_{12}\tau_{12}, \end{aligned} \qquad (3)$$

where

$$\begin{aligned} K_{11} &= A_{1111} + B_{1111}\alpha_{11} + \\ &+0,5[B_{1111}\alpha_{11}(1-\alpha_{11}^2) - B_{2222}\alpha_{22}^3] + \\ &+B_{1122}\alpha_{22}(1-\alpha_{11}^2 - \alpha_{11}\alpha_{22}); \\ K_{12} &= K_{21} = A_{1122} + B_{1122}(\alpha_{11} + \alpha_{22}); \end{aligned}$$

In the above relations: A_{iijj}, B_{iijj}, A_{kkkk}, B_{kkkk} – celastic constants of the material; $\alpha_{11} = \sigma_{11}/S$, $\alpha_{22} = \sigma_{22}/S$ – relative stresses; ω_{1T}, ω_{2T} – oefficients of thermal expansion along the anisotropy axes.

The algorithm for determining elastic properties through mechanical testing of specimens manufactured along the principal material axes of the composite system is presented in bibliographic references [22–24].

In the considered studies, in addition to conducting experiments, approximating functions for processing experimental data were obtained. Based on these, dependencies relating the engineering constants A_{kkkk}, B_{kkkk}, A_{iijj}, B_{iijj} to the technical parameters of the material were derived. For use within this two-dimensional boundary value problem, the specified dependencies were adapted and presented in the following form $i, j, k = 1, 2$:

$$\begin{aligned} A_{kkkk} &= (1/E_k^+ + 1/E_k^-)/2; \\ A_{iijj} &= -(\nu_{ij}^+/E_j^+ + \nu_{ij}^-/E_j^-)/2; \\ \nu_{ij}^+/E_j^+ &= \nu_{ji}^+/E_i^+; \\ B_{kkkk} &= (1/E_k^+ - 1/E_k^-)/2; \\ B_{iijj} &= -(\nu_{ij}^+/E_k^+ - \nu_{ij}^-/E_j^-)/2;\ \nu_{ij}^-/E_j^- = \nu_{ji}^-/E_i^-. \end{aligned}$$

Furthermore, the bibliographic sources [22–24] provide reference data on the mechanical constants of a wide range of orthotropic materials that exhibit different resistance to tension and compression.

For the case of thin-walled curved structures, the derivation of the resolving system of differential equations, formulated in terms of displacements, is based on the complete set of fundamental equations of the mechanics of deformable solids. This procedure requires inverting the physical equations (3) to express the components of the stress tensor through the corresponding deformation characteristics.

$$\begin{aligned} \sigma_{11} &= E_{11}e_{11} + E_{12}e_{22} - \varphi_{1T}; \\ \sigma_{22} &= E_{12}e_{11} + E_{22}e_{22} - \varphi_{2T}; \\ \tau_{12} &= E_{66}e_{12}; \end{aligned} \qquad (4)$$

where $E_{11} = K_{22}/\Psi$; $E_{22} = K_{11}/\Psi$;

$$\begin{aligned} E_{12} &= -K_{12}/\Psi;\ E_{66} = 1/K_{12};\ \Psi = K_{11}K_{22} - K_{12}^2; \\ \varphi_{1T} &= E_{11}\omega_{1T}\theta^{\circ} + E_{12}\omega_{2T}\theta^{\circ}; \\ \varphi_{2T} &= E_{12}\omega_{1T}\theta^{\circ} + E_{22}\omega_{2T}\theta^{\circ}. \end{aligned}$$

The formulation of equilibrium conditions for shell systems is implemented through integral force variables of membrane and bending types. In the axisymmetric case, the model includes N_{11}, N_{22}, M_{11}, M_{22} and Q_{11}. The numerical values of the first two forces and moments are determined by integral averaging of stresses along the normal to the middle surface (coordinate x_3):

$$\begin{aligned} N_{11} &= \int_{-h/2}^{h/2} \sigma_{11} dx_3; \quad N_{22} = \int_{-h/2}^{h/2} \sigma_{22} dx_3; \\ N_{12} &= \int_{-h/2}^{h/2} \sigma_{12} dx_3; \quad M_{11} = \int_{-h/2}^{h/2} \sigma_{11} x_3 dx_3; \end{aligned} \qquad (5)$$

$$M_{22} = \int_{-h/2}^{h/2} \sigma_{22} x_3 dx_3 .$$

The transverse force Q_{11} is defined by differentiating the moment M_{11} with respect to the coordinate X_1:

$$Q_{11} = M_{11,1} + N_{11} w_{,1} . \quad (6)$$

By jointly using expressions (1)–(4), a functional relationship is established between the given forces/moments and the deformational-geometric parameters (components of the strain tensor and changes in the principal curvatures) of the middle surface of the shell:

$$\begin{gathered} N_{11} = L_{11}\varepsilon_{11} + J_{11}\chi_{11} + L_{12}\varepsilon_{22} + J_{12}\chi_{22} - \eta_{1T}; \\ N_{22} = L_{12}\varepsilon_{11} + J_{21}\chi_{11} + L_{22}\varepsilon_{22} + J_{22}\chi_{22} - \eta_{2T}; \\ N_{12} = L_{66}\varepsilon_{12} + J_{66}\chi_{12}; \\ M_{11} = J_{11}\varepsilon_{11} + R_{11}\chi_{11} + J_{12}\varepsilon_{22} + R_{12}\chi_{22} - \gamma_{1T}; \\ M_{22} = J_{12}\varepsilon_{11} + R_{21}\chi_{11} + J_{22}\varepsilon_{22} + R_{22}\chi_{22} - \gamma_{2T}; \\ M_{12} = J_{66}\varepsilon_{12} + R_{66}\chi_{12}; \end{gathered} \quad (7)$$

where $L_{ij} = \int_{-h/2}^{h/2} E_{ij} dx_3$; $J_{ij} = \int_{-h/2}^{h/2} E_{ij} z\, dx_3$;

$$R_{ij} = \int_{-h/2}^{h/2} E_{ij} z^2 dx_3 ; \ \eta_{iT} = \int_{-h/2}^{h/2} \varphi_{iT} dx_3 ;$$

$$\gamma_{iT} = \int_{-h/2}^{h/2} \varphi_{iT} z\, dx_3 ; \ (i, j = 1, 2) .$$

Static equilibrium equations are invariant regarding the type of constitutive relations. In the context of the considered shell with positive curvature, for small parameter $zk << 1$ [25], they are expressed as follows:

$$\begin{cases} N_{11,1} + N_{12,2} = 0; \\ N_{12,1} + N_{22,2} = 0; \\ M_{11,11} + M_{22,22} + 2M_{12,12} - N_{11}(w_{,11} + k_1) - \\ - N_{22}(w_{,22} + k_2) - 2N_{12} w_{,12} = q_3; \end{cases} \quad (8)$$

The nonlinear nature of the problem, identified from the system of equations (1)–(8), manifests itself in three aspects: material properties, kinematics, and the nonlinearity of the computational model. Therefore, the governing system of differential equations is constructed and solved using the two-step method of successive parameter perturbations, developed by V. V. Petrov [26]. The first step of this method involves approximating the nonlinear dependencies with linear relations based on the incremental loading technique.

LINEARIZATION OF THE SYSTEM OF DIFFERENTIAL EQUATIONS

As a result of the linearization of dependencies (2), equations are obtained that relate the increments of the arguments and functions:

$$\begin{gathered} \Delta\chi_{11} = -\Delta w_{,11}; \\ \Delta\chi_{22} = -\Delta w_{,22}; \\ \Delta\chi_{12} = -2\Delta w_{,12}; \\ \Delta\varepsilon_{11} = \Delta u_{,1} - k_1 \Delta w + w_{,1} \Delta w_{,1}; \\ \Delta\varepsilon_{22} = \Delta v_{,1} - k_2 \Delta w + w_{,2} \Delta w_{,2}; \\ \Delta\varepsilon_{12} = \Delta v_{,1} + \Delta u_{,2} + w_{,1} \Delta w_{,2} + w_{,2} \Delta w_{,1}; \\ \Delta e_{11} = \Delta\varepsilon_{11} + x_3 \Delta\chi_{11}; \\ \Delta e_{22} = \Delta\varepsilon_{22} + x_3 \Delta\chi_{22}; \\ \Delta e_{12} = \Delta\gamma_{12} + x_3 \Delta\chi_{12}; \end{gathered} \quad (9)$$

where Δ – is the increment of the arguments.
Following the approach of [27], we will linearize the constitutive equations (1) by expanding them into a Taylor series and retaining first-order smallness terms:

$$\begin{gathered} \Delta e_{11} = \frac{\partial e_{11}}{\partial \sigma_{11}} \Delta\sigma_{11} + \frac{\partial e_{11}}{\partial \sigma_{22}} \Delta\sigma_{22} + \omega_{1T} \frac{\partial e_{11}}{\partial \theta^\circ} \Delta\theta^\circ ; \\ \Delta e_{22} = \frac{\partial e_{22}}{\partial \sigma_{11}} \Delta\sigma_{11} + \frac{\partial e_{22}}{\partial \sigma_{22}} \Delta\sigma_{22} + \omega_{2T} \frac{\partial e_{22}}{\partial \theta^\circ} \Delta\theta^\circ ; \\ \Delta e_{12} = \frac{\partial e_{12}}{\partial \tau_{12}} \Delta\tau_{12} \end{gathered} \quad (10)$$

By inverting equations (10) with respect to the increments of stresses, we obtain:

$$\begin{aligned}\Delta\sigma_{11} &= D_{11}\Delta e_{11} + D_{12}\Delta e_{22} - \Delta\varphi_{1T};\\ \Delta\sigma_{22} &= D_{21}\Delta e_{11} + D_{22}\Delta e_{22} - \Delta\varphi_{2T};\\ \Delta\tau_{12} &= D_{66}\Delta e_{12};\end{aligned} \qquad (11)$$

где $D_{11} = \Omega_{22}/\Omega;$

$$D_{12} = D_{21} = -\Omega_{21}/\Omega = -\Omega_{12}/\Omega;$$

$$D_{22} = \Omega_{11}/\Omega;\quad D_{66} = \Omega_{66}/\Omega;$$

$$\Omega_{11} = \frac{\partial e_{11}}{\partial\sigma_{11}};\ \Omega_{12} = \Omega_{21} = \frac{\partial e_{11}}{\partial\sigma_{22}} = \frac{\partial e_{22}}{\partial\sigma_{11}};$$

$$\Omega_{22} = \frac{\partial e_{22}}{\partial\sigma_{22}};\ \Omega_{66} = \frac{\partial e_{66}}{\partial\sigma_{66}};\ \Omega_{1T} = \frac{\partial e_{11}}{\partial\theta^{\circ}};$$

$$\Omega_{2T} = \frac{\partial e_{22}}{\partial\theta^{\circ}};$$

$$\Omega = \Omega_{11}\Omega_{22} - \Omega_{12}\Omega_{21};$$

$$\Delta\varphi_{1T} = (\Omega_{12}\Omega_{2T} - \Omega_{1T}\Omega_{22})/\Omega;$$

$$\Delta\varphi_{2T} = (\Omega_{21}\Omega_{1T} - \Omega_{2T}\Omega_{11})/\Omega.$$

The transition from stress increments (11) to increments of forces and moments is carried out according to the same rules as (5):

$$\begin{aligned}\Delta N_{11} &= \int_{-h/2}^{h/2}\Delta\sigma_{11}dx_3;\\ \Delta N_{22} &= \int_{-h/2}^{h/2}\Delta\sigma_{22}dx_3;\\ \Delta M_{11} &= \int_{-h/2}^{h/2}\Delta\sigma_{11}zdx_3;\\ \Delta M_{22} &= \int_{-h/2}^{h/2}\Delta\sigma_{22}zdx_3;\end{aligned} \qquad (12)$$

where ΔN_{11}, ΔN_{22}, ΔM_{11}, ΔM_{22} – the increments of the corresponding forces and moments. By applying expressions (12) to the increment equations (11), we obtain:

$$\begin{aligned}\Delta N_{11} &= L_{11}{}^{\Delta}\Delta\varepsilon_{11} + J_{11}{}^{\Delta}\Delta\chi_{11} + L_{12}{}^{\Delta}\Delta\varepsilon_{22} +\\ &+J_{12}{}^{\Delta}\Delta\chi_{22} - \Delta\eta_{1T};\\ \Delta N_{22} &= L_{12}{}^{\Delta}\Delta\varepsilon_{11} + J_{21}{}^{\Delta}\Delta\chi_{11} + L_{22}{}^{\Delta}\Delta\varepsilon_{22} +\\ &+J_{22}{}^{\Delta}\Delta\chi_{22} - \Delta\eta_{2T};\\ \Delta N_{12} &= L_{66}{}^{\Delta}\Delta\varepsilon_{12} + J_{66}{}^{\Delta}\Delta\chi_{12};\\ \Delta M_{11} &= J_{11}{}^{\Delta}\Delta\varepsilon_{11} + R_{11}{}^{\Delta}\Delta\chi_{11} + J_{12}{}^{\Delta}\Delta\varepsilon_{22} +\\ &+R_{12}{}^{\Delta}\Delta\chi_{22} - \Delta\gamma_{1T};\\ \Delta M_{22} &= J_{12}{}^{\Delta}\Delta\varepsilon_{11} + R_{21}{}^{\Delta}\Delta\chi_{11} + J_{22}{}^{\Delta}\Delta\varepsilon_{22} +\\ &+R_{22}{}^{\Delta}\Delta\chi_{22} - \Delta\gamma_{2T};\\ \Delta M_{12} &= J_{66}{}^{\Delta}\Delta\varepsilon_{12} + R_{66}{}^{\Delta}\Delta\chi_{12};\end{aligned} \qquad (13)$$

where $L_{ij}^{\Delta} = \int_{-h/2}^{h/2} D_{ij}dx_3;\ J_{ij}^{\Delta} = \int_{-h/2}^{h/2} D_{ij}z\,dx_3;$

$$R_{ij}^{\Delta} = \int_{-h/2}^{h/2} D_{ij}z^2dx_3;\ \Delta\eta_{iT} = \int_{-h/2}^{h/2}\Delta\varphi_{iT}dx_3;$$

$$\Delta\gamma_{iT} = \int_{-h/2}^{h/2}\Delta\varphi_{iT}z\,dx_3;\ (i,j=1,2).$$

The statics equations (8) after transformation through increments are written in the form:

$$\begin{cases}\Delta N_{11,1} + \Delta N_{12,2} = 0;\\ \Delta N_{12,1} + \Delta N_{22,2} = 0;\\ -N_{11}\Delta w_{,11} - \Delta N_{11}w_{,11} - \Delta N_{11}k_1 -\\ -N_{22}\Delta w_{,22} - \Delta N_{22}w_{,22} - \Delta N_{22}k_2 -\\ -2N_{12}\Delta w_{,12} - 2\Delta N_{12}w_{,12} +\\ +\Delta M_{11,11} + \Delta M_{22,22} + 2\Delta M_{12,12} = \Delta q_3;\end{cases} \qquad (14)$$

where Δq_3 – increment of transverse load intensity.

The linearized equations in increments of displacements of the middle surface of the Gaussian curvature shell were obtained by reducing expressions (9), (13), and (14) to a common form:

$$\begin{aligned}&L_{11,1}^{\Delta}[\Delta u_{,1} - k_1\Delta w + w_{,1}\Delta w] + L_{11}^{\Delta}[\Delta u_{,11} - k_1\Delta w_{,1} +\\ &+w_{,11}\Delta w_{,1} + w\Delta w_{,11}] - J_{11,1}^{\Delta}\Delta w_{,11} - J_{11}^{\Delta}\Delta w_{,111} +\\ &+L_{12}^{\Delta}[-\Delta wk_2 + w_{,2}\Delta w + \Delta v_{,2}] + L_{12}^{\Delta}[-\Delta w_{,1}k_2 +\\ &+w_{,12}\Delta w_{,2} + w_{,2}\Delta w_{,12}] + \Delta v_{,12} - J_{12,1}^{\Delta}\Delta w_{,22} -\end{aligned}$$

$$
\begin{aligned}
&-J_{12}^{\Delta}\Delta w_{,122}-\Delta\eta_{1T},_1+L_{66}^{\Delta},_2[w_{,1}\Delta w_{,12}+\Delta w_{,1}w_{,2}+\\
&+\Delta u_{,2}+\Delta v_{,1}]+L_{66}^{\Delta}[w_{,12}\Delta w_{,2}+w_{,1}\Delta w_{,12}+\\
&+w_{,12}\Delta w_{,12}+\Delta w_{,1}w_{,22}+\Delta u_{,22}+\Delta u_{,12}]-\\
&-2L_{66}^{\Delta}[\Delta w_{,122}]=0\\
&L_{66}^{\Delta},_1[w_{,1}\Delta w_{,2}+\Delta w_{,1}w_{,2}+\Delta u_{,2}+\Delta v_{,1}]+\\
&+L_{66}^{\Delta}[w_{,11}\Delta w_{,2}+w_{,1}\Delta w_{,2}+w_{,11}\Delta w_{,2}+\Delta w_{,1}w_{,12}+\\
&+\Delta u_{,122}+\Delta v_{,11}]-2J_{66}^{\Delta}\Delta w_{,112}+L_{12}^{\Delta},_2[\Delta u_{,1}-k_1\Delta w+\\
&+w_{,1}\Delta w]+L_{12}^{\Delta}[\Delta u_{,12}-k_1\Delta w_{,2}+\Delta w_{,1}w_{,12}+\\
&+w_{,1}\Delta w_{,12}]-J_{12}^{\Delta}\Delta w_{,112}+L_{22}^{\Delta},_2[-wk_2+w_{,2}\Delta w_{,2}+\\
&+\Delta v_{,2}]+L_{22}^{\Delta},_2[-\Delta w_{,2}k_2+\Delta w_{,22}+w_{,2}\Delta w_{,22}+\\
&+\Delta v_{,22}]-J_{22}^{\Delta}\Delta w_{,22}-J_{22}^{\Delta}\Delta w_{,222}-\Delta\eta_{2T},_2=0\\
&-\Delta\gamma_{1T},_{11}-\Delta\gamma_{2T},_{22}-R_{11}^{\Delta}\Delta w_{,1111}+J_{12}^{\Delta},_{11}[-wk_2+\\
&+w_{,2}\Delta w_{,2}+\Delta v_{,2}]++2J_{12}^{\Delta},_1[-\Delta wk_2+w_{,12}\Delta w_{,12}+\\
&+w_{,2}\Delta w_{,12}+\Delta v_{,12}]+J_{12}^{\Delta}[-\Delta w_{,11}k_2+w_{,112}\Delta w_{,2}+\\
&+2w_{,12}\Delta w_{,12}+w_{,2}\Delta w_{,112}+\Delta v_{,112}]-\\
&-2\{L_{66}^{\Delta},_1[w_{,1}\Delta w_{,2}+\Delta w_{,1}w_{,2}+\Delta u_{,2}+\Delta v_{,1}]-\\
&-2J_{66}^{\Delta}\Delta w_{,12}\}w_{,12}-\{L_{11}[u_{,1}-k_1w+0,5(w_{,1})^2]-\\
&-J_{11}w_{,11}+L_{12}[v_{,2}-k_2w+0,5(w_{,2})^2]-\\
&-J_{12}w_{,22}-\eta_{1T}\}\Delta w_{,11}-\{L_{11}^{\Delta}[\Delta u_{,1}-k_1\Delta w+\\
&+w_{,1}\Delta w_{,1}]-J_{11}^{\Delta}\Delta w_{,11}+L_{12}^{\Delta}[-\Delta wk_2+w_{,2}\Delta w_{,12}+\\
&+\Delta v_{,2}]-J_{12}^{\Delta}\Delta w_{,22}-\eta_{1T}\}w_{,11}-\{L_{11}[\Delta u_{,1}-k_1\Delta w+\\
&+w_{,1}\Delta w_{,1}]-J_{11}^{\Delta}\Delta w_{,11}+L_{12}^{\Delta}[-\Delta wk_2+w_{,2}\Delta w_{,12}+\\
&+\Delta v_{,2}]-J_{12}^{\Delta}\Delta w_{,22}-\eta_{1T}\}k_1-\{L_{12}[u_{,2}-k_2w+\\
&+0,5(w_{,1})^2]-J_{12}w_{,11}+L_{22}[v_{,2}-k_2w+0,5(w_{,2})^2]-\\
&-J_{22}w_{,22}-\eta_{2T}\}\Delta w_{,22}-\{L_{12}^{\Delta}[\Delta u_{,1}-k_1\Delta w+\\
&+w_{,1}\Delta w_{,1}]-J_{12}^{\Delta}\Delta w_{,11}+L_{22}^{\Delta}[-\Delta wk_2+w_{,2}\Delta w_{,2}+\\
&+\Delta v_{,2}]-J_{22}^{\Delta}\Delta w_{,22}-\Delta\eta_{2T}\}w_{,22}-\{L_{12}^{\Delta}[\Delta u_{,1}-\\
&-k_1\Delta w+w_{,1}\Delta w_{,1}]-J_{12}^{\Delta}\Delta w_{,11}+L_{22}^{\Delta}[-\Delta w,k_2+\\
&+w_{,2}\Delta w_{,2}+\Delta v_{,2}]-J_{22}^{\Delta}\Delta w_{,22}-\eta_{2T}\}k_2-\\
&-2\{L_{66}[u_{,2}-v_{,1}+w_{,1}\Delta w_{,2}]-2J_{66}w_{,12}\}\Delta w_{,12}-\\
&-R_{11}^{\Delta},_{11}\Delta w_{,11}-2R_{11}^{\Delta}\Delta w_{,111}+J_{11}^{\Delta},_{11}[\Delta u_{,1}-\\
&-k_1\Delta w+w_{,1}\Delta w_{,1}]+2J_{11}^{\Delta}[\Delta u_{,11}-k_1\Delta w_{,1}+\\
&+w_{,11}\Delta w_{,1}+w_{,1}\Delta w_{,11}]+J_{11}^{\Delta}[\Delta u_{,111}-k_1\Delta w_{,11}+\\
&+w_{,111}\Delta w_{,1}+2w_{,11}\Delta w_{,11}+w_{,1}\Delta w_{,111}]+\\
&+J_{12}^{\Delta},_{22}[\Delta u_{,1}-k_1\Delta w+w_{,1}\Delta w_{,1}]+\\
&+2J_{12}^{\Delta},_2[\Delta u_{,12}-k_1\Delta w_{,2}+w_{,1}\Delta w_{,12}+w_{,1}\Delta w_{,12}]+\\
&+J_{12}^{\Delta}[\Delta u_{,122}-k_1\Delta w_{,22}+2w_{,12}\Delta w_{,12}+\\
&+\Delta w_{,1}w_{,122}+w_{,1}\Delta w_{,122}]-R_{12}^{\Delta}\Delta w_{,1122}+\\
&+J_{22}^{\Delta},_{22}[-\Delta wk_2+w_{,2}\Delta w_{,2}+\Delta v_{,2}]+\\
&+2J_{22}^{\Delta}[-\Delta w_{,2}k_2+w_{,22}\Delta w_{,2}+w_{,2}\Delta w_{,22}+\\
&+\Delta v_{,22}]+J_{22}^{\Delta}[-\Delta w_{,22}k_2+w_{,222}\Delta w_{,2}+\\
&+2w_{,22}\Delta w_{,22}+w_{,2}\Delta w_{,222}+\Delta v_{,222}]+\\
&+2J_{66}^{\Delta}[w_{,112}\Delta w_{,2}+w_{,11}\Delta w_{,22}+2w_{,12}\Delta w_{,12}+\\
&+w_{,1}\Delta w_{,122}+w_{,12}\Delta w_{,122}+\Delta w_{,11}w_{,22}+\\
&+\Delta w_{,1}w_{,112}+\Delta u_{,122}\Delta v_{,112}]-4R_{66}^{\Delta}\Delta w_{,1122}-\\
&-R_{12}^{\Delta},_{11}\Delta w_{,22}-2R_{12}^{\Delta}\Delta w_{,122}-R_{12}^{\Delta}\Delta w_{,1122}+\\
&+2J_{66}^{\Delta},_2[w_{,11}\Delta w_{,2}+w_{,1}\Delta w_{,12}+\Delta w_{,11}w_{,2}+\\
&+\Delta w_{,1}w_{,12}+\Delta u_{,12}+\Delta v_{,11}]+2J_{66}^{\Delta},_1[w_{,12}\Delta w_{,2}+\\
&+w_{,1}\Delta w_{,22}+\Delta w_{,2}w_{,12}+\Delta w_{,1}w_{,22}+\\
&+\Delta u_{,22}+\Delta v_{,12}]-R_{22}^{\Delta},_{22}\Delta w_{,22}-2R_{22}^{\Delta},_2\Delta w_{,222}-\\
&-R_{22}^{\Delta}\Delta w_{,2222}+2J_{66}^{\Delta},_{12}[w_{,1}\Delta w_{,2}+\\
&+w_{,1}\Delta w_{,2}+\Delta u_{,2}+\Delta v_{,1}]=\Delta q
\end{aligned}
\tag{15}
$$

To ensure a closed formulation of the problem, boundary conditions must be added to the differential equations (15), also expressed in terms of increments of displacements.

The rigid clamping of the support contour is specified by the following relations:

$$\Delta u=0;\quad \Delta w=0;\quad \Delta w_{,r}=0. \tag{16}$$

THE TEMPERATURE COMPONENT OF THE PROBLEM

The differential heat conduction equation [28] adequately describes the heat propagation process in structurally orthotropic solids:

$$T_{,t}=\Lambda_1\cdot T_{,11}+\Lambda_2\cdot T_{,22}+\Lambda_3\cdot T_{,33}, \tag{17}$$

where Λ_1, Λ_2, Λ_3 – thermophysical material constants along the principal axes, defining the thermal inertia of the material;; t – time; T – temperature.

Within the framework of the given problem, the temperature distribution is formed exclusively in the cross-section of the shell, and the heat transfer process is one-dimensional along the x_3 -axis. In this regard, the differential heat conduction equation (17) admits significant simplification and can be presented in the following form:

$$T_{,t} = \Lambda_3 \cdot T_{,33}, \qquad (18)$$

where $\Lambda_3 = \lambda / c$ – thermal diffusivity coefficient in the direction normal to the shell surface λ – eat transfer coefficient; c – specific heat capacity per unit volume.

The subject of numerical investigation were shell systems made of fiberglass materials and composites with similar properties, possessing significant heat transfer coefficients. Due to high thermal conductivity, in thin-walled structures, the formation of a steady temperature gradient across the thickness occurs rapidly, and the spatial temperature distribution is characterized by linearity. This fact allows the related thermoelastic problem to be considered after reaching a steady-state regime with a constant temperature gradient along the coordinate x_3. As a result, the temperature across the shell section is determined by the expression (Figure 1b):

$$T(x_3) = (T_2 - T_1)\, x_3 / h + (T_1 + T_2)/2 - T_0. \qquad (19)$$

SOLUTION OF THE PROBLEM AND ANALYSIS OF THE RESULTS

As a representative orthotropic material, fiberglass composite was investigated. The mechanical property values used in this study, including the tensile elastic moduli along the principal anisotropy axes, are consistent with data from references [13, 14]: E_1^+ =140 GPa, E_2^+ =280 GPa, at axial compressions: E_1^- =70 GPa, and E_2^- =140 GPa; corresponding coefficients of transverse deformation: $\nu_{12}^+ = 0,2$; $\nu_{12}^- = 0,3$; coefficients of linear thermal expansion in the directions of the principal material axes: $\omega_{1T} = 3,3 \cdot 10^{-6} (^\circ C)^{-1}$; $\omega_{2T} = 4,0 \cdot 10^{-6} (^\circ C)^{-1}$ [13, 14].

Integration of the linearized system of differential operators (15) satisfying boundary conditions (16) and considering the temperature profile through the thickness of the structure (19) was implemented based on a high-order accuracy finite difference scheme, including central approximations at internal nodes and one-sided formulas in boundary regions. Spatial discretization was performed by placing 200 nodal points along the radial coordinate with simultaneous division of the thickness into 21 layers to implement Simpson's quadrature formula. The resulting algebraic system of linear equations was solved by the Gauss-Seidel iterative method with the application of Lüsternik relaxation acceleration. Numerical integration along the loading path was performed using Adams extrapolation scheme. The developed computational algorithm with branched logic was implemented as part of specialized software built on the open environment "SCILAB".

Verification of the developed approach was carried out by comparing the calculated data with results based on alternative constitutive models from publications [8–13]. A generalized analysis was conducted in the following directions:

a) with results obtained using advanced constitutive relations for orthotropic materials (Model 1);

b) calculation employing averaged mechanical characteristics while neglecting induced deformation anisotropy properties (Model 2);

c) results from the developed model with thermal effects excluded (Model 3);

d) data obtained following the theory of C. W. Bert – J. N. Reddy [8, 9] (Model 4);

e) solutions based on the model by R. M. Jones – D. A. R. Nelson [10, 13] (Model 5).

f) with solutions of S. A. Ambartsumyan (Model 6).

Figures 2-5 and 8-11 show the calculated results of the normal stresses σ_{11} and σ_{22}; Figures 14-18 show the displacements and deflections of the middle surface of the considered

shell, obtained using various state equations for structurally orthotropic materials exhibiting deformational inhomogeneity (variable resistance) during loading. Figures 6, 7, 12, and 13 present characteristic stress distributions through the thickness of the shell in a specified cross-section.

The results of calculating the stress-strain state of a shell with positive Gaussian curvature under combined transverse loading and temperature gradient revealed their significant dependence on the choice of constitutive relations for orthotropic media that exhibit different behavior under various stress state types.

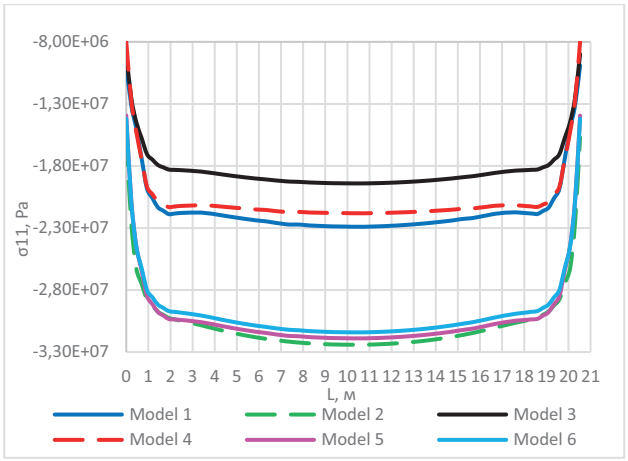

Figure 2. Normal stresses σ_{11} at the top along the long side along the Y axis, Pa

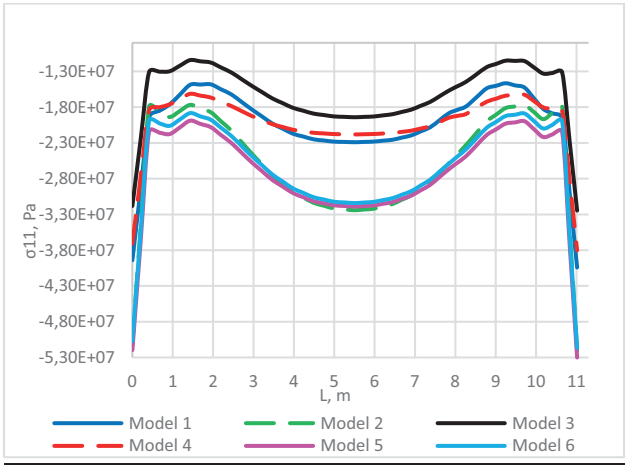

Figure 3. Normal stresses σ_{11} at the top along the short side along the X axis, Pa

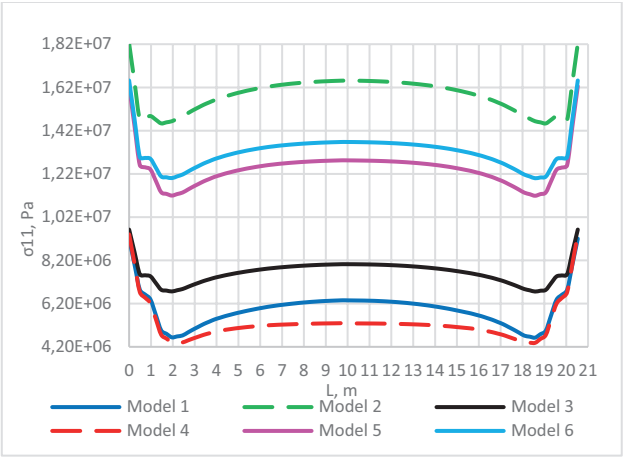

Figure 4. Normal stresses σ_{11} at the bottom along the long side along the Y axis, Pa

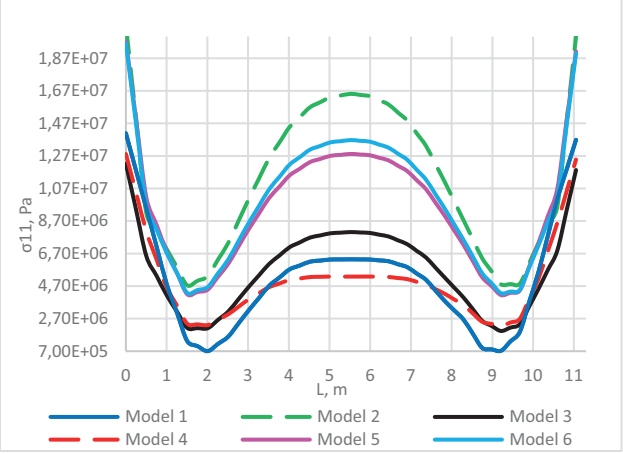

Figure 5. Normal stresses σ_{11} at the bottom along the short side along the X axis, Pa

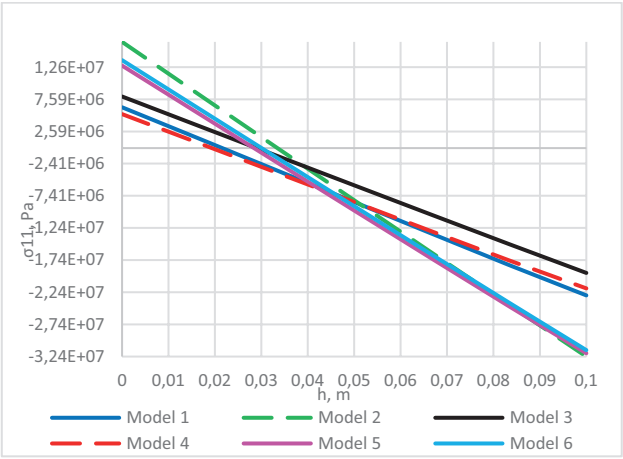

Figure 6. Normal stresses σ_{11} at the center through the thickness, Pa

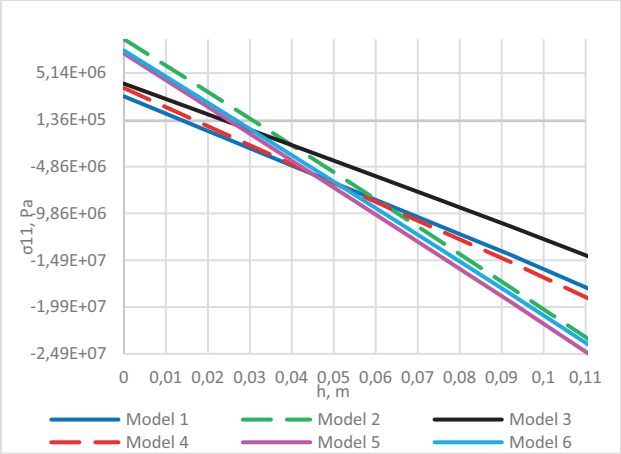

Figure 7. Normal stresses σ_{11} at ¼ length to the left along the X axis through the thickness, Pa

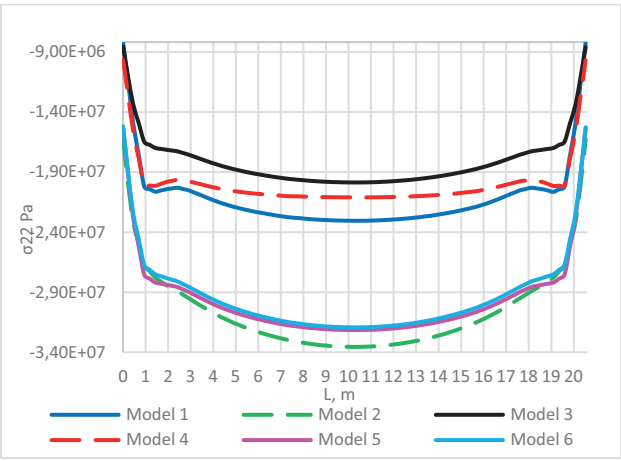

Figure 8. Normal stresses σ_{22} at the top along the long side along the Y axis, Pa

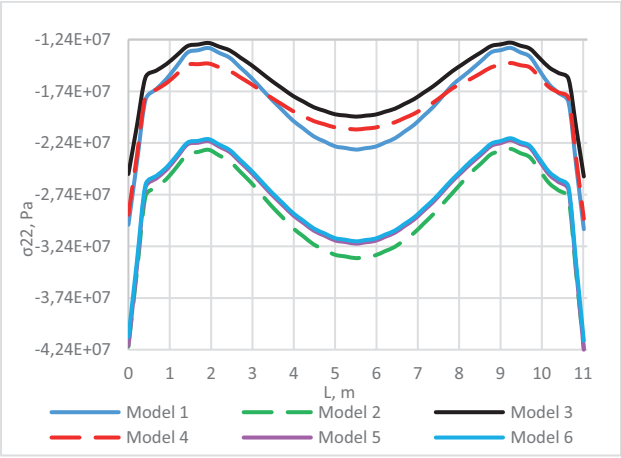

Figure 9. Normal stresses σ_{22} at the top along the short side along the X axis, Pa

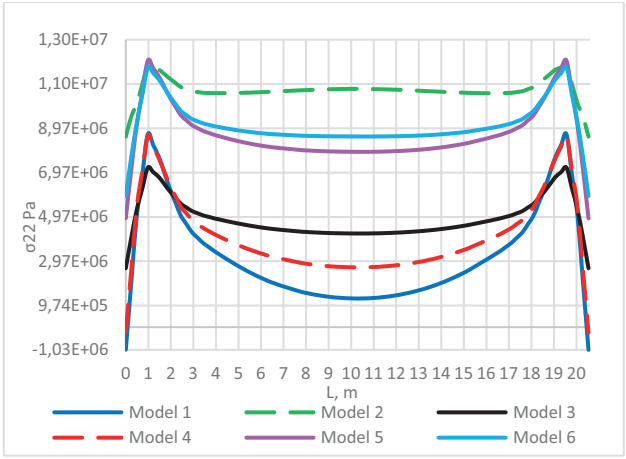

Figure 10. Normal stresses σ_{22} at the bottom along the long side along the Y axis, Pa

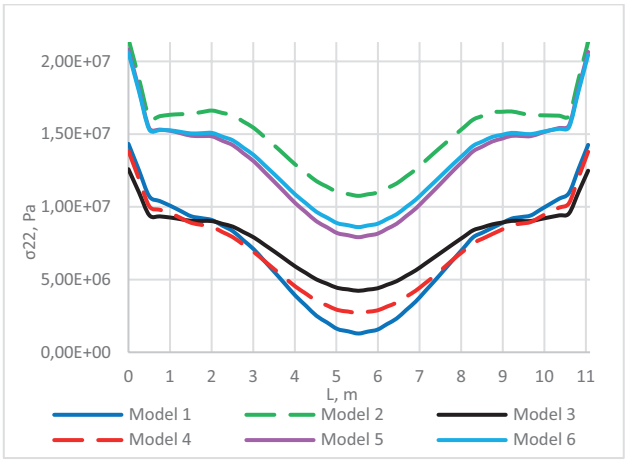

Figure 11. Normal stresses σ_{22} at the bottom along the short side along the X axis, Pa

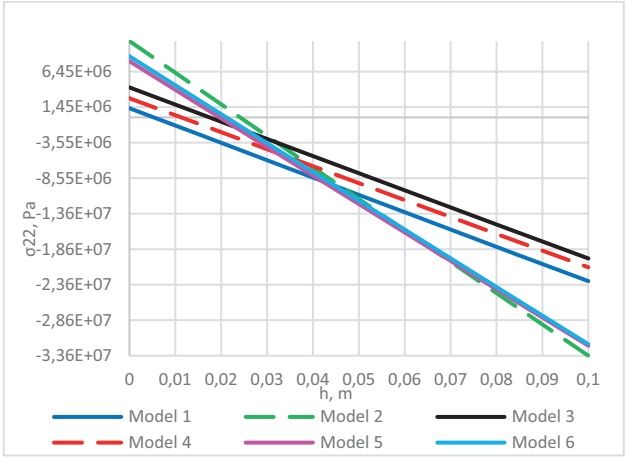

Figure 12. Normal stresses σ_{22} at the center through the thickness, Pa

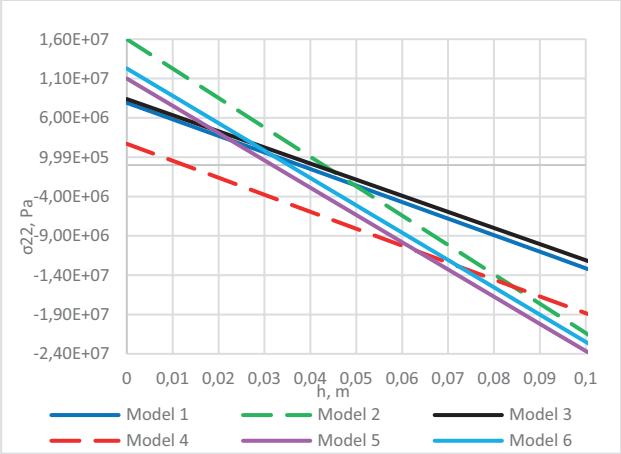

Figure 13. Normal stresses σ_{22} at ¼ to the left along the X axis through the thickness, Pa

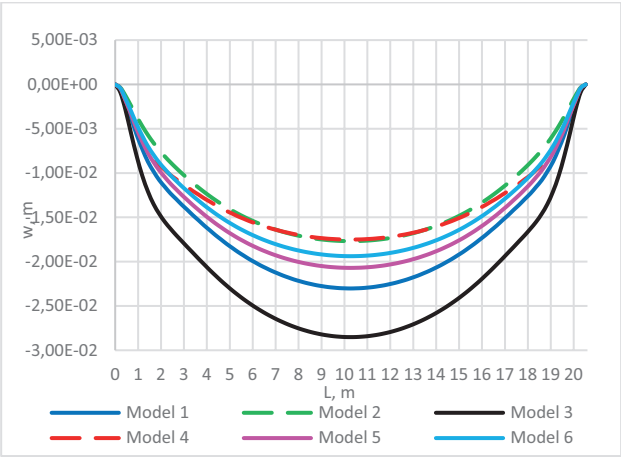

Figure 14. Displacements W along the long side, m

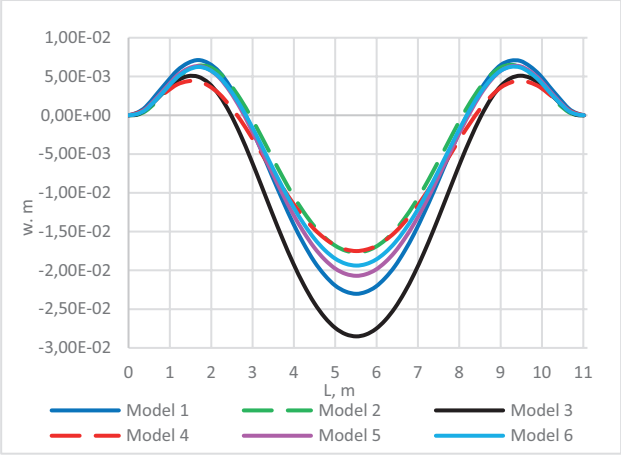

Figure 15. Displacements W along the short side, m

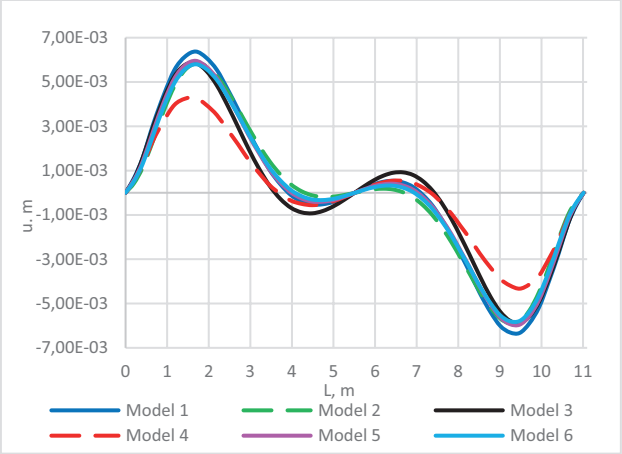

Figure 16. Displacements U along the long side, m

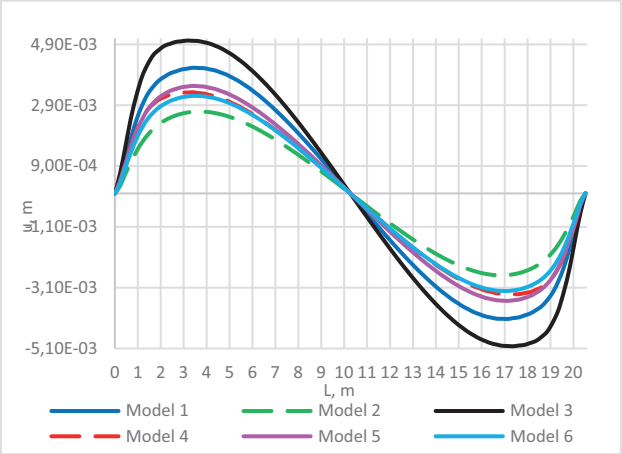

Figure 17. Displacements U along the long side, m

Through numerical analysis of the thermomechanical deformation of a positively curved orthotropic shell made of fiberglass, a set of characteristic patterns was established:

1.The discrepancy in the values of normal stresses σ_{11} compared to the classical theory, which ignores the anisotropy of deformation properties and uses averaged constants, reaches up to 41,5%, ignoring thermal effects yields deviations of 15,3%; compared to the theory of C. W. Bert – J. N. Reddy, the deviation is 4,8%; with the application of the relations by R. M. Jones – D. A. R. Nelson, it is 39,3%; and under all equal thermomechanical loading conditions, it is 37,2% compared to calculations based on equations by S. A. Ambartsumyan;

2. For the normal stresses σ_{22}, the differences from the classical approach reach 45,9%; without considering thermal effects, 13,7%; compared to C. W. Bert – J. N. Reddy's theory, 8,3%; using R. M. Jones – D. A. R. Nelson's relations, 39,8%; and under equal thermomechanical loading conditions, 38,8% relative to calculations by S. A. Ambartsumyan;
3. For displacements W, the discrepancy reaches 23,1% relative to calculations by traditional orthotropic shell theory with averaged material characteristics, 24,1% without thermal gradient consideration, 23,9% compared to C. W. Bert – J. N. Reddy's model, 10% relative to R. M. Jones – D. A. R. Nelson's variant, and 15,7% compared to S. A. Ambartsumyan's theory;
4. For displacements U, the discrepancy is 12,5% relative to traditional orthotropic shell theory with averaged characteristics, 22% without temperature gradient, 23% compared to S. A. Ambartsumyan's theory, 6,5% compared to C. W. Bert – J. N. Reddy's model, and 17,5% relative to R. M. Jones – D. A. R. Nelson's variant.

CONCLUSIONS SUPPORTED BY RESEARCH

The implemented computational experiment program for evaluating the stress-strain state parameters of an orthotropic shell structure with positive Gaussian curvature, formulated in the normalized tensor space of stresses, the correctness of which was demonstrated by verification with experimental data in publications [13], provides the basis for the following conclusions:
1. The application of the proposed mathematical model guarantees enhanced reliability and engineering accuracy in the analysis of thin-walled spatial systems compared to traditional approaches presented in other researchers' works;
2. Computational experiments clearly demonstrate that the correct accounting of induced deformational anisotropy in numerical algorithms reveals significant limitations of traditional methods for predicting the stress state of curved shell elements. Ignoring this phenomenon can generate substantial deviations in forecasting the mechanical response of spatial structures.

REFERENCES

1. **Amelina E.V., Glushko S.K., Erasov V.S., Idimeshev S.V., Nemirovskiy Yu.V., Semisalov B.V., Yurchenko A.V., Yakovlev N.O.** On nonlinear deformation of carbon plastics: experiment, model, calculation // IVT SB RAS: Computational Technologies. – 2015. – Vol. 20, No. 5. – P. 27–52.
2. **Kayumov R.A., Lukankin S.A., Paimushin V.N., Kholmogorov S.A.** Identification of mechanical characteristics of fiber-reinforced composites // Scientific Notes of Kazan University. Physical and Mathematical Sciences. – 2015. – Vol. 157, Book 4. – P. 112–132.
3. **Shafigullin L.N., Bobrishev A.A., Erofeev V.T., Treshchev A.A., Shafigullina A.N.** Development of the recommendations on selection of glass-fiber reinforced polyurethanes for vehicle parts // International Journal of Applied Engineering Research. – 2015. – Vol. 10, No. 23. – P. 43758–43762.
4. **Bobryshev A.A., Shafigullin L.N., Gumerov I.F., Treshchev A.A., Shafigullina G.R.** Properties of composite materials with powder polymer modifiers // Bulletin of Kazan State Technical University named after A. N. Tupolev. – 2016. – No. 3. – P. 57–64.
5. **Yusupova A.A., Bobryshev A.A., Treschev A.A.** Development of Sulfur and Silicon Dioxide Activation Method in the Sulfur Concrete Technology // Solid State Phenomena. – 2018. – Vol. 284. – P. 1114–1118.
6. **Shafigullin L.N., Romanova N.V., Gabdrakhmanov A.T., Shafigullina G.R., Treshchev A.A.** Using Tire Reclaim for Production of Rubber Wheels of Waste Containers // Lecture Notes in Mechanical Engineering. ICIE 2022: Proceedings of the 8th

International Conference on Industrial Engineering. – 2022. – P. 164–173.
7. **Shafigullina L.N., Romanova N.V., Sokolova Yu.A., Erofeev V.T., Treshchev A.A., Shafigullina G.R., Lakhno A.V.** Development of fire-resistant polyethylene composite for cable polymer wells // University News. Construction. – 2024. – No. 2. – P. 40–51.
8. **Bert C.W., Reddy J.N., Chao W.C.** Bending of Thick Rectangular Plates Laminated of Bimodulus Composite Materials // AIAA Journal. – 1981. – Vol. 19, No. 10. – P. 1342–1349.
9. **Bert C.W., Gordaninejad F.** Deflection of Thick Beams of Multimodular Materials // International Journal for Numerical Methods in Engineering. – 1984. – Vol. 20. – P. 479–503.
10. **Jones R.M.** Modeling Nonlinear Deformation of Carbon-Carbon Composite Materials // AIAA Journal. – 1980. – Vol. 18, No. 8. – P. 995–1001.
11. **Ambartsumyan S.A.** Axisymmetric problem of circular cylindrical shell made of material with different tension and compression resistances // Proceedings of the USSR Academy of Sciences. Mechanics Series. – 1965. – No. 4. – P. 77–85.
12. **Ambartsumyan S.A.** Fundamental equations and relations of the different modulus theory of elasticity for anisotropic bodies // Proceedings of the USSR Academy of Sciences. MTT. – 1969. – No. 3. – P. 51–61.
13. **Jones R.M.** Stress-Strain Relations for Materials with Different Moduli in Tension and Compression // AIAA Journal. – 1977. – Vol. 15, No. 1. – P. 16–25.
14. **Zolochevskiy A.A., Kuznetsov V.N.** Calculation of anisotropic shells from materials with different moduli under non-axisymmetric loading // Dynamics and Strength of Heavy Machinery. – Dnepropetrovsk: DGU, 1989. – P. 84–92.
15. **Nguyen Sh. T., Khristich D. V.** Identification of parameters of quadratic model of elastic anisotropic material // Bulletin of the Chuvash State Pedagogical University named after I. Ya. Yakovlev. Series: Mechanics of Limit States. – 2021. – No. 3 (49). – P. 3–11.
16. **Nguyen Sh.T.** Nonlinear elasticity models of orthotropic material // Bulletin of the Chuvash State Pedagogical University named after I. Ya. Yakovlev. Series: Mechanics of Limit States. – 2021. – No. 4 (50). – P. 25–32.
17. **Treschev A.A.** Potential dependence between deformations and stresses for orthotropic physically nonlinear materials // Fundamental and Applied Problems of Engineering and Technology. – Orel: OGU. – 2017. – No. 4–1 (324). – P. 71–74.
18. **Treschev A.A.** Theory of deformation and strength of materials with initial and induced stress-state sensitivity. Governing relations. – Moscow – Tula: RAASN; TulGU, 2016. – 326 p.
19. **Treschev A.A.** Theory of deformation and strength of materials with different resistance. – Tula: TulGU Publishing House, 2020. – 359 p.
20. **Treschev A.A., Delyagin M.Yu.** Modeling of isotropic material shell with different resistance to tension and compression using volumetric finite elements considering stress and temperature coupling // Materials Physics and Mechanics. – 2013. – No. 17. – P. 59–70.
21. **Treschev A.A., Delyagin M.Yu., Astakhov D.S.** Mathematical model of coupled thermoelasticity of significantly nonlinear materials sensitive to the stress state // Bulletin of the Chuvash State Pedagogical University named after I. Ya. Yakovlev. Mechanics of Limit States. – Cheboksary: Chuvash State Pedagogical University. – 2013. – No. 3 (17). – P. 72–79.
22. **Treschev A.A., Monastyrev Yu.A., Chibrikina V.D., Zavyalova Yu.A., Lapshina M.A.** Description of deformation of orthotropic materials with different resistance // Construction Mechanics and Structures. – Voronezh: VGTU. – 2019. – No. 1 (20). – P. 7–13.

23. **Treschev A.A., Zavyalova Yu.A., Lapshina M.A.** Variant of the deformation model for orthotropic composite materials // Expert: Theory and Practice. – 2020. – No. 3 (6). – P. 62–68.
24. **Treschev A.A., Zavyalova Yu.A., Lapshina M.A., Gvozdev A.E., Kuzovleva O.V., Krupitsyn E.S.** Defining equations of deformation of materials with double anisotropy // Chebyshevskii Sbornik. – 2021– Vol. 22, No. 4. – P. 369–383.
25. **Ambartsumyan S.A.** General Theory of Anisotropic Shells. – Moscow: Nauka, 1974. – 446 p.
26. **Petrov V.V., Krivoshein I.V.** Methods for Calculating Structures Made of Nonlinearly Deformable Material. – Moscow: ASV Publishing, 2009. – 208 p.
27. **Treschev A.A.** Isotropic plates and shells made of materials sensitive to the stress state. – Moscow – Tula: RAASN; TulGU, 2013 – 249 p.
28. **Kovalenko A.D.** Thermoelasticity. – Kiev: Higher School, 1975. – 216 p.
29. **Varvak P.M., Varvak L.P.** Mesh Method in Construction Design Problems. – Moscow: Stroizdat, 1977. − 160 p.
30. **Treschev A.A., Telichko V.G., Doroshenko D.I.** Thermomechanical loading of an orthotropic spherical shell with a hole // Construction Mechanics and Structures. – Tula: TulGU, 2025. – No. 2 (45). – P. 34–49.

СПИСОК ЛИТЕРАТУРЫ

1. **Амелина Е.В., Глушко С.К., Ерасов В.С., Идимешев С.В., Немировский Ю.В., Семисалов Б.В., Юрченко А.В., Яковлев Н.О.** О нелинейном деформировании углепластиков: эксперимент, модель, расчет // ИВТ СО РАН: Вычислительные технологии. – 2015. – Т. 20, № 5. – С. 27–52.
2. **Каюмов Р.А., Луканкин С.А., Паймушин В.Н., Холмогоров С.А.** Идентификация механических характеристик армированных волокнами композитов // Ученые записки Казанского университета. Физико-математические науки. – 2015. – Т. 157, кн. 4. – С. 112–132.
3. **Shafigullin L.N., Bobrishev A.A., Erofeev V.T., Treshchev A.A., Shafigullina A.N.** Development of the recommendations on selection of glass-fiber reinforced polyurethanes for vehicle parts // International Journal of Applied Engineering Research. – 2015. – Vol. 10, № 23. – P. 43758–43762.
4. **Бобрышев А.А., Шафигуллин Л.Н., Гумеров И.Ф., Трещев А.А., Шафигуллина Г.Р.** Свойства композитных материалов с порошковыми полимерными модификаторами // Вестник Казанского государственного технического университета им. А. Н. Туполева. – 2016. – № 3. – С. 57–64.
5. **Yusupova A.A., Bobryshev A.A., Treschev A.A.** Development of Sulfur and Silicon Dioxide Activation Method in the Sulfur Concrete Technology // Solid State Phenomena. – 2018. – Vol. 284. – P. 1114–1118.
6. **Shafigullin L.N., Romanova N.V., Gabdrakhmanov A.T., Shafigullina G.R., Treshchev A.A.** Using Tire Reclaim for Production of Rubber Wheels of Waste Containers // Lecture Notes in Mechanical Engineering. ICIE 2022: Proceedings of the 8th International Conference on Industrial Engineering. – 2022. – P. 164–173.
7. **Шафигуллин Л.Н., Романова Н.В., Соколова Ю.А., Ерофеев В.Т., Трещев А.А., Шафигуллина Г.Р., Лахно А.В.** Разработка огнестойкой полиэтиленовой композиции для кабельных полимерных колодцев // Известия вузов. Строительство. – 2024. – № 2. – С. 40–51.
8. **Bert C.W., Reddy J.N., Chao W.C.** Bending of Thick Rectanqular Plates Laminated of Bimodulus Composite Materials // AIAA

Journal. – 1981. – Vol. 19, № 10. – P. 1342–1349.
9. **Bert C.W.** Gordaninejad F.Deflection of Thick Beams of Multimodular Materials // International Journal for Numerical Methods in Engineering. – 1984. – Vol. 20. – P. 479–503.
10. **Jones R.M.** Modeling Nonlinear Deformation of Carbon-Carbon Composite Materials // AIAA Journal. – 1980. – Vol. 18, №8. – P. 995–1001.
11. **Амбарцумян С.А.** Осесимметричная задача круговой цилиндрической оболочки, изготовленной из материала, разносопротивляющегося растяжению и сжатию // Изв. АН СССР. Сер. Механика. – 1965. – № 4. – С. 77–85.
12. **Амбарцумян С.А.** Основные уравнения и соотношения разномодульной теории упругости анизотропного тела // Изв. АНСССР. МТТ. – 1969. – № 3. – С. 51–61.
13. **Jones R.M.** Stress-Strain Relations for Materials with Different Moduli in Tension and Compression // AIAA Journal. – 1977. – Vol. 15, № 1. – P. 16–25.
14. **Золочевский А.А., Кузнецов В.Н.** Расчет анизотропных оболочек из разномодульных материалов при неосесимметричном нагружении // Динамика и прочность тяжелых машин. – Днепропетровск: ДГУ, 1989. – С. 84–92.
15. **Нгуен Ш.Т., Христич Д.В.** Идентификация параметров квадратичной модели упругого анизотропного материала // Вестник Чувашского государственного педагогического университета им. И. Я. Яковлева. Сер.: Механика предельного состояния. – 2021. – № 3 (49). – С. 3–11.
16. **Нгуен Ш.Т.** Нелинейные модели упругости ортотропного материала // Вестник Чувашского государственного педагогического университета им. И. Я. Яковлева. Сер.: Механика предельного состояния. – 2021. – № 4 (50). – С. 25–32.
17. **Трещев А.А.** Потенциальная зависимость между деформациями и напряжениями для ортотропных физически нелинейных материалов // Фундаментальные и прикладные проблемы техники и технологии. – Орел: ОГУ. – 2017. – № 4–1 (324). – С. 71–74.
18. **Трещев А.А.** Теория деформирования и прочности материалов с изначальной и наведенной чувствительностью к виду напряженного состояния. Определяющие соотношения. – М. – Тула: РААСН; ТулГУ, 2016. – 326 с.
19. **Трещев А.А.** Теория деформирования и прочности разносопротивляющихся материалов. – Тула: Изд-во ТулГУ, 2020. – 359 с.
20. **Трещев А.А., Делягин М.Ю.** Моделирование оболочки из изотропного разносопротивляющегося графита с помощью объемных конечных элементов с учетом связанности напряжений и температур // Materials Physics and Mechanics. – 2013. – № 17. – P. 59–70.
21. **Трещев А.А., Делягин М.Ю., Астахов Д.С.** Математическая модель связанной термоупругости существенно нелинейных материалов, чувствительных к виду напряженного состояния // Вестник Чувашского государственного педагогического университета им. И. Я. Яковлева. Механика предельного состояния. – Чебоксары: Чувашский гос. пед. ун-т. – 2013. – № 3 (17). – С. 72–79.
22. **Трещев А.А., Монастырев Ю.А., Чибрикина В.Д., Завьялова Ю.А., Лапшина М.А.** Описание деформирования ортотропных разносопротивляющихся материалов // Строительная механика и конструкции. – Воронеж: ВГТУ, 2019. – № 1 (20). – С. 7–13.
23. **Трещев А.А., Завьялова Ю.А., Лапшина М.А.** Вариант модели деформирования ортотропных композитных материалов // Эксперт: теория и практика. – 2020. – №3 (6). – С. 62–68.

24. **Treschev A.A., Zavyalova Yu.A., Lapshina M.A., Gvozdev A.E., Kuzovleva O.V., Krupitsyn E.S.** Defining equations of deformation of materials with double anisotropy // Chebyshevskii sbornik. – 2021– Vol. 22, № 4. – P. 369–383.
25. **Амбарцумян С.А.** Общая теория анизотропных оболочек. – М.: Наука, 1974. – 446 с.
26. **Петров В.В., Кривошеин И.В.** Методы расчета конструкций из нелинейно деформируемого материала. – М.: Изд-во АСВ, 2009. – 208 с.
27. **Трещев А.А.** Изотропные пластины и оболочки, выполненные из материалов, чувствительных к виду напряженного состояния. – М. – Тула: РААСН; ТулГУ, 2013 – 249 с.
28. **Коваленко А.Д.** Термоупругость. – Киев: Вища школа, 1975. – 216 с.
29. **Варвак П.М., Варвак Л.П.** Метод сеток в задачах расчёта строительных конструкций. – М.: Стройиздат, 1977. – 160 с.
30. **Трещев А.А., Теличко В.Г., Дорошенко Д.И.** Термомеханическое нагружение ортотропной сферической оболочки с отверстием // Строительная механика и конструкции. – Тула: ТулГУ, 2025. – № 2 (45). – С. 34–49.

Alexander An. Treschev – Corresponding Member of the Russian Academy of Architecture and Construction Sciences (RAACS), Doctor of Technical Sciences, Professor, Head of the Department of "Construction, Building Materials and Structures", Tula State University (TulSU), Tula, 300600, Russia, taa58@yandex.ru, +7(905)622-90-58.

Victor Gr. Telichko – Doctor of Technical Sciences, Associate Professor, Professor of the Department of Construction, Building Materials, and Structures, Tula State University (TulSU), Tula, 300600, Russia, katranv@yandex.ru, +7(952) 019-84-65.

Denis Ig. Doroshenko – Postgraduate Student of the Department of "Construction, Building Materials and Structures", Tula State University (TulSU), Tula, 300600, Russia, doroshenki2@gmail.com, +7(915)411-10-79.

Трещев Александр Анатольевич – Чл.-кор. РААСН, д-р техн. наук, проф., зав. кафедрой «Строительство, строительные материалы и конструкции», Тульский государственный университет (ТулГУ), г. Тула, 300600, Россия, taa58@yandex.ru, +7(905)622-90-58.

Теличко Виктор Григорьевич – Доктор технических наук, доцент, профессор кафедры «Строительство, строительные материалы и конструкции», Тульский государственный университет (ТулГУ), г. Тула, 300600, Россия, katranv@yandex.ru, +7(952) 019-84-65.

Дорошенко Денис Игоревич – Аспирант кафедры «Строительство, строительные материалы и конструкции», Тульский государственный университет (ТулГУ), г. Тула, 300600, Россия, doroshenki2@gmail.com, +7(915)411-10-79.

International Journal for Computational Civil and Structural Engineering, 22(2) 176–188 (2026)

DOI:10.22337/2587-9618-2026-22-2-176-188

COMPUTATIONAL METHOD OF BINARY SEMANTIC SEGMENTATION OF BUILDING STRUCTURE DEFECTS BASED ON CONVOLUTIONAL NEURAL NETWORKS

Maxim O. Bakanov, Vladimir N. Sidorov, Elena A. Makarova, Nikita S. Bondarenko

National Research Moscow State University of Civil Engineering, Moscow, RUSSIA

Abstract. The problem of automated diagnostics of defects in building structures is due to the high labor intensity and subjectivity of visual inspections. The paper presents a prototype computer vision system based on an architecture featuring a lightweight feature extraction encoder, designed for the binary semantic segmentation of cracks in building surface images. The new proposal is to adapt the specified architecture to the problem of detecting thin extended objects on a non-uniform background using a combined loss function that combines binary cross-entropy and the Dice coefficient. The paper provides the mathematical formulation of the problem, a formal description of the modified optimization criterion, a data preprocessing methodology that accounts for JPEG compression artifacts, and the results of computational experiments. Evaluated on an independent test set, the resulting metrics—specifically the Dice coefficient and Jaccard index (IoU)—validate the effectiveness of the proposed approach and outline directions for further technological improvements.

Keywords: computer vision, deep learning, semantic segmentation, defects of building structures, cracks, U Net, MobileNetV2, Dice loss function

ВЫЧИСЛИТЕЛЬНЫЙ МЕТОД БИНАРНОЙ СЕМАНТИЧЕСКОЙ СЕГМЕНТАЦИИ ДЕФЕКТОВ СТРОИТЕЛЬНЫХ КОНСТРУКЦИЙ НА ОСНОВЕ СВЕРТОЧНЫХ НЕЙРОННЫХ СЕТЕЙ

М.О. Баканов, В.Н. Сидоров, Е.А. Макарова, Н.С. Бондаренко

Национальный исследовательский Московский государственный строительный университет, г. Москва, РОССИЯ

Аннотация. Проблема автоматизированной диагностики дефектов строительных конструкций обусловлена высокой трудоемкостью и субъективностью визуальных обследований. В статье предложен прототип системы компьютерного зрения на основе архитектуры с облегченным блоком извлечения визуальных признаков (энкодером), предназначенный для бинарной семантической сегментации трещин на изображениях строительных поверхностей. Новое предложение заключается в адаптации указанной архитектуры к задаче выделения тонких протяженных объектов на неоднородном фоне с применением комбинированной функции потерь, объединяющей бинарную кросс-энтропию и коэффициент Дайса. Приведены математическая постановка задачи, формальное описание модифицированного критерия оптимизации, методика подготовки данных с учетом артефактов JPEG-сжатия, а также результаты вычислительных экспериментов. Полученные в работе на независимой тестовой выборке метрики значения коэффициента Дайса и индекса Жаккара (IoU) подтверждают работоспособность предложенного подхода и определяют направления дальнейшего совершенствования технологии.

Ключевые слова: компьютерное зрение, глубокое обучение, семантическая сегментация, дефекты строительных конструкций, трещины, архитектура U Net, энкодер MobileNetV2, функция потерь Дайса

1. INTRODUCTION

The methodological basis for technical examination of the condition of building structures is traditionally their visual inspection followed by an expert assessment of the degree of their damage [1-10]. This approach is characterized by high labor intensity, dependence on the specialist's qualifications, and the difficulty of achieving a sufficient level of reproducibility of results. At the same time, the development of remote sensing methods, including aerial photography from unmanned aerial vehicles, makes it possible to obtain high-resolution digital images suitable for automated analysis using deep learning algorithms. The key task of automation is the so-called semantic segmentation of cracks – identifying pixels in the image that contain defects and separating them from the background.

Initial approaches to automated crack detection relied on classical computer vision methods – thresholding, morphological operations, and gradient filtering. These methods were computationally efficient, but demonstrated low resistance to non-uniform backgrounds, shadows, and textures of materials, primarily concrete, due to their reliance on local brightness features without taking into account contextual information. The subsequent development of machine learning methods with manual feature construction partially compensated for these limitations, but transferred the problem to the vast area of subjectivity of feature selection by the developer. In parallel with the evolution of image processing algorithms, attempts were made to solve problems of construction flaw detection using expert systems designed to accumulate and formalize the knowledge of expert engineers for comprehensive damage diagnostics [13-28]. However, such symbolic approaches faced the classic "intellectual bottleneck" problem of knowledge extraction and required labor-intensive manual creation of rigid productive rule bases. They typically lacked built-in mechanisms for directly extracting features from raw image data, which significantly limited their scalability and practical use. The use of convolutional neural networks, in particular their U-Net architecture [29], provides the ability to simultaneously extract hierarchical features and preserve spatial localization in end-to-end learning mode. However, the direct use of "heavy" models without taking into account the specifics of building surfaces – small crack widths (down to fractions of a pixel), noisy masks, high image resolution – led to a compromise between accuracy and computational efficiency: high-performance models prove unsuitable for mobile platforms, while lightweight architectures do not achieve sufficient localization accuracy for the aforementioned defects. Resolving this contradiction is the central objective of this study.

The objective of this work is to develop and experimentally verify a prototype of binary semantic segmentation of cracks based on the U Net architecture with the MobileNetV2 encoder, trained using a combined loss function that simultaneously optimizes pixel-by-pixel classification and spatial overlap measure. The article presents a formal statement of the problem, a description of the architecture, a data preparation methodology, and the results of computational experiments confirming the viability of the proposed approach. In order to accurately place this work within the overall structure of the field of research, it is necessary to critically examine the key results achieved by the global community in recent years.

2. PROBLEM AREA ANALYSIS

The evolution of methods for automatic analysis of defects in building structures is characterized by a consistent increase in the complexity of problem statements. The initial stage focused on the task of binary image classification, namely, based on the presence/absence of a crack. This approach, abstracting from the spatial characteristics of the defect, made it possible to achieve high accuracy rates. For example, a team

led by S. Siva Rama Krishnan, using the Inception V3 architecture, achieved an accuracy (Accuracy ≈) of 99.98% on a dataset of 40,000 images [30]. However, the classification approach does not provide spatial localization of the defect, which limits its applicability for quantitative damage assessment.

The next stage of development is associated with the transition to semantic segmentation. In 2020, S. Bhowmick et al. demonstrated the effectiveness of the U-Net architecture for crack detection in UAV videos followed by morphological post-processing to quantify geometric parameters [31]. In 2021, P. Kumar et al. implemented a real-time system based on YOLO-v3, achieving a detection accuracy of 94.24% with a frame processing time of 0.033 s [32]. In 2022, V. Gharehbaghi et al. proposed a 12-layer deep network, FastCrackNet, optimized for crack identification in noise and shadows [33].

The analysis of the above key works indicates the following limitations:

1. The contradiction between the accuracy of segmentation, assessed by the coefficient of geometric overlap of predicted and actual crack contours (mIoU > 0.7), and the high computational complexity of such models.
2. Reduced segmentation quality due to training on limited datasets with JPEG compression artifacts and subjective labeling.
3. The limitations of the binary formulation of the problem, which does not allow classifying defects by type and degree of danger.

The current stage of research is characterized by the development of integrated approaches aimed at overcoming these limitations. On the one hand, multi-class and multi-modal systems are being developed – B. Gürer and M. E. Karslıgil (2024) obtained mIoU = 0.77 for damage segmentation using the OneFormer model and mIoU = 0.52 for damage level classification using the SegFormer model on data from the earthquake in Turkey [34]. On the other hand, lightweight architectures and combined loss functions are introduced to simultaneously optimize pixel-by-pixel accuracy and spatial connectivity. A significant factor in the development of the field is the emergence of open multimodal datasets such as BRIGHT [35], which provide an objective basis for training and comparing algorithms. Additionally, work on damage assessment based on post-event SAR data [36], the use of visual language models for damage classification [37], and the rapid deployment of UAV-based AI systems in real-world conditions [38] are noted. As a result, the field is moving away from isolated classification and segmentation solutions towards end-to-end systems that integrate multimodality, post-processing, and deployment on onboard computing platforms. This work develops this direction. The prototype proposed in this paper retains the U-Net architecture with skip connections to preserve spatial details, but uses the lightweight MobileNetV2 encoder and a combined loss function (BCE + Dice). This choice is due to the need to ensure a compromise between the accuracy of fine crack detection and computational efficiency sufficient for integration into mobile platforms.

3. MATHEMATICAL STATEMENT OF THE PROBLEM

The problem is formulated as follows. Let a set of "image – true binary mask" pairs $\{X_i, Y_i\}_{i=1}^{N}$ be given, where $X_i \in \mathbb{R}^{H\times W\times 3}$ is a color image of the surface of a building structure, and $Y_i \in \mathbb{R}^{H\times W}$ is the corresponding mask (a pixel is equal to 1 if it belongs to a crack, and 0 otherwise). It is required to construct a parameterized mapping $f(\cdot;\theta)\colon \mathbb{R}^{H\times W\times 3} \to [0,1]^{H\times W}$ that associates with each pixel the probability of its belonging to the "crack" class. Thus, the binarized forecast $\hat{Y}_i$ is obtained by applying the threshold τ=0.5:

$$\hat{Y}_i(j) = \begin{cases} 1, & p_{i,j} \geq \tau, \\ 0, & p_{i,j} < \tau, \end{cases} \quad (1)$$

where each pixel $p_{i,j} = P_i(j)$ is interpreted as the probability of belonging to the "crack" class.

The optimal parameters θ^* are calculated by minimizing the empirical risk:

$$\theta^* = \arg\min_{\theta} \frac{1}{N}\sum_{i=1}^{N} \mathcal{L}(f(X_i;\theta), Y_i). \quad (2)$$

The choice of the loss function $\mathcal{L}$ is a critical aspect of the formulation. When using exclusively binary cross-entropy, where $M = H \times W$ is the total number of pixels in the image:

$$\mathcal{L}_{BCE} = -\frac{1}{M}\sum_{j=1}^{M}\left[y_j \log p_j + (1-y_j)\log(1-p_j)\right], \quad (3)$$

the model optimizes pixel-by-pixel classification, but does not take into account the spatial connectivity of objects. For thin cracks occupying a small fraction of the frame area, this leads to fragmentation of the forecast. When using a loss function based on the Dice coefficient:

$$\mathcal{L}_{Dice} = 1 - \frac{2\sum_j p_j y_j + \varepsilon}{\sum_j p_j + \sum_j y_j + \varepsilon}, \varepsilon = 10^{-7}, \quad (4)$$

the model focuses on the measure of spatial overlap. This can result to blurring of boundaries and reduced pixel accuracy.

To balance between local accuracy and global shape, a combined loss function is used in this work:

$$\mathcal{L}(P,Y) = \mathcal{L}_{BCE}(P,Y) + \mathcal{L}_{Dice}(P,Y), \quad (5)$$

This formulation provides simultaneous optimization of pixel-wise classification and spatial integrity of segmented objects.

The quality of the trained model is assessed on an independent test sample using the Dice coefficient and the Jaccard index (IoU):

$$Dice = \frac{2\sum_j \hat{y}_j y_j}{\sum_j \hat{y}_j + \sum_j y_j}, \quad (6)$$

$$IoU = \frac{\sum_j \hat{y}_j y_j}{\sum_j \hat{y}_j + \sum_j y_j - \sum_j \hat{y}_j y_j}. \quad (7)$$

4. NEURAL NETWORK ARCHITECTURE

The U-Net architecture [29] includes an analytical branch (encoder), which sequentially compresses the image to highlight the characteristic features of the defect - its contrast, shape and texture, and a restoration branch (decoder). The latter one, based on these features, forms the final segmentation map with the original spatial resolution. Diagnostic bridges (skip connections) between symmetrical levels of the analytical and restorative branches ensure direct transfer of geometric details. This is critical for accurately detecting fine structures such as cracks a few pixels wide.

The classic implementation of U-Net with a full-size encoder is characterized by high computational complexity, which limits its applicability on mobile platforms. In this paper, MobileNetV2 [39], pre-trained on the ImageNet dataset, is used as the encoder. Using a pre-trained model ensures efficient initialization of low-level filters and accelerates convergence when training a neural network on a limited, specialized dataset.

The MobileNetV2 core block with expansion factor t and kernel of size $k \times k$ transforms the input tensor $x \in \mathbb{R}^{C_{in} \times H \times W}$ into the output $y \in \mathbb{R}^{C_{out} \times H' \times W'}$ via operator composition:

$$y = \text{LinearBottleneck}(x) = \text{BN}\left(\text{Conv}_{1\times1}^{C_{in}\to tC_{in}}(x)\right) \circ \text{ReLU6} \circ \text{BN}\left(\text{DWConv}_{k\times k}^{tC_{in}}(x)\right) \circ \text{ReLU6} \circ \circ \text{BN}\left(\text{Conv}_{1\times1}^{C_{in}\to tC_{in}}(x)\right) + \text{skip}(x), \quad (8)$$

where Conv is a regular convolution, DWConv is a depthwise convolution, BN is a batch normalization, ReLU6 is an activation function, skip(x) is a residual connection (if the dimensions are consistent). Pretraining on ImageNet provides good initialization of low-level filters, which speeds up convergence when training on a small dataset. The decoding part of the architecture sequentially increases the spatial resolution of feature maps using bilinear interpolation or transposed convolutions and combines them with the corresponding encoder maps via skip connections. The final layer is a 1×1 convolution with sigmoid activation, forming a single-channel probability mask of the size of the original image (Fig. 1).

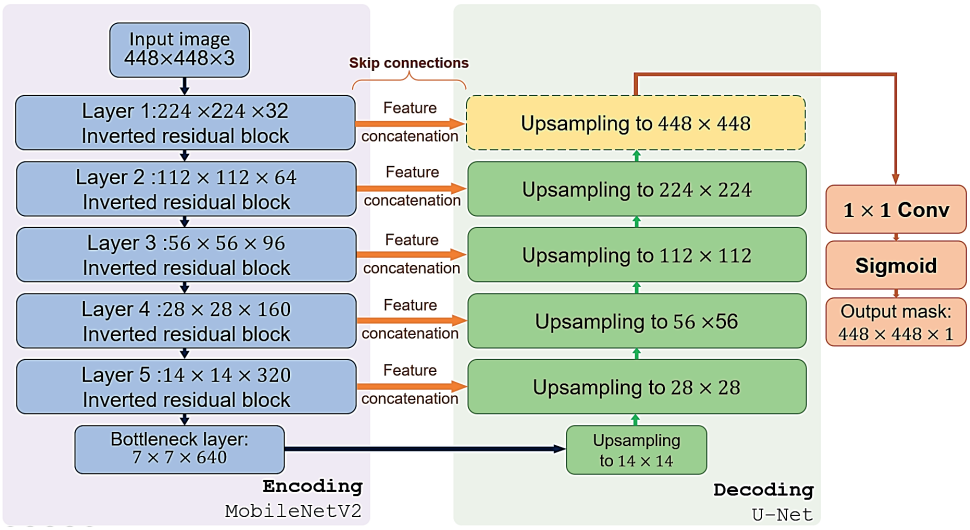

Figure 1. Architecture of the U Net neural network with the MobileNetV2 encoder for binary crack segmentation: schematic representation of the encoding and decoding branches, skip connections, and the final sigmoid activation layer

The choice of MobileNetV2 as an encoder was driven by the requirements for computational efficiency for subsequent integration into mobile platforms and on-board systems of unmanned aerial vehicles.

5. DATA PREPARATION AND AUGMENTATION

The experiments were conducted on a specialized dataset [40] containing pairs of images of concrete surfaces and corresponding binary crack masks. The original masks were saved in JPEG format, which introduced compression artifacts near the crack boundaries. To minimize the influence of artifacts, preliminary binarization of masks was performed with a threshold of 127: pixels with a value >127 were classified as belonging to a crack, the rest were classified as background. This operation reduced the noise level, but did not completely eliminate the blurring of edges caused by losses during JPEG compression. To increase the diversity of the training sample and improve the generalization ability of the model, augmentations were used: random horizontal and vertical reflections, rotations at angles multiples of 90°.

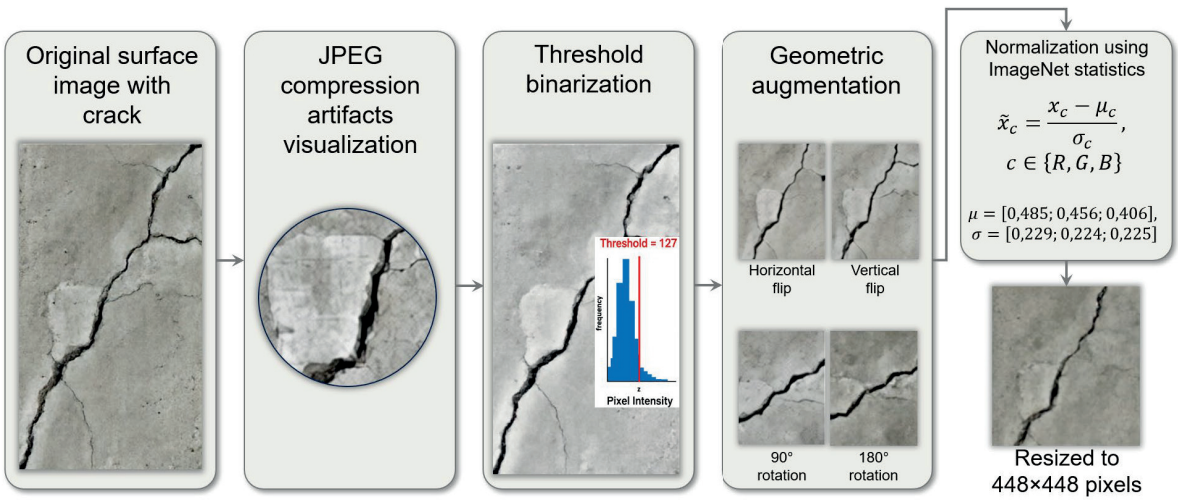

Figure 2. Schematic of the dataset preprocessing pipeline for crack detection

Geometric transformations were performed synchronously for images and masks using bilinear interpolation for images and the nearest neighbor method for masks. The input tensors were normalized based on RGB channel statistics computed from the ImageNet dataset (Fig. 2):

$$\tilde{x}_c = \frac{x_c - \mu_c}{\sigma_c}, c \in \{R, G, B\}, \quad (9)$$

where

$\mu = [0.485; 0{,}456; 0{,}406]$, $\sigma = [0.229; 0{,}224; 0{,}225]$.

All images and masks are resized to a fixed size of 448×448 pixels using bilinear interpolation (images) and nearest neighbor (masks). The final input tensor had dimensions 3×448×448, the output mask – 1×448×448.

6. TRAINING THE MODEL

Training was performed using the stochastic gradient descent method with the AdamW optimizer, combining adaptive learning rate adjustment with L2 regularization (weight decay). The learning rate is set to $1 \cdot 10^{-4}$, the mini-batch size is 4 images. The maximum number of training epochs is 30, with the best model based on the Dice coefficient value on the validation set being preserved.

The learning rate is set to $1 \cdot 10^{-4}$ level, the mini-batch size is 4 images. The maximum number of training epochs is 30, with the best model based on the Dice coefficient value on the validation set being preserved.

The original dataset is randomly divided into training (80%) and validation (20%) subsamples. An independent test set, not involved in the training process, was used for the final metrics evaluation.

The dynamics of training demonstrates a monotonic decrease in the loss function and an increase in metrics during the first 10–15 epochs, after which a plateau is reached in the region of the Dice coefficient value: Dice ≈ 0,70. The absence of a significant discrepancy between training and validation metrics indicates the adequacy of the chosen architecture and the absence of overfitting. The best model was recorded at the 24th epoch.

7. EXPERIMENTAL RESULTS AND DISCUSSION

The quantitative learning outcomes are presented in Table 1.

Table 1. Quality metrics for binary crack segmentation

Metrics	Validation set (at the best training epoch)	Test samples
Losses (BCE + Dice)	0,4984	0,4907
Dice coefficient (Dice)	0,7090	0,7118
Jaccard index (IoU)	0,584	0,5875

The comparability of validation and test values confirms the high generalization ability of the model. Visual analysis of the predicted masks on test images showed stable detection of main crack areas while correctly ignoring background textures, including concrete roughness, shadows, and local color changes.

However, the following limitations of the method were observed:

1. Blurring of boundaries in areas with a crack width of 1–2 pixels, caused by both the architectural limitations of the MobileNetV2 encoder (effective receptive size) and the original quality of the masks (JPEG compression artifacts) (Fig. 3). Fragmentation of extended cracks in cases of local decrease in contrast or intersection with shaded areas.
2. The achieved values: Dice > 0.7 confirm the viability of the proposed prototype as a basis for

further research. Increasing the accuracy to the level of mIoU ≥ 0.85, necessary for an acceptable quality level of practical engineering diagnostics, involves solving the following problems:
– creation of a new data set with masks saved in PNG format without lossy compression, and with the involvement of expert markup from professional builders;
– transition to multi-class segmentation with classification of defects by type (cracks, chips, corrosion, etc.);
– use of more complex architectures (DeepLabV3+, HRNet, models with attention mechanisms) and specialized loss functions (Focal Loss, Tversky Loss);
– implementation of morphological post-processing, including skeletonization, closure, and false-positive filtering.

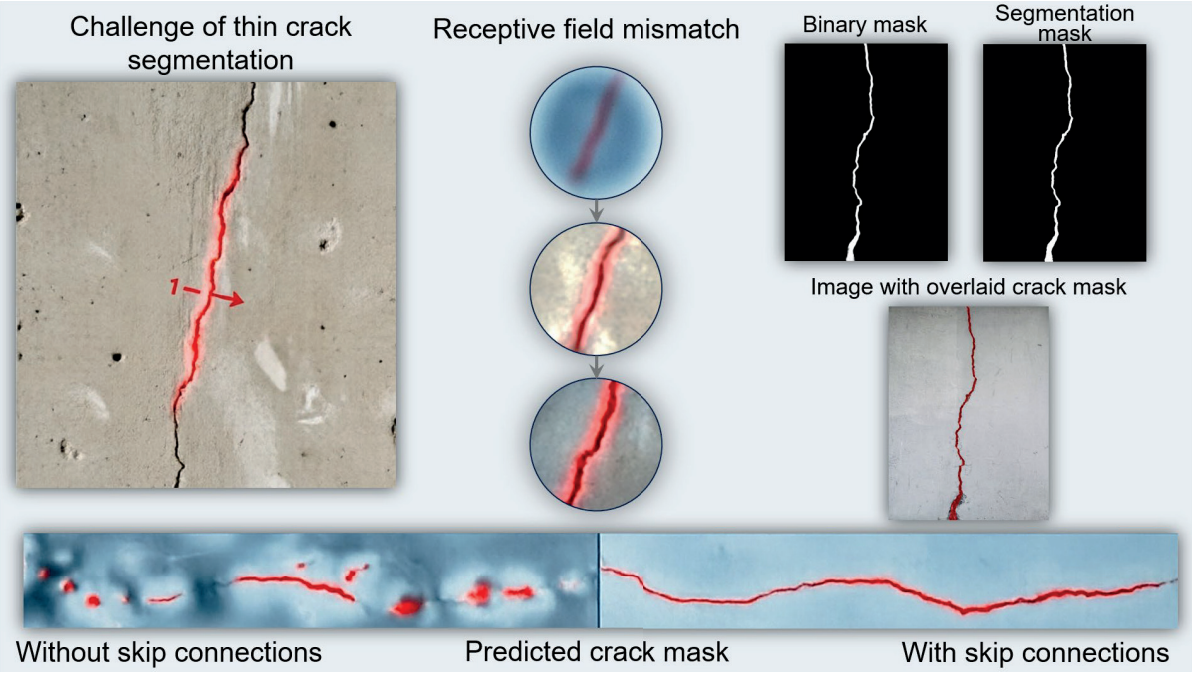

Figure 3. Visualization of the ultra-thin cracks segmentation problem: the influence of the encoder receptive field and the role of skip connections in maintaining spatial continuity of 1–2 pixel wide defects

8. CONCLUSION

The developed prototype of binary semantic segmentation of cracks on concrete surfaces based on U-Net with MobileNetV2 encoder, trained using a combined loss function (BCE + Dice), demonstrated robust ability to highlight defects in real images of building structures. An approach is proposed for adapting a lightweight architecture to the task of segmenting thin extended objects on noisy data, as well as for experimentally substantiating the influence of compression artifacts of the original masks on the quality of the model. The obtained metrics (Test Dice = 0.7118, IoU = 0.5875) meet the requirements of the proof-of-concept stage and define the basic parameters for the development of a full-scale automated diagnostic system. Promising research areas include the formation of a representative dataset with high-quality masks, the implementation of a multi-class defect detector, and the integration of a prototype into a software package for processing aerial photography data. The practical result of this stage of research is the automatic generation of defect lists and damage cartograms in accordance with the requirements of GOST 31937–2024.

REFERENCES

1. GOST 31937-2024. Buildings and Structures. Rules for Surveying and Monitoring Technical Condition: Interstate Standard. Moscow: Standartinform, 2024. (in Russian)
2. GOST 31937-2011. Buildings and Structures. Rules for Surveying and Monitoring Technical Condition: Interstate Standard. Moscow: Standartinform, 2011. (in Russian)
3. SP 13-102-2003. Rules for Surveying Load-Bearing Building Structures of Buildings and Structures. Moscow: Gosstroy of Russia, 2004. (in Russian)
4. GOST R 53778-2010. Buildings and Structures. Rules for Surveying and Monitoring Technical Condition: National Standard of the Russian Federation. Moscow: Standartinform, 2010. (in Russian)
5. **Pichueva A.S.** Methods for Surveying Buildings and Structures // Paradigm. – 2025. – No. 5-2. – pp. 355–360. – EDN BMNNNI. (in Russian)
6. **Grushkovsky P.A., Shchelnikov V.N., Sitnikov A.V.** Assessment of the Technical Condition of Building Structures and Facilities by Visual and Instrumental Methods // Bulletin of Tula State University. Technical Sciences. – 2021. – No. 6. – pp. 208–212. – DOI 10.24412/2071-6168-2021-6-208-212. – EDN KKJSSV. (in Russian)
7. **Petrova I.Yu., Mostovoy O.O.** Review of the Building and Structure Inspection Process. Problems and Solutions // Caspian Engineering and Construction Bulletin. – 2021. – No. 1 (35). – pp. 69–75. – EDN KGUCUU. (in Russian)
8. **Bogomolov S.I.** Analysis of methods for assessing the current technical condition of buildings and structures // Bulletin of Tula State University. Technical sciences. - 2021. - No. 10. - pp. 287-290. - DOI 10.24412/2071-6168-2021-10-287-290. - EDN WFCCXA. (in Russian)
9. **Snegireva A.I., Murashkin V.G.** On the issue of surveying building structures, buildings and structures // Expert: theory and practice. - 2021. - No. 6 (15). - pp. 45-51. - DOI 10.51608/26867818_2021_6_45. - EDN JKHDHA. (in Russian)
10. **Semenov A.S.** Organization of technical survey of housing stock buildings // Housing construction. – 2010. – No. 12. – pp. 23–25. – EDN NQUBOF. (in Russian)
11. **Kunin, Yu.S.** Diagnostics of a unique structure – a 100-meter-high radio tower / Yu.S. Kunin, T.V. Potapova, S.G. Muzychenko // Construction production. – 2023. – No. 2. – pp. 54–61. – DOI 10.54950/26585340_2023_2_54. – EDN QODNCJ. (in Russian)
12. **Kunin, Yu.S.** Vibroacoustic methods of quality control of building structures of buildings and structures / Yu. S. Kunin, A. S. Perunov // Industrial and civil engineering. – 2023. – No. 3. – pp. 55–61. – DOI 10.33622/0869-7019.2023.03.55-61. – EDN XRKUCN (in Russian)
13. **Kashevarova G.G., Tonkov Yu.L.** Expert system for practical diagnostics of building structures // Academia. Architecture and Construction. – 2022. – No. 2. – pp. 58-91. – DOI 10.22337/2077-9038-2022-1-85-91. (in Russian)
14. **Kashevarova G.G., Tonkov Yu.L.** Intelligent technologies in the inspection of building structures // Academia. Architecture and Construction. – 2018. – No. 1. – pp. 92-99. – DOI: 10.22337/2077-9038-2018-1-92-99. (in Russian)
15. **Kashevarova G.G.** "Artificial intelligence", or "logical reasoning and reasonable decisions" in technical diagnostics of construction projects // Academia. Architecture and Construction. – 2023. – No. 4. – pp. 166-180. – DOI: 10.22337/2077-9038-2023-4-166-180. (in Russian)
16. **Kuksov, A.S.** Prerequisites for the Development of Expert Systems in the Field of Inspection and Diagnostics of Building Structures / A.S. Kuksov, P.I. Andreeva,

R.R. Kazaryan // BST: Bulletin of Construction Equipment. – 2020. – No. 5(1029). – pp. 47-49. – EDN VMHOYL (in Russian)
17. **Shesterikov, Yu.A.** Information Systems and Technologies for Inspection of Buildings and Structures / Yu.A. Shesterikov, O.A. Stifeeva // Russian journal of transport engineering. – 2020. – Vol. 7, No. 1. – P. 4. – 10.15862/05SATS120. (in Russian)
18. **Nikolyukin, A.N.** Self-learning intelligent systems in construction / A. N. Nikolyukin, P.V. Monastyrev. – Tambov: Tambov State Technical University, 2025. – 167 p. – ISBN 978-5-8265-2908-9. – EDN FTSUTJ (in Russian)
19. **Krylov S.A., Kashevarova G.G.** Automation of the process of assessing the technical condition of external walls of brick buildings using machine learning technology // Bulletin of DSTU. Technical sciences. – 2025. – No. 3. – pp. 61-70. – DOI: 10.21822/2073-6185-2025-52-3-61-70. (in Russian)
20. **Soldatenko T.N.** Model for identification and prediction of defects in a building structure based on the results of its inspection // Magazine of Civil Engineering. – 2011. – No. 7. – pp. 52-61. (in Russian)
21. **Samigullina A.G.** The need to develop a model of an expert system for diagnosing the technical condition of building structures // Young scientist. – 2017. – No. 51 (185). – pp. 88–90. – EDN ZXXDMN. (in Russian)
22. **Bugakova T.Yu., Sharapov A.A.** Improving the methods of visual inspection of buildings and engineering structures by introducing computer vision and intelligent data processing technologies // Bulletin of SSUGiT (Siberian State University of Geosystems and Technologies). – 2022. – No. 6. – pp.108–119. – DOI 10.33764/2411-1759-2022-27-6-108-119. – EDN MFBIIV. (in Russian)
23. **Hamed G.M.** An expert system for concrete diagnosis: диссертация / G.M. Hamed; King Fahd University of Petroleum and Minerals. – Dhahran, 1983.
24. **Bernat E., Gil L.** Aided diagnosis of structural pathologies with an expert system // Advances in Structural Engineering. – 2013. – Vol. 16, № 2. – pp. 379–393. – DOI 10.1260/1369-4332.16.2.379.
25. **Moselhi O., Hegazy T., Fazio P.** Neural networks as tools in construction // Journal of Construction Engineering and Management. – 1991. – Vol. 117, № 4. – pp. 606–625. – DOI 10.1061/(ASCE)0733-9364(1991)117:4(606).
26. **Nuhu B.K. [et al.]** Distributed network-based structural health monitoring expert system // Building Research & Information. – 2021. – Vol. 49, № 1. – pp. 144–159. – DOI 10.1080/09613218.2020.1854083. – EDN BKCFCV.
27. **Arora S.** Deep learning-based structural crack detection framework for structural health monitoring of reinforced concrete buildings // Asian Journal of Civil Engineering. – 2026. – pp. 1–11. – DOI 10.1007/s42107-026-01713-8.
28. **de Brito J. [et al.]** Expert knowledge-based inspection systems // Inspection, Diagnosis and Repair of the Building Envelope. – Cham: Springer, 2020. – DOI 10.1007/978-3-030-42446-6.
29. **Ronneberger O., Fischer P., Brox T.U.** Net**:** Convolutional Networks for Biomedical Image Segmentation // Medical Image Computing and Computer Assisted Intervention – MICCAI 2015. – Springer, 2015. – pp. 234–241.
30. **Siva Rama Krishnan S., Nalla Karuppan M.K., Khadidos A.O. et al.** Inception V3 for automated binary classification of construction surface cracks // Scientific Reports. – 2025. – DOI: 10.1038/s41598-025-85983-3.
31. **Bhowmick S., Nagarajaiah S., Veeraraghavan A.** Automated crack detection and quantification from UAV videos using U-Net // Sensors. – 2020. – Vol.

20(21). – Art. 6299. – DOI: 10.3390/s20216299.
32. **Kumar P., Batchu S., Swamy N.S., Kota S.R.** Real-time structural health monitoring using multi-copter network and edge computing // IEEE Access. – 2021. – Vol. 9. – pp. 1234–1245. – DOI: 10.1109/ACCESS.2021.3102647.
33. **Gharehbaghi V., Noroozinejad Farsangi E., Yang T.Y. et al.** FastCrackNet: Identification of concrete cracks under noise and shadows using a 12-layer deep network // Sensors. – 2022. – Vol. 22(22). – Art. 8986. – DOI: 10.3390/s22228986.
34. **Gürer B., Karslıgil M.E.** Earthquake damage assessment using deep learning-based segmentation on drone imagery // Proc. SIU 2024. – IEEE, 2024. – DOI: 10.1109/SIU61531.2024.10601138.
35. **Chen H., Song J., Dietrich O. et al.** BRIGHT: A globally distributed multimodal dataset for automated building damage assessment after disasters // Earth System Science Data. – 2025. – DOI: 10.5194/essd-2025-269.
36. **Russo L., Tapete D., Ullo S.L., Gamba P.** Post-event SAR-only building damage assessment framework integrating geospatial data // arXiv preprint. – 2025. – arXiv:2506.22338.
37. **Hoier C., Ahmed K.M.** UAV video super-resolution and VLM-based building damage classification // arXiv preprint. – 2025. – arXiv:2508.17130.
38. **Manzini T., Perali P., Murphy R.R.** Operational deployment of sUAS-based AI for building damage assessment during hurricanes Debby and Helene // arXiv preprint. – 2025. – arXiv:2511.03132.
39. **Sandler M., Howard A., Zhu M., Zhmoginov A., Chen L.C.** MobileNetV2: Inverted Residuals and Linear Bottlenecks // Proceedings of the IEEE Conference on Computer Vision and Pattern Recognition (CVPR). – 2018. – pp. 4510–4520.
40. **Khanh Ha.** Crack Segmentation: [program code] / Khanh Ha. – Text: electronic // GitHub: [site]. – URL: https://github.com/khanhha/crack_segmentation

СПИСОК ЛИТЕРАТУРЫ

1. ГОСТ 31937-2024. Здания и сооружения. Правила обследования и мониторинга технического состояния: межгосударственный стандарт. – Москва: Стандартинформ, 2024.
2. ГОСТ 31937-2011. Здания и сооружения. Правила обследования и мониторинга технического состояния: межгосударственный стандарт. – Москва: Стандартинформ, 2011.
3. СП 13-102-2003. Правила обследования несущих строительных конструкций зданий и сооружений. – Москва: Госстрой России, 2004.
4. ГОСТ Р 53778-2010. Здания и сооружения. Правила обследования и мониторинга технического состояния: национальный стандарт Российской Федерации. – Москва: Стандартинформ, 2010.
5. **Пичуева А.С.** Методы обследования зданий и сооружений // Парадигма. – 2025. – № 5-2. – С. 355–360. – EDN BMNNNI.
6. **Грушковский П.А., Щельников В.Н., Ситников А.В.** Оценка технического состояния строительных конструкций зданий и сооружений визуальными и инструментальными методами // Известия Тульского государственного университета. Технические науки. – 2021. – № 6. – С. 208–212. – DOI 10.24412/2071-6168-2021-6-208-212. – EDN KKJSSV.
7. **Петрова И.Ю., Мостовой О.О.** Обзор процесса проведения обследования зданий и сооружений. Проблемы и пути решения // Инженерно-строительный вестник Прикаспия. – 2021. – № 1 (35). – С. 69–75. – EDN KGUCUU.
8. **Богомолов С.И.** Анализ методов оценивания текущего технического

состояния зданий и сооружений // Известия Тульского государственного университета. Технические науки. – 2021. – № 10. – С. 287–290. – DOI 10.24412/2071-6168-2021-10-287-290. – EDN WFCCXA.

9. **Снегирёва А.И., Мурашкин В.Г.** К вопросу обследования строительных конструкций, зданий и сооружений // Эксперт: теория и практика. – 2021. – № 6 (15). – С. 45–51. – DOI 10.51608/26867818_2021_6_45. – EDN JKHDHA.
10. **Семенов А.С.** Организация технического обследования зданий жилищного фонда // Жилищное строительство. – 2010. – № 12. – С. 23–25. – EDN NQUBOF.
11. **Кунин, Ю.С.** Диагностика уникального сооружения - радиобашни высотой 100 метров / Ю. С. Кунин, Т. В. Потапова, С. Г. Музыченко // Строительное производство. – 2023. – № 2. – С. 54-61. – DOI 10.54950/26585340_2023_2_54. – EDN QODNCJ.
12. **Кунин, Ю.С.** Виброакустические методы контроля качества строительных конструкций зданий и сооружений / Ю. С. Кунин, А. С. Перунов // Промышленное и гражданское строительство. – 2023. – № 3. – С. 55-61. – DOI 10.33622/0869-7019.2023.03.55-61. – EDN XRKUCN
13. **Кашеварова Г.Г., Тонков Ю.Л.** Экспертная система для практической диагностики строительных конструкций // Academia. Архитектура и строительство. – 2022. – № 2. – С. 58-91. – DOI 10.22337/2077-9038-2022-1-85-91.
14. **Кашеварова Г.Г., Тонков Ю.Л.** Интеллектуальные технологии в обследовании строительных конструкций // Academia. Архитектура и строительство. – 2018. – № 1. – С. 92-99. – DOI: 10.22337/2077-9038-2018-1-92-99.
15. **Кашеварова Г.Г.** «Искусственный интеллект», или «логические рассуждения и разумные решения» в технической диагностике объектов строительства // Academia. Архитектура и строительство. – 2023. – № 4. – С. 166-180. – DOI: 10.22337/2077-9038-2023-4-166-180.
16. **Куксов, А.С.** Предпосылки развития экспертных систем в области обследования и диагностирования строительных конструкций / А.С. Куксов, П.И. Андреева, Р.Р. Казарян // БСТ: Бюллетень строительной техники. – 2020. – № 5(1029). – С. 47-49. – EDN VMHOYL
17. **Шестериков, Ю.А.** Информационные системы и технологии обследования зданий и сооружений / Ю. А. Шестериков, О. А. Стифеева // Интернет-журнал «Транспортные сооружения». – 2020. – Т. 7, № 1. – С. 4. – DOI: 10.15862/05SATS120.
18. **Николюкин, А.Н.** Самообучающиеся интеллектуальные системы в строительстве / А. Н. Николюкин, П. В. Монастырев. – Тамбов: Тамбовский государственный технический университет, 2025. – 167 с. – ISBN 978-5-8265-2908-9. – EDN FTSUTJ
19. **Крылов С.А., Кашеварова Г.Г.** Автоматизация процесса оценки технического состояния наружных стен кирпичных зданий с использованием технологии машинного обучения // Вестник ДГТУ. Технические науки. – 2025. – № 3. – С. 61-70. – DOI: 10.21822/2073-6185-2025-52-3-61-70.
20. **Солдатенко Т.Н.** Модель идентификации и прогноза дефектов строительной конструкции на основе результатов ее обследования // Инженерно-строительный журнал. – 2011. – № 7. – С. 52-61.
21. **Самигуллина А.Г.** Необходимость разработки модели экспертной системы диагностики технического состояния строительных конструкций // Молодой ученый. – 2017. – № 51 (185). – С. 88–90. – EDN ZXXDMN.

22. **Бугакова Т.Ю., Шарапов А.А.** Совершенствование методов визуального осмотра зданий и инженерных сооружений путем внедрения технологий компьютерного зрения и интеллектуальной обработки данных // Вестник СГУГиТ (Сибирского государственного университета геосистем и технологий). – 2022. – № 6. С.108–119. – DOI 10.33764/2411-1759-2022-27-6-108-119. – EDN MFBIIV.
23. **Hamed G.M.** An expert system for concrete diagnosis: диссертация / G. M. Hamed; King Fahd University of Petroleum and Minerals. – Dhahran, 1983.
24. **Bernat E., Gil L.** Aided diagnosis of structural pathologies with an expert system // Advances in Structural Engineering. – 2013. – Vol. 16, № 2. – pp. 379–393. – DOI 10.1260/1369-4332.16.2.379.
25. **Moselhi O., Hegazy T., Fazio P.** Neural networks as tools in construction // Journal of Construction Engineering and Management. – 1991. – Vol. 117, № 4. – pp. 606–625. – DOI 10.1061/(ASCE)0733-9364(1991)117:4(606).
26. **Nuhu B. K. [et al.]** Distributed network-based structural health monitoring expert system // Building Research & Information. – 2021. – Vol. 49, № 1. – pp. 144–159. – DOI 10.1080/09613218.2020.1854083. – EDN BKCFCV.
27. **Arora S.** Deep learning-based structural crack detection framework for structural health monitoring of reinforced concrete buildings // Asian Journal of Civil Engineering. – 2026. – pp. 1–11. – DOI 10.1007/s42107-026-01713-8.
28. **de Brito J. [et al.]** Expert knowledge-based inspection systems // Inspection, Diagnosis and Repair of the Building Envelope. – Cham: Springer, 2020. – DOI 10.1007/978-3-030-42446-6.
29. **Ronneberger O., Fischer P., Brox T.U** Net**:** Convolutional Networks for Biomedical Image Segmentation // Medical Image Computing and Computer Assisted Intervention – MICCAI 2015. – Springer, 2015. – P. 234–241.
30. **Siva Rama Krishnan S., Nalla Karuppan M.K., Khadidos A.O. et al.** Inception V3 for automated binary classification of construction surface cracks // Scientific Reports. – 2025. – DOI: 10.1038/s41598-025-85983-3.
31. **Bhowmick S., Nagarajaiah S., Veeraraghavan A.** Automated crack detection and quantification from UAV videos using U-Net // Sensors. – 2020. – Vol. 20(21). – Art. 6299. – DOI: 10.3390/s20216299.
32. **Kumar P., Batchu S., Swamy N.S., Kota S.R.** Real-time structural health monitoring using multi-copter network and edge computing // IEEE Access. – 2021. – Vol. 9. – pp. 1234–1245. – DOI: 10.1109/ACCESS.2021.3102647.
33. **Gharehbaghi V., Noroozinejad Farsangi E., Yang T.Y. et al.** FastCrackNet: Identification of concrete cracks under noise and shadows using a 12-layer deep network // Sensors. – 2022. – Vol. 22(22). – Art. 8986. – DOI: 10.3390/s22228986.
34. **Gürer B., Karslıgil M.E.** Earthquake damage assessment using deep learning-based segmentation on drone imagery // Proc. SIU 2024. – IEEE, 2024. – DOI: 10.1109/SIU61531.2024.10601138.
35. **Chen H., Song J., Dietrich O. et al.** BRIGHT: A globally distributed multimodal dataset for automated building damage assessment after disasters // Earth System Science Data. – 2025. – DOI: 10.5194/essd-2025-269.
36. **Russo L., Tapete D., Ullo S.L., Gamba P.** Post-event SAR-only building damage assessment framework integrating geospatial data // arXiv preprint. – 2025. – arXiv:2506.22338.
37. **Hoier C., Ahmed K.M.** UAV video super-resolution and VLM-based building damage classification // arXiv preprint. – 2025. – arXiv:2508.17130.

38. **Manzini T., Perali P., Murphy R.R.** Operational deployment of sUAS-based AI for building damage assessment during hurricanes Debby and Helene // arXiv preprint. – 2025. – arXiv:2511.03132.
39. **Sandler M., Howard A., Zhu M., Zhmoginov A., Chen L.C.** MobileNetV2: Inverted Residuals and Linear Bottlenecks // Proceedings of the IEEE Conference on Computer Vision and Pattern Recognition (CVPR). – 2018. – pp. 4510–4520.
40. **Khanh Ha.** Crack Segmentation: [программный код] / Khanh Ha. – Текст: электронный // GitHub: [сайт]. – URL: https://github.com/khanhha/crack_segmentation

---

Maksim O. Bakanov, doctor of technical sciences, Professor, Department of Computer Science and Applied Mathematics, Moscow State University of Civil Engineering, 129337, Russia, Moscow, Yaroslavskoe Shosse, 26, e-mail: mask-13@mail.ru

Vladimir N. Sidorov, Full Member of RAACS, doctor of technical sciences, Professor, Head of the Department of Computer Science and Applied Mathematics, Moscow State University of Civil Engineering, 129337, Russia, Moscow, Yaroslavskoe Shosse, 26, e-mail: sidorov.vladimir@gmail.com

Elena A. Makarova, assistant professor, Department of Computer Science and Applied Mathematics, Moscow State University of Civil Engineering, 129337, Russia, Moscow, Yaroslavskoe Shosse, 26; e-mail: MakarovaEA@gic.mgsu.ru

Nikita S. Bondarenko, undergraduate student, Institute of Digital Technologies and Modeling in Construction, Moscow State University of Civil Engineering, 129337, Russia, Moscow, Yaroslavskoe Shosse, 26, e-mail: nyesenin@gmail.com

Баканов Максим Олегович, доктор технических наук, профессор, кафедра информатики и прикладной математики Национального исследовательского Московского государственного строительного университета; 129337, Россия, г. Москва, Ярославское шоссе, д. 26; e-mail: mask-13@mail.ru

Сидоров Владимир Николаевич, академик РААСН, доктор технических наук, профессор, заведующий кафедрой информатики и прикладной математики Национального исследовательского Московского государственного строительного университета; 129337, Россия, г. Москва, Ярославское шоссе, д. 26; e-mail: sidorov.vladimir@gmail.com

Макарова Елена Александровна, преподаватель, кафедра информатики и прикладной математики Национального исследовательского Московского государственного строительного университета; 129337, Россия, г. Москва, Ярославское шоссе, д. 26; e-mail: MakarovaEA@gic.mgsu.ru

Бондаренко Никита Сергеевич, студент, Институт цифровых технологий и моделирования в строительстве Национального исследовательского Московского государственного строительного университета; 129337, Россия, г. Москва, Ярославское шоссе, д. 26; e-mail: nyesenin@gmail.com

DOI:10.22337/2587-9618-2026-22-2-189-205

THE BENDING CAPACITY OF THREE-LAYER PRECAST REINFORCED CONCRETE STRUCTURES ACCOUNTING FOR THE CONTINUOUS VARIATION IN COMPRESSIVE STRENGTH OF THE CONTACT LAYERS

Vu Dinh Tho [1], Pham Thi Hien [1], Elena A. Korol [2], Le Ngoc Lan [1], Pham Tuan Anh [1]

[1] University of Transport Technology, Hanoi, VIET NAM

[2] National Research Moscow State University of Civil Engineering, Moscow, RUSSIA

Abstract: This paper presents the flexural strength of precast three-layer reinforced concrete structures made from different types of concrete. The three-layer reinforced concrete structure consists of an outer layer of ordinary concrete with strength grades from B12.5 to B30 and an inner layer of lightweight polystyrene concrete. Experiments involving the fabrication of 150x150x150 mm concrete samples using two different materials – B25 normal concrete and B0.75 polystyrene concrete showed that when two layers are poured consecutively with a rest time of less than 2 hours, a contact layer forms between the two materials. This contact layer has a structure with decreasing density from the outer layer using normal concrete to the inner layer using lightweight concrete with low compressive strength. This paper proposes a method for calculating the flexural strength of precast three-layer reinforced concrete structures accounting for the continuous variation in the compressive strength of the contact layer. Calculation results for the load-bearing capacity of three-layer reinforced concrete beam specimens using traditional methods, proposed methods, and experiments have shown that considering the contact layer in the bending behavior of three-layer reinforced concrete beams yields results closer to experimental values than traditional methods. Increasing the thickness and characteristics of the contact layer increases the structure's load-bearing capacity by up to 1%. When the compressive strength of the outer concrete layer is increased from B15 to B25, the load-bearing capacity of the structural plate can increase by up to 59%. When the compressive strength of the inner concrete layer is increased from B5 to B15 while keeping the outer layer's concrete type unchanged, the load-bearing capacity of the three-layer structure can increase by up to 40.1%. The proposed method for calculating three-layer reinforced concrete structures with different materials, accounting for the material properties of the contact layer, accurately captures the phenomena observed during the practical fabrication of such structures.

Keywords: three-layer reinforced concrete structures; the contact layer; normal concrete; lightweight concrete; polystyrene concrete

НЕСУЩАЯ СПОСОБНОСТЬ ИЗГИБАЕМЫХ СБОРНЫХ ТРЁХСЛОЙНЫХ ЖЕЛЕЗОБЕТОННЫХ КОНСТРУКЦИЙ С УЧЁТОМ НЕПРЕРЫВНОГО ИЗМЕНЕНИЯ ПРОЧНОСТИ НА СЖАТИЕ БЕТОНА КОНТАКТНЫХ СЛОЁВ

Ву Динь Тхо [1], Фам Тхи Хиен [1], Елена А. Король [2], Ле Нгок Лан [1], Фам Туан Ань [1]

[1] Университет транспортных технологий, г. Ханой, ВЬЕТНАМ

[2] Национальный исследовательский Московский государственный строительный университет, г. Москва, РОССИЯ

Аннотация: В данной статье представлены данные о прочности на изгиб сборных трехслойных железобетонных конструкций, изготовленных из различных типов бетона. Трехслойная железобетонная конструкция состоит из внешнего слоя из обычного бетона с классами прочности от B12.5 до B30 и внутреннего слоя из легкого полистиролбетона. Эксперименты с изготовлением бетонных образцов размером 150x150x150 мм из двух различных материалов – обычного бетона класса B25 и полистиролбетона класса B0.75 – показали, что при последовательной заливке двух слоев с интервалом

выдержки менее 2 часов, между двумя материалами образуется контактный слой. Этот контактный слой имеет структуру с уменьшающейся плотностью от внешнего слоя из обычного бетона к внутреннему слою из легкого бетона с низкой прочностью на сжатие. В данной статье предлагается метод расчета прочности на изгиб сборных трехслойных железобетонных конструкций, учитывающий непрерывное изменение прочности бетона контактных слоёв на сжатие. Результаты расчетов несущей способности трехслойных железобетонных балок с использованием традиционных методов, предложенных методов и экспериментов показали, что учет контактного слоя при изгибном поведении трехслойных железобетонных балок дает результаты, более близкие к экспериментальным значениям, чем традиционные методы. Увеличение толщины и характеристик контактного слоя повышает несущую способность конструкции до 1%. При увеличении прочности на сжатие бетона наружного слоя с B15 до B25, несущая способность балки может увеличиться до 59%. При увеличении прочности на сжатие внутреннего бетонного слоя с B5 до B15 и при сохранении неизменного типа бетона наружного слоя, несущая способность трехслойной конструкции может увеличиться до 40,1%. Предложенный метод расчета трехслойных железобетонных конструкций из различных материалов, учитывающий свойства материала контактного слоя, точно отражает явления, наблюдаемые при практическом изготовлении таких конструкций.

Ключевые слова: трехслойные железобетонные конструкции; контактный слой; конструктивный бетон; легкий бетон; полистиролбетон

1. INTRODUCTION

Multilayer reinforced concrete structures with different features are widely used in civil and industrial works [1], [2]. These multilayer structures are used extensively as enclosure structures to ensure load-bearing, sound insulation, and heat insulation requirements [3], [4]. The structure of three-layer reinforced concrete structures includes: the middle layer is made from ordinary concrete material with strength grade B12.5 to B30 [5], [6] and the inner layer is made from lightweight concrete types such as porous concrete [7–9], Lightweight aggregate concrete [10], arbolite concrete [11]. The thickness of the middle layer is determined based on the calculation of sound insulation, heat insulation or according to the desired performance requirements. The thickness of the outer layer is usually chosen to ensure load-bearing requirements and to ensure the concrete layer protects the steel reinforcement [12, 13].

Currently, there are many methods for calculating multi-layered reinforced concrete structures. In the studies by the authors [14], [15] this method for calculating multi-layered reinforced concrete structures was presented by converting cross-sections of various materials into I-shaped cross-sections of the same material, based on the elastic modulus ratio of the layers. This calculation method does not account for the distinct strength and strain characteristics of the various types of concrete used in multi-layered reinforced concrete structures. Therefore, the calculation results using this method often have significant errors.

The stress and strain state of multilayer reinforced concrete under load is a complex issue influenced by many factors. It has been studied by many authors. In publications [16], [17] the authors studied the influence of the mechanical properties of concrete and the geometric parameters of the inner and outer layers of multilayer structures on the structure's stress and strain. In research [18,19], the authors studied the stress-strain state of multilayer structures considering the nonlinear properties of concrete. The inner structural layer of multilayer reinforced concrete is often made of lightweight, low-strength concrete. Under load, this structure can easily develop small cracks in the inner concrete layer. To address this issue, the author [20] studied the influence of cracks appearing in the middle layer on the stress and strain state of a three-layer structure.

To consider the influence of different mechanical properties of different types of

concrete on the stress-strain state of three-layer reinforced concrete structures, the authors Korol E. A and colleagues developed a method for calculating three-layer structures [21, 22]. In this method, the authors based their hypothesis on the assumption that the strain in the cross-section at the contact point between two different materials is the same, but that the relationship between strength and strain in each layer is different. This method allows consideration of the different mechanical properties of different types of materials.

In the study [23, 24], based on experiments on test samples of two-layer concrete structures with different materials, the authors found that during the production of these structures, a contact layer forms between the two layers. This bonding layer is formed on the basis of the penetration of aggregate particles of the outer layer into the inner layer and vice versa, the penetration of aggregate particles of the inner layer into the outer layer. Therefore, several solutions have been developed to analyze multilayer reinforced concrete structures with different materials. Authors V. I. Andreev and colleagues [25, 26] presented a method for calculating three-layer reinforced concrete structures with a thin contact layer, homogeneous material with elastic or plastic properties. This method for calculating multi-layer structures does not accurately reflect the material properties of the bonding layer and their working state under the action of loads.

In studies [27, 28], the stress-strain state of three-layer reinforced concrete beams was analyzed using the finite element method (on ANSYS). However, these studies were mainly based on the assumption that the bonding layer was either ignored or treated as a homogeneous material. This is clearly limited. In studies [14], [23, 24], [29] Tho VD and colleagues presented a method for calculating three-layer reinforced concrete structures that accounts for the contact layer formed between different material layers. The mechanical properties of the contact layer were determined by assuming an average of the concrete mixtures from the inner and outer layers.

However, these studies have not yet captured the nature of contact layer formation, which arises from the penetration of aggregate particles from the high-strength concrete layer into the lower-strength concrete layer, and vice versa. Consequently, the compressive strength of the concrete in the contact layer decreases continuously from the high compressive strength of the outer concrete layer to the low compressive strength of the inner concrete layer. Therefore, studying the formation of the contact layer and proposing a solution for calculating the stress-strain behavior of three-layer reinforced concrete structures, taking into account the continuous variation in the compressive strength of the contact layer, are necessary.

2. MATERIALS AND METHODS

2.1. Materials

In this study, in the outer layer of the three-layer reinforced concrete structure, heavy concrete with strength grade B12.5 – B30 was used [5], [6] and in the inner layer, lightweight polystyrene concrete with strength grade B0.75 [14] and lightweight concrete with strength grades B5, B10, and B15 [30] were used.

The stress-strain relationship diagram of concrete is described by equations (1), (2) & (3) and Figure 1a [14], [27], [30].

Algebraic expressions for the three-line diagram of the deformation of compressed concrete can be represented as:

When $0 \leq \varepsilon \leq \varepsilon_{b1}$, with $\sigma_b = E_{b,red}.\varepsilon_b$ (1)

When $\varepsilon_{b1} \leq \varepsilon \leq \varepsilon_{b0}$, with

$$\sigma_b = \left[\left(1 - \frac{\sigma_{b1}}{R_b}\right)\frac{\varepsilon_b - \varepsilon_{b1}}{\varepsilon_{b0} - \varepsilon_{b1}} + \frac{\sigma_{b1}}{R_b}\right]R_b \quad (2)$$

(3)

When $\varepsilon_{b0} \leq \varepsilon \leq \varepsilon_{b2}$, with $\sigma_b = R_b$

Ứng suất $\sigma_{b1} = 0.6\,R_b$

The stress-strain relationship diagram for the reinforcement is described by equations (4) and (5) and shown in Figure 1b [30].

When $0 \leq \varepsilon \leq \varepsilon_y$, with

$$\sigma_s = E_s.\varepsilon_{s0} \quad (4)$$

The ε_{su} value is taken as 0.025.

When $\varepsilon_y \leq \varepsilon \leq \varepsilon_{su}$, with

$$\sigma_s = \sigma_y + \frac{\sigma_u - \sigma_y}{\varepsilon_u - \varepsilon_y}(\varepsilon_s - \varepsilon_y) \quad (5)$$

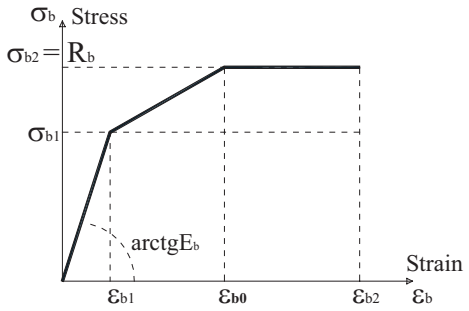

Figure 1a. Diagram of concrete compression

Where: σ_b – compressive stresses of concrete;
R_b – prismatic strength of concrete;
ε_b – the deformation of concrete;
ε_{b1}; ε_{b0}; ε_{b2} – the deformation of concrete corresponding to the stress $\sigma_{b1}=0.6*R_b$; $\sigma_{b0}=R_b = \sigma_{b2}$

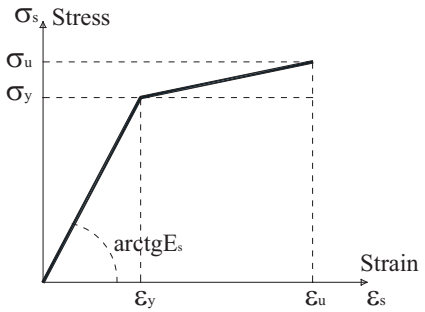

Figure 1b. Stress-strain diagram for reinforcement

Where: σ_y – yield *strength* of steel;
σ_u – ultimate strength of steel;
ε_y – the deformation *of* steel when σ_y;
ε_u – the deformation *of* steel when σ_u.

2.2. A contact layer between layers of a three-layer concrete structure

In the research results [14], [23,24] the authors studied the formation of the contact layer between different types of materials: normal concrete B25 and lightweight polystyrene concrete B0.75. The concrete mix proportions are described in the following table 1 [23,24].

Table 1. Composition of concrete mixtures

Class of concrete	Density, kg/m^3	Cement (M400), kg	Water, l	Crushed limestone (sizes from 0.5 to 1 cm), kg	Sand (sizes from 0 to 2 mm), kg	Expanded polystyrene granules EPS (sizes from 2 to 5 mm), kg	Chemical additives, SilkRoad SR-5000F, g
B0.75	346	330	105	-	-	0.69	710
B25	2376	439	195	1121	621	-	-

Research results published [23, 24] have shown that, during the construction of concrete structures from different types of concrete with a waiting time of less than 2 hours, a bonding layer is formed between the different material layers, due to the movement of aggregate particles from the inner layer to the outer layer and aggregate particles from the outer layer moving into the inner layer, as shown in Figure 2. The thickness of this bonding layer is from 0 cm to 1 cm.

Because the contact layer is formed by the movement of aggregate particles of different

types of concrete mixtures from the inner layer to the outer layer and vice versa, determining the mechanical properties of the concrete bond layer is very complex. Based on microstructural analysis, the authors in publications [23, 24] also showed that the aggregate particles in the heavy concrete mixture from the outer layer penetrating into the inner layer gradually decrease with the thickness of the bond layer and conversely, the aggregate particles in the polystyrene concrete mixture in the inner layer penetrating into the outer layer also gradually decrease with the thickness of the bond layer. This also forms the basis for the authors' proposal of a model for calculating structures with this type of bond under the action of a load. Without loss of generality, we can assume that the mechanical properties of the bonded layer between two different types of materials are as follows: Compressive strength of concrete R_b^*, Compressive strength of concrete R_{bt}^* and initial elastic modulus E_b^*; thickness of the bonded concrete layer h^*.

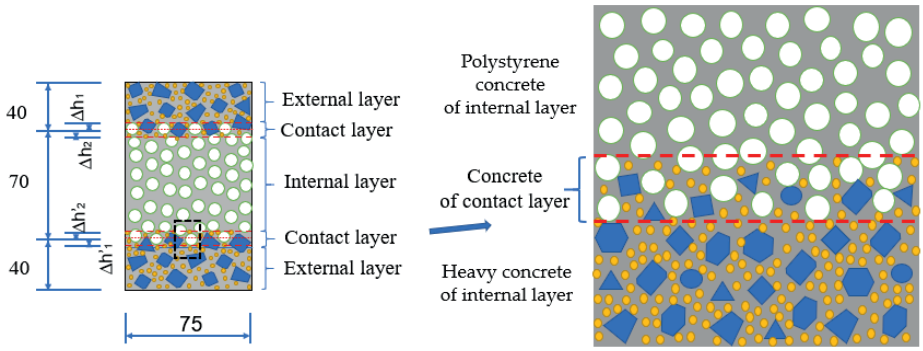

Figure 2. The *contact zone of layers of multilayer reinforced concrete structures*

2.3. Bending capacity of three-layer reinforced concrete beams

2.3.1. Bending capacity of three-layer reinforced concrete beams (without considering the contact layer)

In the studies [14], [24], [29], the authors presented a method for calculating the strength and deformation of a three-layer reinforced concrete structure with a monolithic section. The main provisions of TCVN 5574-2018 [30] can be applied after reducing the composite section to an I-beam. The stress-strain state of three-layer bent layers with a monolithic connection of sections normal to the longitudinal axis is determined by the positions of the elements' neutral axes under load. Then, the stress and strain calculation diagram of the structure before failure is shown in Figure 3 [14].

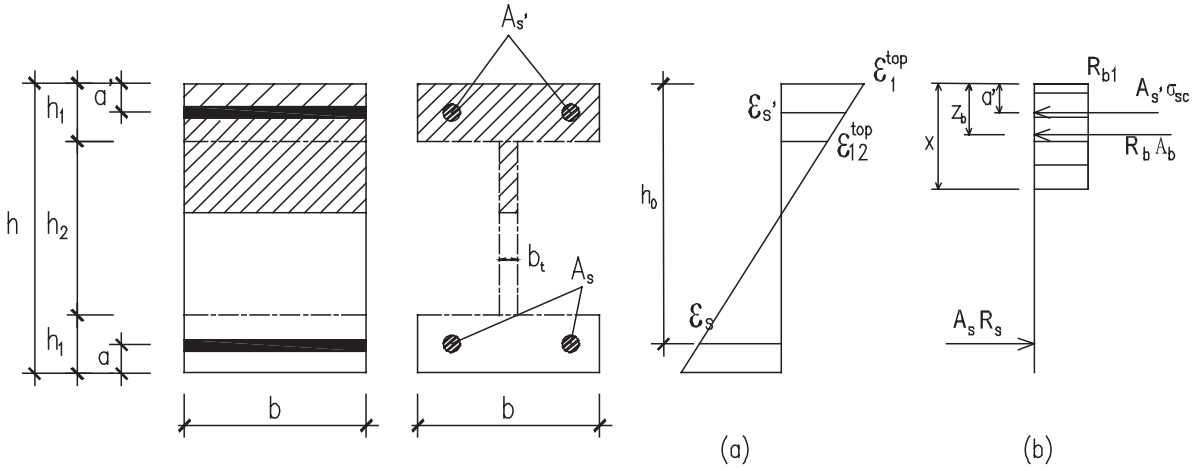

Figure 3. *Scheme 1 for calculating the stress and strain of a three-layer reinforced concrete structure*

The bearing capacity of the structure is calculated on the following conditions:

$$M \leq M_{ult} \quad (6)$$

With M_{ult} – Limit bending moment of the member;
M – Bending moment from loads.
Moment M_{ult} determined by the formula:

$$M_{ult} = R_{b1} b h_1 (h_0 - \frac{h_1}{2}) + R_{b1} b \frac{E_{b2}}{E_{b1}} (x - h_1)(h_0 - h_1 - \frac{x - h_1}{2}) + \sigma_{sc} A_{s'} (h_0 - a') \quad (7)$$

The height of the compression zone of concrete is determined by the condition:

$$R_s A_s = R_{b1} b h_1 + R_{b1} b \frac{E_{b2}}{E_{b1}} (x - h_1) + \sigma_{sc} A_s^{'} \quad (8)$$

2.3.2. Bending capacity of three-layer reinforced concrete beams (Considering the contact layer, which is hypothesized to be a homogeneous layer of material)

The research results of authors Tho V. D, Korol E. A and colleagues have developed a method for calculating three-layer reinforced concrete structures with a middle layer of polystyrene concrete, taking into account the bond layer formed between two different material layers [23, 24]. The above studies are based on the hypothesis that the mechanical properties of the bond layer are those of a homogeneous material layer. Then, the stress and strain calculation scheme for the structure before failure is shown in Figure 4 [14]. The initial elastic modulus of the concrete of the contact layer is determined:

$$R_{b*} = \frac{R_{b1} + R_{b2}}{2}$$

With: h* is the thickness of the bonding layer; R_{b*} is the compressive strength of the bonding layer; R_{b1} is the compressive strength of the outer concrete layer; R_{b2} is the compressive strength of the inner concrete layer.

The thicknesses of the outer and inner material layers are changed as follows: $h_1^{'} = h_1 - 0.5h_*$ and $h_2^{'} = h_2 - h_*$

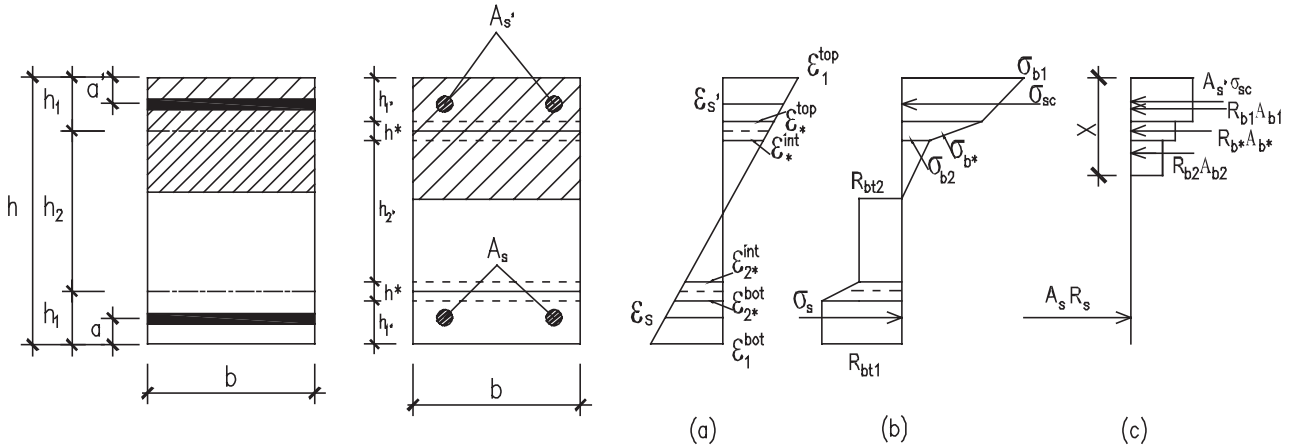

Figure 4. Scheme 2 for calculating of stress and strain of a three-layer reinforced concrete structure, during destruction (with contact layers)

The bearing capacity of the structure is calculated on the following conditions:

$$M \le M_{ult} \quad (9)$$

With M_{ult} – Limit bending moment of the member;

M – Bending moment from loads.

Moment M_{ult} determined by the formula:

$$M_{ult} = R_{b1} b h_{1'} [h_0 - \frac{h_{1'}}{2}] + R_{b*} b h^* [h_0 - h_{1'} - \frac{h^*}{2}]$$
$$+ R_{b2} b [x - h_{1'} - h^*][h_0 - h_{1'} - h^* - \frac{x - h_{1'} - h^*}{2}] + \sigma_{sc} A_{s'} (h_0 - a') \quad (10)$$

The height of the compression zone of concrete is determined by the condition:

$$R_s A_s = R_{b1} b h_{1'} + R_{b*} b h^* + R_{b2} b [x - h_{1'} - h^*] + \sigma_{sc} A_{sc} \quad (11)$$

2.3.3. Development of a method for calculating multi-layer reinforced concrete structures considering the contact layer (Considering the contact layer, which is hypothesized to be a layer of material with continuously changing properties)

Experimental results [23, 24] have shown that this material layer undergoes continuous changes from the outer layer to the inner layer. Therefore, in this study, the authors hypothesize that the compressive and tensile strengths of the concrete in the bonding layer vary continuously with height *h**, with these mechanical properties gradually decreasing from the outer to the inner layer.

$$R_{b*} = R_{b2} + \int_0^{h_*} \frac{(R_{b1} - R_{b2})}{h_*} dz$$

The thicknesses of the outer and inner material layers are changed as follows: $h_1^{'} = h_1 - 0.5 h_*$ and $h_2^{'} = h_2 - h_*$.

Then, the stress and strain calculation scheme for the structure before crack formation and before failure is shown in Figure 5.

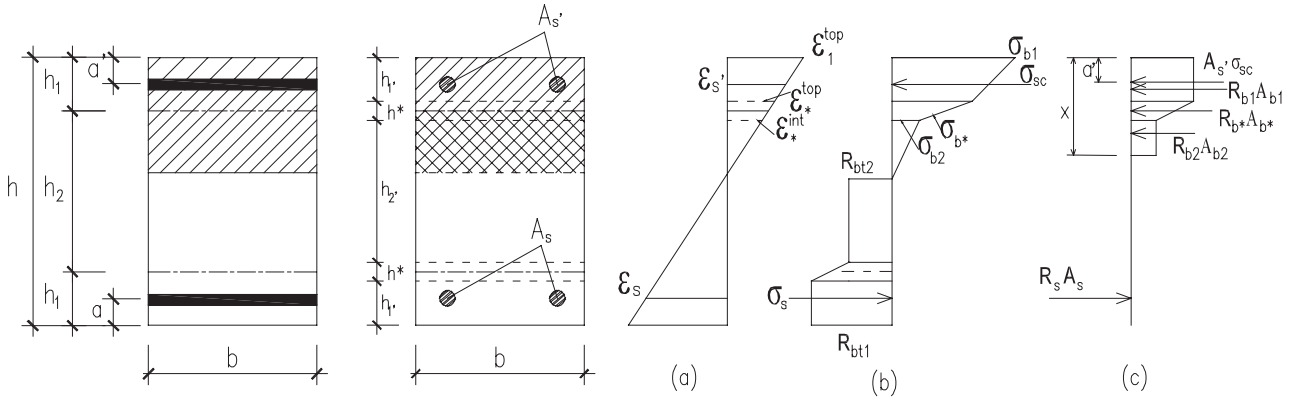

Figure 5. Scheme 3 for calculating the stress and strain of a three-layer reinforced concrete structure with contact layers

The bearing capacity of the structure is calculated on the following conditions:

$$M \le M_{ult} \quad (12)$$

With M_{ult} – Limit bending moment of the member; M – Bending moment from load.

Moment M_{ult} determined by the formula:

$$M_u = R_{b1}bh_{1'}(h_0 - \frac{h_{1'}}{2}) + R_{b2}bh_*(h_0 - h_{1'} - \frac{h_*}{2}) + \frac{1}{2}(R_{b1} - R_{b2})bh_{1*}(h_0 - h_{1'} - \frac{h_*}{3})$$
$$+R_{b2}b(x - h_{1'} - h_*)(h_0 - h_{1'} - h_* - \frac{x - h_{1'} - h_*}{2}) + \sigma_{sc}A_{s'}(h_0 - a') \quad (13)$$

The condition determines the height of the compression zone of concrete:

$$R_sA_s = R_{b1}bh_{1'} + R_{b2}bh_{1*} + \frac{1}{2}(R_{b1} - R_{b2})bh_{1*} + R_{b2}b(x - h_{1'} - h_*) + \sigma_{sc}A_{sc} \quad (15)$$

3. RESULTS AND DISCUSSION

3.1. Experimental and theoretical results on the load-bearing capacity of three-layer reinforced concrete structures and a comparison of analytical results

The results of stress-strain state analysis of multi-layer reinforced concrete structures using calculation methods according to Scheme 1, Scheme 2, the proposed Scheme 3, and the experiment were carried out on a beam sample (B-1) of a three-layer reinforced concrete beam with width b = 200mm, height h = 200mm, and length l = 2200mm. The structural and material parameters are shown in Figures 6 and 7 and in Table 1 [14].

Parameters of reinforcement used in the test beam: diameter 8mm, type of steel in test beam CB400-V, shown in Table 2 [14].

Table 1. Geometric and material parameters of a three-layer reinforced concrete beams

Test beam	Thickness of outer layers, mm	Class of concrete of the outer layer	Thickness of inner layers, mm	Class of concrete of the inner	Thickness of contact layers, mm
B1 (B1-1; B1-2; B1-3)	50	B25	100	B0.75	*h**

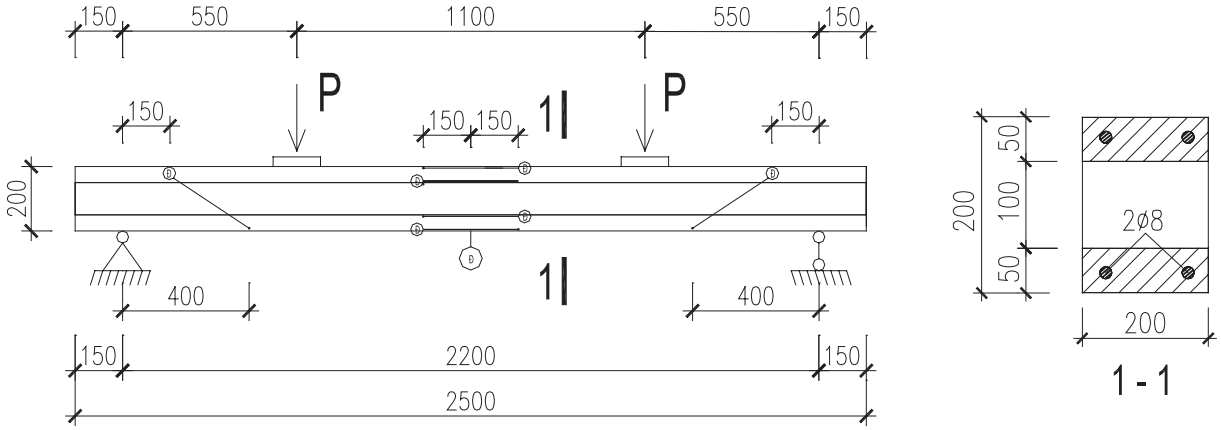

Figure 6. Parameters and dimensions of the test beam

Figure 7. The scheme of the layout instruments for bending testing

Table 2. Characteristics of steel in experimental tests

Diameter (mm)	f_y, MPa	f_u, Mpa	E_s 10^{-3}, Mpa
8	390	560	206

Table 3. Characteristics of concrete in experimental tests

Class of concrete	Density, kg/m^3	Compressive strength at different ages of 28 days R_b, MPa	Ultimate tensile strength in bending at the age of 28 days R_{bt}, MPa	Young's modulus E_b, MPa
B0.75	346	0.75	0.23	570
B25	2376	18.06	2.56	33200

The experimental results of the relationship between moment and deflection of test beam B1 under the action of load are shown in Figures 8, 9 [14] [24] and Table 4.

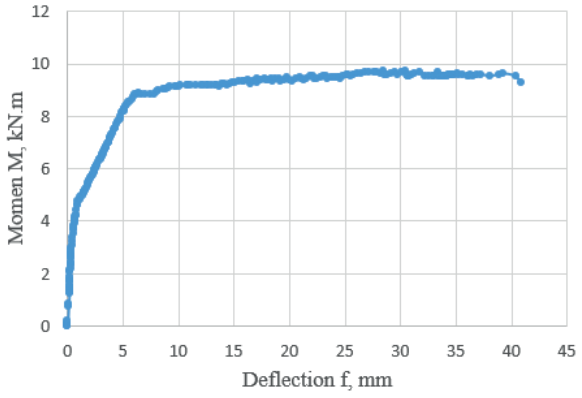

Figure 8. The relationship between the moment and the deflection of test beam B1

Figure 8. Views of the destruction of the tested beam samples

Table 4. The results of the destructive bending moment

Nº	Test beam	Destructive bending moment, kN.m							
		The test results [14]	Average value of test results	By using the scheme 1 [14]		By using the scheme 2 [14]		By using the scheme 3 (c)	
				When stress in steel					
				$1,2\sigma_y$	σ_u	$1,2\sigma_y$	σ_u	$1,2\sigma_y$	σ_u
1	B1-1	9.25	9.55	8.43	9.92	8.48	9.94	8.50	9.95
2	B1-2	9.56							
3	B1-3	9.84							

From the results obtained in Table 5, it has been shown that the destructive bending moment by the test beam is larger than the value calculated according to scheme 1 (converted to the equivalent cross-section of the letter I), scheme 2 and scheme 3, respectively, by 13.2%, 12.66% and 12.4% (when stress in steel is 1,2σy). Based on the results obtained, we make the following observations: Using the proposed model to calculate the strength and strain of multi-layer reinforced concrete beams yields results consistent with the beams' actual behavior.

3.2. Numerical analysis of the load-bearing capacity of a three-layer reinforced concrete beam considering the contact layer

Based on the analysis of experimental results and applied theoretical models regarding the performance of three-layer reinforced concrete structures, the author finds that the model proposed in section 2.3.3 can be applied to calculate the load-bearing capacity of multi-layer reinforced concrete structures made of different materials, taking into account the continuously changing characteristics of the bonding layer between the material layers. The authors analyzed the load-bearing capacity of three-layer reinforced concrete beams using beam specimens, as described in section 3.1, accounting for variations in the concrete types of the inner and outer layers. In particular, the authors also considered variations in the thickness of the contact layer formed when constructing two layers of different concrete types. The reinforcing steel bars used in the analytical beam are 2 ∅ 14, types of CB400V [30]. The material properties and parameters of the test beam are shown in Tables 6 & 7.

Table 5. Characteristics of concrete in beam tests

STT	Type of concrete	Class of concrete	Compressive strength R_b, MPa	Ultimate tensile strength in bending R_{bt}, MPa	Young's modulus E_b, MPa
1	Normal concrete	B15	8.5	0.75	24000
2		B20	11.5	0.9	27500
3		B25	14.5	1.05	30000
4	Lightweight concrete	B5	2.8	0.37	5000
5		B10	6	0.56	8000
6		B15	8.5	0.75	10500

Table 6. Parameters of three-layer beams

Beam	Thickness of outer layers, mm	Concrete of the **outer** layer		Thickness of inner layers, mm	Concrete of the inner layer		Ratio of R_{b1}/R_{b2}
		Class of normal concrete	Compressive strength R_{b1}, MPa		Class of lightweight concrete	Compressive strength R_{b2}, MPa	
B2-1	50	B25	14.5	100	B5	2.8	5.18
B2-2	50	B20	11.5	100	B5	2.8	4.11
B2-3	50	B15	8.5	100	B5	2.8	3.04
B3-1	50	B25	14.5	100	B10	6	2.42
B3-2	50	B20	11.5	100	B10	6	1.92
B3-3	50	B15	8.5	100	B10	6	1.42
B4-1	50	B25	14.5	100	B15	8.5	1.71
B4-2	50	B20	11.5	100	B15	8.5	1.35
B4-3	50	B15	8.5	100	B15	8.5	1.00

The results of the load-bearing capacity analysis of three-layer reinforced concrete beams under varying concrete types in the inner and outer layers, and with varying thickness of the bonding layer, are shown in Table 7.

Table 7. The results of the destructive bending moment of a three-layer beams when changing the thickness of the contact layer

*	Destructive bending moment Mu, kN.m								
	B2-1	B2-2	B2-3	B3-1	B3-2	B3-3	B4-1	B4-2	B4-3
0	25.875	20.714	16.277	26.235	24.428	21.869	26.33	24.831	22.81
0.4	25.878	20.717	16.278	26.232	24.429	21.87	26.331	24.832	22.81
0.8	25.883	20.722	16.28	26.241	24.431	21.872	26.333	24.834	22.81
1	25.885	20.731	16.282	26.243	24.433	21.874	26.335	24.836	22.81
Ratio of R_{b1}/R_{b2}	5.18	4.11	3.04	2.42	1.92	1.42	1.71	1.35	1

The moment of failure values of the beam samples described in Table 7 indicate that, as the thickness of the connection layer increases, the load-bearing capacity of the beam increases. However, the difference in the beam's load-bearing capacity when considering the thickness of the connection layer versus not considering it is negligible (less than 1%).

The results shown in Table 7 and Figure 9 indicate that the compressive strengths of concrete in the outer and inner layers affect the load-bearing capacity of a three-layer reinforced concrete beam.

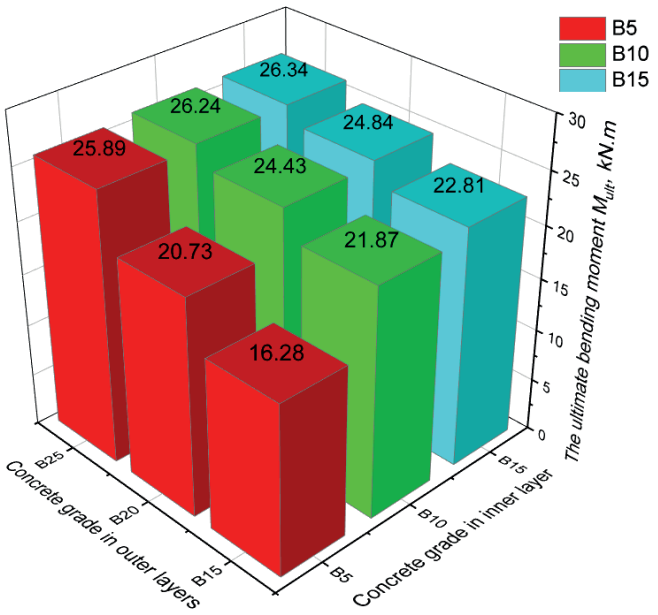

Figure 9. Change of the ultimate bending moment of a three-layer beam when changing the types of concrete in the outer layer and in the inner layer

With the same concrete grade of outer layer, when the grade of lightweight concrete in the internal layer increases from B5 to B15, the ultimate bending moment of the test beam can be increased from 16.28 kN.m to 22.81 kN.m (increase by 40.1%). With the same concrete grade of inner layer, when the grade of normal concrete in the outer layer increases from B15 to B25, the ultimate moment of the test beam can be increased from 16.28 kN.m to 25.89 kN.m (increase by 59%).

When the concrete grade of the inner concrete layer is B15, changing the concrete grade of the outer concrete layer results in the least change in the ultimate moment of the three-layer structure. This can be understood to mean that when the difference in compressive strength between the outer and inner concrete layers is small, the change in the ultimate bending moment is small.

4. CONCLUSIONS

Based on the results analyzed above, the author draws the following conclusions:

- This paper has proposed a method for calculating the load-bearing capacity of three-layer reinforced concrete beams, taking into account the continuous variation of the strength of the contact layer. The results of the load-bearing capacity analysis of three-layer reinforced concrete beams using the proposed method closely match the experimental results of beam samples.
- The load-bearing capacity of a three-layer reinforced concrete beam in cases where the thickness of the connection layer is taken into account differs insignificantly from the case where the thickness of the contact layer is not taken into account. The difference in limiting moments in the analysis of three-layer reinforced concrete beams in this study is less than 1%.
- The compressive strength of the outer and inner concrete layers significantly affects the change in the load-bearing capacity of a three-layer reinforced concrete beam. In the structural analysis of this study, the difference in load-bearing capacity can reach up to 59% when varying the compressive strength of the structure's outer concrete layer. For a change in

the inner concrete layer of the structure, the load-bearing capacity of the three-layer beam can differ by up to 40.1%.

The research results have contributed to the development of the theory of calculating the structural design of three-layer reinforced concrete structures using different types of materials. Considering the properties of the bonding layers helps to more accurately describe the actual phenomena occurring during the construction of these concrete structures. However, this study only examined a few specific cases. To make the research more practically significant, a comparative analysis with many other experimental cases is needed.

REFERENCES

1. **Halwatura RU, Jayasinghe MTR**. (2008) Thermal performance of insulated roof slabs in tropical climates. Energy and Buildings, no.40.pp.1153–60. doi:10.1016/j.enbuild.2007.10.006;
2. **Tho VD, Korol E, Hoang NH**. (2018) Analysis of the effectiveness of thermal insulation of a multi-layer reinforced concrete slab using layer of concrete with low thermal conductivity under the climatic conditions of Vietnam. MATEC Web Conf. no.251.pp.04026. doi:10.1051/matecconf/201825104026;
3. **Santamouris M.** (2015) Analyzing the heat island magnitude and characteristics in one hundred Asian and Australian cities and regions. Science of The Total Environment. no.512–513.pp.582–98. doi:10.1016/j.scitotenv.2015.01.060;
4. **Lam T, Vu T, Dien V, Korol E, Bulgakov B.** (2019) Properties and thermal insulation performance of light-weight concrete. Magazine of Civil Engineering. no.84.pp.173–91. doi:10.18720/MCE.84.17;
5. **Vu T, Lam T, Bulgakov B, Korol E.** (2020) Heat-Insulating Properties of Effective Light Weight Concretes for Three-Layer Protecting Coverings of Buildings. Promyshlennoe i Grazhdanskoe Stroitel stvo [Industrial and Civil Engineering]. no.5.pp.36–44. doi:10.33622/0869-7019.2020.05.36-44;
6. **Belyaev A, Nesvetaev G, Mailyan D.** (2018) The Issues of Energy-Efficiency Increase of Three-Layer Reinforced Concrete Plate Constructions. In: Murgul V, Popovic Z, editors. International Scientific Conference Energy Management of Municipal Transportation Facilities and Transport EMMFT 2017. Cham: Springer International Publishing. p. 529–35. doi:10.1007/978-3-319-70987-1_56;
7. **Korol E, Berlinova M.** (2018) Calculation of multilayer enclosing structures with middle layer of polystyrene concrete. MATEC Web Conf. no.193.pp.03020. doi:10.1051/matecconf/201819303020;
8. **Huang Y, Yang C, Ji X, Lu D, Song Q.** (2024) Seismic response of expanded polystyrene (EPS) sandwiched concrete panels system in buildings: Damage distribution and correlation analysis of parameters. Journal of Building Engineering. no.91.pp.109608. doi:10.1016/j.jobe.2024.109608;
9. **Fernando PLN, Jayasinghe MTR, Jayasinghe C.** (2017) Structural feasibility of Expanded Polystyrene (EPS) based lightweight concrete sandwich wall panels. Construction and Building Materials. no.139.pp.45–51. doi:10.1016/j.conbuildmat.2017.02.027;
10. **Santos DOJ dos, Lima PRL, Filho RDT.** (2025) Flexural Behavior of Lightweight Sandwich Panels with Rice Husk Bio-Aggregate Concrete Core and Sisal Fiber-Reinforced Foamed Cementitious Faces. Materials. no.18. doi:10.3390/ma18081850;
11. **Khusnitdin A, Jaloliddin T.** (2025) Calculation of Deformations of Flexural Three-Layer Reinforced Concrete Elements with A Middle Layer of Arbolite. European International Journal of Multidisciplinary

Research and Management Studies. no.5.pp.8–12. doi:10.55640/eijmrms-05-06-02;
12. **Tho VD, Korol EA.** (2019) Influence of Geometrical Parameters of the Cross Section, Strength and Deformability of the Materials Used on Stress-strain State of Three-layered Reinforced Concrete. IOP Conf Ser: Mater Sci Eng. no.661.pp.012121. doi:10.1088/1757-899X/661/1/012121;
13. **Mugahed Amran YH, Rashid RSM, Hejazi F, Abang Ali AA, Safiee NA, Bida SM.** (2018) Structural Performance of Precast Foamed Concrete Sandwich Panel Subjected to Axial Load. KSCE Journal of Civil Engineering. no.22.pp.1179–92. doi:10.1007/s12205-017-1711-6;
14. **Vu T, Pham T.A. (**2023) Method for calculating flexural multi-layer reinforced concrete structures. Vietnam Institute for Building Science and Technology. no.2023.pp.22–33. doi:10.59382/j-ibst.2023.vi.vol2-3;
15. **Tho VĐ, Anh PT, Hien PT, Lan VTH, Lan LN, Tâm NTT.** (2024) The study on the influence of concrete and reinforcement content on the crack resistance of three-layer panel slab. Vietnam Construction Magazine. Vol 12. pp. 98 – 101;
16. **Aydogdu M.** (2005) Vibration analysis of cross-ply laminated beams with general boundary conditions by Ritz method. International Journal of Mechanical Sciences. no.47.pp.1740–55. doi:10.1016/j.ijmecsci.2005.06.010;
17. **Shams A, Hegger J, Horstmann M.** (2014) An analytical model for sandwich panels made of textile-reinforced concrete. Construction and Building Materials. no.64.pp.451–9. doi:10.1016/j.conbuildmat.2014.04.025;
18. **Gara F, Ragni L, Roia D, Dezi L.** (2012) Experimental behaviour and numerical analysis of floor sandwich panels. Engineering Structures. no.36.pp.258–69. doi:10.1016/j.engstruct.2011.12.011;
19. **Gara F, Ragni L, Roia D, Dezi L.** (2012) Experimental tests and numerical modelling of wall sandwich panels. Engineering Structures. no.37.pp.193–204. doi:10.1016/j.engstruct.2011.12.027;
20. **Marčiukaitis G, Juknevičius L.** (2002) Influence of the Internal Layer Cracks on the Cracking of Flexural Three-Layer Concrete Members. Journal of Civil Engineering and Management.no.8.pp.153–8. doi:10.1080/13923730.2002.10531270;
21. **Korol EA.** (2018) The choice of the rational parameters of three-layer reinforced concrete inclosing structures with monolithic bond of layers by computer simulation. IOP Conf Ser: Mater Sci Eng. no.456.pp.012075. doi:10.1088/1757-899X/456/1/012075;
22. **Korol E, Tho VD, Kustikova Y.** (2018) Model of stressed-strained state of multi-layered reinforced concrete structure with the use of composite reinforcement. IOP Conf Ser: Mater Sci Eng. no.365.pp.052033. doi:10.1088/1757-899X/365/5/052033;
23. **Korol EA, Dinh Tho V.** (2021) Geometric and physio-mechanical characteristics of the contact layer area of multilayer reinforced concrete structures. IOP Conf Ser: Mater Sci Eng. no.1015.pp.012034. doi:10.1088/1757-899X/1015/1/012034;
24. **Vu T, Korol E, Vatin N, Hoang Minh D.** (2021) The Stress-Strain State of Three-Layer Precast Flexural Concrete Enclosure Structures with the Contact Interlayers. Buildings. no.11.pp.3. doi:10.3390/buildings11030088;
25. **Andreev V, Turusov R, Tsybin N.** (2017) The contact layer method in calculating of the shear compounds. MATEC Web Conf. no.117.pp.00008. doi:10.1051/matecconf/201711700008;
26. **Andreev VI, Turusov RA, Tsybin NYu.** (2016) Application of the Contact Layer in the Solution of the Problem of Bending the Multilayer Beam. Procedia Engineering.

XXV Polish – Russian – Slovak Seminar “Theoretical Foundation of Civil Engineering"153:59–65. doi:10.1016/j.proeng.2016.08.080;
27. **Tho VD, Korol E, Rimshin V, Anh PT.** (2022) Model Of Stress-Strain State Of Three-Layered Reinforced Concrete Structure By The Finite Element Methods. International Journal for Computational Civil and Structural Engineering. no.18.pp.62–73. doi:10.22337/2587-9618-2022-18-2-62-73;
28. **Khai LTQ, Dung DTM**. (2024) Input parameters of three-layer steel fiber concrete beams. Magazine of Civil Engineering. no.17. doi:10.34910/mce.126.4;
29. **Vu Dinh Tho, Korol EA.** (2020) Influence of contact layers on cracking resistance of bending three-layer structures. Vestnik MGSU. no.988.pp.98. doi:10.22227/1997-0935.2020.7.988-998;
30. TCVN 5574:2018. (2018) Design of concrete and reinforced concrete structures.

СПИСОК ЛИТЕРАТУРЫ

1. **Halwatura RU, Jayasinghe MTR.** (2008) Thermal performance of insulated roof slabs in tropical climates. Energy and Buildings, no.40.pp.1153–60. doi:10.1016/j.enbuild.2007.10.006;
2. **Tho VD, Korol E, Hoang NH.** (2018) Analysis of the effectiveness of thermal insulation of a multi-layer reinforced concrete slab using layer of concrete with low thermal conductivity under the climatic conditions of Vietnam. MATEC Web Conf. no.251.pp.04026. doi:10.1051/matecconf/201825104026;
3. **Santamouris M.** (2015) Analyzing the heat island magnitude and characteristics in one hundred Asian and Australian cities and regions. Science of The Total Environment. no.512–513.pp.582–98. doi:10.1016/j.scitotenv.2015.01.060;
4. **Лам Т.В., Ву Д., Зиен В., Булгаков Б.И., Король Е.А.** (2018) Свойства и теплоизоляционные эффективности легких бетонов. Инженерно-строительный журнал. № 8(84). С. 173–191. doi:10.18720/MCE.84.17;
5. **Тхо В. Д., Лам Т. В., Король Е. А., Булгаков Б. И., Александрова О. В., Ларсен О. А.** (2020) Теплоизоляционные свойства эффективных легких бетонов для трехслойных ограждающих покрытий зданий. Промышленное и гражданское строительство. 2020. №5. С. 36-44. DOI: 10.33622/0869-7019.2020.05.36-44.
6. **Belyaev A, Nesvetaev G, Mailyan D.** (2018) The Issues of Energy-Efficiency Increase of Three-Layer Reinforced Concrete Plate Constructions. In: Murgul V, Popovic Z, editors. International Scientific Conference Energy Management of Municipal Transportation Facilities and Transport EMMFT 2017. Cham: Springer International Publishing. p. 529–35. doi:10.1007/978-3-319-70987-1_56;
7. **Korol E, Berlinova M.** (2018) Calculation of multilayer enclosing structures with middle layer of polystyrene concrete. MATEC Web Conf. no.193.pp.03020. doi:10.1051/matecconf/201819303020;
8. **Huang Y, Yang C, Ji X, Lu D, Song Q.** (2024) Seismic response of expanded polystyrene (EPS) sandwiched concrete panels system in buildings: Damage distribution and correlation analysis of parameters. Journal of Building Engineering. no.91.pp.109608. doi:10.1016/j.jobe.2024.109608;
9. **Fernando PLN, Jayasinghe MTR, Jayasinghe C.** (2017) Structural feasibility of Expanded Polystyrene (EPS) based lightweight concrete sandwich wall panels. Construction and Building Materials. no.139.pp.45–51. doi:10.1016/j.conbuildmat.2017.02.027;
10. **Santos DOJ dos, Lima PRL, Filho RDT**. (2025) Flexural Behavior of Lightweight

Sandwich Panels with Rice Husk Bio-Aggregate Concrete Core and Sisal Fiber-Reinforced Foamed Cementitious Faces. Materials. no.18. doi:10.3390/ma18081850;

11. **Khusnitdin A, Jaloliddin T.** (2025) Calculation of Deformations of Flexural Three-Layer Reinforced Concrete Elements with A Middle Layer of Arbolite. European International Journal of Multidisciplinary Research and Management Studies. no.5.pp.8–12. doi:10.55640/eijmrms-05-06-02;
12. **Tho VD, Korol EA.** (2019) Influence of Geometrical Parameters of the Cross Section, Strength and Deformability of the Materials Used on Stress-strain State of Three-layered Reinforced Concrete. IOP Conf Ser: Mater Sci Eng. no.661.pp.012121. doi:10.1088/1757-899X/661/1/012121;
13. **Mugahed Amran YH, Rashid RSM, Hejazi F, Abang Ali AA, Safiee NA, Bida SM.** (2018) Structural Performance of Precast Foamed Concrete Sandwich Panel Subjected to Axial Load. KSCE Journal of Civil Engineering. no.22.pp.1179–92. doi:10.1007/s12205-017-1711-6;
14. **Vu T, Pham T. A.** (2023) Method for calculating flexural multi-layer reinforced concrete structures. Vietnam Institute for Building Science and Technology. no.2023.pp.22–33. doi:10.59382/j-ibst.2023.vi.vol2-3;
15. **Tho VĐ, Anh PT, Hien PT, Lan VTH, Lan LN, Tâm NTT.** (2024) The study on the influence of concrete and reinforcement content on the crack resistance of three-layer panel slab. Vietnam Construction Magazine. Vol 12. pp. 98 – 101;
16. **Aydogdu M.** (2005) Vibration analysis of cross-ply laminated beams with general boundary conditions by Ritz method. International Journal of Mechanical Sciences. no. 47. pp. 1740–55. doi:10.1016/j.ijmecsci.2005.06.010;
17. **Shams A, Hegger J, Horstmann M.** (2014) An analytical model for sandwich panels made of textile-reinforced concrete. Construction and Building Materials. no.64.pp.451–9. doi:10.1016/j.conbuildmat.2014.04.025;
18. **Gara F, Ragni L, Roia D, Dezi L.** (2012) Experimental behaviour and numerical analysis of floor sandwich panels. Engineering Structures. no.36.pp.258–69. doi:10.1016/j.engstruct.2011.12.011;
19. **Gara F, Ragni L, Roia D, Dezi L.** (2012) Experimental tests and numerical modelling of wall sandwich panels. Engineering Structures. no.37.pp.193–204. doi:10.1016/j.engstruct.2011.12.027;
20. **Marčiukaitis G, Juknevičius L.** (2002) Influence of the Internal Layer Cracks on the Cracking of Flexural Three-Layer Concrete Members. Journal of Civil Engineering and Management.no.8.pp.153–8. doi:10.1080/13923730.2002.10531270;
21. **Korol EA.** (2018) The choice of the rational parameters of three-layer reinforced concrete inclosing structures with monolithic bond of layers by computer simulation. IOP Conf Ser: Mater Sci Eng. no.456.pp.012075. doi:10.1088/1757-899X/456/1/012075;
22. **Korol E, Tho VD, Kustikova Y.** (2018) Model of stressed-strained state of multi-layered reinforced concrete structure with the use of composite reinforcement. IOP Conf Ser: Mater Sci Eng. no.365.pp.052033. doi:10.1088/1757-899X/365/5/052033;
23. **Korol EA, Dinh Tho V.** (2021) Geometric and physio-mechanical characteristics of the contact layer area of multilayer reinforced concrete structures. IOP Conf Ser: Mater Sci Eng. no.1015.pp.012034. doi:10.1088/1757-899X/1015/1/012034;
24. **Vu T, Korol E, Vatin N, Hoang Minh D.** (2021) The Stress-Strain State of Three-Layer Precast Flexural Concrete Enclosure Structures with the Contact Interlayers. Buildings. no.11.pp.3. doi:10.3390/buildings11030088;

25. **Andreev V, Turusov R, Tsybin N.** (2017) The contact layer method in calculating of the shear compounds. MATEC Web Conf. no.117.pp.00008. doi:10.1051/matecconf/201711700008;
26. **Andreev VI, Turusov RA, Tsybin NYu.** (2016) Application of the Contact Layer in the Solution of the Problem of Bending the Multilayer Beam. Procedia Engineering. XXV Polish – Russian – Slovak Seminar “Theoretical Foundation of Civil Engineering"153:59–65. doi:10.1016/j.proeng.2016.08.080;
27. **Tho VD, Korol E, Rimshin V, Anh PT.** (2022) Model Of Stress-Strain State Of Three-Layered Reinforced Concrete Structure By The Finite Element Methods. International Journal for Computational Civil and Structural Engineering. no.18.pp.62–73. doi:10.22337/2587-9618-2022-18-2-62-73;
28. **Khai LTQ, Dung DTM.** (2024) Input parameters of three-layer steel fiber concrete beams. Magazine of Civil Engineering. no.17. doi:10.34910/mce.126.4;
29. **Ву Динь Тхо, Король Е.А.** (2020) Влияние контактных слоев на трещиностойкость изгибаемых трехслойных конструкций // Вестник МГСУ. Т. 15. Вып. 7. С. 988–998. DOI: 10.22227/1997-0935.2020.7.988-998;
30. TCVN 5574:2018. (2018) Design of concrete and reinforced concrete structures.

Vu Dinh Tho – PhD in Technical Sciences, Teacher of the Department of Construction of civil engineering and industrial engineering, University of Transport Technology (UTT), (Vietnam), 100000, 54-Trieu Khuc, Thanh Liet, Ha Noi, Vietnam; e-mail: thovd@utt.edu.vn; 0000-0001-7374-9424.

Elena A. Korol – doctor of Technical Sciences, Professor, Professor of the Department "Housing and Communal Complex", National Research Moscow State University of Civil Engineering" (NIU MGSU); 129337, 26, Yaroslavskoye Shosse, Moscow, Russia; e-mail: KorolEA@mgsu.ru; 0000-0002-5019-3694.

Pham Tuan Anh – PhD in Technical Sciences, Associate Professor, Department of Construction of civil engineering and industrial engineering « University of Transport Technology (UTT)» (Vietnam), 100000, 54-Trieu Khuc, Thanh Liet, Ha Noi, Vietnam; ; e-mail: anhpt@utt.edu.vn; 0000-0001-9484-1916.

Pham Thi Hien – Master of Engineering, Teacher of the Department of Construction of civil engineering and industrial engineering, University of Transport Technology (UTT), (Vietnam), 100000, 54-Trieu Khuc, Thanh Liet, Ha Noi, Vietnam; e-mail: hienpt89@utt.edu.vn

Le Ngoc Lan – PhD in Technical Sciences, Teacher of the Department of Construction of civil engineering and industrial engineering, University of Transport Technology (UTT), (Vietnam), 100000, 54-Trieu Khuc, Thanh Liet, Ha Noi, Vietnam; e-mail: lanln@utt.edu.vn; 0009-0001-1361-471X

Ву Динь Тхо – канд. техн. наук, преподаватель кафедры "Промышленное и гражданское строительство", Университет транспортных технологий; 100000, 54- Чиеу Хук, Тхань Лиет, Ха Ной, Вьетнам; e-mail: thovd@utt.edu.vn; 0000-0001-7374-9424.

Король Елена Анатольевна – доктор технических наук, профессор, профессор кафедры «Жилищно-коммунальный комплекс», Федеральное государственное бюджетное образовательное учреждение высшего образования «Национальный исследовательский Московский государственный строительный университет» (ФГБОУ ВО «НИУ МГСУ»); 129337, г. Москва, Ярославское шоссе, д. 26; e-mail: KorolEA@mgsu.ru.; 0000-0002-5019-3694.

Фам Туань Ань – канд. техн. наук, доцент, преподаватель кафедры "Промышленное и гражданское строительство", Университет транспортных технологий; 100000, 54- Чиеу Хук, Тхань Лиет, Ха Ной, Вьетнам; e-mail: anhpt@utt.edu.vn; 0000-0001-9484-1916.

Фам Тхи Хиен – магистр, преподаватель кафедры "Промышленное и гражданское строительство", Университет транспортных технологий; 100000, 54- Чиеу Хук, Тхань Лиет, Ха Ной, Вьетнам; e-mail: hienpt89@utt.edu.vn;

Ле Нгок Лан – канд. техн. наук, преподаватель кафедры "Промышленное и гражданское строительство", Университет транспортных технологий; 100000, 54- Чиеу Хук, Тхань Лиет, Ха Ной, Вьетнам; e-mail: lanln@utt.edu.vn; 0009-0001-1361-471X.

International Journal for Computational Civil and Structural Engineering, 22(2) 206–229 (2026)

DOI:10.22337/2587-9618-2026-22-2-206-229

NUMERICAL PARAMETRIC ANALYSIS OF AXIALLY COMPRESSED CIRCULAR STEEL TUBE CONFINED CONCRETE COLUMNS

Vladislav V. Vershinin

National Research Moscow State University of Civil Engineering, Moscow, RUSSIA

Abstract: Axially compressed circular steel tube confined concrete columns have been parametrically analyzed through numerical simulation with the general aim to confirm the effectiveness of concrete confinement and quantitatively estimate it. Numerical models have been assembled using SIMULIA Abaqus finite element analysis commercial software and its relevant tools, in particular Abaqus/Explicit module, the general contact algorithm, and the concrete damaged plasticity model. The limit states of the first group and corresponding failure mechanisms have been defined for the considered columns and investigated, qualitatively and quantitatively, with regard to their dependence onto column structural scheme, steel tube thickness and concrete grade. Totally, 33 different cases have been simulated and analyzed.

Keywords: steel tube confined concrete column, numerical simulation, parametrical analysis, concrete damaged plasticity model

ЧИСЛЕННЫЙ ПАРАМЕТРИЧЕСКИЙ АНАЛИЗ ЦЕНТРАЛЬНО СЖАТЫХ ТРУБОБЕТОННЫХ КОЛОНН

В.В. Вершинин

Национальный исследовательский Московский государственный строительный университет, г. Москва, РОССИЯ

Аннотация: Выполняется численный параметрический анализ центрально сжатых трубобетонных колонн с целью подтвердить положительное влияние стеснения поперечных деформаций бетона на несущую способность конструктивного элемента и количественно оценить его эффект. Построение численных моделей выполняется в коммерческом программном комплексе конечно-элементного анализа SIMULIA Abaqus с использованием соответствующих инструментов, в частности модуля Abaqus/Explicit, универсального метода решения контактных задач и математической модели неупругого поведения бетона. Определяются предельные состояния первой группы и соответствующие им механизмы разрушения конструктивного элемента. Проводится качественный и количественный анализ зависимости значений их параметров от расчётной схемы колонны, толщины стальной трубы и класса бетона по прочности на одноосное сжатие. Всего рассматриваются 33 различных случая.

Ключевые слова: трубобетонная колонна, численное моделирование, параметрический анализ, математическая модель неупругого поведения бетона

1. INTRODUCTION

Concrete, similarly to many other materials, exhibits pronounced dependence of its strength onto a stress state. For instance, according to Russian building code SP 63.13330.2018 “Concrete and reinforced concrete structures. General provisions” [1], the ratio of normal-weight concrete strength under uniaxial compression to its strength under uniaxial tension varies from 7.6 for grade B5 concrete to 21.6 for grade B100 concrete, exhibiting non-linear, viz. power, increase with concrete grade. Typical experimental values of the ratio of concrete strength under biaxial compression to its strength under uniaxial compression are in the range from 1.10 to 1.16 [2]. These concrete strength properties were reflected into elaborate strength criteria, developed in 1970s specifically to describe concrete inelastic behaviour [3-6].

Concrete, being relatively inexpensive and available almost everywhere, is one of the most widely used construction materials. In construction, its strength properties described above are utilized in conjunction with various structural measures. The most common way is using reinforced concrete instead of plain one, so that tensile stresses in structural elements are taken up by the reinforcement, while concrete withstands to compressive stresses. Yet, commonly employed structural measures do not completely exploit concrete high compressive strength, especially under complex stress states.

While most vertical structural elements (columns, shear walls and composite elements) experience complex loading – axial compression, shear in horizontal direction, bending about a horizontal axis, and torsion around the vertical axis, – compressive stresses are predominant in most cases, except, probably, an earthquake excitation, when horizontal inertia forces can result in shear stresses of the same order of magnitude as the compressive stresses. The corresponding stress state can be characterized as close to the uniaxial one. And only for structures with large length-to-width ratio the stress state is close to the plane strain compression. Yet, concrete strength under biaxial compression, plane strain compression, and all-around compression is significantly higher than that under uniaxial compression. Hence, there is an evident profit from changing the stress state of a structural element from a uniaxial one to some more complex through some structural measures. An effective measure is to restrict lateral straining of vertical structural elements, so that their response becomes close to uniaxial straining and, hence, triaxial compression. A common way to provide concrete confinement is to use a steel tube. Such a structural solution is called “steel tube confined concrete” and is commonly employed for columns, especially for heavily loaded ones.

The steel tube confined concrete columns, despite working mainly under uniaxial compression, exhibit rather complex behaviour. Complex response of such columns is caused by several factors.

First of all, it is a structural scheme of the considered element. Some structural solutions provide loads acting onto ends of both steel and concrete parts of the column, while in other cases only a concrete core is loaded, and steel tube acts only as a confinement. Evidently, this yields two different schemes of interaction between the steel tube and the concrete core.

Secondly, Young’s moduli of steel and concrete differ from each other by almost an order of magnitude, and values of their Poisson’s ratios differ by 50%. Moreover, not only concrete compressive-to-tensile strength ratio increases with grade, so does its Young’s modulus.

In the third place, construction steel is a highly plastic material, whose strains at failure exceed unity under some stress states, while concrete is a quasi-brittle material, which, being inelastically deformed, experiences either cracking (under tension) or crushing and pronounced dilation (under compression or shear).

Finally, the level of strains under which concrete loses almost all of its bearing capacity (approximately 0.003-0.004) corresponds to the very beginning of a plastic phase of straining for construction steel, which retains its strength and stiffness well beyond this level of plastic straining.

In the present work, axially compressed circular steel tube confined concrete columns have been parametrically analyzed through numerical simulation. The first group of column limit states and corresponding column failure mechanisms have been investigated, qualitatively and quantitatively, with regard to their dependence onto column structural scheme, steel tube thickness and concrete grade.

2. PROBLEM FORMULATION

The steel tube confined concrete column with a circular cross-section subjected to an axial compressive load has been considered. The reference cross-section diameter has been chosen

to be equal to 720 mm. The column height has been set equal to 3 m.

Axial loading of the column has been performed through two rigid dies. The bottom die has been fixed, and the top die has been able to move only in vertical direction.

The top die has been loaded through the Kelvin-Voigt viscoelastic element, that has allowed one to obtain decreasing parts of a "force-displacement" curve and damp out oscillations in the curve, which have appeared due to concrete cracking and crushing. This Kelvin-Voigt viscoelastic element has been assumed to simulate the actuator of the test machine and have the following properties: the elastic stiffness $K = 1.0 \cdot 10^9$ N/m, and the damping factor $C = 1.0 \cdot 10^4$ N·s/m.

For each die an artificial associated mass has been specified in the form of a point mass located at its center and having the following properties: 20 kg for translational degrees of freedom and $0.02\ \text{kg} \cdot \text{m}^2$. A point mass with the same properties has been specified for the free end of the Kelvin-Voigt viscoelastic element.

Loading of the column has been carried out through assigning a constant velocity of 0.4 m/s in the vertical direction to the free end of the Kelvin-Voigt viscoelastic element.

At the contact interfaces between the dies and the column ends, the isotropic Coulomb friction has been assumed to take place with the friction factor μ being equal to 0.2 for the contact interfaces between the dies and the steel tube ends, and 0.35 for the contact interfaces between the dies and the concrete core ends.

The isotropic Coulomb friction has been assumed to take place at the contact interface between the concrete core and the steel tube as well. The friction factor μ has been assumed to be equal to 0.35 at this contact interface.

Since the parametrical analysis has been performed, a four index notation of the form

$$A\text{-}B\text{-}C\text{-}D \qquad (1)$$

has been established to distinguish particular cases.

The first index, *A*, specifies the column structural scheme. It equals to 1 in the case, when the axial load acts onto ends of both steel and concrete parts of the column, and equals to 2 in the case, when only the concrete core is subjected to axial loading, while the steel tube acts only as a confinement.

The second index, *B*, specifies the concrete grade. Totally, three normal weight concrete grades have been considered – B30, B60, and B90, – with index *B* taking these particular values. Also a reference case with no concrete core, but only steel tube has been considered to be able to determine what fraction of a column load-bearing capacity is provided by the steel tube. In this case, index *B* equals to zero.

The third index, *C*, specifies the steel tube thickness. Totally, three different steel tube thickness values have been considered, – 10 mm, 20 mm, and 30 mm, – with index *C* taking these particular values. Also a reference case with no steel tube, but plain concrete column has been considered to quantitatively determine the effectiveness of concrete confinement. In this case, index *C* equals to zero.

The fourth index, *D*, specifies the concrete core diameter. According to the index *C* possible values, the corresponding values of index *D* are 720, 700, 680, and 660.

All in all, 33 different cases have been simulated and analyzed: 1-0-10-0, 1-B30-10-700, 1-B60-10-700, 1-B90-10-700, 1-0-20-0, 1-B30-20-680, 1-B60-20-680, 1-B90-20-680, 1-0-30-0, 1-B30-30-660, 1-B60-30-660, 1-B90-30-660, 2-B30-0-720, 2-B60-0-720, 2-B90-0-720, 2-B30-0-700, 2-B60-0-700, 2-B90-0-700, 2-B30-0-680, 2-B60-0-680, 2-B90-0-680, 2-B30-0-660, 2-B60-0-660, 2-B90-0-660, 2-B30-10-700, 2-B60-10-700, 2-B90-10-700, 2-B30-20-680, 2-B60-20-680, 2-B90-20-680, 2-B30-30-660, 2-B60-30-660, 2-B90-30-660.

In all the relevant cases, the ends of the concrete core have been reinforced with a single rebar mat. It has been assumed, that these mats have had a 100×100 mm grid and have been made of

class A500C (according to Russian standards) steel rods with the diameter of 6 mm. In the cases, when the concrete core has been confined by the steel tube, these rebar mats have been welded to the tube.

The steel tube has been assumed to be made of class C355 (according to Russian standards) steel in all the relevant cases.

3. NUMERICAL MODELS

Numerical models of the considered steel tube confined concrete column have been assembled and analyzed using SIMULIA Abaqus finite element analysis commercial software. Some of them are presented in Fig. 1.

The considered problem has been solved quasi-statically, with geometrical nonlinearity taken into account, using Abaqus/Explicit module, in which the central difference time integration scheme of the second order of accuracy is implemented. To fulfil the Courant-Friedrichs-Lewy stability condition, a stable time increment has been automatically determined by the solver itself during the solution. (An interested reader is referred to software documentation [7, 8] for more details.)

At each contact interface a contact problem, with all the features described above in Section 2, has been solved through a General Contact algorithm implemented into Abaqus/Explicit, within which contact constraints are enforced through a penalty contact algorithm. The surfaces of the concrete core and the steel tube at their contact interface have been smoothed using a Surface Smoothing tool to preclude artificial contact stress oscillations and high peaks appeared due to approximation of a smooth curved surfaces with faceted ones. (For more details on contact formulations and numerical methods, interested readers are referred to the software documentation [7, 8].)

Spatial discretization of the problem has been performed using finite elements of various types. (For details on formulation of various types of finite elements implemented into SIMULIA Abaqus an interested reader is referred to the software documentation [7, 8].)

The concrete core and the steel tube have been discretized through, respectively, 17 280 and 7 680 continuum finite elements of the type C3D8R (see Fig. 2(a)). Each die has been discretized through four rigid finite elements of the type R3D4 with the point mass finite element of the type MASS located at its center. The actuator is discretized through one spring finite element of the type SPRINGA and one dashpot finite element of the type DASHPOTA with the point mass finite element of the type MASS located at its free end. The rebar mats have been discretized through structural finite elements of the type B31 (see Fig. 2(b)). Depending on the particular case, each mat has been meshed with 355, 372, 389, or 480 finite elements.

In all the relevant cases, the welded joints between the rebar rods and the tube have been simulated using a Tie Constraint tool (see Fig. 3(b)). To tie nodes of the beam finite elements with six degrees of freedom to nodes of the continuum finite elements with three degrees of freedom, the internal surface of the tube has been covered with 1 920 surface finite elements of the type SFM3D4R which have zero stiffness. These surface elements have been specified an artificial areal density of 1 kg/m^2 and tied in each node to corresponding nodes on the tube internal surface (see Fig. 3(a)).

Interaction between the reinforcement and the concrete has been simulated through an Embedded Element tool. Translational degrees of freedom of embedded nodes belonging to the reinforcement elements have been constrained to the interpolated values of the corresponding degrees of freedom of the host concrete elements, while rotational degrees of freedom of the embedded nodes have been remained free of constraints. (For more information on the Embedded Element tool an interested reader is referred to the software documentation [7, 8].)

The steel elements of the column have been modeled as made of homogeneous isotropic elastic-plastic non-damageable material with the Maxwell-von Mises yield criterion, an associated

flow rule, and isotropic hardening, that instantly fractures when an accumulated plastic strain reaches its limit value.

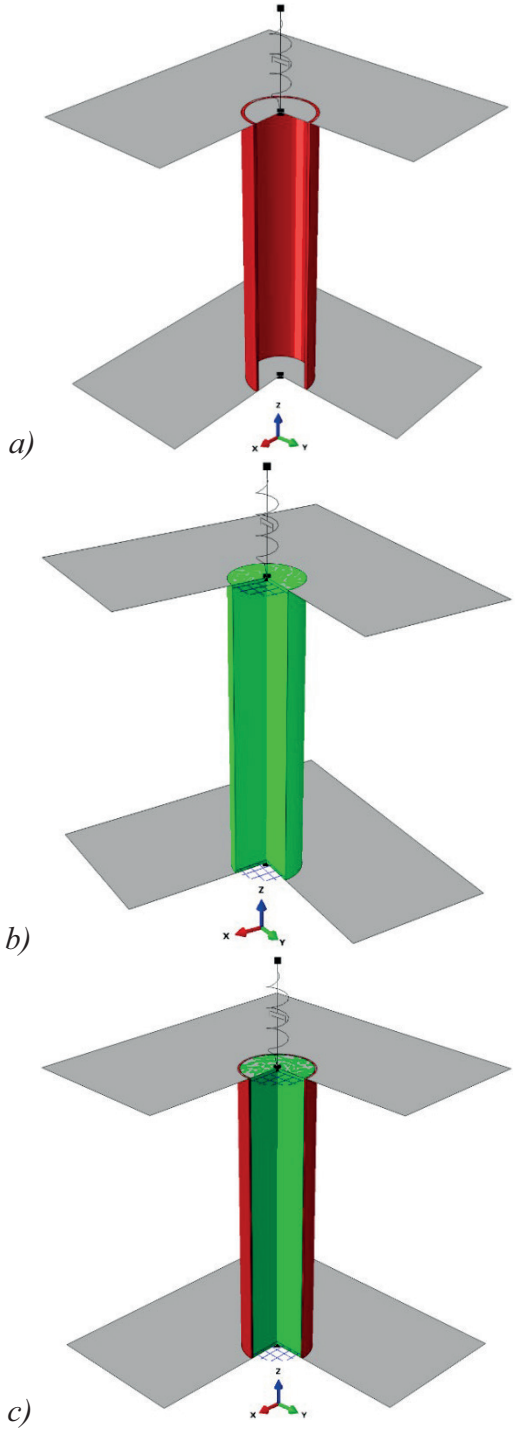

Figure 1. Numerical models for the cases: a) 1-0-30-0; b) 2-B30-0-700, 2-B60-0-700, 2-B90-0-700; c) 1-B30-20-680, 1-B60-20-680, 1-B90-20-680, 2-B30-20-680, 2-B60-20-680, 2-B90-20-680

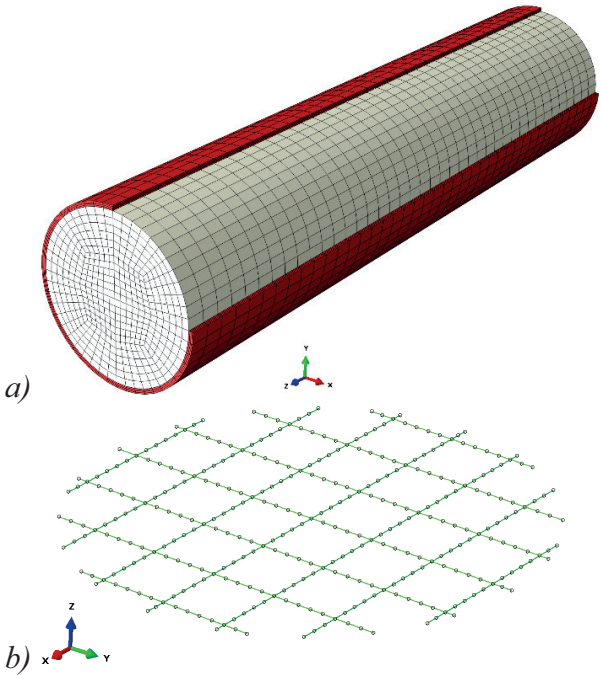

Figure 2. Finite element mesh of: a) the steel tube with the wall thickness of 20 mm and the concrete core (the tube wall is discretized with four continuum finite elements through the thickness); b) the reinforcement mat (nodes are labeled with small black circles)

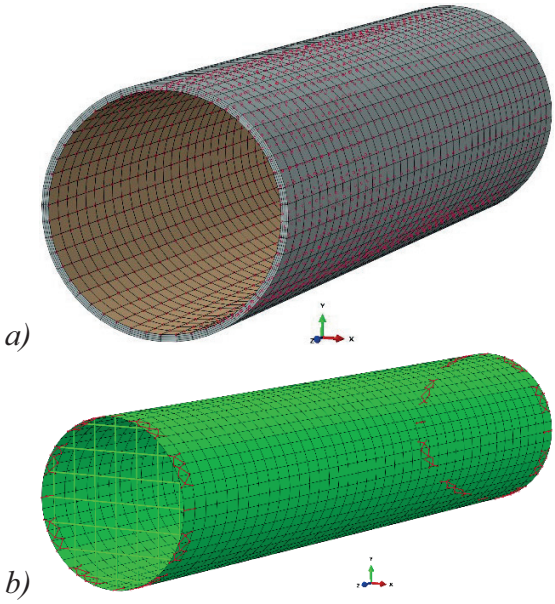

Figure 3. Tie constraints between: a) the auxiliary surface with zero stiffness and the internal tube surface; b) the reinforcement mats and the auxiliary surface (an assembly used in the cases 1-B30-20-680, 1-B60-20-680, and 1-B90-20-680 is presented)

Elastic properties of steel have been described through the Hooke's law for isotropic materials [9]:

$$\hat{\boldsymbol{\sigma}} = \hat{\hat{\mathbf{C}}} : \hat{\boldsymbol{\varepsilon}}_{el} = \lambda \operatorname{tr}\left(\hat{\boldsymbol{\varepsilon}}_{el}\right)\hat{\mathbf{I}} + 2\mu\hat{\boldsymbol{\varepsilon}}_{el}, \tag{2}$$

where $\hat{\boldsymbol{\sigma}}$ is the Cauchy stress tensor, $\hat{\boldsymbol{\varepsilon}}_{el}$ is the Green-Lagrangian elastic strain tensor, $\hat{\hat{\mathbf{C}}}$ is the elastic stiffness tensor of the fourth order, $\hat{\mathbf{I}}$ is the unit tensor, $\operatorname{tr}(\ )$ is the trace operator, and λ and μ are the Lame constants.

The Maxwell-von Mises yield criterion adopted for steel reads [10, 11]:

$$\Phi\left(\hat{\boldsymbol{\sigma}},\ \hat{\mathbf{h}}_k\right) = q - \sigma_y = 0, \tag{3}$$

where $\hat{\mathbf{h}}_k\left(\hat{\boldsymbol{\sigma}},\ \hat{\mathbf{h}}_i\right)\ \ (i,\ k = 1,\ ...,\ N;\ i \neq k)$ are state variables, q is the von Mises equivalent stress, and $\sigma_y \equiv \sigma_y\left(\overline{\varepsilon}_{pl}\right)$ is the yield stress, which, being the function of the accumulated plastic strain measured, as mentioned above, through the von Mises equivalent plastic strain $\overline{\varepsilon}_{pl}$, provides isotropic hardening.

The associated flow rule reads [12]:

$$\dot{\hat{\boldsymbol{\varepsilon}}}_{pl} = \dot{\Lambda}\frac{\partial\Phi}{\partial\hat{\boldsymbol{\sigma}}}, \tag{4}$$

where a dot above a variable hereinafter denotes its material time derivative, and $\dot{\Lambda} \geq 0$ is a scalar function determined from the compatibility condition [12]:

$$\dot{\Phi}\left(\hat{\boldsymbol{\sigma}},\ \hat{\mathbf{h}}_k\right) = 0 \quad (k = 1,\ ...,\ N), \tag{5}$$

which implies that during yielding at some material point the end of a stress vector must stay on a yield surface.

To describe steel strength properties, a simple constant fracture strain criterion, named after Mariotte, Poncelet, and de Saint-Venant [10, 13], has been adopted:

$$\overline{\varepsilon}_{pl} = \overline{\varepsilon}_{pl,f}. \tag{6}$$

It states that fracture in a material point occurs when the accumulated plastic strain (measured through the von Mises equivalent plastic strain $\overline{\varepsilon}_{pl}$) reaches its limit value $\overline{\varepsilon}_{pl,f}$, the von Mises equivalent plastic strain at fracture.

Damage of material microstructure, that occurs during material plastic straining, and its influence onto material elastic properties have not been taken into account within the constructed numerical models. It has been assumed that, once the condition (6) is reached in a material point, the material instantly fractures. Finite elements, at which integration points the fracture criterion had been met, have been eroded from the numerical model, yet their nodes have been retained, in particular as free-floating masses, if all the adjacent finite elements have been eroded.

Properties of the reinforcement material have been taken from the Russian building code SP 63.13330.2018 [1] and are given in Tables 1 and 2.

Table 1. Physical and mechanical properties of the reinforcement material (A500C grade steel according to the Russian standards)

Parameter	Value
Density ρ, $\mathrm{kg/m^3}$	7850
Young's modulus E, GPa	200
Poisson's ratio ν	0.3
Initial yield (true) stress $\sigma_y(0)$, MPa	300.45
Ultimate accumulated (engineering) strain ε_{s2}	0.024693
Von Mises equivalent plastic strain at fracture $\overline{\varepsilon}_{pl,f}$	0.023155
Ultimate (true) stress $\sigma_y\left(\overline{\varepsilon}_{pl,f}\right)$, MPa	307.50

It should be noted here, that material properties in Russian building codes are provided in terms

of engineering stresses and engineering strains. Within the numerical models all stress and strain variables have been defined in terms of true stresses and true strains. Below in the text, both engineering and true stresses and strains are used, so that comments on whether this an engineering or a true variable are given where necessary.

Table 2. True stress-true strain relationship of the reinforcement material under uniaxial tension or compression

σ, MPa	$\overline{\varepsilon}$	$\overline{\varepsilon}_{pl}$
0	0	0
300.45	0.001498876	0
307.50	0.024693	0.023155

Table 3. Physical and mechanical properties of the tube material (C355 grade steel according to the Russian standards) of various thickness t

Parameter	Value	
	$t = 10$ mm	$t = 20,\ 30$ mm
Density ρ, kg/m^3	7850	
Young's modulus E, GPa	206	
Poisson's ratio ν	0.3	
Initial yield (true) stress $\sigma_y(0)$, MPa	280.38	272.36
Ultimate accumulated (engineering) strain ε_f	0.231073	0.225161
Von Mises equivalent plastic strain at fracture $\overline{\varepsilon}_{pl,f}$	0.228308	0.222485
Ultimate (true) stress $\sigma_y\left(\overline{\varepsilon}_{pl,f}\right)$, MPa	569.55	551.21

Properties of the tube material have been taken from the Russian building code SP 16.13330.2017 "Steel structures" [14] and are given in Tables 3-5.

Concrete has been modeled as a homogeneous isotropic elastic-plastic damageable material with the non-associated flow rule, and isotropic hardening and softening using the Concrete Damaged Plasticity (CDP) model based onto the works by Lubliner et al. [2] and Lee and Fenves [15], and implemented into SIMULIA Abaqus software with a thorough description given in the software documentation [7, 8]. Some basic relationships of the CDP model are presented below.

Table 4. True stress-true strain relationship of the tube material of thickness $t = 10$ mm under uniaxial tension or compression

σ, МПа	$\overline{\varepsilon}$	$\overline{\varepsilon}_{pl}$
0	0	0
280.38	0.001358	0
351.01	0.002884	0.001180
359.51	0.026822	0.025076
569.55	0.139783	0.137018
569.55	0.231073	0.228308

Table 5. True stress-true strain relationship of the tube material of thickness t = 20, 30 mm under uniaxial tension or compression

σ, МПа	$\overline{\varepsilon}$	$\overline{\varepsilon}_{pl}$
0	0	0
272.36	0.001320	0
340.95	0.002802	0.001147
348.98	0.026065	0.024371
551.21	0.136049	0.133373
551.21	0.225161	0.222485

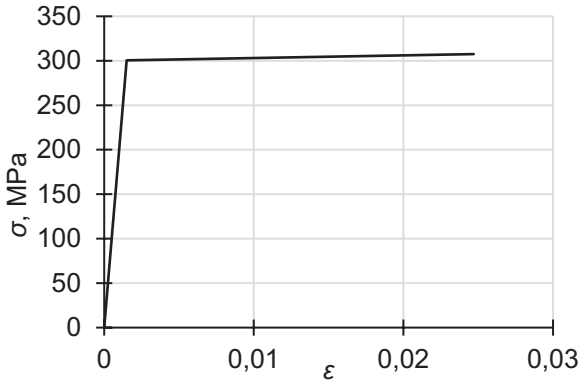

Figure 4. True stress-true strain curve of the reinforcement material (A500C grade steel according to the Russian standards) under uniaxial tension or compression

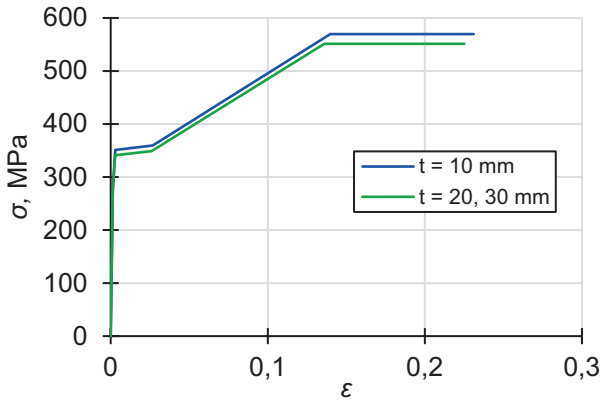

Figure 5. True stress-true strain curve of the tube material (C355 grade steel according to the Russian standards) of various thickness under uniaxial tension or compression

Damage of the material is characterized through two independent variables, d_t and d_c, scalar damage measures under tension and compression, respectively, which are functions of plastic strains, temperature and other field variables. Being increasing functions of the equivalent plastic strains $\overline{\varepsilon}_{pl,t}$ and $\overline{\varepsilon}_{pl,c}$ (accumulated during tension and compression, respectively), these scalar damage measures equal to zero for an intact material and equal to unity for a completely damaged material. Yet, to avoid problems with solution convergence, it is recommended to limit values of the damage variables to 0.99.

Within the CDP model, it is assumed that, under a general stress state, concrete elastic stiffness degradation due to its damage is isotropic. This assumption allows one to use a single scalar measure, d, to describe material damage. Using effective stresses, instead of ordinary stresses, to describe the material stress state, it appears to be possible to keep the general form of the Hooke's law (see Eq. (2)) to describe concrete elastic behaviour:

$$\hat{\bar{\boldsymbol{\sigma}}} = \hat{\mathbf{C}} : \hat{\boldsymbol{\varepsilon}}_{el}, \tag{7}$$

where $\hat{\bar{\boldsymbol{\sigma}}} = \hat{\boldsymbol{\sigma}} / (1-d)$ is the Cauchy effective stress tensor, and a colon denotes a double tensor contraction. The scalar damage measure d is defined in the following way:

$$(1-d) = (1-s_t d_c)(1-s_c d_t), \tag{8}$$

where

$$s_t = 1 - w_t r \quad (0 \le w_t \le 1), \tag{9}$$

$$s_c = 1 - w_c (1-r) \quad (0 \le w_c \le 1), \tag{10}$$

$$r(\hat{\bar{\boldsymbol{\sigma}}}) = \frac{\sum_{i=1}^{3} \langle \bar{\sigma}_i \rangle}{\sum_{i=1}^{3} |\bar{\sigma}_i|} \quad (0 \le r \le 1). \tag{11}$$

Here $\bar{\sigma}_i$ $(i = 1, 2, 3)$ are eigenvalues of the Cauchy effective stress tensor $\hat{\bar{\boldsymbol{\sigma}}}$, $\langle\ \rangle$ is the Macaulay brackets, and w_t and w_c are weight factors, which are considered to be material properties and determine the extent of stiffness recovery of the damaged material during stress sign change from compression to tension and from tension to compression, respectively. For instance, the value $w_c = 1$ means that material damage accumulated during tension cycles has no influence onto its compressive stiffness. And vice versa, the $w_c = 0$ means that material damage accumulated during tension cycles has a

direct effect onto its compressive stiffness. Intermediate values of the factor w_c correspond to partial compressive stiffness recovery. The above becomes valid for the factor w_t through simple replacement of the term "tension" by "compression", and vice versa. (For more details, an interested reader is referred to the software documentation [7, 8].)

It is commonly assumed that, when the stress sign changes from tension to compression, complete concrete stiffness recovery occurs through the crack closing mechanism, that is $w_c = 1$. At the same time, it is assumed that in the opposite case, when the stress sign changes from compression to tension, there is no stiffness recovery, i.e. $w_t = 0$.

It must be emphasized that, within the CDP model, stress state parameters are defined in terms of the effective stresses and correspondingly denoted with an over-bar. (This notation is applied only for stress variables. So, one should not confuse it with the over-bar used to denote the equivalent strain.)

Despite all the calculations within the material code are performed using the equivalent plastic strains $\overline{\varepsilon}_{pl,t}$ and $\overline{\varepsilon}_{pl,c}$ (accumulated during tension and compression, respectively), that refer to the damaged state of a material, to input material damage properties, the equivalent cracking strain $\overline{\varepsilon}_{ck,t}$ and the equivalent inelastic strain $\overline{\varepsilon}_{in,c}$, that refer to the intact state of a material, are utilized for tension and compression, respectively. The relationships between these strain measures under uniaxial loading conditions are the following:

$$\overline{\varepsilon}_{pl,t} = \overline{\varepsilon}_{ck,t} - \frac{d_t}{\left(1-d_t\right)}\frac{\sigma_t}{E_0}, \tag{12}$$

$$\overline{\varepsilon}_{pl,c} = \overline{\varepsilon}_{in,c} - \frac{d_c}{\left(1-d_c\right)}\frac{\sigma_c}{E_0}, \tag{13}$$

where E_0 is the Young's modulus of an intact material, and σ_t and σ_c are the absolute values of tensile and compressive stress, respectively. (For some graphical representation of the given relationships, an interested reader is referred to the software documentation [7, 8].)

In the CDP model, the yield criterion developed by Lubliner et al. [2] and modified by Lee and Fenves [15], to take into account that concrete properties under tension and compression are different, is implemented:

$$\Phi\left(\hat{\overline{\boldsymbol{\sigma}}},\ \hat{\mathbf{h}}_k\right) = \frac{1}{1-\alpha}\left(\sqrt{3\overline{J}_2} + \alpha\overline{I}_1 + \beta\left\langle\overline{\sigma}_1\right\rangle - \gamma\left\langle-\overline{\sigma}_1\right\rangle\right) - \overline{\sigma}_c = 0 \qquad \left(k = 1,\ \ldots,\ n\right), \tag{14}$$

where

$$\beta = \frac{\overline{\sigma}_c}{\overline{\sigma}_t}\left(1-\alpha\right) - \left(1+\alpha\right), \tag{15}$$

$\overline{I}_1$ is the first invariant of the Cauchy effective stress tensor $\hat{\overline{\boldsymbol{\sigma}}}$, $\overline{J}_2$ is the second invariant of the effective stress deviator $\hat{\overline{\mathbf{S}}}$, α and γ are non-dimensional material parameters, and $\overline{\sigma}_t \equiv \overline{\sigma}_t\left(\overline{\varepsilon}_{pl,t}\right)$ and $\overline{\sigma}_c \equiv \overline{\sigma}_c\left(\overline{\varepsilon}_{pl,c}\right)$ are the effective elastic limits under uniaxial tension and compression, respectively.

The parameter α can be determined through the following relationship:

$$\alpha = \frac{\sigma_{b0} - \sigma_{c0}}{2\sigma_{b0} - \sigma_{c0}}, \tag{16}$$

where σ_{c0} is the initial elastic limit of a material under uniaxial compression, σ_{b0} is the initial elastic limit of a material under uniform biaxial compression. As experiments revealed [2], the ratio $\sigma_{b0}/\sigma_{c0} \in \left[1.10,\ 1.16\right]$ is common for concrete, that yields $\alpha \in \left[0.08,\ 0.12\right]$.

The parameter γ can be defined as follows:

$$\gamma = \frac{3\left(1-K_c\right)}{2K_c-1}, \tag{17}$$

where for points on the yield surface (14), provided $\bar{\sigma}_1 < 0$ and $\bar{I}_1$ takes some compatible value,

$$K_c = \frac{\sqrt{3\bar{J}_2}\Big|_{\bar{\theta}=0}}{\sqrt{3\bar{J}_2}\Big|_{\bar{\theta}=\pi/3}}. \tag{18}$$

Here $\bar{\theta}$ is the effective Lode angle. A typical value [2] for concrete is $K_c = 2/3$, that yields $\gamma = 3$.

In the CDP model the non-associated flow rule is adopted:

$$\dot{\hat{\boldsymbol{\varepsilon}}}_{pl} = \dot{\Lambda}\frac{\partial \Pi}{\partial \hat{\bar{\boldsymbol{\sigma}}}}, \tag{19}$$

where the plastic potential Π is defined through the hyperbolic function:

$$\Pi\left(\hat{\bar{\boldsymbol{\sigma}}},\ \hat{\mathbf{h}}_k\right) = \sqrt{\left(\zeta\sigma_{t0}\tan\left(\psi\right)\right)^2 + 3\bar{J}_2} + \frac{1}{3}\bar{I}_1\tan\left(\psi\right) \qquad \left(k=1,\ \ldots,\ n\right). \tag{20}$$

Here ψ is the dilation angle at high confining pressure, ζ is a parameter, referred to as the eccentricity, that defines the rate at which the function (20) approaches the asymptote.

(For some graphical information on the yield surface (14) and the plastic flow potential surface (20), interested readers are referred to the software documentation [7, 8].)

To facilitate solution convergence, a viscoplastic regularization of the constitutive equations, viz. a generalization of the Duvaut-Lions regularization [16], is implemented into the CDP model. Instead of an elastic-plastic material, an elastic-viscoplastic one is considered, so that the compatibility condition (5) may not be strictly met, i.e. stresses are permitted to be outside the yield surface (14). Governing equations are as follows:

$$\dot{\hat{\boldsymbol{\varepsilon}}}_{vpl} = \frac{1}{\mu}\left(\hat{\boldsymbol{\varepsilon}}_{pl} - \hat{\boldsymbol{\varepsilon}}_{vpl}\right), \tag{21}$$

$$\dot{d}_v = \frac{1}{\mu}\left(d - d_v\right). \tag{22}$$

Here $\hat{\boldsymbol{\varepsilon}}_{vpl}$ is the viscoplastic strain tensor, $\hat{\boldsymbol{\varepsilon}}_{pl}$ is the plastic strain tensor evaluated for the original elastic-plastic material, d_v is the viscous scalar damage measure, d is the scalar damage measure evaluated for the original elastic-plastic material, and μ is the viscosity parameter, that represents the relaxation time of an elastic-viscoplastic material. For such an artificial elastic-viscoplastic material, the generalized Hooke's law (7) takes the following form:

$$\hat{\boldsymbol{\sigma}} = \left(1-d_v\right)\hat{\hat{\mathbf{C}}}:\left(\hat{\boldsymbol{\varepsilon}} - \hat{\boldsymbol{\varepsilon}}_{vpl}\right). \tag{23}$$

It must be emphasized, that in the CDP model the total damage of a material is not allowed for, and, hence, there is no element erosion during solution of any problem. While cracks cannot be modeled explicitly with such restrictions, they still can be simulated through material stiffness degradation due to damage along some planes. At the same time, with the stiffness recovery during stress sign change, implemented into the material model, and without element erosion, which forms a crack that have a finite dimension in the direction of the normal to its edges, it is possible to accurately simulate crack opening and closing.

Adopted values of the CDP model parameters for various concrete grades are given in Table 6. Some of them have been taken from Russian building code SP 63.13330.2018 "Concrete and

reinforced concrete structures. General provisions" [1], while for other parameters recommended values have been defined (see the software documentation [7, 8]).

Table 6. Physical and mechanical properties of concrete of various grades

Parameter	Value		
	B30	B60	B90
Density ρ, kg/m^3	2500		
Poisson's ratio ν	0.2		
Young's modulus E, GPa	32.5	39.5	42.5
Dilation angle ψ, °	30		
Eccentricity ζ of the plastic flow potential Π	0.1		
Ratio σ_{b0}/σ_{c0} of initial elastic limit under uniform biaxial compression to initial elastic limit under uniaxial compression	1.16		
K_c	0.67		
Relaxation time μ, s	0		
Extent w_c of stiffness recovery of the damaged material during stress sign change from tension to compression	1.0		
Extent w_t of stiffness recovery of the damaged material during stress sign change from compression to tension	0		

Adopted stress-strain and damage-strain relationships for various concrete grades are presented in Tables 7-12 and Figs. 6-11. The stress-strain relationships are based onto data from Russian building code SP 63.13330.2018 "Concrete and reinforced concrete structures. General provisions" [1], which have been recalculated in terms of true stresses and true strains. The damage-strain relationships, also specified in terms of true strains, have been established based on the author's experience and provide scalar damage measures d_t and d_c being increasing functions of the equivalent plastic strains $\overline{\varepsilon}_{pl,t}$ and $\overline{\varepsilon}_{pl,c}$, respectively.

Table 7. True stress-true strain and damage-true strain relationships for B30 grade concrete under uniaxial compression

σ_c, MPa	ε_c	$\varepsilon_{in,c}$	d_c
0	0	0	0
10.203	0.0003138	0	0
17.034	0.0019980	0.0014739	0.25
17.060	0.0034939	0.0029690	0.55
0.3417	0.0049875	0.0049770	0.99

Table 8. True stress-true strain and damage-true strain relationships for B30 grade concrete under uniaxial tension

σ_t, MPa	ε_t	$\varepsilon_{ck,t}$	d_t
0	0	0	0
0.6900	0.00002123	0	0
1.1501	0.00010000	0.00006461	0.25
1.1502	0.00014999	0.00011460	0.55
0.0230	0.00149888	0.00149817	0.99

Table 9. True stress-true strain and damage-true strain relationships for B60 grade concrete under uniaxial compression

σ_c, MPa	ε_c	$\varepsilon_{in,c}$	d_c
0	0	0	0
19.810	0.0005011	0	0
33.066	0.0019980	0.0011609	0.25
33.116	0.0034939	0.0026555	0.55
0.6633	0.0049875	0.0049707	0.99

Table 10. True stress-true strain and damage-true strain relationships for B60 grade concrete under uniaxial tension

σ_t, MPa	ε_t	$\varepsilon_{ck,t}$	d_t
0	0	0	0
1.0800	0.00002734	0	0
1.8002	0.00010000	0.00005442	0.25
1.8003	0.00014999	0.00010441	0.55
0.0361	0.00149888	0.00149796	0.99

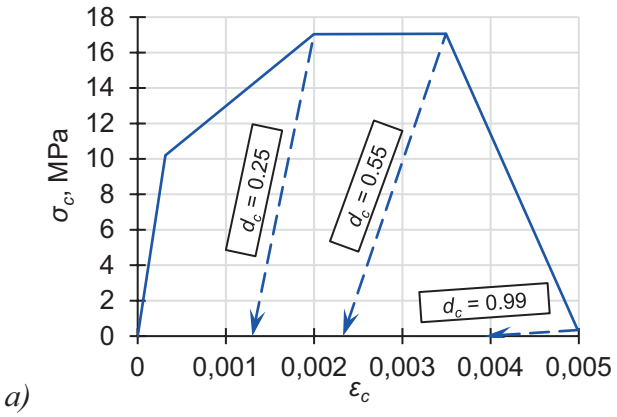

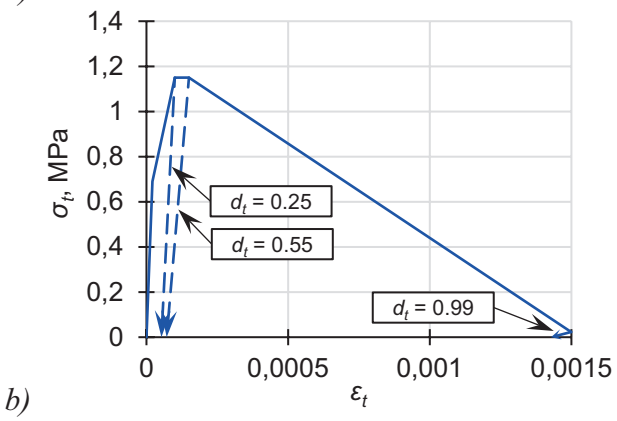

Figure 6. True stress-true strain curves for B30 grade concrete under: a) uniaxial compression; b) uniaxial tension

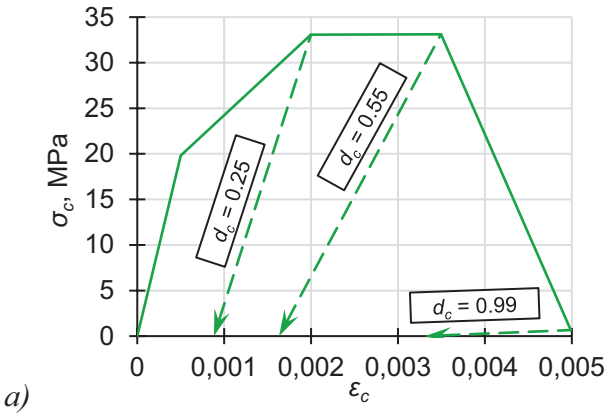

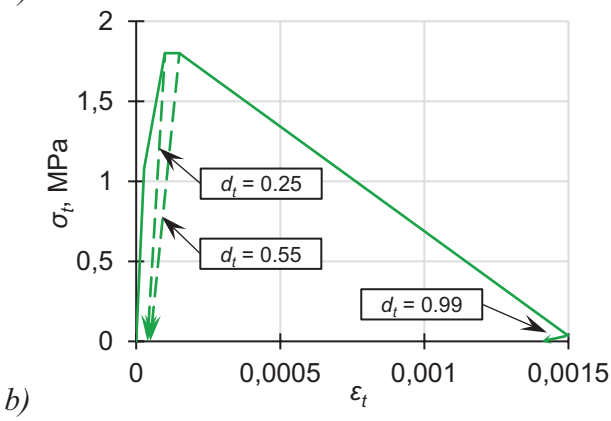

Figure 7. True stress-true strain curves for B60 grade concrete under: a) uniaxial compression; b) uniaxial tension

Table 11. True stress-true strain and damage-true strain relationships for B90 grade concrete under uniaxial compression

σ_c, MPa	ε_c	$\varepsilon_{in,c}$	d_c
0	0	0	0
26.416	0.0006210	0	0
44.088	0.0019980	0.0009606	0.25
44.131	0.0029656	0.0019272	0.55
0.8844	0.0049875	0.0049667	0.99

Table 12. True stress-true strain and damage-true strain relationships for B90 grade concrete under uniaxial tension

σ_t, MPa	ε_t	$\varepsilon_{ck,t}$	d_t
0	0	0	0
1.2900	0.00003035	0	0
2.1502	0.00010000	0.00004940	0.25
2.1503	0.00014999	0.00009939	0.55
0.0431	0.00149888	0.00149786	0.99

4. RESULTS

For each of the 33 cases considered a force-displacement curve and stress-strain states at different levels of axial compressive load, in particular limit states of the first group corresponding to local maxima of the force-displacement curve. Several force-displacement curves are presented in Fig. 12.

It has been revealed that the limit states are qualitatively similar for the cases with similar features. For instance, in the cases when vertical load acts only onto the concrete (irrespective of whether there is the steel tube or not), there is only one extremum on the force-displacement curve (see Fig. 12(c), (d)) and only one limit state of the first group corresponding to it, at which strains throughout the concrete part of some cross-section along the column reach the value of

limit strain of concrete under short-time compression, ε_{b2}.

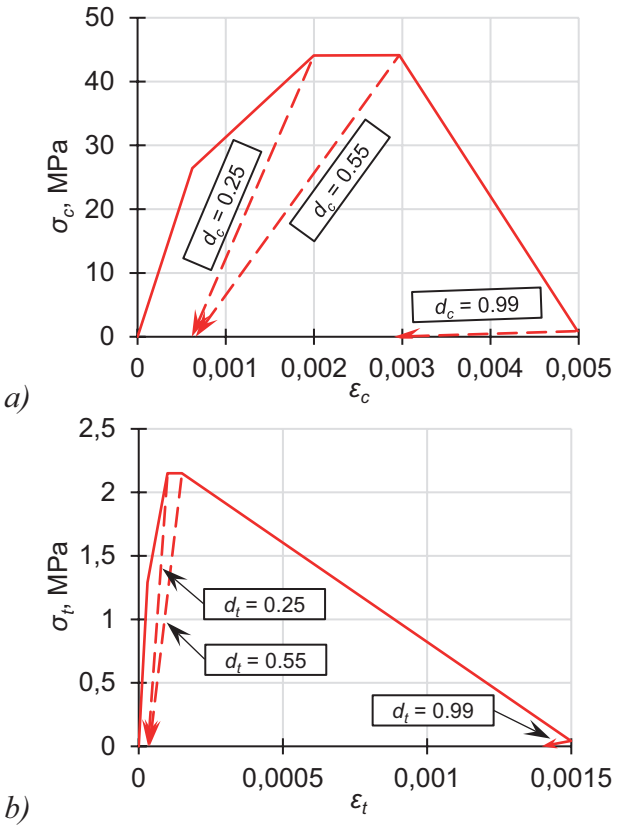

Figure 8. True stress-true strain curves for B90 grade concrete under: a) uniaxial compression; b) uniaxial tension

Such a state is also the first one of the first group of limit states for the cases when vertical load is applied onto both steel tube and concrete core. In all such cases the corresponding force-displacement curves have two extrema (see Fig. 12(b)). The second limit state of the first group corresponds to failure of the steel tube at some circumferential cross-section along the column.

In the cases when there is no concrete core and vertical load acts only onto the steel tube, also two limit states of the first group can be singled out, yet the corresponding force-displacement curves also have only one extremum (see Fig. 12(a)). The first limit state of the first group takes place when some cross-section along the column reaches plastic state throughout its area. The second limit state of the first group, as for the set of cases mentioned above, corresponds to failure of the steel tube at some circumferential cross-section along the column and is identified by the local maximum of the force-displacement curve.

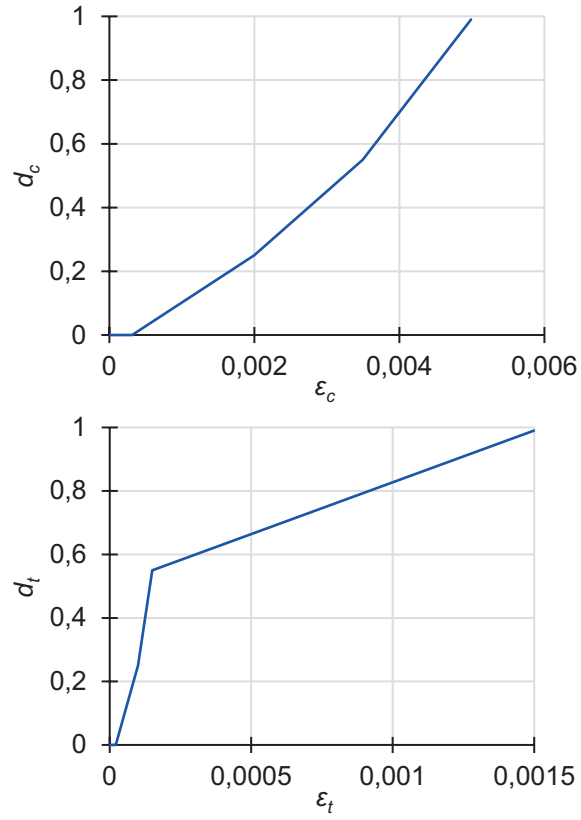

Figure 9. Damage-true strain curves for B30 grade concrete under: a) uniaxial compression; b) uniaxial tension

Examples of the limit states of the first group obtained in the considered cases are given in Fig. 13.

It is worth noting that the problem formulation when the vertical load acts only onto the concrete core can be translated into practice only within limited deformation of concrete in the vertical direction. After some deformation of the concrete core such a column in the vertical direction structural elements below and above it (for instance, floors or girders) inevitably come into contact with the ends of the steel tube. Evidently, this will change the structural scheme of the column and make it similar to the one when the vertical load from the very beginning acts onto the ends of both the steel tube and the concrete core, so that the second limit state of the first

group, viz. failure of the steel tube at some circumferential cross-section along the column, will eventually appear, if the vertical loading continues.

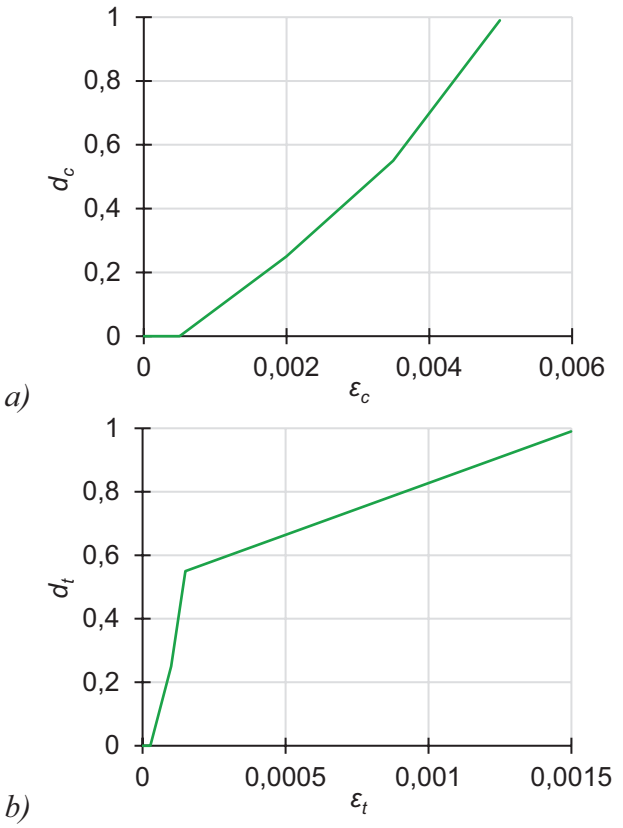

Figure 10. Damage-true strain curves for B60 grade concrete under: a) uniaxial compression; b) uniaxial tension

Moreover, in all the cases with the steel tube and the concrete core failure of the tube at some circumferential cross-section along the column does not immediately lead to a complete loss of structural element capacity. Even the fractured tube continues retaining the concrete core, which is totally crushed by this point, until it will be ruptured by internal pressure created by the concrete crumbles, that can be even considered as the third limit state of the first group.

Since both of the issues mentioned above take place only under very high deformation of the concrete core in the vertical direction, they have not been considered within the present research, because it has no practical sense.

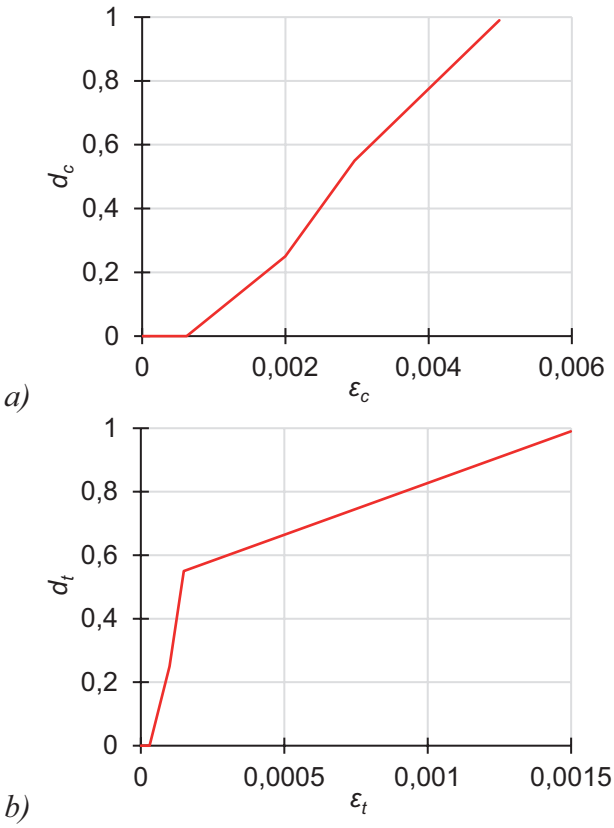

Figure 11. Damage-true strain curves for B90 grade concrete under: a) uniaxial compression; b) uniaxial tension

Parameters of the limit states of the first group calculated for all the 33 cases considered are given in Tables 13 and 14.

Below, in Figs. 14, 16, and 18, force-displacement curves are presented for the simulated cases, grouped by different shared features to facilitate their comparison and estimation of influence of various problem parameters onto the steel tube confined concrete column strength.

In Figs. 15, 17, and 19, parameters of the limit states of the first group for the cases given in Figs. 14, 16, and 18, respectively, are depicted. Again, grouping the cases by different shared features allows one to identify, which problem parameters have the largest effect onto the steel tube confined concrete column strength and whether their influence is monotonic or not.

Table 13. Parameters of the first limit state of the first group calculated for all the 33 cases

Case No.	Displacement of the top die, m	Load, kN
1-0-10-0	0.0113	7851.377
1-B30-10-700	0.0079	16867.18
1-B60-10-700	0.0083	21739.31
1-B90-10-700	0.0051	22855.93
1-0-20-0	0.0106	15001.11
1-B30-20-680	0.0081	24701.27
1-B60-20-680	0.0079	28890.05
1-B90-20-680	0.0056	29228.33
1-0-30-0	0.0106	22199.15
1-B30-30-660	0.0106	32186.44
1-B60-30-660	0.0083	35736.06
1-B90-30-660	0.0057	35078.73
2-B30-0-720	0.0032	5187.777
2-B60-0-720	0.0031	9260.619
2-B90-0-720	0.0027	11707.21
2-B30-0-700	0.0035	4856.732
2-B60-0-700	0.0033	8747.732
2-B90-0-700	0.0032	11234.92
2-B30-0-680	0.0040	4761.817
2-B60-0-680	0.0033	8275.723
2-B90-0-680	0.0028	10379.59
2-B30-0-660	0.0034	4195.609
2-B60-0-660	0.0034	7837.114
2-B90-0-660	0.0029	9879.836
2-B30-10-700	0.0108	19250.89
2-B60-10-700	0.0104	24840.17
2-B90-10-700	0.0082	24992.45
2-B30-20-680	0.0125	29500.08
2-B60-20-680	0.0127	34545.12
2-B90-20-680	0.0101	31897.50
2-B30-30-660	0.0155	39266.76
2-B60-30-660	0.0150	43777.00
2-B90-30-660	0.0107	36855.08

In Fig. 20, and Tables 15 and 16 a steel tube confined concrete column strength increase factor k is given. It has been calculated through the following relation:

$$k = F/F_0 , \qquad (24)$$

where F is the steel tube confined concrete column strength, and F_0 is the strength of the column made of plain concrete with the diameter equal to that of the concrete core of the steel tube confined concrete column.

Table 14. Parameters of the second limit state of the first group calculated for the relevant cases

Case No.	Displacement of the top die, m	Load, kN
1-0-10-0	0.5648	15972.75
1-B30-10-700	0.5573	24272.70
1-B60-10-700	0.5560	25232.82
1-B90-10-700	0.5462	25434.39
1-0-20-0	0.4084	27563.00
1-B30-20-680	0.5046	37025.38
1-B60-20-680	0.5056	38384.91
1-B90-20-680	0.5130	39368.96
1-0-30-0	0.3573	37933.93
1-B30-30-660	0.3857	45513.13
1-B60-30-660	0.3878	47007.78
1-B90-30-660	0.3836	47231.08

Table 15. Steel tube confined concrete column strength increase relative to that of the column made of plain concrete in the cases, when the vertical load acts onto both the steel tube and the concrete core

Tube thickness, mm	Concrete grade		
	B30	B60	B90
0	1	1	1
10	3.47	2.49	2.03
20	5.19	3.49	2.82
30	7.67	4.56	3.55

Table 16. Steel tube confined concrete column strength increase relative to that of the column made of plain concrete in the cases, when the vertical load acts only onto the concrete core

Tube thickness, mm	Concrete grade		
	B30	B60	B90
0	1	1	1
10	3.96	2.84	2.22
20	6.20	4.17	3.07
30	9.36	5.59	3.73

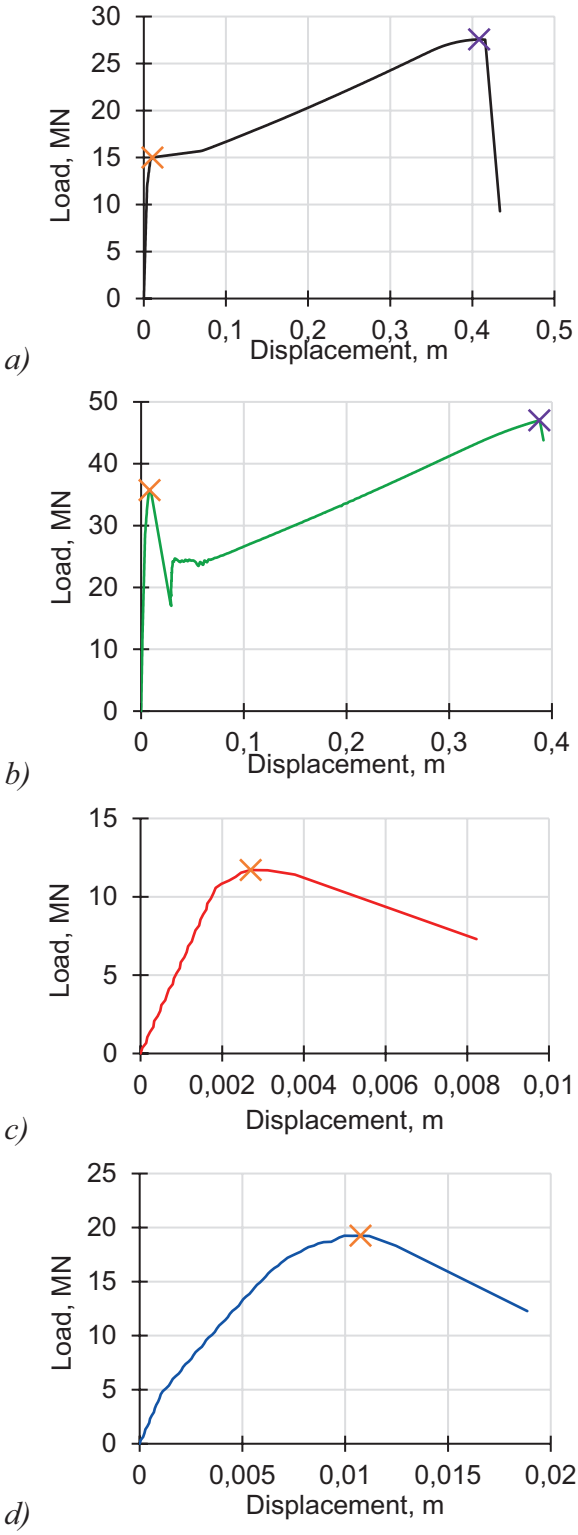

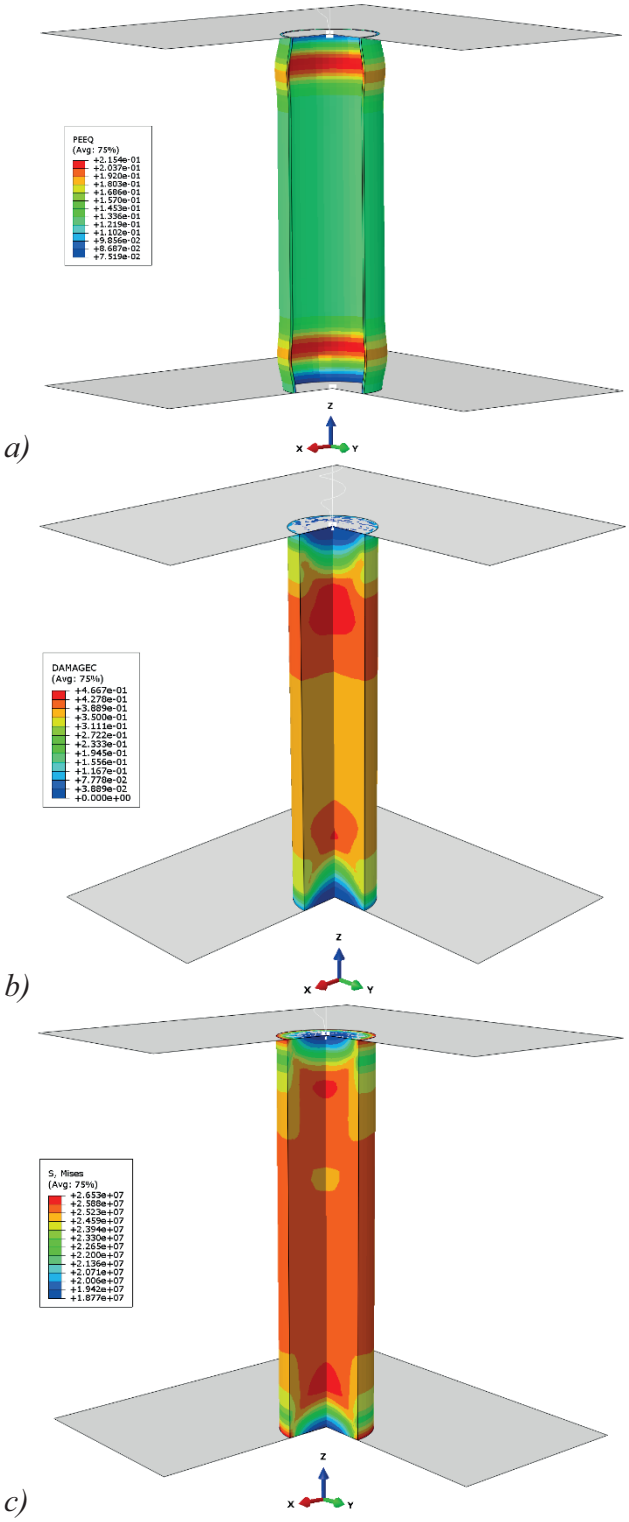

Figure 12. Force-displacement curves obtained for the cases: a) 1-0-20-0; b) 1-B60-30-660; c) 2-B90-0-720; d) 2-B30-10-700 (limit states of the first group are marked with orange and purple oblique crosses)

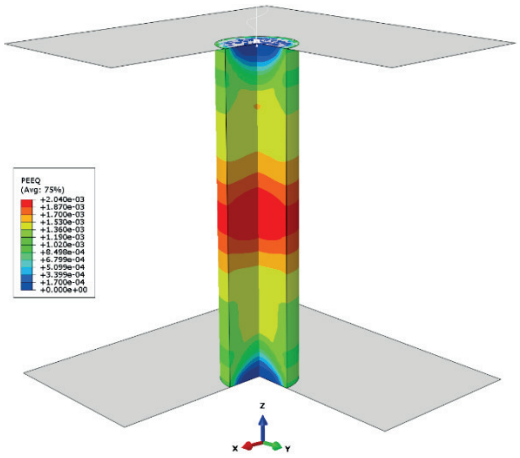

d)

Figure 13. Limit states of the first group obtained in different cases: a) the von Mises equivalent plastic strain $\overline{\varepsilon}_{pl}$ prior to tube failure in the case 1-0-20-0; b) scalar measure of concrete damage due to compression d_c prior to concrete core failure in the case 1-B60-30-660; c) the von Mises equivalent stress q prior to concrete failure in the case 2-B90-0-720; d) the von Mises equivalent plastic strain $\overline{\varepsilon}_{pl}$ in the concrete core prior to its failure in the case 2-B30-10-700

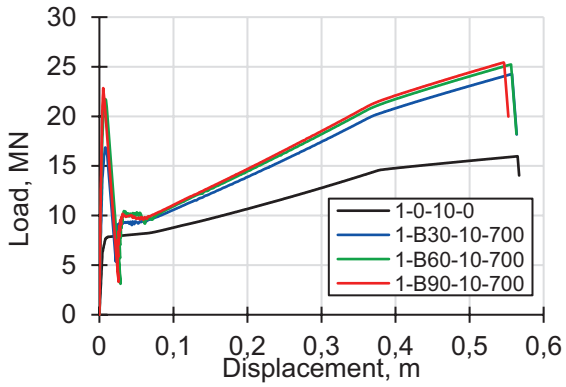

a)

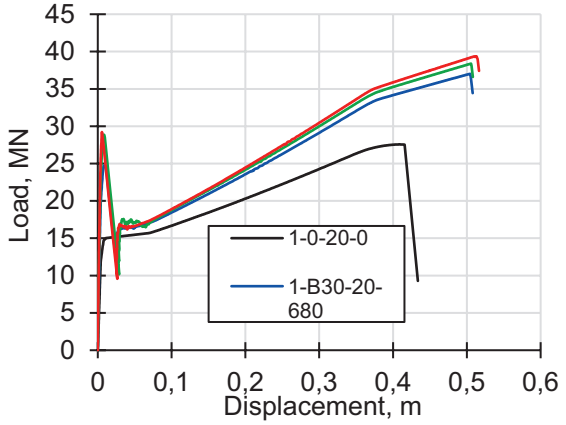

b)

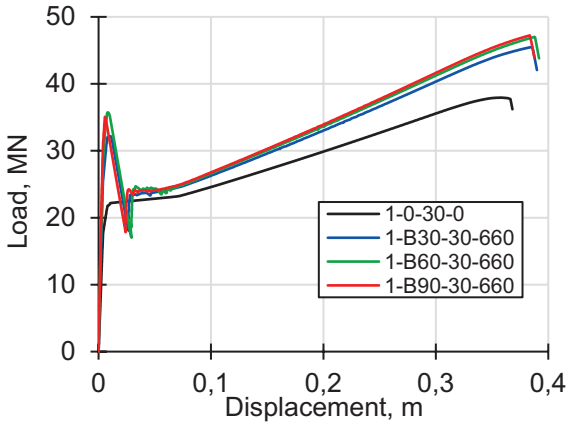

c)

Figure 14. Force-displacement curves for different groups of cases: a) 10 mm thick steel tube; b) 20 mm thick steel tube; c) 30 mm thick steel tube

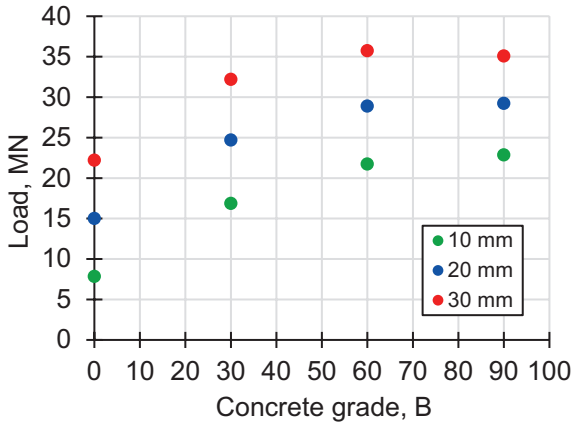

a)

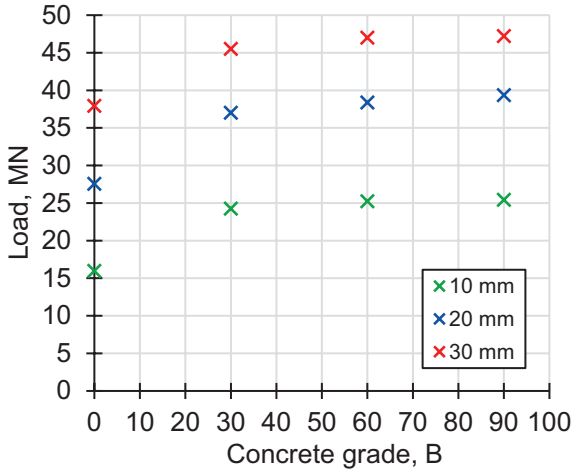

b)

Figure 15. Influence of the concrete grade and the tube thickness onto parameters of the limit states of the first group in the cases, which force-displacement curves are given in Fig. 14: a) the first limit state of the first group; b) the second limit state of the first group

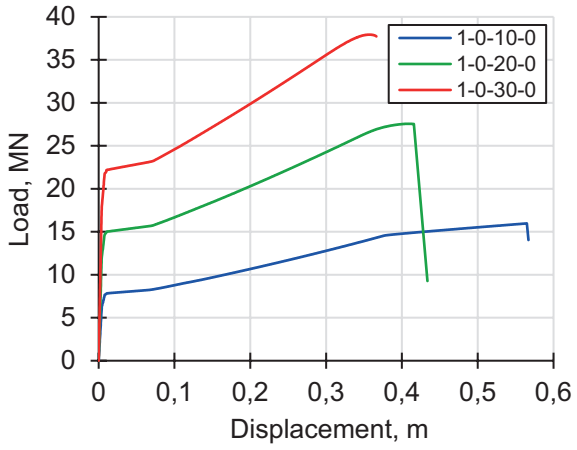

a)

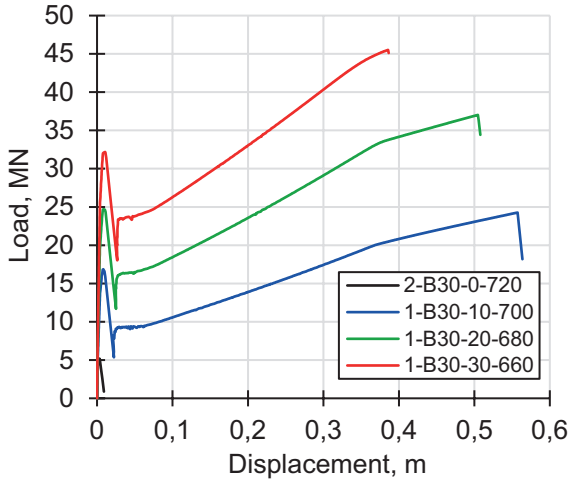

b)

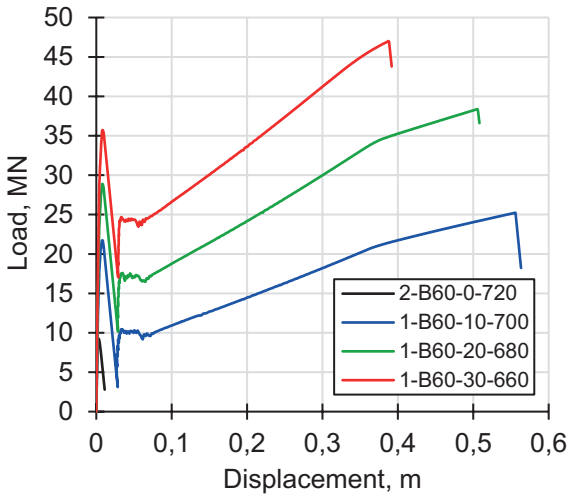

c)

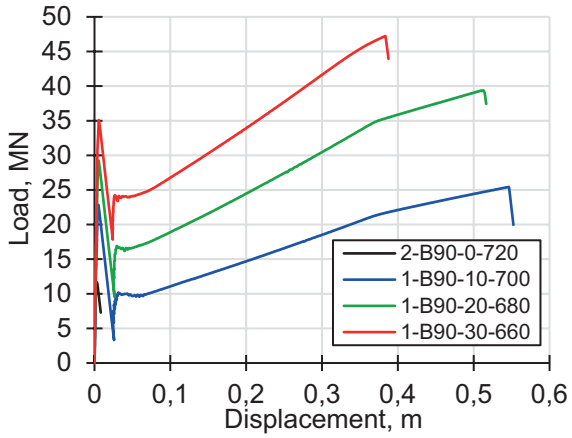

d)

Figure 16. Force-displacement curves for different groups of cases: a) no concrete; b) B30 grade concrete; c) B60 grade concrete; d) B90 grade concrete

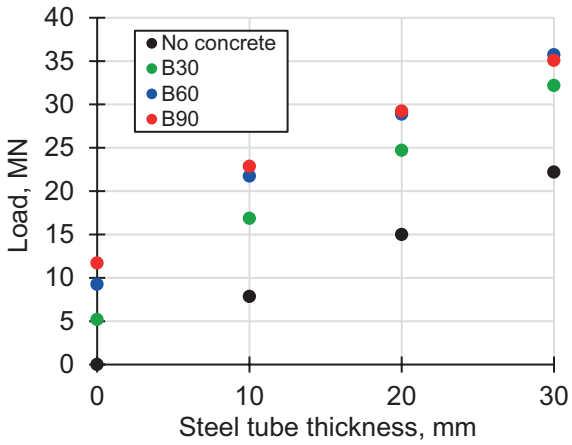

a)

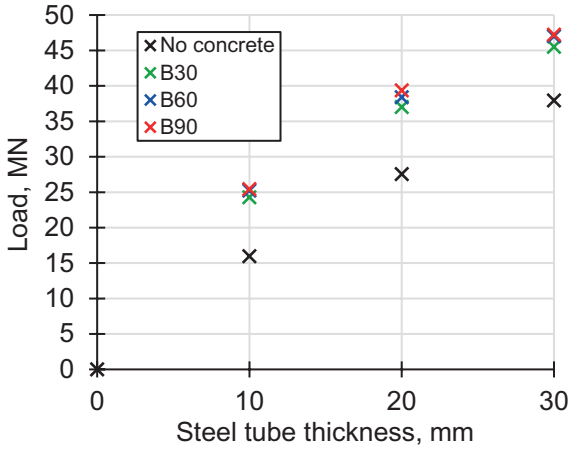

b)

Figure 17. Influence of the concrete grade and the tube thickness onto parameters of the limit states of the first group in the cases, which force-displacement curves are given in Fig. 16: a) the first limit state of the first group; b) the second limit state of the first group

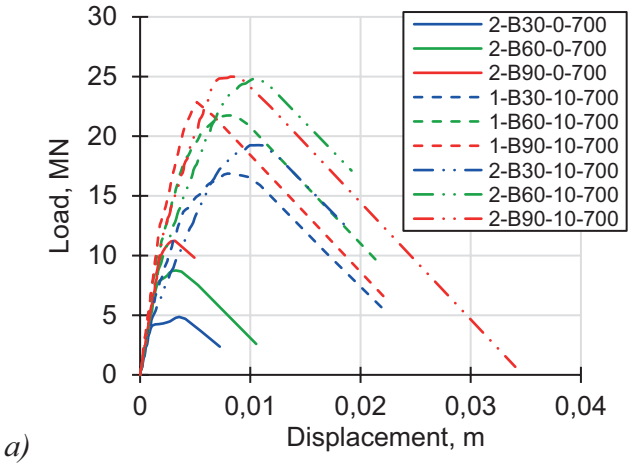

a)

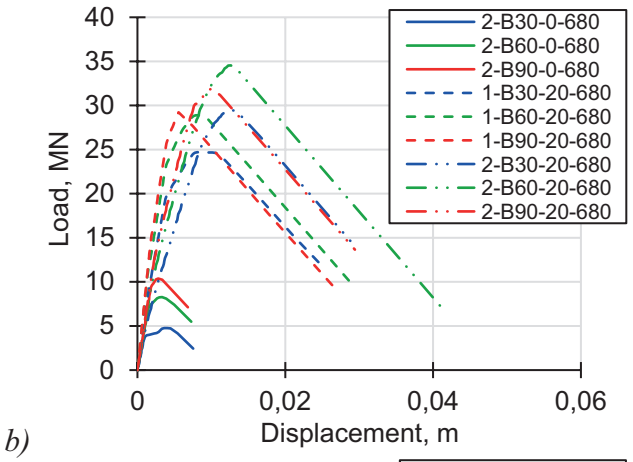

b)

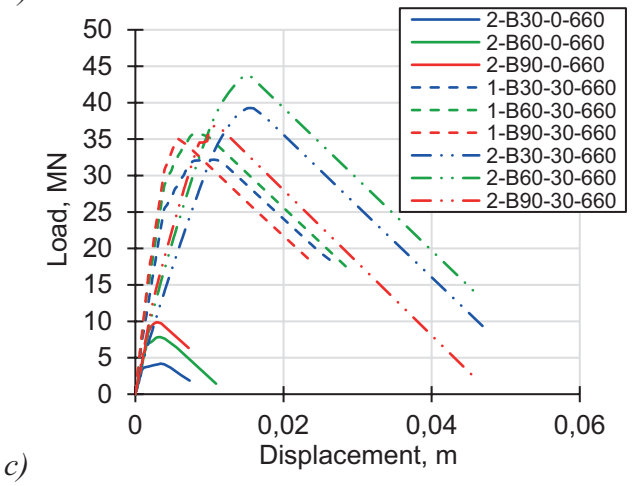

c)

Figure 18. Force-displacement curves for different groups of cases: a) concrete core diameter of 700 mm; b) concrete core diameter of 680 mm; c) concrete core diameter of 660 mm

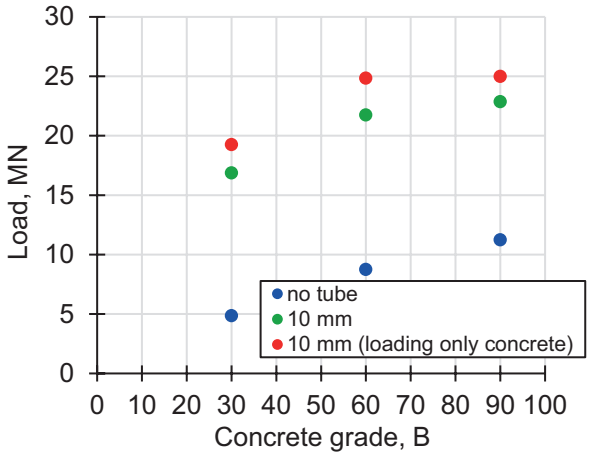

a)

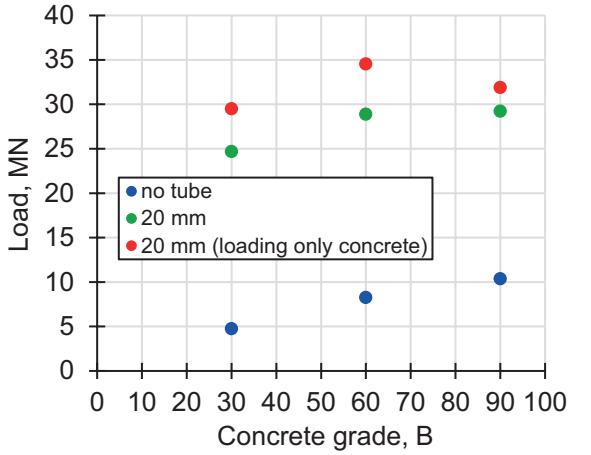

b)

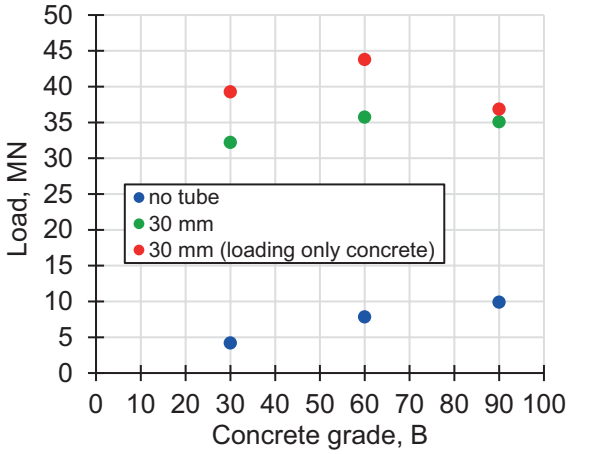

c)

Figure 19. Parameters of the first limit state of the first group in the cases, which force-displacement curves are given in: a) Fig. 10(a); b) Fig. 10(b); c) Fig. 10(c)

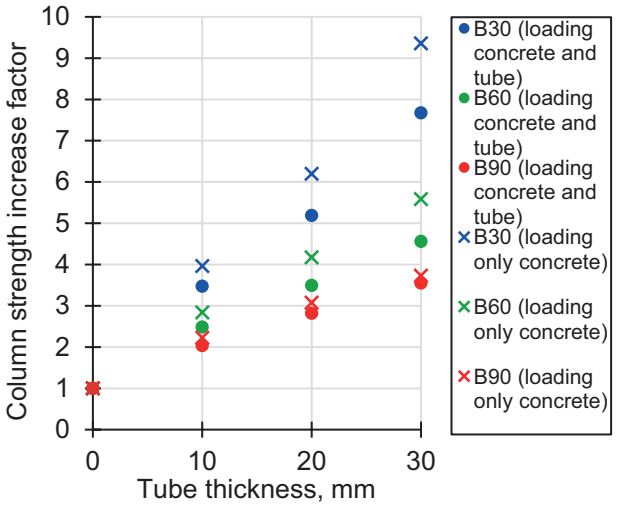

Figure 20. Steel tube confined concrete column strength increase relative to that of the column made of plain concrete

5. DISCUSSION

First of all, the very concept of the steel tube confined concrete column has been confirmed to be viable and effective. Taking the calculated values of the ultimate load for the first limit state of the first group (see Table 13) in the cases, for instance, 1-0-20-0 and 2-B30-0-680, that are 15 001.11 kN and 4 761.82 kN, respectively, one can see that their sum, which equals to 19 762.93 kN, is less than the values of the ultimate load (for the first limit state of the first group) in the relevant cases 1-B30-20-680 and 2-B30-20-680, that are 24701.27 kN and 29500.08 kN, respectively. The synergy effect of the steel tube and the concrete core is clear. (Using Table 13, one can ascertain that this is true for all other combinations.)

Several important conclusions concerning effects of concrete grade and steel tube thickness onto column strength can be made already from Figs. 14 and 15. In the cases, when the vertical load acts onto the ends of both the concrete core and the steel tube, the strength of the steel tube confined concrete column, measured through parameters of both the first and the second limit states of the first group, increases (as anticipated) with the tube thickness and (or) concrete grade. Yet, influence of these problem parameters is non-linear.

Considering the first limit state of the first group and comparing the ultimate vertical load for the steel tube confined concrete column with that for the tubular steel column, one can see, that concrete core contribution to the column strength remains almost the same in absolute terms with the tube thickness increase for all the considered concrete grades, but diminishes in relative terms. Moreover, increasing the concrete grade above B60 has insignificant (even negative in the case 1-B90-30-660) effect onto the column strength (see also Fig. 17(a)). The reason is simple. The guideline value of the limit strain under short-time compression ε_{b2} decreases with the grade for the concrete grades above B60, i.e. the high-strength concrete is more brittle. And this limit strain decrease (almost) balances out the increase of the concrete compressive strength with regard to the amount of inelastic work being able to be done by the concrete of a particular grade.

Looking at the shape of the force-displacement curves given in Fig. 14, it becomes evident that the second limit state of the first group is governed by the strength of the steel tube. Yet, the very existence of the concrete core has a significant positive effect onto the tube strength, and the thinner is the tube, the larger is the effect. Despite the concrete core is totally crushed by the time the second limit state of the first group is reached, it still has a residual bulk stiffness and facilitates tube stability. Since the second limit state of the first group is governed by the tube buckling, such an effect caused by the concrete core is unsurprising. At the same time, the concrete grade has a minor effect onto the parameters of the second limit state of the first group, that is clearly seen in Fig. 17(b). It is also expected. The bulk stiffness of the concrete crumbles is only a small fraction of that of intact concrete, so that the difference between various concrete grades is small in absolute terms.

One can see in Figs. 14 and 16 that, in the cases when the vertical load acts onto both the steel tube and the concrete core, the value of the displacement corresponding to the second limit state of the first group decreases with the tube thickness, and it is almost independent of the

concrete grade. This is caused by the tube deformation pattern, that is buckling, during which the tube wall experiences local bending along the circumference. During single-axis bending, providing the same curvature of the neutral axis, the larger is the structural element thickness, the higher is its strain along the neutral axis. Hence, for a thick tube, the ultimate strain is accumulated earlier during its buckling than for a thinner tube.

As it can be seen in Fig. 17, in the cases when the vertical load acts onto both the steel tube and the concrete core, the ultimate load values for both limit states of the first group vary almost linearly with the tube thickness for all the considered concrete grades. This linear dependence also takes place in the case of the tubular steel column, depicted in Fig. 17 as well.

It follows from Figs. 18 and 19, that the steel tube confinement increases the column strength, characterized by the first limit state of the first group, several times compared to that of the column made of plain concrete and having the same diameter, as the diameter of the concrete core. Moreover, in the cases, when the steel tube acts only as a confinement (and the vertical load acts only onto the concrete core), its effect onto the steel tube confined concrete column strength is even greater than in the cases, when the vertical load acts onto the ends of both the steel tube and the concrete core. The explanation is simple. The steel tube is barreling under compression, that decreases its confining effect.

From Fig. 20, it is clear that the steel tube confined concrete column strength, associated with the first limit state of the first group, varies almost linearly with the tube thickness for both considered structural schemes of the column, and for all the considered concrete grades, as has been already partially discussed above.

6. CONCLUSION

In the present work, the axially compressed circular steel tube confined concrete columns have been parametrically analyzed through numerical simulation. Several reference cases with the plain concrete circular columns and the tubular steel columns have also been simulated. Totally, 33 different cases have been considered. The general aim has been to confirm the effectiveness of concrete confinement and quantitatively estimate it.

To perform the parametrical analysis, two limit states of the first group, characterized by values of the vertical displacement of the column end and the vertical load, have been defined for the considered cases. The first limit state of the first group has been associated with either concrete failure throughout some cross-section along the column or, for tubular steel columns, transition of some cross-section along the column into the plastic phase throughout its area. The second limit state of the first group has been associated with failure of the steel tube (in the relevant cases) at some circumferential cross-section along the column.

The first group of column limit states and corresponding column failure mechanisms have been investigated, qualitatively and quantitatively, with regard to their dependence onto column structural scheme (viz. whether the vertical load acts onto the end of both the concrete core and the steel tube or only the concrete core is subjected to axial loading, while the steel tube acts only as a confinement), steel tube thickness and concrete grade.

The effectiveness of concrete confinement has been clearly confirmed.

It has been revealed that the steel tube confined concrete column strength, associated with the first limit state of the first group, varies almost linearly with the tube thickness for both considered structural schemes of the column, and for all the considered concrete grades. The largest value of the column strength increase factor k (defined as the ratio of the steel tube confined concrete column strength to the strength of the column made of plain concrete with the diameter equal to that of the concrete core of the steel tube confined concrete column) amounts to 9.36 and has been calculated for the B30 grade concrete and the structural scheme of the column,

in which the steel tube with the thickness of 30 mm acts only as a confinement.

It has also appeared that, when the steel tube acts only as a confinement and the vertical load acts only onto the concrete core, the steel tube confining effect is stronger and the column strength is higher than in the case, when the vertical load acts onto the end of both the concrete core and the steel tube.

Finally, it has been shown that it is ineffective to utilize concrete grades above B60, since the high-strength concrete is more brittle.

Speculating onto directions for future research, one may propose to extend the present one onto eccentric compression and other shapes of the column cross-section. Various techniques of steel confinement anchorage into the concrete core also seems to be a prospective area of research.

7. ACKNOWLEDGEMENT

The research was funded by the National Research Moscow State University of Civil Engineering.

REFERENCES

1. SP 63.13330.2018. Concrete and reinforced concrete structures. General provisions / Russian Building Codes and Regulations 52-01-2003. – With Revs. 1, 2. – Moscow, Russia: Standartinform, 2018, 2020; Russian Standardization Institute, 2022. – VI, 143 p., 21 p., 12 p. : illust.
2. **Lubliner, J., Oliver, J., Oller, S., Oñate, E.** A plastic-damage model for concrete // Int. J. Solids Struct. – 1989. – Vol. 25. – Iss. 3. – P. 229-326.
3. **Argyris, J.H., Faust, G., Szimmat, J., Warnke, E.P., Willam, K.J**. Recent developments in the finite element analysis of prestressed concrete reactor vessels // Nucl. Engng. Design. – 1974. – Vol. 28. – Iss. 1. – P. 42-75.
4. **Willam, K.J., Warnke, E.P.** Constitutive model for the triaxial behavior of concrete / In: IABSE reports. Volume 19. Proceedings of the Seminar on Concrete Structures Subjected to Triaxial Stresses, Bergamo, Italy, 1974. – Zurich, Switzerland: IABSE, 1975. – P. 1-30.
5. **Ottosen, N.S.** A failure criterion for concrete // J. Engng. Mech. Div., Proc. ASCE. – 1977. – Vol. 103. – Iss. EM4. – P. 527-535.
6. **Hsieh, S.S., Ting, E.C., Chen, W.F.** An elastic-fracture model for concrete / In: Proceedings of the 3rd ASCE-EMD Specialty Conference on Mechanics in Engineering, Austin, TX, USA, 1979. – [New York, NY, USA]: [ASCE], 1979. – P. 437-441.
7. Abaqus Analysis User's Manual / Providence, RI, USA: Dassault Systèmes Simulia Corp., 2025.
8. Abaqus Theory Manual / Providence, RI, USA: Dassault Systèmes Simulia Corp., 2025.
9. **Nowacki, W.** The theory of elasticity (in Russian) / Transl. from Pol. by B.E. Pobedrya. – Moscow, USSR: Mir, 1975. – 872 p.
10. **Timoshenko, S.P.** History of strength of materials. With a brief account of the history of theory of elasticity and theory of structures / New York, NY, USA: McGraw-Hill Book Company, 1953. – 452 p.
11. **Von Mises, R.** Mechanik der festen Körper im plastisch deformablen Zustand // Nachr. Ges. Wiss. Göttingen. Math.-Phys. – 1913. – Vol. 1. – P. 582-592.
12. **Khan, A.S., Huang, S.** Continuum theory of plasticity / New York, NY, USA: John Wiley & Sons, 1995. – 431 p.
13. **Mariotte, M.** Traité du mouvement des eaux et des autres corps fluides / Divisé en cinq parties, par feu M. Mariotte de l'Académie Royale des Sciences, mis en lumière par les soins de M. de la Hire, lecteur et professeur du Roy pour les mathématiques et de l'Académie Royale des Sciences. – Paris, France: E. Michallet, 1686.

14. SP 16.13330.2017. Steel structures / Russian Building Codes and Regulations II-23-81*. – With Revs. 1, 2, 3, 4, 5, 6. – Moscow, Russia: Standartinform, 2017, 2019, 2020; Russian Standardization Institute, 2022, 2022, 2023, 2025. – V, 140 p., 8 p., 17 p., 18 p., 2 p., 6 p., 13 p. : illust.
15. **Lee, J., Fenves, G.L.** Plastic-damage model for cyclic loading of concrete structures // J. Eng. Mech. – 1998. – Vol. 124. – Iss. 8. – P. 892-900.
16. **Duvaut, G., Lions, J.L.** Les inéquations en Mécanique et en Physique / Paris, France: Dunod, 1972. – XX, 387 p.

СПИСОК ЛИТЕРАТУРЫ

1. СП 63.13330.2018 «СНиП 52-01-2003. Бетонные и железобетонные конструкции. Основные положения» : Свод правил : Изд. офиц. : Утв. … " " 2019 г. ; с Изм. 1, 2, утв. … " " 2020 г., 2022 г. / Министерство строительства и жилищно-коммунального хозяйства Российской Федерации (Минстрой РФ). – М.: Стандартинформ, 2018, 2020; Российский институт стандартизации, 2022. – VI, 143 с., 21 с., 12 с. : ил.
2. **Lubliner, J., Oliver, J., Oller, S., Oñate, E.** A plastic-damage model for concrete // Int. J. Solids Struct. – 1989. – Vol. 25. – Iss. 3. – P. 229-326.
3. **Argyris, J.H., Faust, G., Szimmat, J., Warnke, E.P., Willam, K.J.** Recent developments in the finite element analysis of prestressed concrete reactor vessels // Nucl. Engng. Design. – 1974. – Vol. 28. – Iss. 1. – P. 42-75.
4. **Willam, K.J., Warnke, E.P.** Constitutive model for the triaxial behavior of concrete / In: IABSE reports. Volume 19. Proceedings of the Seminar on Concrete Structures Subjected to Triaxial Stresses, Bergamo, Italy, 1974. – Zurich, Switzerland: IABSE, 1975. – P. 1-30.
5. **Ottosen, N.S.** A failure criterion for concrete // J. Engng. Mech. Div., Proc. ASCE. – 1977. – Vol. 103. – Iss. EM4. – P. 527-535.
6. **Hsieh, S.S., Ting, E.C., Chen, W.F.** An elastic-fracture model for concrete / In: Proceedings of the 3rd ASCE-EMD Specialty Conference on Mechanics in Engineering, Austin, TX, USA, 1979. – [New York, NY, USA]: [ASCE], 1979. – P. 437-441.
7. Abaqus Analysis User's Manual / Providence, RI, USA: Dassault Systèmes Simulia Corp., 2025.
8. Abaqus Theory Manual / Providence, RI, USA: Dassault Systèmes Simulia Corp., 2025.
9. **Новацкий, В.** Теория упругости / Пер. с пол. Б.Е. Победри. – М.: Мир, 1975. – 872 с.
10. **Timoshenko, S.P**. History of strength of materials. With a brief account of the history of theory of elasticity and theory of structures / New York, NY, USA: McGraw-Hill Book Company, 1953. – 452 p.
11. **Von Mises, R.** Mechanik der festen Körper im plastisch deformablen Zustand // Nachr. Ges. Wiss. Göttingen. Math.-Phys. – 1913. – Vol. 1. – P. 582-592.
12. **Khan, A.S., Huang, S.** Continuum theory of plasticity / New York, NY, USA: John Wiley & Sons, 1995. – 431 p.
13. **Mariotte, M**. Traité du mouvement des eaux et des autres corps fluides / Divisé en cinq parties, par feu M. Mariotte de l'Académie Royale des Sciences, mis en lumière par les soins de M. de la Hire, lecteur et professeur du Roy pour les mathématiques et de l'Académie Royale des Sciences. – Paris, France: E. Michallet, 1686.
14. СП 16.13330.2017 «СНиП II-23-81*. Стальные конструкции» : Свод правил : Изд. офиц. : Утв. … " " 2017 г. ; с Изм. 1, 2, 3, 4, 5, 6, утв. … " " 2019 г., 2020 г., 2022 г., 2022 г, 2023 г, 2025 г. / Министерство строительства и жилищно-коммунального хозяйства Российской Федерации (Минстрой РФ). – М.: Стандартинформ, 2017, 2019, 2020; Российский институт

стандартизации, 2022, 2022, 2023, 2025. – V, 140 с., 8 с., 17 с., 18 с., 2 с., 6 с., 13 с. : ил.
15. **Lee, J., Fenves, G.L.** Plastic-damage model for cyclic loading of concrete structures // J. Eng. Mech. – 1998. – Vol. 124. – Iss. 8. – P. 892-900.
16. **Duvaut, G., Lions, J.L.** Les inéquations en Mécanique et en Physique / Paris, France: Dunod, 1972. – XX, 387 p.

Vladislav Vladimirovich Vershinin – senior lecturer at the Department of Structural Metal and Timber, National Research Moscow State University of Civil Engineering (NRU MGSU), 26 Yaroslavskoe shosse, Moscow, 129337, Russia; vlodya_91@mail.ru; +79165225509.

Владислав Владимирович Вершинин – старший преподаватель кафедры Металлических и деревянных конструкций, Национальный исследовательский Московский государственный строительный университет (НИУ МГСУ), д. 26, Ярославское шоссе, г. Москва, 129337, Россия; vlodya_91@mail.ru